

**Characterisation of Silicon Oxide Coatings using Microwave
Plasma Enhanced Chemical Vapour Deposition**

Emily May McNulty

Submitted in accordance with the requirements for the degree of
Doctor of Philosophy

The University of Leeds
School of Mechanical Engineering

May 2022

The candidate confirms that the work submitted is her own, except where work which has formed part of jointly authored publications has been included. The contribution of the candidate and the other authors to this work has been explicitly indicated below. The candidate confirms that appropriate credit has been given within the thesis where reference has been made to the work of others.

Cross-section scanning electron microscopy and preparation of samples for transmission electron microscopy was undertaken by Stuart Micklethwaite and John Harrington. Transmission electron microscope operation was carried out by Dr Zabeada Aslam. Xray photoelectron spectroscopy measurements were completed at HarwellXPS.

This copy has been supplied on the understanding that it is copyright material and that no quotation from the thesis may be published without proper acknowledgement.

© 2022 The University of Leeds and Emily May McNulty

Acknowledgments

First and foremost, I would like to extend my deepest gratitude to my supervisor Dr Liuquan Yang for his guidance and support throughout this thesis. Your insight and encouragement has made the whole process very enjoyable, thank you.

I would also like to thank my secondary supervisors Dr Michael Bryant and Dr Wassim Taleb for their unwavering support throughout this research project, it has been a pleasure to work with you both. Thanks also goes to Hauzer Techno Coating for sponsoring this PhD and providing guidance and support throughout.

I would like to thank the technical staff within iFS and LEMAS for their help and support throughout my time at Leeds, specifically Stuart and John for their help with electron imaging. Thank you to Chun, for her training and assistance on much of the lab equipment.

To the members of the iT-CDT, it has been a pleasure to work with you and to share this journey together. A very special thank you goes to Kimberley Matthews and Professor Anne Neville who have supported me both academically and personally throughout this project, without your support and encouragement, this thesis would not have been possible.

Finally, and most importantly, a big thank you to my family and fiancé. I would never have made it this far without the love, wisdom and support you have given to me. To my amazing Dad, sister and brother, I would not be the person I am today without you. I hope I have made you proud.

For Mum

Abstract

The drive towards net zero carbon usage has been increasingly important over the past couple of decades. The reduction of fossil fuels and the need for renewable energy resources is predominant within the automotive industry. Hydrogen fuel cells are an excellent alternative to the current internal combustion engines, however, the need to find suitable materials and coatings, which can withstand the corrosive environments encountered is becoming more prevalent. Silicon oxide (SiO_x) coatings are a potential coating for the use in hydrogen fuel cells to withstand the corrosive environments and enhance the lifetime of the fuel cells.

In this study, the use of microwave plasma enhanced chemical vapour deposition (MW-PECVD) has been investigated as a way to deposit SiO_x coatings onto high-speed steel (HSS) substrates. A matrix of coatings has been developed using different hexamethyl disiloxane (HMDSO) and oxygen (O_2) ratios during the deposition processes, to characterise the mechanical, composition and microstructural properties. The corrosion behaviour of the coatings has also been established, using electrochemical techniques in a 1 molar sodium chloride (NaCl) solution. A further matrix of coatings has also been developed and characterised with a variation in the coating thickness.

A Hauzer Flexicoat 850 deposition system at the University of Leeds was used to deposit 20 unique SiO_x coatings using a novel MW-PECVD technique. The coatings were characterised to quantify their hardness, Young's modulus, chemical and structural composition, and to determine the corrosion behaviour using polarisation techniques and electrochemical impedance spectroscopy (EIS).

This study has shown that varying the HMDSO:O₂ ratios of the SiO_x coatings can affect both the mechanical, chemical and microstructural composition of the coatings, leading to coatings with different chemistries and stoichiometries. The corrosion performance of MW-PECVD deposited SiO_x coatings has shown that the HMDSO:O₂ ratios can affect the corrosion resistance of the coatings, and increasing the thickness of the coatings can have an increased effect on the corrosion performance of the coatings.

Table of Contents

Acknowledgements	i
Abstract	iii
Table of Contents	v
List of Figures	ix
List of Tables	xv
Abbreviations	xviii
Chapter 1 – Introduction	1
1.1 Aim.....	5
1.2 Objectives	5
1.3 Thesis Outline	6
1.4 Thesis Structure.....	7
Chapter 2 – Background	8
2.1 Introduction	8
2.2 Theory of surface engineering	8
2.3 Theory of Plasma.....	10
2.4 Theory of Deposition Techniques	14
2.5 Physical vapour deposition (PVD).....	15
2.5.1 Evaporation.....	16
2.5.2 Sputtering	16
2.6 Chemical vapour deposition (CVD).....	17
2.6.1 Low pressure chemical vapour deposition (LPCVD).....	19
2.6.2 Atmospheric pressure chemical vapour deposition (APCVD) ...	19
2.7 Plasma enhanced chemical vapour deposition (PECVD)	20
2.7.1 Microwave plasma enhanced chemical vapour deposition (MW-PECVD)	22
2.8 Advantages, limitations and applications of coating methods	23
Chapter 3 – Literature Review	25
3.1 Introduction	25
3.2 Silicon dioxide	25
3.2.1 Structure of silicon dioxide	26
3.3 A comparison of the precursors, deposition techniques and substrates for the deposition of SiO _x coatings	28
3.3.1 Precursors for depositing SiO _x coatings.....	29
3.3.2 Deposition methods for depositing SiO _x coatings	35

3.4	The properties and applications of SiO _x coatings.....	41
3.4.1	The gas barrier properties of SiO _x coatings	41
3.4.2	The dielectric properties of SiO _x coatings	43
3.5	Theory of corrosion	44
3.5.1	The corrosion cell.....	44
3.5.2	Methods of corrosion prevention.....	46
3.6	The corrosion resistance of SiO _x coatings	47
3.6.1	Electrochemical Impedance Spectroscopy (EIS) of SiO _x coatings	49
3.7	Summary of chapter and rationale	54
Chapter 4	– Experimental procedures and analysis techniques	56
4.1	Introduction	56
4.2	Methods of Coating Deposition.....	56
4.2.1	Substrate and sample preparation	58
4.2.2	Precursors	61
4.2.3	MW-PECVD Coating Procedure	61
4.3	Deposition parameters.....	64
4.3.1	Batch 1 coatings – varying HMDSO:O ₂ ratios.....	64
4.3.2	Batch 2 coatings – varying HMDSO:O ₂ ratios and thicknesses.....	65
4.4	Characterisation of the SiO _x coatings	66
4.5	Mechanical characterisation	66
4.5.1	Calo Test	66
4.5.2	Scratch Test.....	68
4.5.3	Nanoindentation.....	71
4.6	Chemical characterisation.....	73
4.6.1	Scanning electron microscopy with electron dispersive x-ray (SEM/EDX) spectroscopy.....	73
4.6.2	Fourier Transform Infrared (FT-IR) spectroscopy	77
4.6.3	XPS analysis.....	78
4.6.4	X-ray diffraction (XRD).....	80
4.7	Electrochemical techniques	86
4.7.1	Polarisation curves for SiO _x coated HSS	87
4.8	The Electrochemical Impedance Spectroscopy (EIS) of SiO _x coated high-speed steel	90
Chapter 5	– Characterisation of SiO_x coatings with varying HMDSO:O₂ ratios.....	97
5.1	Introduction	97

5.2 Mechanical characterisation of the first batch of coatings with varying HMDSO:O ₂ concentrations.....	97
5.2.1 Calo® Test.....	97
5.2.2 Scratch Test.....	100
5.3 Chemical characterisation of the first batch of coatings with varying HMDSO:O ₂ concentrations.....	102
5.3.1 Energy dispersive x ray spectroscopy.....	102
5.3.2 X-ray diffraction (XRD).....	110
5.3.3 FT-IR.....	113
5.4 Summary of chapter.....	116
Chapter 6 – Characterisation of SiO_x coatings with a comparison of the HMDSO:O₂ ratio and thickness.	118
6.1 Introduction to the chapter	118
6.2 Mechanical characterisation of the second batch of coatings	118
6.2.1 Nanoindentation.....	118
6.3 Compositional analysis of the second batch of coatings with varying HMDSO:O ₂ concentrations and varying thickness	120
6.3.1 Scanning Electron Microscopy imaging of the surface of SiO _x coated HSS.	121
6.3.2 Atomic concentration (%) of silicon and oxygen of the SiO _x coatings from EDX analysis	121
6.3.3 Focused ion beam (FIB) cross sectional analysis	125
6.3.4 FT-IR analysis.....	126
6.3.5 XPS analysis.....	128
6.4 Microstructural analysis of the SiO _x coatings	137
6.4.1 X-ray diffraction (XRD).....	138
6.4.2 Calculation of the crystallite size using the Scherrer equation	144
6.4.3 Williamson-Hall analysis	150
6.5 Summary of chapter.....	164
Chapter 7 – Electrochemical behaviour of SiO_x coatings with varying HMDSO:O₂ ratios and thicknesses	167
7.1 Introduction	167
7.2 Corrosion performance of the SiO _x coatings with varying HMDSO:O ₂ ratio	167
7.2.1 Potentiodynamic analysis	167
7.2.2 Electrochemical impedance spectroscopy of the SiO _x coatings	172
7.3 The effect of the corrosion resistance of SiO _x coated HSS with varying thickness	192

7.4 Analysis of samples after corrosion tests.....	197
7.4.1 Mechanical characterisation of the SiO _x coatings after the EIS experiments.....	197
7.4.2 SEM cross sectional analysis with EDX analysis	198
7.4.3 TEM analysis of sample 1:20	201
7.5 Summary of chapter.....	206
7.5.1 The effect of the HMDSO:O ₂ ratio on the corrosion properties of SiO _x coated HSS.....	206
7.5.2 The effect of the thickness on the corrosion properties of SiO _x coated HSS	208
Chapter 8 – Conclusions and Further Work	209
8.1 Conclusions	209
8.1.1 The effect of the HMDSO:O ₂ ratio on the properties of SiO _x coatings.....	209
8.1.2 The effect of the thickness of the SiO _x coatings.....	211
8.2 Further Work	212

List of Figures

Figure 1.1 Schematic of a proton exchange membrane fuel cell (PEMFC) [6].	3
Figure 2.1 Surface engineering method classifications, modified from [17]. ..	8
Figure 2.2 Applications of surface modifications, based on industrial requirements [1]......	9
Figure 2.3. The four matters of state; solid, liquid, gas and plasma [25].	10
Figure 2.4. Properties of different types of plasmas occurring in the natural environment, with the yellow rectangle representing man-made plasmas [30]......	12
Figure 2.5 A summary of the various surface coating methods.	15
Figure 2.6 A schematic of a universal PECVD chamber, plasma created using a radio frequency (RF) field adapted from reference [54]......	21
Figure 3.1 Silicon dioxide in the α - and β -quartz phase, in a SiO_4 tetrahedra arrangement.	26
Figure 3.2 A schematic showing the reversible transitions of silica into its different phases.	27
Figure 3.3 A schematic of the irreversible heating process of α -quartz into β - quartz, and finally into a silica melt.	27
Figure 3.4 The mechanism for the transformation of silica melt into glassy silica through rapid cooling.	28
Figure 3.5 The mechanism of β -tridymite and β -cristobalite into their corresponding α -polymorphs through cooling to temperatures lower than 870°C and 1470°C , respectively.	28
Figure 3.6. The chemical structure of hexamethyldisiloxane (HMDSO).	29
Figure 3.7. Mechanistic reaction scheme for the plasma polymerisation of HMDSO, into its smaller constituents, through to adsorption onto the substrate, mechanism adapted from [105]......	30
Figure 3.8. The chemical structure of tetramethylsilane (TMS).	32
Figure 3.9. Proposed growth mechanism of SiO_x films based on a TMS- O_2 gas mixture [112].	33
Figure 3.10. The chemical structure of tetraethyl orthosilicate (TEOS).	34
Figure 3.11. A corrosion cell made up of the four basic components.	45
Figure 3.12. Schematic diagram of some corrosion protection methods.	46
Figure 3.13 A Randles circuit model across a metal oxide surface, with a solution resistance (R_s), interfacial capacitance (C_{int}) and charge transfer resistance (R_{ct}).	50
Figure 3.14 A simple a) Nyquist and b) Bode plot representing the Randles circuit in Figure 3.13, where $R_s = 100 \Omega$, $R_{\text{ct}} = 1000 \Omega$, and $C_{\text{int}} = 100 \mu\text{F}$ [181]......	51

Figure 4.1 The Hauzer Flexicoat 850 PVD machine.	57
Figure 4.2 Schematic of the coating chamber in the Hauzer Flexicoat 850 PVD system, the microwave source will be the main focus for this study.	57
Figure 4.3. Hauzer Flexicoat 850 schematic of the deposition chamber, a) front view of PVD chamber and b) side view of PVD chamber, with internal dimensions of 800 x 800 x 900 mm.....	58
Figure 4.4 Schematic of the microwave antenna source.	62
Figure 4.5. A schematic of the Calo test measurement and how the thickness is calculated. t =coating thickness, x and y =measurements determined using optical microscopy, d =diameter of the sphere.	67
Figure 4.6. The Tribotechnic Scratch Tester Millennium 200 to characterise the adherence of the SiO_x coating onto the HSS substrate.	68
Figure 4.7. A typical load displacement curve for the nanoindentation process (E represents Young's modulus) [190].	72
Figure 4.8 A simple schematic of the scanning electron microscope process adapted from reference [194].	74
Figure 4.9. A schematic showing the plan-view positions of the five measurements taken for each sample.	76
Figure 4.10. A simple schematic of the XPS analysis process, for a coated material. The primary beam emits a photon onto the surface of the sample, the secondary beam detects the electron that is lost.	79
Figure 4.11 A schematic to show the production of x-rays using a heated filament, electron beam and a metal target (usually Cu, Mo or Co).	80
Figure 4.12 A schematic representation to show the process of the XRD technique.	81
Figure 4.13. A schematic of the EIS set up for the SiO_x coated samples.	87
Figure 4.14. Tafel extrapolation example for the sample with HMDSO: O_2 ratio 1:12 and DOE thickness 2 μm	88
Figure 4.15 Nyquist plot examples with the corresponding equivalent circuits [206].	92
Figure 4.16 Bode plot examples with the corresponding equivalent circuits [206].	93
Figure 4.17 A simple equivalent circuit for a real coating. R_{sol} = resistance of the solution, R_{por} = pore resistance within the coating, C_c = coating capacitance, C_{dl} = capacitance at the double layer.	94
Figure 4.18 An equivalent circuit for a coating that exhibits corrosion. R_{sol} = resistance of the solution, R_{por} = pore resistance within the coating, C_c = coating capacitance, C_{dl} = capacitance at the double layer, R_{ct} = resistance of the charge transfer.	95
Figure 5.1. The average calculated thickness for the SiO_x coatings with varying HMDSO: O_2 ratios and a DOE thickness of 2 μm , including error bars.	99

Figure 5.2 The atomic concentration (%) of carbon present in the SiO _x coatings with increasing HMDSO:O ₂ ratio and DOE thickness 2 μm.	103
Figure 5.3 The atomic concentration (%) of carbon present in the SiO _x coatings with increasing HMDSO:O ₂ ratio and DOE thickness 2 μm, and the atomic concentration of carbon present in the HMDSO and O ₂ precursor mixture present within the PVD chamber.....	104
Figure 5.4 The atomic concentration (%) of both silicon and oxygen present in the SiO _x coatings with increasing HMDSO:O ₂ ratio and DOE thickness 2 μm, including error bars.	105
Figure 5.5 The Si:O ratio calculated from the EDX atomic concentrations of silicon and oxygen for SiO _x coatings with varying HMDSO:O ₂ ratios and DOE thickness 2 μm.	106
Figure 5.6 The atomic concentration (%) of both silicon and oxygen present in the SiO _x coatings and the atomic % of silicon and oxygen present in the precursors with increasing HMDSO:O ₂ ratio.	107
Figure 5.7. The reaction scheme for the plasma process of the breakdown of HMDSO into its smaller constituents during the deposition process of SiO _x . Figure taken from reference [105].	109
Figure 5.8. The stacked diffractograms of the SiO _x coatings with varying HMDSO:O ₂ ratios and DOE thickness 2 μm.	111
Figure 5.9. A graph to show the FT-IR spectra for the samples with increasing HMDSO:O ₂ ratio. Plotted as a function of wavenumber (cm ⁻¹) against absorbance (a.u).	114
Figure 6.1 Focused ion beam (FIB) cross section of the SiO _x coating with HMDSO:O ₂ ratio 1:20 and DOE thickness 2 μm. The EDX elemental mapping area is highlighted.....	125
Figure 6.2. Elemental mapping for the FIB cross section of the coating with HMDSO:O ₂ ratio 1:20 at 2 μm thickness.....	126
Figure 6.3 FT-IR spectra for the SiO _x coatings with varying HMDSO:O ₂ ratios and a DOE thickness of 2 μm. Plotted as a function of wavenumber (cm ⁻¹) against absorbance (a.u).....	127
Figure 6.4 XPS survey spectra for the SiO _x coated samples at varying HMDSO:O ₂ ratios. The undefined peak is Si 2s and is not included in the high resolution spectra.....	131
Figure 6.5 The XPS Si 2p high resolution spectra for the SiO _x coated samples at varying HMDSO:O ₂ ratios. The spectra are fitted with Gaussian curves using a U2 Tougaard background.	132
Figure 6.6 The XPS O 1s high resolution spectra with fittings for the SiO _x coated samples at varying HMDSO:O ₂ ratios. The spectra are fitted with Gaussian curves using a U2 Tougaard background.	133
Figure 6.7 The XPS C 1s high resolution spectra with fittings for the SiO _x coated samples at varying HMDSO:O ₂ ratios. The spectra are fitted with Gaussian curves using a U2 Tougaard background.	134

Figure 6.8 The stacked XRD diffractograms for samples with HMDSO:O ₂ ratios 1:10, 1:12, 1:14, 1:16 and 1:20, with a DOE thickness of 1 μm.	140
Figure 6.9 The stacked XRD diffractograms for samples with HMDSO:O ₂ ratios 1:10, 1:12, 1:14, 1:16, 1:20, 1:24 and 1:36 with a DOE thickness of 2 μm.....	141
Figure 6.10 The stacked XRD diffractograms for samples with HMDSO:O ₂ ratios 1:12, 1:14, 1:16 and 1:20, with a DOE thickness of 3.5 μm.	141
Figure 6.11 The stacked XRD diffractograms for samples with HMDSO:O ₂ ratios 1:12, 1:14, 1:16 and 1:20, with a DOE thickness of 5 μm.	142
Figure 6.12 The micro strain (ε) of the coatings calculated from the Scherrer equation increases with an increase in the dislocation density (m ⁻²) of the SiO _x coatings, with DOE thicknesses of 1 μm, 2 μm, 3.5 μm and 5 μm.....	148
Figure 6.13 A comparison of the average crystallite sizes (nm) with the DOE thickness (μm) of the SiO _x coatings with HMDSO:O ₂ ratios 1:12, 1:14, 1:16 and 1:20.....	150
Figure 6.14 Williamson-Hall plot for SiO _x coated samples with varying HMDSO:O ₂ ratios and a DOE thickness of 1 μm, with error bars calculated from the Gaussian peak fittings using OriginPro software.	153
Figure 6.15 Williamson-Hall plots for the SiO _x coated samples with varying HMDSO:O ₂ ratios and a DOE thickness of 2 μm. Error bars are calculated from Gaussian peak fitting using Origin Pro.	155
Figure 6.16 The average crystallite sizes (nm) calculated from the Williamson Hall UDM method versus the hardness (GPa), for SiO _x coatings with varying HMDSO:O ₂ ratios and a DOE thickness 2 μm.	157
Figure 6.17 The microstrain of the SiO _x coatings calculated from the Williamson Hall UDM method versus the hardness (GPa), for SiO _x coatings with varying HMDSO:O ₂ ratios and DOE thickness 2 μm....	158
Figure 6.18 Williamson-Hall plots for the SiO _x coated samples with varying HMDSO:O ₂ ratios and a DOE thickness of 3.5 μm, using the UDM method. Error bars are calculated from Gaussian peak fitting using Origin Pro.....	160
Figure 6.19 Williamson-Hall plots for the SiO _x coated samples with varying HMDSO:O ₂ ratios and a DOE thickness of 5 μm, using the UDM method. Error bars are calculated from Gaussian peak fitting using Origin Pro.....	161
Figure 6.20 A graph showing the comparison of the average crystallite size (nm) calculated from the Williamson Hall method versus the thickness μm of the coatings.	163
Figure 7.1. The Tafel extrapolation curves for SiO _x coated HSS with a DOE 2 μm thickness with varying HMDSO:O ₂ ratios. The annotation on the graph is for the uncoated HSS with a E_{corr} value = - 535 mV and i_{corr} = 6.86 μA cm ⁻²	169

Figure 7.2. Nyquist plot for the SiO _x coated sample with HMDSO:O ₂ ratio 1:20 and a DOE thickness of 2 μm, at 1 h, 72 h and 168 h.	173
Figure 7.3. Bode plots for the SiO _x coated sample with HMDSO:O ₂ ratio 1:20 and a DOE thickness of 2 μm, at 1 h, 72 h and 168 h.	174
Figure 7.4. Equivalent circuit for the SiO _x coatings, with the following components: R_s = solution resistance, CPE_C = coating capacitance, R_C = coating resistance, CPE_2 = corrosion layer capacitance, R_2 = corrosion layer resistance, CPE_{dl} = double layer capacitance, R_{ct} = charge transfer resistance.	176
Figure 7.5. Nyquist and Bode equivalent circuit fits for the SiO _x coated sample with HMDSO:O ₂ ratio 1:20 and a DOE thickness of 2 μm, at 1 h, 72 h and 168 h.	178
Figure 7.6 The R_{ct} (Ω cm ²) of the SiO _x coated samples with varying HMDSO:O ₂ ratios and a DOE thickness of 2 μm, calculated from the EIS data after 1 h, 72 h and 168 h.	180
Figure 7.7 A corrosion mechanism for the reaction of NaCl with HSS, adapted from [255].	182
Figure 7.8. Regression fit of the average crystallite sizes (nm) calculated from the Scherrer equation vs the R_{ct} (Ω cm ²) x10 ⁵	185
Figure 7.9 Regression fit of the average crystallite sizes (nm) calculated from the Williamson-Hall plots vs the R_{ct} (Ω cm ²) x10 ⁵	185
Figure 7.10. A comparison of the CPE_{dl} (Ω ⁻¹ cm ⁻² s ⁿ) values of the SiO _x coated samples with varying HMDSO:O ₂ ratios and a DOE thickness of 2 μm, calculated from the EIS data at 1 h, 72 h and 168 h.	186
Figure 7.11 A comparison of the average crystallite sizes (nm) of the SiO _x coatings calculated from the Scherrer equation, versus the CPE_{dl} values (Ω ⁻¹ cm ⁻² s ⁿ).	188
Figure 7.12 A comparison of the average crystallite sizes (nm) of the SiO _x coatings calculated from the Williamson-Hall plots, versus the CPE_{dl} values (Ω ⁻¹ cm ⁻² s ⁿ) determined from the EIS data.	189
Figure 7.13. A schematic highlighting the three capacitive loops – CPE_C for the coating, CPE_2 for the corrosive layer, and CPE_{dl} for the double layer, determined from fitting equivalent circuits to Nyquist and Bode plots.	191
Figure 7.14. A comparison of the coating resistance (R_{ct}) over time for the SiO _x coatings with a HMDSO:O ₂ ratio 1:12 and varying thicknesses.	194
Figure 7.15. A comparison of the CPE_{dl} values over time (1 h, 72 h and 168 h) for the SiO _x coatings with HMDSO:O ₂ ratio 1:12 and varying thicknesses.	196
Figure 7.16. SEM images for the sample with HMDSO:O ₂ ratio 1:20, and DOE thickness of 2 μm, pre and post EIS experiments at different magnifications. a) 1:20 before EIS and b) 1:20 after EIS at 20 000x magnification, c) 1:20 before EIS and d) 1:20 after EIS at 50 000x magnification.	199

Figure 7.17 FIB cross section of the SiO_x coated sample with HMDSO:O₂ ratio 1:20 and DOE thickness 2 μm, a) before EIS and b) after EIS. .200

Figure 7.18. EDX line scans for SiO_x coating with HMDSO:O₂ ratio 1:20 and a DOE thickness 2 μm after 168 h EIS experiment.....201

Figure 7.19. Theoretical mechanism for the trends occurring in the resistance values of the SiO_x coatings with HMDSO:O₂ ratio 1:16, 1:20 and 1:24, and a DOE thickness of 2 μm.202

Figure 7.20 TEM imaging of SiO_x coating with HMDSO:O₂ ratio 1:20 with a DOE thickness 2 μm showing the SiO_x coating and HSS interface with a ~5 nm corrosion layer, after 168 h.203

Figure 7.21 The EDX elemental mapping of SiO_x coating with HMDSO:O₂ ratio 1:20 and a DOE thickness 2 μm, from the TEM image, after 168 h.204

Figure 7.22. Line scan data from the TEM sample, 1:20 after the 168 hour EIS experiment.205

Figure A.9.1 SEM micrographs for the SiO_x samples coated at varying HMDSO:O₂ ratios a) 1:10, b) 1:12, c) 1:14, d) 1:16, e) 1:20, f) 1:24 and g) 1:36, all with a 2 μm DOE thickness.236

List of Tables

Table 2.1 A general overview of the deposition techniques, with pressures, temperatures, advantages, limitations and applications.	24
Table 3.1 An overview of the deposition methods, precursors, substrates and applications for SiO _x coatings.	36
Table 3.2 An overview of the corrosion properties of silica based coatings, on a variety of metallic substrates.....	49
Table 4.1. General grades of high-speed steel [184].	59
Table 4.2. The mechanical characteristics of HSS 1.3343, DIN HS S-6-5-2.60	
Table 4.3. The chemical composition of the high-speed steel (HSS) substrates used for the SiO _x coatings, from reference [185]......	60
Table 4.4 Coating deposition step parameters.....	63
Table 4.5. The argon, HMDSO and oxygen flow rates for the 1 st batch of coated SiO _x samples, with varying HMDSO:O ₂ ratios and a 2 μm design thickness.....	64
Table 4.6. The argon, HMDSO and oxygen flow rates for the second batch of coated SiO _x samples, with varying HMDSO:O ₂ ratios and different thicknesses.	65
Table 4.7. The scratch test conditions for all SiO _x coated samples.....	69
Table 4.8 Classifications of the scratch test results [188].	70
Table 4.9. The main FT-IR characteristic bonding vibrations for SiO _x coatings.	78
Table 4.10. A table to show the seven different crystal systems and their cell parameters.....	82
Table 4.11. A table to show the XRD conditions for all coated samples.	84
Table 4.12 Passive elements which serve as components of an electrical circuit.	91
Table 4.13. The matrix of samples used for the determination of the resistivity and capacitance of SiO _x coated samples using EIS.	96
Table 5.1. A list of the SiO _x coated samples with HMDSO:O ₂ ratio, nominal thickness (μm) and actual thickness (μm) calculated using Calo® Test.	98
Table 5.2. Critical load values (LC ₁ , LC ₂ and LC ₃) for the SiO _x coated HSS with varying HMDSO:O ₂ ratios.....	100
Table 5.3. The oxygen, silicon and carbon concentrations for the samples with varying HMDSO:O ₂ ratios, acquired from EDX analysis.....	106
Table 5.4. The average crystallite sizes (nm) of the SiO _x coatings with varying HMDSO:O ₂ ratios and DOE thickness 2 μm.	112
Table 5.5 The main characteristic peaks present in the SiO _x coated samples.	114

Table 5.6. FT-IR data for the peak positions of the Si-O-Si asymmetric stretching peaks, with varying HMDSO:O ₂ ratios.....	115
Table 6.1. The hardness (<i>H</i>) and young's modulus (<i>E</i>) values of the SiO _x coatings.	119
Table 6.2 – The atomic concentration of oxygen and silicon from the EDX analyses.....	122
Table 6.3 Si:O ratio calculated from the EDX analyses.	124
Table 6.4 FT-IR vibration modes for SiO _x coated HSS with varying HMDSO:O ₂ ratios at a DOE thickness of 2 μm.	128
Table 6.5. The Si, O and C concentrations of the SiO _x coatings from XPS data analyses before Ar cluster bombardment, with respect to the HMDSO:O ₂ ratio.	129
Table 6.6 The binding energies and full width at half maximum (FWHM) of Si 2p and O1s high resolution spectra for SiO _x coatings with design thickness 2 μm.....	135
Table 6.7 The Si, O and C concentrations and Si:O ratio of the SiO _x coatings from XPS survey spectra after Ar bombardment, with respect to HMDSO:O ₂ ratio.	137
Table 6.8 Calculated lattice constant (<i>a</i>) from XRD diffraction data at varying HMDSO:O ₂ ratios and a DOE thickness of 2 μm.	139
Table 6.9. Average crystallite sizes (nm), strain and dislocation densities of the SiO _x coatings with varying HMDSO:O ₂ ratios and varying DOE thicknesses, calculated from the Scherrer equation.	145
Table 6.10 A comparison of the average crystallite sizes of the HMDSO:O ₂ ratio with a DOE thickness of 2 μm, with the hardness and elastic modulus from nanoindentation results.	149
Table 6.11 Geometric parameters of the SiO _x coatings, with a design thickness of 1 μm.....	154
Table 6.12 Geometric parameters, calculated from the UDM method and Scherrer equation, of the SiO _x coatings with a design thickness of 2 μm	156
Table 6.13 A comparison of the average crystallite size calculated from the Williamson-Hall method, with the hardness values from nanoindentation.	157
Table 6.14 Geometric parameters, calculated from the UDM method and Scherrer equation, of the SiO _x coatings with a design thickness of 3.5 μm.....	159
Table 6.15 Geometric parameters, calculated from the UDM method and Scherrer equation, of the SiO _x coatings with a design thickness of 5 μm	161
Table 6.16 The average crystallite size calculated from the Williamson Hall method, for samples 1:12, 1:14, 1:16 and 1:20, with a comparison to the DOE thicknesses.	162

Table 7.1. Tafel extrapolation results related to the polarization curves from Figure 7.1, for samples coated to a 2 μm thickness with varying HMDSO:O ₂ ratios.....	170
Table 7.2. The coating resistance and capacitance values for the SiO _x coated samples, with varying HMDSO:O ₂ ratios and a DOE thickness of 2 μm , calculated from EIS spectra.....	179
Table 7.3 A comparison of the coating resistance values after 168 hours, with the average crystallite sizes calculated from the Scherrer equation and Williamson-Hall plots of the SiO _x coated HSS samples at DOE thickness 2 μm	184
Table 7.4 A comparison of the average crystallite sizes with the capacitance values from the EIS data at 168 hours.....	187
Table 7.5. Resistance and capacitance values for HMDSO:O ₂ sample 1:12, at different coating thicknesses (1 μm , 2 μm , 3.5 μm and 5 μm). Values are evaluated at 1 hour, 72 hours and 168 hours.	195
Table 7.6 A comparison of the hardness of the SiO _x coatings with varying HMDSO:O ₂ ratios and a DOE thickness of 2 μm , prior to EIS and after EIS (168 h).....	198

List of Abbreviations

AC	Alternating current
APCVD	Atmospheric pressure chemical vapour deposition
Ar	Argon
ATR	Attenuated total reflectance
CPE	Constance phase element
CPE-dl	Constant phase element of double layer
CVD	Chemical vapour deposition
DC	Direct current
DOE	Design of experiments
EB	Electron beam
ECR	Electron cyclotron resonance
EDX	Energy dispersive x-rays
EIS	Electrochemical impedance spectroscopy
FT-IR	Fourier transform infrared
FWHM	Full width at half maximum
GDP	Gross domestic product
H	Hardness
HiPIMS	High power impulse magnetron sputtering
HMDSO	Hexamethyldisiloxane
HSS	High speed steel
LPCVD	Low pressure chemical vapour deposition
LPR	Linear polarisation resistance
MW-PECVD	Microwave plasma enhanced chemical vapour deposition
NaCl	Sodium chloride
O ₂	Oxygen
PECVD	Plasma enhanced chemical vapour deposition
PEMFC	Proton exchange membrane fuel cell
PET	Polyethylene terephthalate

PVD	Physical vapour deposition
R_{ct}	Resistance of charge transfer
RF	Radio frequency
SCCM	Standard cubic centimetres per minute
SCE	Saturate calomel electrode
SEM	Scanning electron microscopy
SiO_x	Silicon oxide
SiO_2	Silicon dioxide
SS	Stainless steel
TEM	Transmission electron microscopy
TEOS	Tetraethyl orthosilicate
TMS	Tetramethyl silane
UDM	Uniform deformation model
W-H	Williamson-Hall
XPS	Xray photoelectron spectroscopy
XRD	Xray diffraction

List of Symbols and Units

A	Ampere (Amps)
Å	angstrom
AE	acoustic emission
β	FWHM
β_a	anodic Tafel constant
β_c	cathodic Tafel constant
cm^{-1}	wavenumber
E	Young's Modulus
E_{corr}	Corrosion potential
E_r	Reduced modulus
eV	electron volts
GHz	gigahertz
GPa	gigapascals
Hz	Hertz
i_{corr}	Corrosion current density
K	Kelvin
λ	lambda
M	mol dm^{-3}
mbar	millibar
mm	millimetre
mmpy	millimetre per year
mV	millivolts
N	Newton
nm	nanometre
ρ	density
θ	theta
μm	micron
V	volts

ν	Poisson's ratio
W	watts
χ^2	chi-squared
Z	real impedance
$-Z'$	imaginary impedance

Chapter 1 – Introduction

Surface engineering is a multidisciplinary subject which involves the modification of solid matter in order to improve the functionality of a material. It can be applied to a wide range of subject areas including materials science, mechanical engineering, electrical engineering and chemistry. Both metallic and non-metallic surfaces can be modified to enhance the properties of a material and may also be utilised for decorative purposes. Surface engineering can be applied to numerous applications, ranging from biomedical (including hip and knee replacements) to automotive and aerospace applications.

The engineering of surfaces plays an important role in the corrosion, friction and wear of surfaces, which in turn leads to significant economic and environmental impacts for multiple industries [1]. Over the past couple of decades, it has been estimated that the corrosion costs of materials contribute between 3 and 4% of the gross domestic product (GDP) of a country every year [2]. Friction and wear of materials also contributes to a loss of between 1 and 2% of the GDP per year in Great Britain and Germany [3]. Overcoming these issues has led to the increased demand of surface treatments, applied to materials that are sensitive to corrosion and wear [1]. The automotive industry is just one industry where surface modifications will enhance the lifetime of materials; such as carbon steel, particularly for the use in fuel cells.

The drive towards green energy and the net-zero emissions target by 2050 has been accelerated dramatically over the past decade. The need to cut down on fossil fuels and find alternative energy sources is of utmost importance to combat greenhouse gas emissions, which in turn lead to an increase in global temperature. One solution to the supply of green energy is with hydrogen fuel

cells. This environmentally friendly, low carbon alternative can be considered a substitute for fossil fuels [4], benefiting the environment, climate change and providing a source of clean production.

Fuel cells are a promising alternative to fossil fuels and can be used as energy storage for the renewable energy supply chain, or in engine technology to replace the current internal combustion engine, turbines, and boilers [5]. Although this alternative fuel source proves to be a promising alternative, there are several challenges that need to be addressed.

1. Cost
2. Performance
3. Durability

A proton exchange membrane fuel cell (PEMFC) is an electrochemical cell which converts chemical energy from a fuel (hydrogen) and an oxidizing agent (oxygen), into electrical energy, through redox reactions. The fuel cell stack consists of; an anode backing, electrolyte membrane and cathode backing, sandwiched between two bipolar plates (BP) – anode and cathode, shown in Figure 1.1.

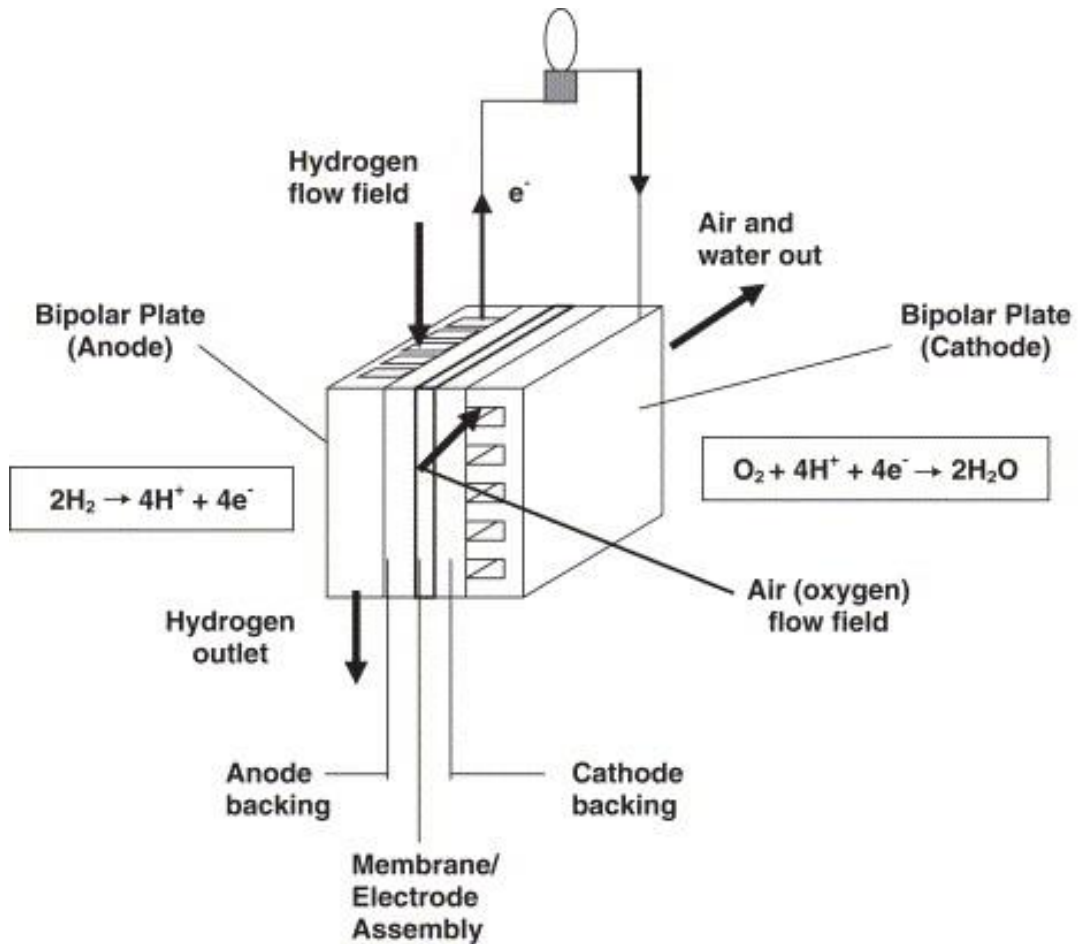


Figure 1.1 Schematic of a proton exchange membrane fuel cell (PEMFC) [6].

The BPs make up 80% of the total weight of the fuel cell, and around 45% of the cost. The role is to evenly distribute the fuel and the oxygen around the cell, carry current from cell to cell, prevent the leakage of reactants and facilitate heat management. Thus, it is important for the material of the BPs to have the chemical and physical properties, as proposed by Mehta and Cooper [7], and Borup and Vanderborgh [8]:

- H₂ permeability - < 10⁻⁴ cm³ cm⁻² s
- Electrical conductivity - < 0.01 Ω cm²
- Thermal conductivity – as high as is possible
- Compressive strength - > 0.15 MPa

- Corrosion resistance: corrosion rate $< 0.19 \text{ mm y}^{-1}$

The materials currently being researched can be categorized into: non-metal, metals – both uncoated and coated, and composites. Stainless steels and carbon steels [9] have proven to be a promising material for bipolar plates, due to the lower cost and good mechanical properties [10], [11] however the corrosion resistance is unsuitable for the application in commercial PEMFCs [12]. The application of a suitable coating to the steel surface, however can overcome the unsuitable corrosion resistance. The development of a corrosion resistant and cost-effective coating is significant in the development of metallic bipolar plates [13].

A suitable coating should provide sufficient thermal and electrical conductivity, be corrosion resistant, have a good adhesion to the metal and have little to no defects present [14]. A defect within the coating will reduce the lifetime of the steel and enhance its degradation [15]. The corrosion resistance of high-speed steel (HSS) coated SiO_x , deposited using microwave plasma enhanced chemical vapour deposition (MW-PECVD) is a promising material for bipolar plates and one potential application for SiO_x coatings. The use of MW-PECVD provides a dense uniform coating with minimal defects, thus having the ability to sufficiently protect the substrate. This novel technique can be utilised to deposit SiO_x coatings to understand both the coating performance and the corrosion performance. Electrochemical impedance spectroscopy (EIS) is a useful measurement technique for evaluating the corrosion resistance of SiO_x coatings.

1.1 Aim

To characterise the mechanical, compositional and electrochemical properties of a matrix of SiO_x coatings deposited onto HSS substrates, with a focus on the hexamethyldisiloxane to oxygen (HMDSO:O₂) ratio dependence and the thickness dependence of the coatings.

1.2 Objectives

- To understand how varying the O₂ concentration during the MW-PECVD process of SiO_x coatings affects the mechanical, microstructural and electrochemical properties of the coatings.
- To explore the dependence of the HMDSO:O₂ ratio on the SiO_x coating properties, a matrix of coatings deposited with a wide variability of HMDSO:O₂ ratios will be investigated.
 - Characterisation of the mechanical properties of the coatings and understand how the HMDSO:O₂ ratio can affect these properties.
 - To understand the effect of the HMDSO:O₂ ratio on the chemistry and microstructure of the SiO_x coatings.
- To investigate a selection of SiO_x coatings with different HMDSO:O₂ ratios, coated with varying thicknesses to understand how the thickness of coatings affects the mechanical and structural properties.
- To study the relationship of both the HMDSO:O₂ ratios and the thickness of the SiO_x coatings on the electrochemical behaviour of the coatings.
- To understand and correlate the microstructural findings with the electrochemical behaviour of the SiO_x coatings with varying HMDSO:O₂ ratios.

1.3 Thesis Outline

- Chapter Two: A background introduction to surface engineering methods, plasma theory and general coating deposition techniques.
- Chapter Three: A comprehensive literature review covering an overview of deposition methods, focussing on the deposition techniques used for silicon oxide coatings. It will also cover an insight into the barrier properties, applications and electrochemical behaviours of the SiO_x coatings
- Chapter Four: An overview of the experimental techniques, analysis procedures and parameters used throughout this thesis.
- Chapter Five: The results and discussion for a preliminary batch of SiO_x coated HSS with varying HMDSO:O₂ ratios.
- Chapter Six: The results and discussion for a further matrix of SiO_x coatings, deposited onto HSS. The focus of this chapter is to understand the effects of the HMDS:O₂ ratios and the thickness of the coatings on the mechanical, chemical and microstructural properties of the coatings.
- Chapter Seven: The results and discussions for the corrosion resistance of SiO_x coated HSS, using polarisation techniques and electrochemical impedance spectroscopy (EIS). The discussion will focus on the effect of the HMDSO:O₂ ratios on the corrosion behaviour of the coatings, and also compare the microstructural and mechanical properties with the corrosion behaviour.
- Chapter Eight: The main conclusions taken from the study and suggestions for further work.

1.4 Thesis Structure

Introduction			
Aims and Objectives			
Literature Review			
Experimental Methodology			
Results and Discussion			
The effect of HMDSO:O₂ ratio on SiO_x coatings		The effect of thickness on SiO_x coatings	
Chemical and microstructural characterisation	Mechanical characterisation	Chemical and microstructural characterisation	Mechanical characterisation
Corrosion behaviour of the SiO_x coatings			
AC techniques – Tafel polarisation		Electrochemical characterisation	
Electrochemical characterisation			
Conclusions			
The HMDSO:O ₂ ratio dependence		Thickness dependence	
Further Work			

Chapter 2 – Background

2.1 Introduction

This chapter discusses the general background theories that encompass the overall research. It will emphasise the need to engineer surfaces and different types of surface modifications. The chapter will specifically focus on the different coatings methodologies and their advantages and limitations.

2.2 Theory of surface engineering

There are various surface engineering techniques that can be used to modify the properties of a material (Figure 2.1), these include but are not limited to, altering the surface metallurgy, changing the surface chemistry or applying a coating or surface layer to a bulk material [16]. The methodology used for a material is dependent on the requirements of the surface for its intended application [17].

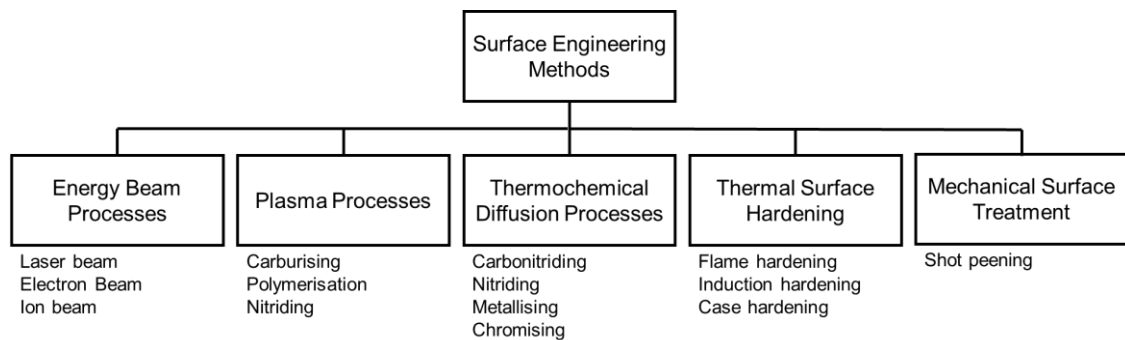


Figure 2.1 Surface engineering method classifications, modified from [17].

The requirements of the material can range from decorative, protective, functional and smart applications (Figure 2.2).

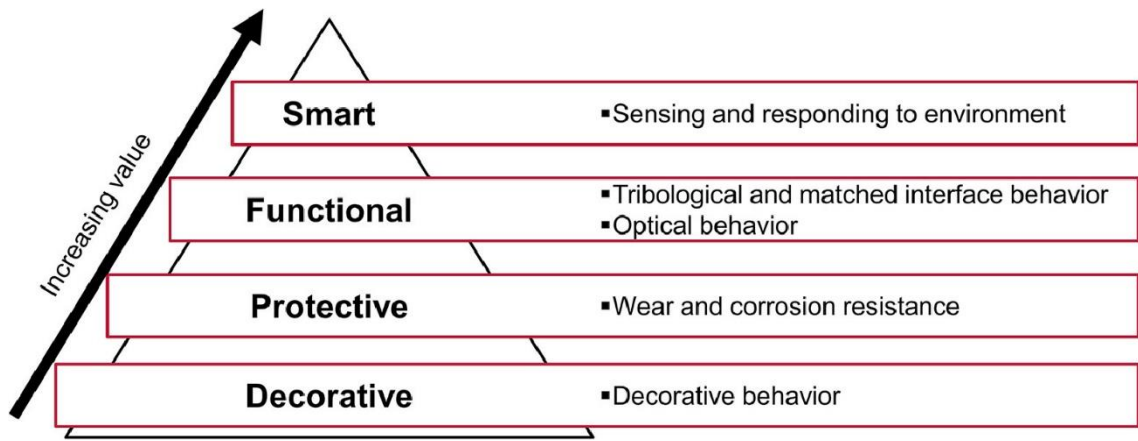


Figure 2.2 Applications of surface modifications, based on industrial requirements [1].

The lifetime of a material can be increased through an increase in the corrosion and wear resistance. Due to the large GDP costs of corrosion and the environmental impacts [18], it is important to find suitable surface modifications to improve the corrosion resistance of said materials.

Approximately 85% of all steel produced is carbon steel, and is susceptible to natural oxidation and corrosion. The corrosion rates for carbon steel can vary from 276 millimetres per year (mm y^{-1}) to 782.5 mm y^{-1} , for wet and dry environments respectively [19]. The protection of carbon steels to increase the corrosion resistance proves to be an important factor for both environmental and economic considerations. Applying a surface coating is the most favourable and common method for protecting carbon steel.

The use of inorganic oxide coatings has proven to be a promising route to aid the corrosion resistance of carbon steels. Silicon oxide (SiO_x), Aluminium oxide (Al_2O_3) and tin oxide (TiO_2) coatings act as oxidation and moisture barriers, and have been utilised to improve the anti-corrosion properties of metals. SiO_x coatings have been explored for their ability as water and oxygen permeation barrier coatings on polymeric substrates. Oxygen transmission rates (OTR) for

SiO_x coated polyethylene terephthalate (PET) have been found to be as low as 0.3 cm³ m⁻² day⁻¹ when compared with uncoated PET at 86.2 cm³ m⁻² day⁻¹ [20]. Similarly, water vapour transmission rates (WVTR) have also been reported to decrease with the addition of a SiO_x barrier layer, from 54.56 g m⁻² day⁻¹ for untreated PET to 0.47 g m⁻² day⁻¹ [21]. More recently SiO_x coatings have been researched for their use as corrosion barriers on steel substrates [22]–[24].

2.3 Theory of Plasma

Plasma is considered to be the fourth fundamental state of matter after solids, liquids and gases (Figure 2.3). It is an electrically conducting material in which there are roughly equal numbers of negatively and positively charged particles, which have been produced through the ionisation of atoms in a gas. The Hauzer Flexicoat 850 system at the University of Leeds uses PVD, PECVD and microwave PECVD deposition techniques, relying heavily on the use of plasma. The use of plasma allows for a more uniform, homogeneous and dense coating, and can also increase deposition rates. Therefore, it is important to understand the principles of plasma and how it is produced in both nature and a laboratory environment.

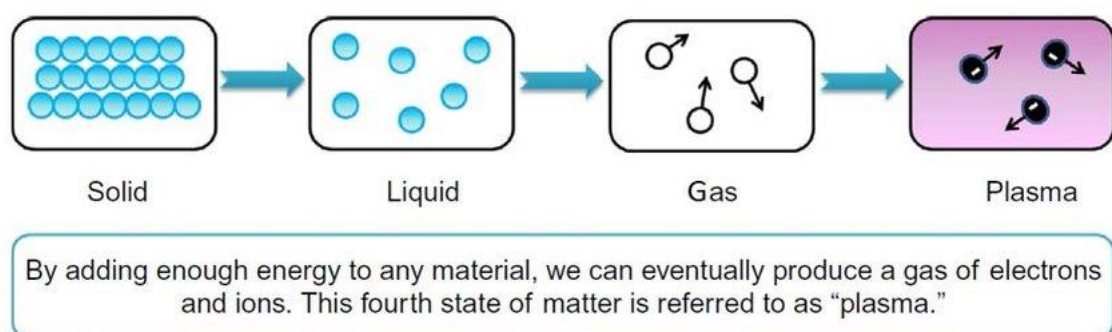


Figure 2.3. The four matters of state; solid, liquid, gas and plasma [25].

Plasma is a quasi-neutral ionised gas, in which an important fraction of the atoms are completely ionised – both ions and electrons are separately free [26]. The negative charge of the plasma is carried by electrons, and the positive charge is carried by the atoms or molecules, that have lost those same electrons. The plasma state is unique due to the magnetic and electric forces acting upon it, and therefore leading plasma to act more like a fluid.

Plasma is created when the energy of matter is increased above the ionisation energy of the species present, which occurs naturally throughout the universe. It has been hypothesised that nearly all visible matter within the universe comprises of plasma [27], predominantly occurring in the plasma form in the Sun, stars and the interstellar and interplanetary space. These natural plasmas identified by their properties can be found in Figure 2.4. Gases within the solar system occur between the range of 10^{33} p/m³ and 10^7 K in the solar core to 10^9 p/m³ and 10^5 K in the Earth's aurora [28]. These properties represent plasmas with valuable physical characteristics and if constructed within a laboratory, may be used in practical devices [29].

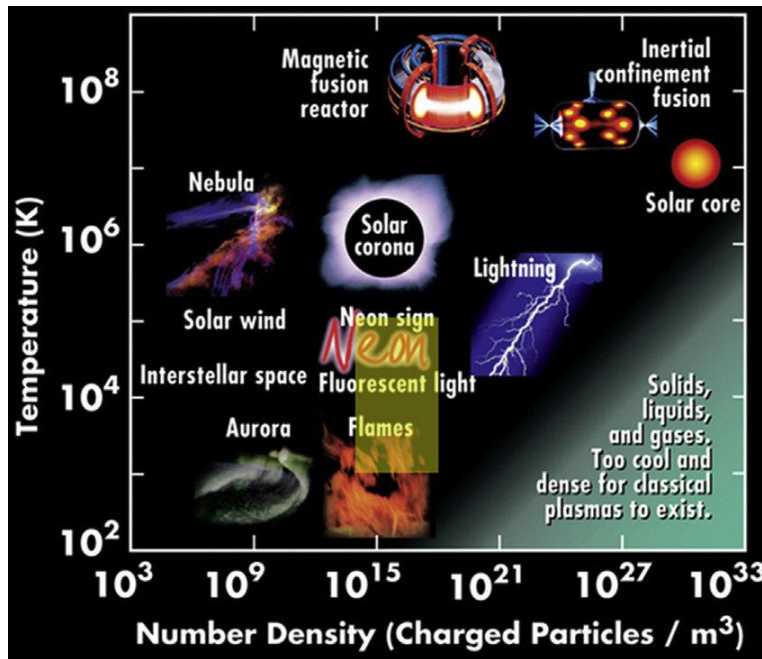


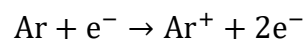
Figure 2.4. Properties of different types of plasmas occurring in the natural environment, with the yellow rectangle representing man-made plasmas [30].

Under normal conditions, plasma cannot be formed on Earth due to the high temperatures and low pressures required to create it. It can, however be found on Earth when these extreme conditions are met. For example; it can be seen as lightning – a high current discharge in the air, created from negative and positive charges accumulating in separate regions [31]. Another natural phenomena that can occur on Earth are the Aurora. This is created from electrons being absorbed into the atmosphere, resulting in the ionisation and excitation of atmospheric constituents, which emit light.

For the use of plasmas in experimental and laboratory applications, they must be created artificially by delivering a sufficient amount of energy into a system. This energy is needed to strip electrons from atoms in order to create the plasma. There are numerous origins in which this energy can be created, including but not limited to; electrical, thermal and light energy. To sustain the plasma within

the system, the energy must remain high enough to ensure enough particles remain ionised. If this energy cannot be upheld, the plasma will recombine into neutral gases.

Methods for creating artificial plasma discharges in the laboratory can be through the use of a direct current (DC), radio frequency (RF) or microwave radiation. The most common method is by applying a potential difference across an anode and cathode. This enables the plasma to be sustained through sustaining both the electron and ion energies. Once an ion and electron have been generated they will be attracted to the cathode and anode, respectively and in the presence of a non-conducting fluid, will continue to collide with other particles. A neutral gas, such as argon (Ar) is commonly used to create a gas discharge plasma in an evacuated chamber which contains the anode and cathode. Once a voltage is applied, the free electrons in the neutral gas become excited and accelerated towards the anode. The free electrons continue to gain energy and collide with the Ar atoms, leading to ionisation (Eq 2.1).



Eq 2.1

In a PVD process, the energised Ar ions will be attracted towards a target cathode and collide with the target atoms with energy high enough to release a target atom. The target atoms will then become ionised by the high energy electrons, resulting in the target being attracted to a negatively biased substrate and therefore leading to deposition. The process for PECVD and MW-PECVD coatings are similar and use a potential difference and negative substrate bias, however the gas will be a mixture of Ar, HMDSO and O₂ (for the deposition of SiO_x coatings). The positive ions will deposit onto the negatively biased

substrates, which in turn leads to a cascade of ionising collisions and therefore a high current density, allowing the plasma to be self-sustaining and stable.

The ionisation of the gases is balanced through the recombination of lower energy ions and electrons, resulting in a 'glow discharge'. The voltage and current of the plasma define the electric discharge and are characterized as the dark discharge, glow discharge and arc regimes. The glow discharge plasmas are most commonly used for laboratory plasmas and the deposition of a wide variety of coatings.

2.4 Theory of Deposition Techniques

This section will briefly discuss some of the deposition techniques that are widely available, for an array of different coatings and thin films. An extensive selection of coating methods and materials are available for an assortment of applications, all with a common purpose of protecting the coated material, which may be exposed to mechanical or chemical damage throughout its lifetime [32]. Figure 2.5 summarises the most commonly used deposition techniques, and the gaseous state techniques will be covered in further detail in this section.

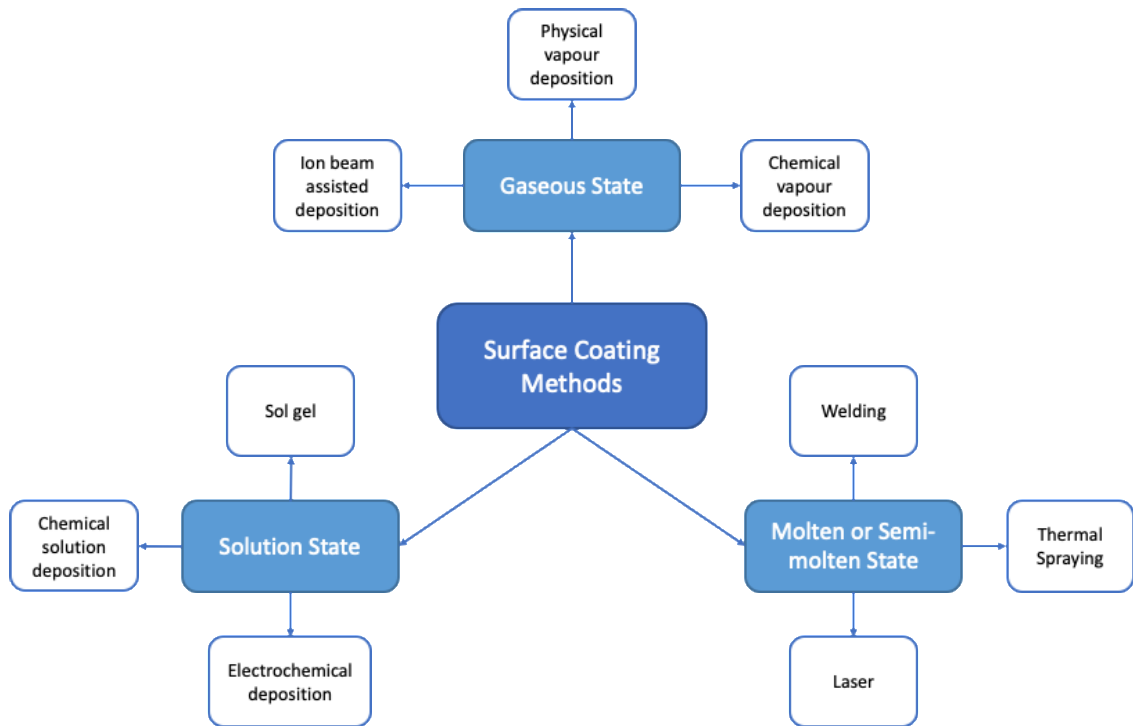


Figure 2.5 A summary of the various surface coating methods.

2.5 Physical vapour deposition (PVD)

The physical vapour deposition (PVD) technique is a process where a material is vaporized from its solid or liquid phase into atoms and/or molecules. These atoms and/or molecules are transported in the vapour phase through a vacuum or plasma environment where they are then deposited onto the substrate surface, condensing to form a solid film [33]. PVD processes allow the deposition of both multi-layer and mono-layer coatings [34], as well as alloy structures and composition [35]. Machining tools are one of the most important applications as they require a plethora of characteristics, e.g. chemical stability, corrosion resistance [36], hardness at high temperatures [37], and abrasion resistance [38]. There are two main types of PVD techniques used; evaporation and sputtering, which are discussed in further detail in sections 2.5.1 and 2.5.2.

2.5.1 Evaporation

The evaporation process involves the thermal vaporisation of a metal under high vacuum. This enables a thin film to be deposited onto a substrate surface with little to no collisions with gas molecules, in between the substrate and the source [33]. The evaporation of a material is the simplest method for processing thin films. The material involved in the process is in the form of either a solid or a liquid and requires thermal energy in order to transform the material into its vapour phase [39]. Once the material has been evaporated, it is transported to the substrate and the film growth occurs [40].

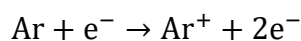
Although the evaporation process is the simplest and most cost-effective process to use, the step coverage of evaporated films is very poor and only employs “line of sight” deposition results. This can be slightly improved by rotating the sample during the evaporation process, however uniform films cannot always be produced.

2.5.2 Sputtering

Sputtering involves the bombardment of a target material using energetic ions, typically argon ions (Ar^+), in a plasma environment. There are four basic steps of the sputtering process;

1. Plasma generation

- Plasma is generated when an inert gas becomes ionised by an electric field.



Eq 2.2

2. Ion bombardment

- Once argon has been ionised, it bombards with the chosen target material with very high energy.

3. Sputtered atom transportation

- The sputtered ions and atoms from the target material result in collisions that may occur during transportation to the substrate.

4. Film growth

- Once the sputtered material has deposited onto the surface of the substrate, growth of the film begins by diffusion of the target material onto the surface.

Sputtering is the preferred PVD technique due to the high energies of the particles involved within the process. The high energy of the particles allows the organisation of high-density films on the surface of the substrate [40]. Sputtering, when compared to evaporation works at higher pressures, enabling the process to be easily automated and for the coating rate to be highly tuneable [40].

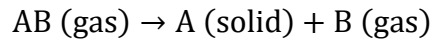
2.6 Chemical vapour deposition (CVD)

Chemical vapour deposition (CVD) is the process of depositing films onto a substrate via a chemical reaction and substrate absorption. Gases are introduced into the chamber and are activated by means of plasma or heat. The substrate absorbs the gases onto its surface and a chemical reaction will begin to take place, allowing a film to be formed on the substrate surface. Any volatile by-products from the reaction are carried away from the substrate and adsorbed into the chamber.

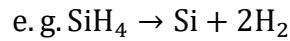
There are four types of chemical reaction that can take place during the CVD process:

1. Pyrolysis

- A reaction involving the chemical or thermal decomposition of a compound.

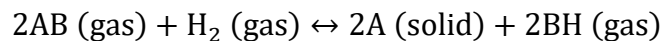


Eq 2.3



2. Reduction

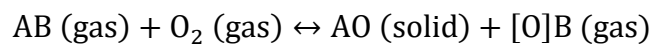
- A chemical reaction involving the gain of electrons of an atom taking part in the reaction, via the removal of oxygen or the addition of hydrogen.



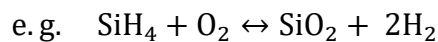
Eq 2.4

3. Oxidation

- A chemical reaction involving the removal of electrons from an atom taking part in the reaction, via the removal of hydrogen or the addition of oxygen.

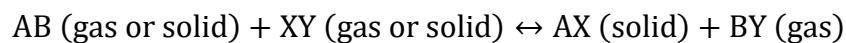


Eq 2.5

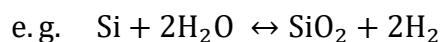


4. Compound formation

- A reaction involving the formation of films and coatings produced by using a variety of precursor gases.



Eq 2.6



The CVD deposition technique uses a multidirectional type of deposition, a distinguishing characteristic, when compared to the PVD line-of-sight technique.

CVD also allows the deposition of various forms of a material, such as; amorphous, crystalline and polycrystalline [41]. This deposition technique is therefore employed in numerous industrial applications for; corrosion resistance [41], [42], wear resistance [43], [44], erosion and high temperature protection [45].

There are a plethora of CVD processes that can be selected for the particular material to be deposited, and the application of its intended use. Such CVD processes include; low pressure CVD (LPCVD), atmospheric pressure CVD (APCVD) and plasma enhanced CVD (PECVD).

2.6.1 Low pressure chemical vapour deposition (LPCVD)

Low pressure CVD (LPCVD) operates at sub-atmospheric pressures [46], usually between 0.1 and 1 Torr and requires vacuum systems in order to control the pressure inside the reactor [47]. LPCVD systems can be divided into hot and cold wall systems. The advantage of a hot wall system is the ability to deposit uniform coatings across the wafer, due to its excellent temperature uniformity [48]. For cold wall systems, there is less deposition onto the walls of the chambers, but the uniformity of the coating across the wafer is significantly reduced.

LPCVD is typically used to deposit nitride, oxide and polysilicon films. The low pressures used in LPCVD help reduce the amount of unwanted gaseous reactions taking place and increase the film thickness uniformity across the entire wafer.

2.6.2 Atmospheric pressure chemical vapour deposition (APCVD)

The APCVD process is a CVD deposition process performed at atmospheric pressure (760 torr) and is used for the deposition of non-doped and doped oxides [49]. The wafers are placed on a conveyor belt, which allows the constant transportation of wafers into the processing area and are heated in-situ by means

of heater elements [47]. The APCVD process is mainly controlled by the processing gas flow rate, temperature and conveyor belt speed [47]. One of the main advantages of APCVD is that the process is able to be scaled for use on large areas, has a high deposition rate, with uniform coating thickness and potential low costs [50]. APCVD systems are generally used to deposit silicon dioxide (SiO_2) anti-reflection coatings, transparent conductive oxide coatings and to grow epitaxial films of silicon (Si).

2.7 Plasma enhanced chemical vapour deposition (PECVD)

PECVD is a process used to deposit a variety of coatings and thin films onto multiple substrates. The process uses much lower temperatures than the conventional CVD processes [51], [52]. PECVD processes have three basic requirements; 1) plasma creation through ionisation of molecules and atoms, 2) pressure control system for maintaining the plasma, and 3) chamber whereby the reaction will take place [53]. The plasma can typically be created by using a direct current (DC) discharge or radio frequency (RF) field between two electrodes. A schematic of a PECVD chamber using an RF field is shown in Figure 2.6. The space in between the electrodes is filled with an inert gas (e.g. argon and helium), inducing a chemical reaction with the chosen reactive gases, and resulting in reactant products being deposited onto the surface of a chosen substrate. The substrate is generally heated between 200°C and 300°C – dependent on the surface coating requirements. The relatively low substrate temperatures required for PECVD, allow substrates to be coated that are not able to withstand the higher temperatures ($600\text{-}800^\circ\text{C}$) needed for CVD methods [52].

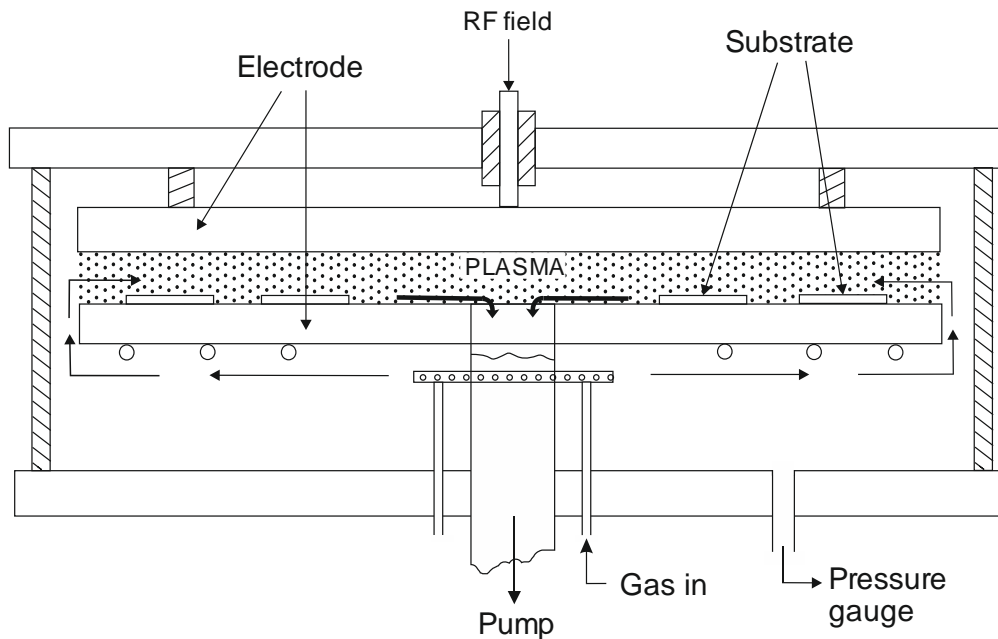


Figure 2.6 A schematic of a universal PECVD chamber, plasma created using a radio frequency (RF) field adapted from reference [54].

There are a variety of films that can be deposited using PECVD, these include; silicon oxides (SiO_x), aluminium oxides (AlO_x), silicon nitride (Si_3N_4), diamond-like carbon (DLC) and amorphous silicon (a-Si). This literature review will further investigate the deposition of silicon oxide (SiO_x) coatings deposited using PECVD and microwave PECVD (MW-PECVD) methods. In comparison to deposition methods such as CVD and sol-gel which operate at temperatures $500\text{-}600^\circ\text{C}$, PECVD operates at much lower temperatures ($200\text{-}300^\circ\text{C}$), sometimes even as low as room temperature [55].

Many research groups have deposited SiO_x films using PECVD with various combinations of gas precursors and excitation gases. One of the most common precursors being hexamethyldisiloxane (HMDSO) [56], however other precursors such as silane/oxygen (SiH_4/O_2), tetraethyl orthosilicate (TEOS), tetramethylsilane (TMS), and tetramethyldisiloxane (TMDSO), and tetramethylsilane (TMS) have also been used to deposit SiO_x coatings onto a variety of substrates [57], these will be discussed in further detail in section 3.3.

2.7.1 Microwave plasma enhanced chemical vapour deposition (MW-PECVD)

The microwave plasma enhanced chemical vapour deposition (MW-PECVD) process is similar to that of PECVD, but instead of the use of an RF field or a DC discharge, a microwave is used to activate the plasma. The microwave plasma is able to further enhance the speed in which the PECVD process is operated [58]. Plasmas created by microwaves are slightly different to other types of plasma, as the microwave frequency enables electrons to oscillate. This allows the collision of electrons with gaseous atoms and molecules to generate a high degree of ionisation [59]. In comparison to RF-PECVD, the MW-PECVD process generally uses a microwave discharge at 2.45 GHz, a much higher frequency than RF (13.56 MHz), thus creating a higher plasma density with higher energy electrons within the chamber. These higher energy electrons result in shorter deposition times and good controllability of the coating [58], [60].

There are two types of microwave discharges that can be used to deposit coatings: 1) a direct plasma source or 2) remote processing. The use of direct plasma processing for the deposition of SiO_x onto plastic substrates can prove difficult, due to the thermal load present during the microwave discharge. Remote processing overcomes this limitation and allows the deposition of SiO_x on to multiple substrates [61]. The remote process allows the carrier gas (e.g. He or Ar) to be introduced to the microwave source, away from the process chamber where the monomer is present. Separating this process reduces the thermal load in the process chamber, thus allowing deposition at lower surface temperatures and increasing the range of substrates that can be used.

Another method for introducing microwave energy into the deposition chamber is by using electron cyclotron resonance (ECR). ECR's were first investigated in the

1960's, used primarily for the construction of space craft propulsion applications [62]. ECR is a process where numerous charged ions are confined to a space, allowing multiple collisions and ionisations to take place, without recombination [62]. The process has been adopted throughout research for semiconductor fabrication, however the scalability of the process has proven to be difficult [63]. The advantages of using ECR can be applied to the plasma assisted deposition of silicon and silicon oxide coatings, allowing the deposition of high quality films at low pressures and substrate temperatures [64].

MW-PECVD is a well-established technique for depositing an array of coatings, such as diamond-like carbon (DLC) coatings. The use of a microwave to deposit SiO_x coatings has been studied over the past few decades, using polymeric substrates, however the most commonly used deposition technique is PECVD for other substrate types to deposit SiO_x .

2.8 Advantages, limitations and applications of coating methods

Table 2.1 gives a general overview of the different deposition techniques for depositing coatings. It highlights the typical pressure and temperature ranges and gives advantages and limitations for each procedure.

Table 2.1 A general overview of the deposition techniques, with pressures, temperatures, advantages, limitations and applications.

Method	Pressure range	Temperature	Advantages	Limitations	Applications
PVD	Evaporation – typically $\sim 10^{-9}$ Pa [65].	Evaporation – 250-350°C [66].	Any material can be deposited using a sputter target.	Relatively low deposition rate [67]. High costs [68].	Barrier layers for semi-conductor metallization [70]
	Sputtering – 1-100 Pa [35].	Sputtering – 350-600°C [35].	Good strength and durability. Reduces hazardous waste [67].	Line-of-sight deposition [69]. Poor adhesion [67].	Optical coatings – metallic and dielectric
CVD	APCVD – atmospheric pressure.	500-1200°C [71].	High deposition rates.	Requires high temperatures [69].	Tool coatings.
	LPCVD – sub-atmospheric pressures.		Short processing times [46].	Precursors may be harmful to the environment [72].	Metallurgical coating industry [73].
	UHVCVD – below 10^{-6} Pa.		Uniform coatings with good adhesion [72].		
PECVD	200-600 Pa.	200-450°C [74], [75]	Low operational temperatures [76]. High deposition rate [77]. Chemical and thermal stability [69]. Good uniformity and adhesion to the substrate [78].	Potential toxic and explosive gases in the plasma [69]. High set-up costs [76].	Deposition of silicate layers [79]. Anti-reflection and anti-scratch layers in optics. High quality SiN and SiO ₂ coatings.
MW-PECVD	0.001-0.1 Pa [80]	RT - 540°C for diamond and silicon based coatings [81]–[84]. >900°C for single crystal diamond [85], [86]	Reduction of pinholes and defects on the coating structure. Good controllability and uniformity. Ability to deposit a non-conducting coating onto a non-conducting substrate.	The scalability of the process is difficult.	Barrier coatings for polymer substrates. Corrosion resistant coatings on steels, for their use in bipolar plates.

Chapter 3 – Literature Review

3.1 Introduction

This chapter reviews the relevant literature for SiO_x coatings. The review will cover an introduction to the structure of silica and its polymorphs, the precursors and deposition processes for depositing SiO_x coatings and the properties and applications of SiO_x coatings..

Silicon oxides are employed for their use in coating and thin film applications due to their hardness, transparency, flexibility, and hydrophilicity [87], [88]. The term SiO_x is used to describe silicon oxide coatings, where x is greater than 1, but less than 2 ($1 < x < 2$), it may also be used interchangeably for silicon dioxide (SiO₂) coatings. In this thesis, SiO_x is used to term all coatings as the value of x lies between 1.7 and 2. SiO_x coatings have been of significant interest for a variety of coating applications [87], including anti-reflective (AR) and scratch resistant coatings on solar cells [89]–[91], water and oxygen barrier coatings for the food and pharmaceutical industries [92]–[94], corrosion protection and as dielectric coatings for thin film transistors.

3.2 Silicon dioxide

Silicon dioxide (SiO₂), also referred to as silica, are transparent crystals that can be found in nature as amethyst, flint, sand, agate, cristobalite, quartz, chalcedony and tridymite, with quartz and sand being the most common. All forms of silica have the same chemical composition (SiO₂); however, the atoms will be arranged in different structures. Silica can be divided into to two different groups, amorphous silica (a-silica) or crystalline silica (c-silica). c-silica is made up of repeating patterns of silicon and oxygen, whereas a-silica structures are more random with respect to c-silica [95].

3.2.1 Structure of silicon dioxide

Quartz (α -quartz) is the most common and most stable form of silica at atmospheric pressure and temperature. It is the only polymorph to be stable at ambient conditions, and all other polymorphs of silica will eventually transform into quartz over time [96]. Quartz can be present in either an alpha (α) or beta (β) phase, with each phase having a different crystal structure. α -quartz can undergo a reversible change in its crystal structure to β -quartz at a temperature of 573°C [97]. The α -quartz phase has a trigonal crystal system, which transitions to a hexagonal crystal system during the transition to the β -quartz phase. Both the α - and β -quartz phase structures are based on the helical arrangements of SiO_4 tetrahedra.

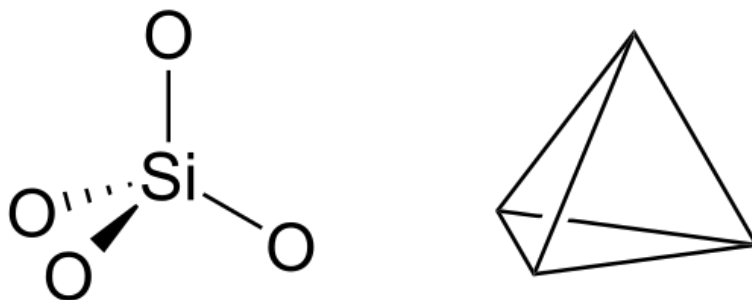


Figure 3.1 Silicon dioxide in the α - and β -quartz phase, in a SiO_4 tetrahedra arrangement.

Once α -quartz has transitioned into β -quartz at 573°C, additional heating will transform β -quartz into β -tridymite at 870°C, which can further transform into β -cristobalite at a temperature of 1470°C [98]. When the temperature reaches 1705°C β -cristobalite hits its melting point and forms a silica melt [99]. The phase changes from α -quartz to silica melt are shown in the figure below:

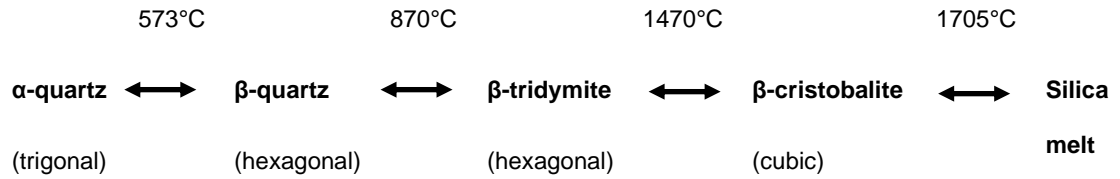


Figure 3.2 A schematic showing the reversible transitions of silica into its different phases.

Increasing the temperature slowly over time allows for a reversible process of the different phases as shown in the schematic in Figure 3.2. This indicates that β -cristobalite can transform back into the original α -quartz phase when it is cooled following a slow heating process. When temperatures are increased or decreased dramatically α -quartz will transform into β -quartz, however the other transformations are “skipped”, and β -quartz will transform straight into a silica melt, as highlighted in Figure 3.3.

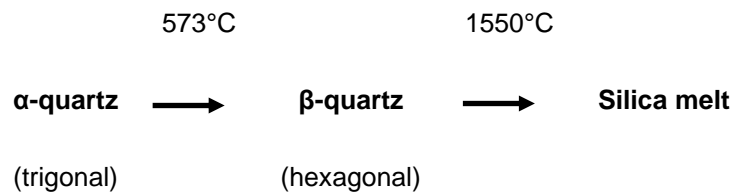


Figure 3.3 A schematic of the irreversible heating process of α -quartz into β -quartz, and finally into a silica melt.

This is an irreversible process, however if the silica melt were to be cooled rapidly, the liquid structure would be preserved, and it would transform into an amorphous glassy silica [96], shown in Figure 3.4.

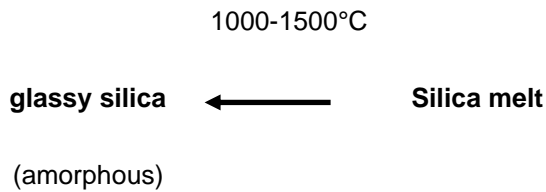


Figure 3.4 The mechanism for the transformation of silica melt into glassy silica through rapid cooling.

Both β -tridymite and β -cristobalite can transform into their corresponding α -polymorphs at temperatures lower than 870°C and 1470°C respectively (Figure 3.5). When cooled β -tridymite transforms into α -tridymite but retains the β -tridymite's hexagonal crystal system. β -cristobalite follows the same pattern and once cooled transforms into α -cristobalite whilst preserving the cubic crystal system of β -cristobalite.

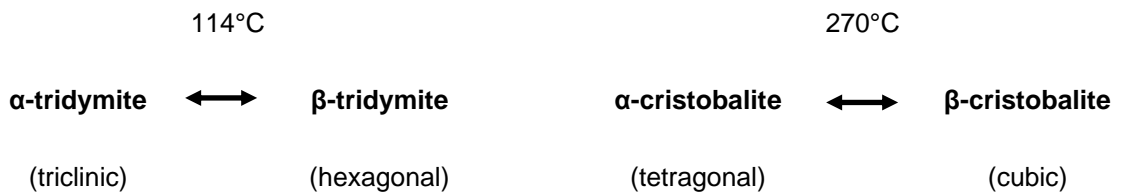


Figure 3.5 The mechanism of β -tridymite and β -cristobalite into their corresponding α -polymorphs through cooling to temperatures lower than 870°C and 1470°C, respectively.

3.3 A comparison of the precursors, deposition techniques and substrates for the deposition of SiO_x coatings

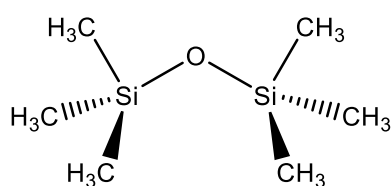
A series of deposition techniques have previously been explored in this literature review, and have been generalised for a wide range of coatings. This section will focus on the main deposition methods used for depositing SiO_x coatings, focussing on the precursors used, substrate materials and coating parameters.

3.3.1 Precursors for depositing SiO_x coatings

There are several monomers that can be used to deposit SiO_x coatings, each affording different chemistries and methods of application. Organosilane compounds are the most popular monomers [100]. These monomers can be broken down into 3 groups; disiloxanes, methoxy silanes and ethoxy silanes. This section will cover a selection of the most commonly used monomers used for SiO_x deposition.

3.3.1.1 Hexamethyldisiloxane (HMDSO)

Liquid hexamethyldisiloxane (HMDSO) is the most commonly used precursor for the deposition of SiO_x films [101]. The structure of HMDSO is shown in Figure 3.6. The plasma polymerisation of HMDSO (ppHMDSO) has been notably studied as it is able to significantly improve the barrier properties and water repellency of many polymers [102]. Hexamethyldisiloxane (HMDSO) has many advantages over other precursors and is used extensively for PECVD due to its chemical inertness, non-toxic character, and relatively high vapour pressure (even at room temperatures) [87].



HMDSO

Figure 3.6. The chemical structure of hexamethyldisiloxane (HMDSO).

HMDSO can be used on its own during the deposition process, or in combination with oxygen (O₂) [103]. When HMDSO is combined with O₂ the coatings produced are predominantly inorganic SiO₂-like, whereas using HMDSO plasmas on their

own produces a polymer-like $\text{SiO}_x\text{C}_y\text{H}_z$ coating which has a more organic nature [104].

The mechanism for the breakdown of HMDSO during the PECVD process has been studied by Sonnenfeld et al. Studying the chemical kinetics of the reaction has provided two possible breakdown mechanisms for depositing SiO_x , using HMDSO and O_2 [105]. Understanding the breakdown of the monomer in the chamber can lead to highly defined coatings with exceptional film quality. The chemical plasmas were analysed using gas chromatography (GC), in either an Ar or He environment. A schematic is presented in Figure 3.7 and specifies the plasma polymerisation of HMDSO (pp-HMDSO), and the conversion of the species to SiO_x , through adsorption onto the substrate.

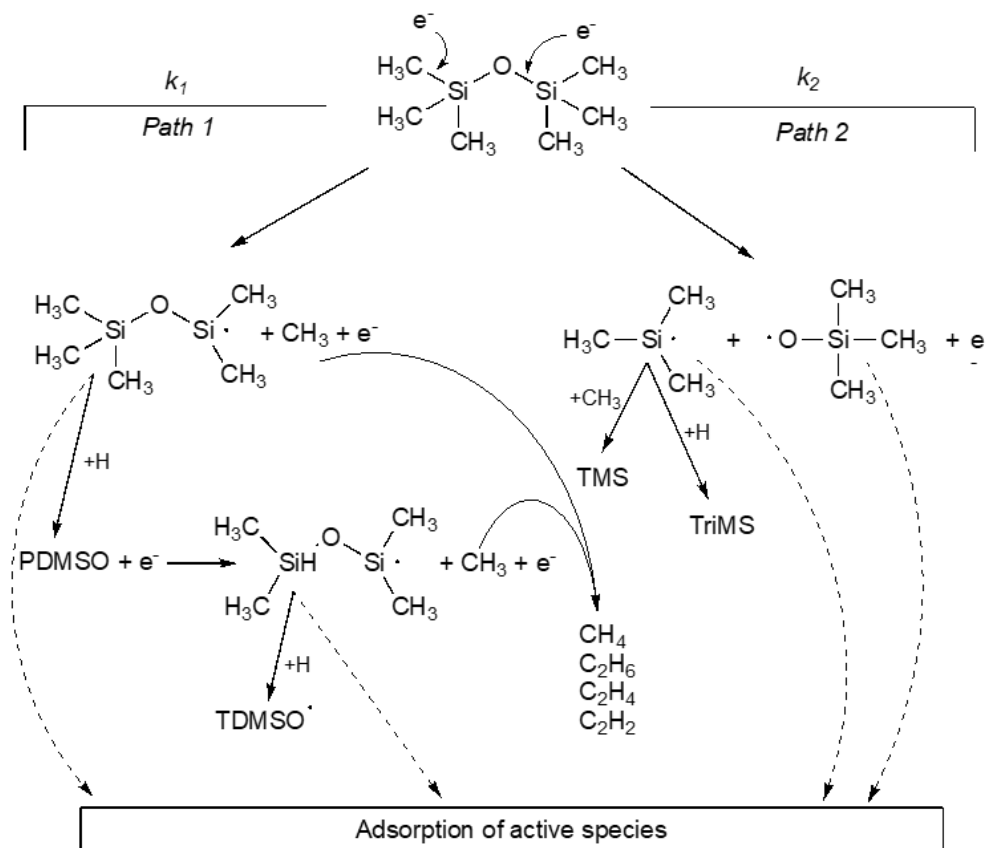


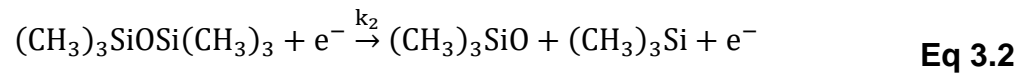
Figure 3.7. Mechanistic reaction scheme for the plasma polymerisation of HMDSO, into its smaller constituents, through to adsorption onto the substrate, mechanism adapted from [105].

The two possible reactions have been defined based on the chemical species present in the GC analysis:

Reaction 1:



Reaction 2:



The two reaction paths, 1 and 2, are defined with the reaction rates k_1 and k_2 respectively. The by-products from the reaction are desorbed into the gas phase, and thus do not take part in the polymerisation process. This in turn leads to a coating with lower carbon content [105].

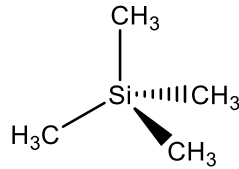
Varying the O_2 concentrations, in combination with HMDSO allows SiO_x coatings to be deposited with differing structures and Si:O ratios. Using higher concentrations of O_2 during the PECVD process will lead to the complete oxidation of HMDSO to stoichiometric SiO_2 [106].

The deposition of scratch resistant coatings can also be achieved with a HMDSO and O_2 gas mixture [107]. One study by Michaeli et al. found that an HMDSO: O_2 ratio of 1:10 produces a very hard, quartz-like film [108]. HMDSO is the most commonly used monomer, due to its very high deposition rate, when using a microwave-excited plasma source.

3.3.1.2 Tetramethylsilane (TMS)

Tetramethylsilane (TMS) is an organosilicon compound and is the simplest of all tetraorganosilanes. The structure of TMS can be found in Figure 3.8. TMS in

combination with oxygen (O_2) is widely used as a precursor for SiO_x coatings as it is easy to handle due to its chemical inertness at room temperature [109] and is non-explosive [55].



TMS

Figure 3.8. The chemical structure of tetramethylsilane (TMS).

PECVD techniques have predominantly been used for the deposition of SiO_x coatings onto polymeric films using TMS. TMS in combination O_2 is mainly used for depositing the coatings, however other combinations of gases have also been used, including; potassium permanganate ($KMnO_4$) and O_2-NH_3 [110], [111]. As long as there is a source of oxygen within the gas mixture, a reaction will occur resulting in the deposition of a SiO_x coating. The addition of NH_3 to a TMS- O_2 gas mixture limits the oxidation of the TMS monomer and can therefore result in a silicon oxynitride (SiO_xN_y) film [110].

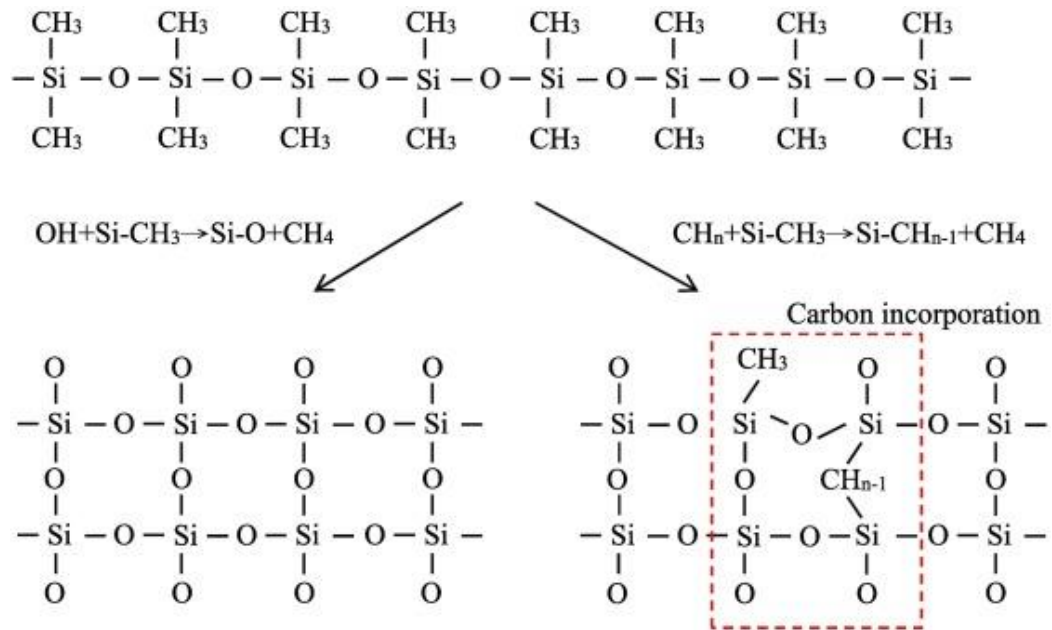
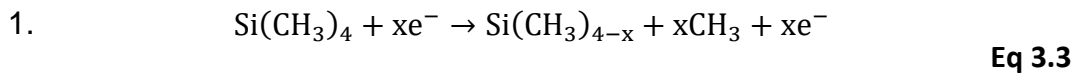


Figure 3.9. Proposed growth mechanism of SiO_x films based on a TMS- O_2 gas mixture [112].

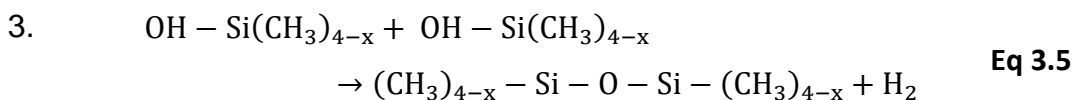
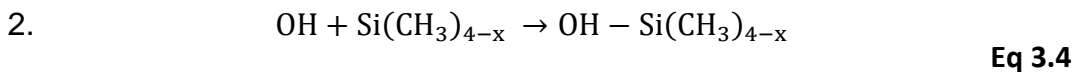
The mechanism for the breakdown of the TMS- O_2 gas mixture and growth of the SiO_x film has been proposed by Lien et al [112], as shown in Figure 3.9. Firstly, the decomposition of TMS via electron bombardment:



Where $x = 1$ to 4.

The CH_3 will decompose into CH_2 and CH , via the removal of hydrogen atoms.

These H atoms can then react with O_2 to form OH radicals.



3.3.1.3 Tetraethyl orthosilicate (TEOS)

Tetraethyl orthosilicate (TEOS), previously known as tetraethoxysilane, is an organosilicon material which can be used as a precursor to produce silicon dioxide (SiO₂) coatings for the semiconductor industry [113].

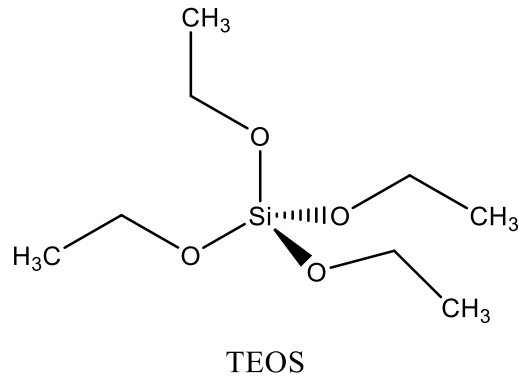
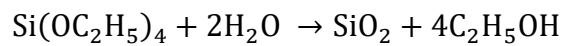


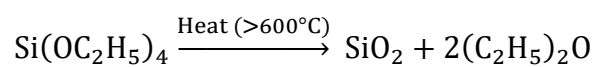
Figure 3.10. The chemical structure of tetraethyl orthosilicate (TEOS).

The use of TEOS has become increasingly popular as it affords a higher film quality and exceptional step coverage [114]. The addition of water to TEOS, with chemical formula Si(OC₂H₅)₄, can be used to easily produce SiO₂:



Eq 3.6

This hydrolysis process is mainly used for the deposition of SiO₂ using a sol-gel process [115]. At higher temperatures (>600°C), TEOS can easily be broken down into SiO₂, a popular method used with low pressure chemical vapour deposition (LPCVD) [116]. The higher temperatures lead to stoichiometric films with exceptional electrical properties [117].



Eq 3.7

The higher temperatures used, are inconvenient for coatings with thermally sensitive substrates, therefore a lower temperature method needs to be considered [117]. Plasma enhanced chemical vapour deposition (PECVD) can be used for depositing SiO₂ coatings at lower temperatures, or TEOS in combination with oxygen (O₂) [100], [118] or ozone (O₃) [114] can also promote deposition of silicon oxides at lower temperatures. TEOS and oxygen react under a radio frequency (RF) discharge, promoting the oxidation of the organic species, in order to deposit silicon oxide [119].

3.3.2 Deposition methods for depositing SiO_x coatings

There are many deposition methods used for depositing SiO_x coatings, with different reaction systems being utilised dependent on the properties to be achieved of the SiO_x coatings. The methods used have advantages and disadvantages and will be investigated further here. An overview of the deposition methods, precursors, substrates and applications is shown in Table 3.1.

Table 3.1 An overview of the deposition methods, precursors, substrates and applications for SiO_x coatings.

Method	Precursors	Substrates	Applications	Hardness (GPa)	Young's modulus (GPa)	Corrosion resistance (Ω cm ²)
PVD	Pure silicon	PET [120], [121]	Barrier layers for semi-conductors [70]	Pulsed magnetron – 8 GPa	Pulsed magnetron – 70 GPa	-
	SiO β -SiC	Quartz [122] Sapphire Fused silica [123] Paper [124]	Optical coatings and dielectrics.	EB – 1.7-4.1 GPa [125]	EB – 15-42 GPa [125]	-
PECVD	HMDSO	PET	Deposition of silicate layers [79].	-	15 – 59 GPa [126]f	1.8x10 ² – 7.4x10 ⁴ [127]
	TMS	PP				
	TEOS	PVC	Anti-reflection and anti-scratch layers in optics.			1.5x10 ⁹ [128]
	SiH ₄					
Sol-gel	TEOS	Ti6Al7Nb alloy	Barrier coatings for biomaterials [129]	-	-	1.2x10 ⁶ – 1.9x10 ⁷ [131]
	Ethyl alcohol	Titanium discs				
	Tetramethoxysilane (TMOS)	PVC	Corrosion mitigation [130]			
MW-PECVD	HMDSO	Polymeric substrates	Barrier coatings for polymer substrates.	-	-	-
	TEOS	Stainless steels	Corrosion resistant coatings on steels, for their use in bipolar plates.			

3.3.2.1 PVD

PVD techniques have been used throughout the literature to deposit SiO_x coatings. The primary method of deposition using this technique is through a silicon (Si) target, sputtered with oxygen (O_2) to deposit a SiO_x coating. These coatings can be deposited using either evaporation or magnetron sputtering. PVD is generally used to deposit stoichiometric silica (SiO_2) coatings onto ceramic substrates, such as zirconia discs or silicon wafers. To deposit SiO_2 coatings using PVD, an RF plasma can be used (13.56 MHz) with the addition of a DC bias. The PVD technique is not the preferred method of choice due to line of sight limitations and poor uniformity of the deposited coatings. Therefore, deposition techniques such as CVD and PECVD are more commonly used and can provide more uniform coatings with higher deposition rates [72], [77], [78].

The PVD methods that can be used to deposit SiO_x coatings include evaporation, sputtering and ion plating. One of the earliest methods developed for PVD technology was evaporation and has previously been used to deposit SiO_x coatings, however due to the thermal decomposition of the process, the coating composition is difficult to control [109]. Electron beam (EB) evaporation has been utilised for depositing SiO_x coatings due to its high deposition rates, dense coatings and low contamination [132]. The method involves the evaporation of a material using thermal vaporisation, allowing the material to reach the substrate with little to no collisions with other gas molecules [133]. The technique is also capable of low temperature depositions and the deposition of multilayer coatings. A study using EB for depositing SiO_x onto 316 SS used a β -silicon carbide (β -SiC) target at 1000°C [134]. Using a high current intensity for the EB, the SiC target will vaporise into Si and C, allowing the Si to react with the metal oxide thin film on the substrate surface. Typically, EB is used commercially for producing

SiO_x gas barrier coatings, due to the higher deposition rates when compared to other PVD and CVD methods [135].

Sputtering methods, using both DC and RF, are the most common PVD techniques used for depositing SiO_x coatings. The RF magnetron sputtering method has been used to deposit SiO_x onto a variety of different substrates including; polyethylene terephthalate (PET) [120], [121], quartz [122], sapphire, fused silica [123] and paper [124]. The targets and precursors used vary depending on the application and properties required of the coatings, and include; pure (99.999%) silicon targets and organo-silicon precursors (TEOS and HMDSO). The DC magnetron sputtering method is used for depositing SiO_x coatings for their optical, gas barrier and electrical properties [136], [137]. The oxygen flow rate during the deposition process is an important factor on the characteristics of the coatings. Typical substrates used for DC sputtering include; PET, n-type Si wafers and glass.

3.3.2.2 CVD

The CVD method is used for depositing coatings through chemical reactions of the precursor gases. The conventional CVD technique is a thermally activated deposition method, so is unsuitable for substrates that are temperature sensitive, such as polymeric substrates. The introduction of plasma into the CVD chamber, however allows the use of lower temperatures and pressures to be used throughout the deposition process. The most commonly used method for depositing SiO_x coatings is the PECVD method. A SiO_x coating may be deposited using PECVD, through creation of the plasma with an RF field, however an interlayer is necessary as a non-conducting coating cannot be deposited onto a conducting substrate using this method.

3.3.2.3 PECVD

PECVD is used widely for the deposition of highly quality SiO_x films at low substrate temperatures [138], making the technique a preferred choice for many different substrates. The properties of SiO_x coatings are dependent on the reactive gases used during the deposition. The main precursor gases have been described in section 3.3.1 and include; HMDSO, TEOS, TMS and SiH_4 . The plasma promotes the decomposition of the gases into silicon radicals, allowing the reaction with oxygen radicals which are added into the system by means of O_2 gas. Different natures of silicon based coatings including, inorganic SiO_x and organic $\text{SiO}_x\text{C}_y\text{H}_z$ can be prepared from different precursors and deposition parameters [139]. SiO_x coatings generated using PECVD can be used for a variety of different applications including, but not limited to; barrier coatings for the food packaging industry [138], microelectronics [140] and semiconductor processing [141]. The PECVD processing methods can be operated using a microwave (2.45GHz), radio frequency (RF) (13.56 MHz) and medium frequency (MF) (kHz range) power supplies.

The RF PECVD system is the most commonly used PECVD method for SiO_x coating and allows the deposition onto PET substrates, using temperatures below $100\text{ }^\circ\text{C}$ [142]. Grüniger et al reported that the use of HMDSO and O_2 using RF PECVD provided coatings with an improved oxygen transmission rate (OTR), when compared with the corresponding MW plasmas [143]. The influence of the HMDSO: O_2 ratio during the deposition can also affect the properties of the SiO_x coating.

Varying the concentration of the oxygen during the deposition process can affect the chemical structure, mechanical and oxygen barrier properties [144]. By varying the oxygen and HMDSO ratios, the resulting coatings can vary from

inorganic-SiO₂ like to polymeric-like [145]. Controlling this ratio allows the properties and structure of the coatings to be controlled, dependent on the particular application. MW discharges using HMDSO:O₂ ratios between 1:8 and 1:10, are used in order to gain high deposition rates [107].

The use of a microwave source to produce the plasma during the PECVD deposition, provides coatings with good uniformity and adhesion, whilst achieving high deposition rates at low temperatures and ambient pressures. This gives the ability to produce high quality SiO_x coatings on a wide variety of substrates, including polymeric materials. The standard MW frequency used for depositing SiO_x coatings is 2.45 GHz. Using a microwave source for the excitation of plasma, allows for very high deposition rates of the HMDSO monomer, in combination with O₂. Wrobel et al. found that a higher deposition rate of 0.4 μm min⁻¹ was achieved using a MW source (2.45GHz), compared with a radiofrequency (RF) deposition rate of 0.1 μm min⁻¹ [146]. This higher deposition rate can be attributed to the higher frequency generated when using a microwave source.

The deposition rates of SiO_x coatings using MW-PECVD have been found to range from 0.063 μm/min up to 0.22 μm/min [147], which are dependent on the composition of the reactant gas, the temperature used, microwave power applied to the chamber and the flow rates of reactant gases. The benefits of microwave plasma allow SiO_x coatings to be deposited with minimal pinholes, due to microwave plasma being denser than other types of plasma. The reduction of pinholes within the SiO_x coating, reduces the ability of hydrogen to flow through the SiO_x film and protecting the coating from H₂ based defects.

The PECVD technique for depositing SiO_x coatings affords low operational temperatures and high deposition rates, whilst also maintaining a uniform

coating. The drawback to PECVD are the high set up costs. The low deposition temperatures allow a variety of substrates to be used, including polymeric substrates such as polypropylene (PP), polyvinylchloride (PVC) and polyethylene terephthalate (PET) [148], [149]. Microwave PECVD (MW-PECVD) has not yet been fully established as a widespread technique for depositing SiO_x coatings, with much of the current literature for the deposition of SiO_x coatings using MW-PECVD, generally focussing on the use of polymeric substrates. The use of MW-PECVD for depositing SiO_x coatings will provide coatings with a good uniformity, and minimal pinholes and defects. The choice of deposition method is also due to the limitations of the current PVD machine at the University of Leeds. As the machine does not have an RF source, the PECVD deposition method was unable to be used. Therefore, due to the University of Leeds facility having the microwave source, it was the desired method for the deposition of SiO_x coatings in this thesis.

3.4 The properties and applications of SiO_x coatings

There are several beneficial properties SiO_x coatings can provide to the chosen coated substrate. The most widely researched properties are as a barrier coating against gas and moisture permeation, for the food packaging industry and as a dielectric coating for thin film transistors. More recently SiO_x coatings have been researched for their potential as a corrosion resistant coating on carbon steel and stainless steel substrates.

3.4.1 The gas barrier properties of SiO_x coatings

SiO_x coatings play an important role in both gas and moisture permeation. The most common use of SiO_x coatings is as a gas barrier coating on polymer substrates. The transparent nature and gas barrier properties of SiO_x coatings

makes them an excellent candidate for food packaging and medical device applications [150]. The deposition of SiO_x coatings onto plastic substrates has attracted much research due to the high barrier properties towards oxygen [139]. The HMDSO: O_2 ratio during the deposition is very important when fabricating gas barrier coatings. Increasing the oxygen concentration (high HMDSO: O_2 ratio) gives a coating with a more inorganic nature and has proven to improve the barrier performance towards oxygen [143], [151].

The type of deposition method can also affect the gas permeation properties of the coatings. PECVD is superior to PVD as electron beam sputtering has shown to include cracking of the coating, even at low temperatures [152], which in turn affects the barrier performance. Grüniger et al [143] found that using a MW-PECVD method without substrate bias can increase the oxygen permeation of the coating. However, using RF-PECVD and a substrate bias yields higher energy bombardment of the substrate surface, which can induce the destruction of the film growth. The oxygen transmission rate can also be decreased with an increase in the RF power, and the addition of oxygen. Increasing the HMDSO: O_2 ratio from 1:3 to 1:18 increases the density of the SiO_x coatings, and reduces the amount of carbon present [153]. Hegemann et al. found that increasing the ratio above 1:6 can produce scratch resistant, low carbon, quartz-like coatings. The addition of the oxygen into the plasma reduces the amount of carbon and hydrogen present in the coatings, due to the formation of CO_2 and H_2O molecules [154]. The resultant coatings are transparent, hard inorganic SiO_2 -like.

Overall, the gas barrier properties of the SiO_x coatings are largely dependent on the method of deposition and the HMDSO: O_2 ratios used throughout the process.

High oxygen concentrations afford hard, SiO₂-like coating, whereas lower concentrations result in softer, polymeric SiO_xC_yH_z like coatings.

3.4.2 The dielectric properties of SiO_x coatings

Silicon oxide coatings present an important role in the field of optical and electronic coatings. It is a widely used dielectric medium due to its excellent insulating properties and compatibility with optical coatings [155]. The deposition of silicon dioxide (SiO₂) coatings via plasma enhanced chemical vapour deposition (PECVD) at low temperatures has become extremely important within the field of semi-conductors [156]. Other deposition techniques such as chemical vapour deposition (CVD) and reactive pulse magnetron sputtering have also been used to assess the electrical properties of silicon dioxide (SiO₂) coatings [136]. Bartzsch et al have researched the electrical properties of both Al₂O₃ and SiO₂ films deposited using reactive pulse magnetron sputtering [157]. The electrical properties investigated included the resistivity, breakdown constant and breakdown strength as a function of deposition rate, substrate bias and the size of contact pads [157]. It was found that the coatings deposited with an additional RF substrate bias gave a higher resistivity and breakdown strength compared to the coatings deposited without bias, and that films deposited in bipolar pulse also gave a higher breakdown strength [157].

The oxygen concentration during the SiO_x deposition can also affect the dielectric properties of the coatings. A higher x value in the SiO_x can be obtained with an increase in the O₂ flow rate. The higher values of x also have an effect on the dielectric constant of the SiO_x coatings, resulting in a lower dielectric constant with increasing x values [158].

3.5 Theory of corrosion

Corrosion can be described as the ‘irreversible interfacial reaction of a material (metal, ceramic, polymer) with its environment, which results in the consumption of the material or dissolution into the material of a component on the environment’ (IUPAC, 2012) [159].

Corrosion in an aqueous environment is an electrochemical process, resulting in the transfer of electrons between a metal surface and a liquid electrolyte solution. This process can be extremely costly and cause serious problems for many different industries and environments [160]. Electrochemical corrosion of metals is the most important type of corrosion, whereby the oxidation process is accelerated by the presence of an electron acceptor (Eq 3.8) – the anodic reaction. The reduction (cathodic) process describes the consumption of the electrons created by the corrosion (anodic) reaction (Eq 3.9).



3.5.1 The corrosion cell

An electrochemical corrosion cell is made up of four components; an anode, a cathode, a metal and an electrolyte. The metal acts as an electrical connection between the anode and the cathode providing a pathway for the flow of current and the movement of electrons, as shown in Figure 3.11.

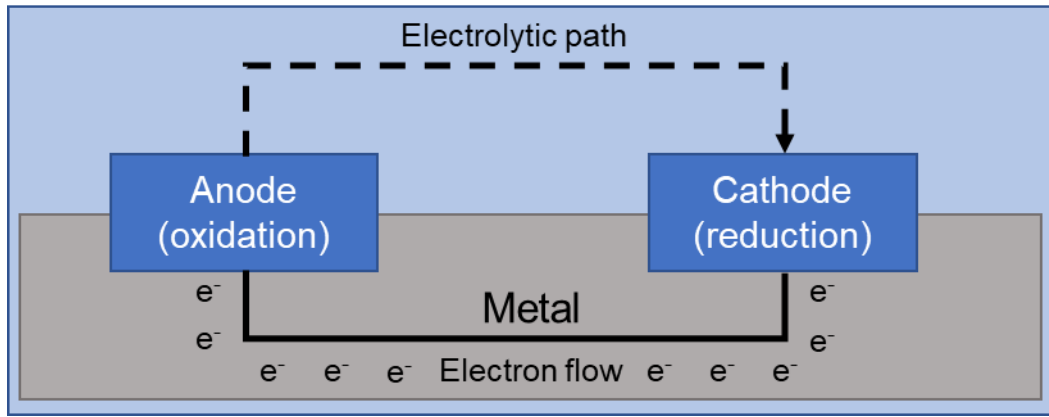
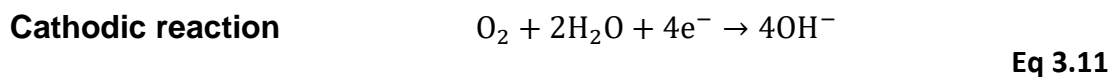
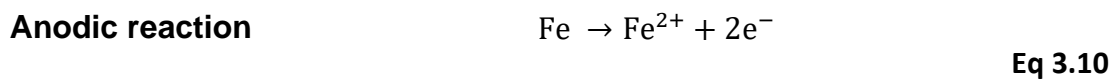
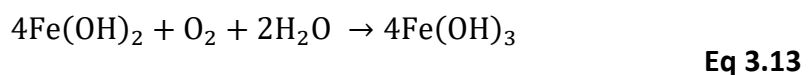
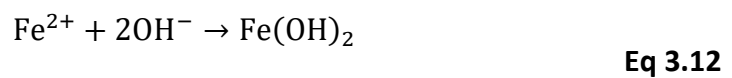


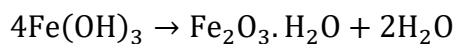
Figure 3.11. A corrosion cell made up of the four basic components.

The anodic and cathodic areas are able to propagate on the same metal surface due to the heterogeneous nature of a metal surface, allowing two electrochemical half-cell reactions to occur [161]. The anodic and cathodic half-cell reactions described in Eq 3.8 and Eq 3.9 are for generic metals, denoted using the letter M. The reactions that take place for carbon steel, in the presence of a neutral or basic electrolyte are shown in Eq 3.10 and Eq 3.11.



The hydroxide ions, OH⁻ from the cathodic reaction and the Fe²⁺ ions from the anodic reaction combine to form ferrous oxide, as shown in Eq 3.12. In the presence of water and oxygen, Fe(OH)₂ will react to form ferric oxide (Eq 3.13), and further reacts to form hydrated ferric oxide (rust) (Eq 3.14).





Eq 3.14

3.5.2 Methods of corrosion prevention

Any method, procedure or measure aimed at avoiding corrosion damage to a metallic surface are called corrosion protection [162]. Significant advancements in the improvement of steel corrosion have been made over the past few decades.

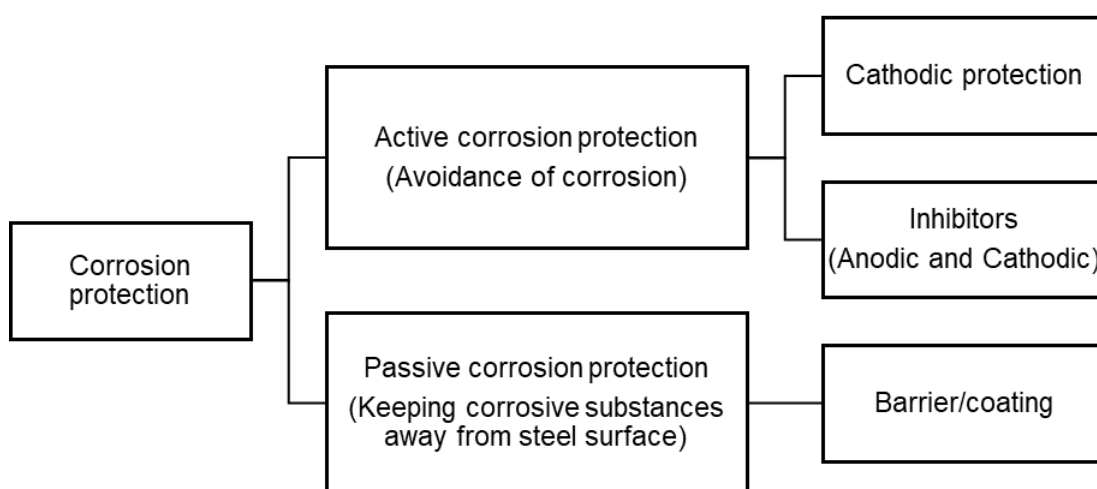


Figure 3.12. Schematic diagram of some corrosion protection methods.

Synthetic corrosion inhibitors are widely used methods for protecting metallic surfaces due to the ease of application within industry and the cost effectiveness [163]. Corrosion inhibitors are able to slow down, reduce or even prevent the corrosion of a metal surface [164]. There are three main types of inhibitors; anodic, cathodic and mixed type. Anodic inhibitors control the rate of the oxidation reaction and a cathodic inhibitor prevents or reduces the rate of the reduction reaction. A mixed type inhibitor is a film forming compound that can reduce both the anodic and cathodic reactions.

Cathodic protection is a technique used to prevent the corrosion of a metal surface by turning it into the cathodic site of an electrochemical cell [165]. It is currently widely used for corrosion control of underground and undersea metallic surfaces, such as pipelines, utility lines and cables [166].

Barrier protection is one of the most widely used methods for protecting metallic surfaces, in order to reduce or prevent corrosion. The principle behind the addition of a barrier layer is to isolate the steel surface from the corrosive environment. If the barrier is free of defects and pinholes, corrosion should not occur as the electrolyte component of the corrosion cell will not be contact with the steel surface. Three important conditions for a protective barrier coating, to enhance the corrosion protection are; good adherence to the metal surface, resistance to mechanical stress and must be corrosion resistant.

3.6 The corrosion resistance of SiO_x coatings

Inorganic coatings, typically oxides and phosphates are able to provide metallic surfaces with an enhanced corrosion resistance. SiO_x films are often utilised as a barrier coating against the corrosion of metals [127]. SiO_x coatings have been applied to stainless steel (SS) substrates using sol-gel methods, to improve the biocompatibility of SS based implants [167]–[169]. Similarly, the use of SiO_x coatings deposited using PECVD has been investigated as a corrosion barrier for carbon based steels [170].

The SiO_x coatings using both sol-gel and PECVD deposition methods have been analysed in different solution media including sodium chloride (NaCl) and sulphuric acid (H₂SO₄). The corrosion properties and scratch resistance of the SS showed an improvement with the silica sol-gel coating, in both NaCl [171] and H₂SO₄ media [22], [172].

The corrosion resistance and corrosion rates of SiO_x coatings have been investigated using Tafel extrapolation of polarisation curves and electrochemical impedance spectroscopy (EIS). The potentiodynamic polarisation measurement methods allow the determination of instantaneous corrosion rates. The total polarisation curves of a corrosion system are determined from both an anodic curve (metal oxidation) and a cathodic curve (reduction of an oxidant from the solution).

A Tafel extrapolation of a polarisation curve is used to determine the corrosion current density of a coated system using potentiodynamic measurements. Silica based coatings have been deposited onto a variety of steel substrates in order to investigate the corrosion protection. An overview of the corrosion current densities (i_{corr}), corrosion potential (E_{corr}), substrates, deposition methods and coating compositions for silica based coatings are shown in Table 3.2. The i_{corr} values vary from 0.005 $\mu\text{A}/\text{cm}^2$ for stainless steel substrates, to 12.001 $\mu\text{A}/\text{cm}^2$ for carbon steel substrates. The E_{corr} values vs. a saturated calomel electrode (SCE) also vary between -1430 mV and -90 mV, dependent on the substrate material and also the nature of the silicon oxide-like coating.

Table 3.2 provides an overview into the types of SiO_x-like coatings that have been investigated using polarisation curves, and the effect the substrate has on the corrosion protection. The stainless steel substrates and tin alloys give the lowest i_{corr} values and the highest E_{corr} values, and can therefore be said to have the best corrosion protection. Particularly when using inorganic silica and SiO₂ coatings. The most commonly used electrolyte is 3.5 % NaCl and the most basic solution for electrochemical testing. Silicon oxycarbide coated carbon steel provides an enhanced corrosion resistance when compared to uncoated carbon

steel. The coatings with the highest corrosion protection are the inorganic SiO₂ coatings deposited onto stainless steel, however little research has been performed with these coatings on carbon substrates. Therefore, opening the research gap for the investigation into the corrosion protection of SiO_x coated carbon steels, using polarisation techniques.

Table 3.2 An overview of the corrosion properties of silica based coatings, on a variety of metallic substrates.

Coating	Substrate	Deposition method	Electrolyte	i_{corr} ($\mu\text{A}/\text{cm}^2$)	E_{corr} (mV)
Silica [173]	Stainless steel	Sol-gel	3.5 % NaCl	0.003	-350
SiO ₂ [131]	Ti-6Al-7Nb alloy	Sol-gel	Simulated body fluid	0.006-0.10	-275 – -90 (SCE)
SiO ₂ [174]	Stainless steel	PACVD	0.5 M NaCl	0.005	-
Silicone-like Silica-like [175]	AZ31 magnesium alloys	PECVD	3.5 % NaCl	7.94 0.158	-1430 -1320 (SCE)
Hybrid organic – inorganic silica [176]	Carbon steel	Sol-gel	3.5 % NaCl	-	-588 – -610
Silicon oxycarbide [177]	Low carbon steel	RF/TEOS plasma	3.5 % NaCl	0.325-12.001	-514 - -809 (SCE)
SiO _x C _y [178]	Carbon steels	Capacitively coupled RF plasma	3.5 % NaCl	0.714 – 12.001	-534 – -809 (SCE)

3.6.1 Electrochemical Impedance Spectroscopy (EIS) of SiO_x coatings

EIS is an important characterisation technique to investigate the properties of a material and the electrode reactions [179]. It is a multifrequency alternating

current (AC) technique which measures the electrical resistance (impedance), of the coating/solution interface over a multitude of frequencies (ω) [180]. The aim of the EIS technique is to measure the impedance as a function of frequency, allowing the resulting spectrum to be analysed to estimate the corrosion rates and mechanisms of a coated system. EIS allows data to be interpreted so that the capacitance and resistance values of a system can be determined from the corresponding Nyquist and Bode plots, through the fitting of an equivalent circuit. Calculating both the resistance and capacitance values of each physical component within a system can help to understand the system that is being analysed.

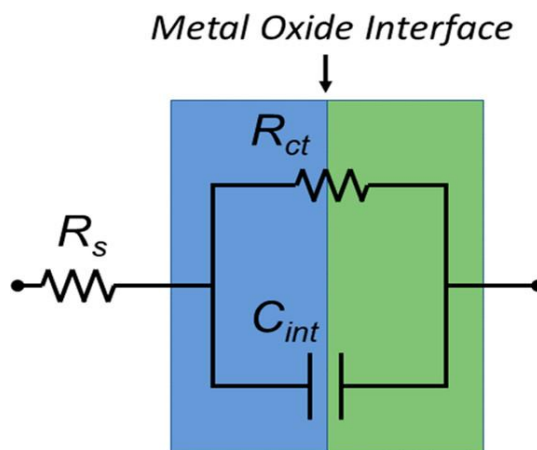


Figure 3.13 A Randles circuit model across a metal oxide surface, with a solution resistance (R_s), interfacial capacitance (C_{int}) and charge transfer resistance (R_{ct}).

The Randles circuit is the most simple equivalent circuit and is made up of an electrolyte/solution resistance (R_s), an interfacial capacitance (C_{int}) and a charge transfer resistance (R_{ct}). A simple Randles circuit model across a metal oxide

interface is demonstrated in Figure 3.13. The corresponding Randles Nyquist and Bode plots are shown in Figure 3.14.

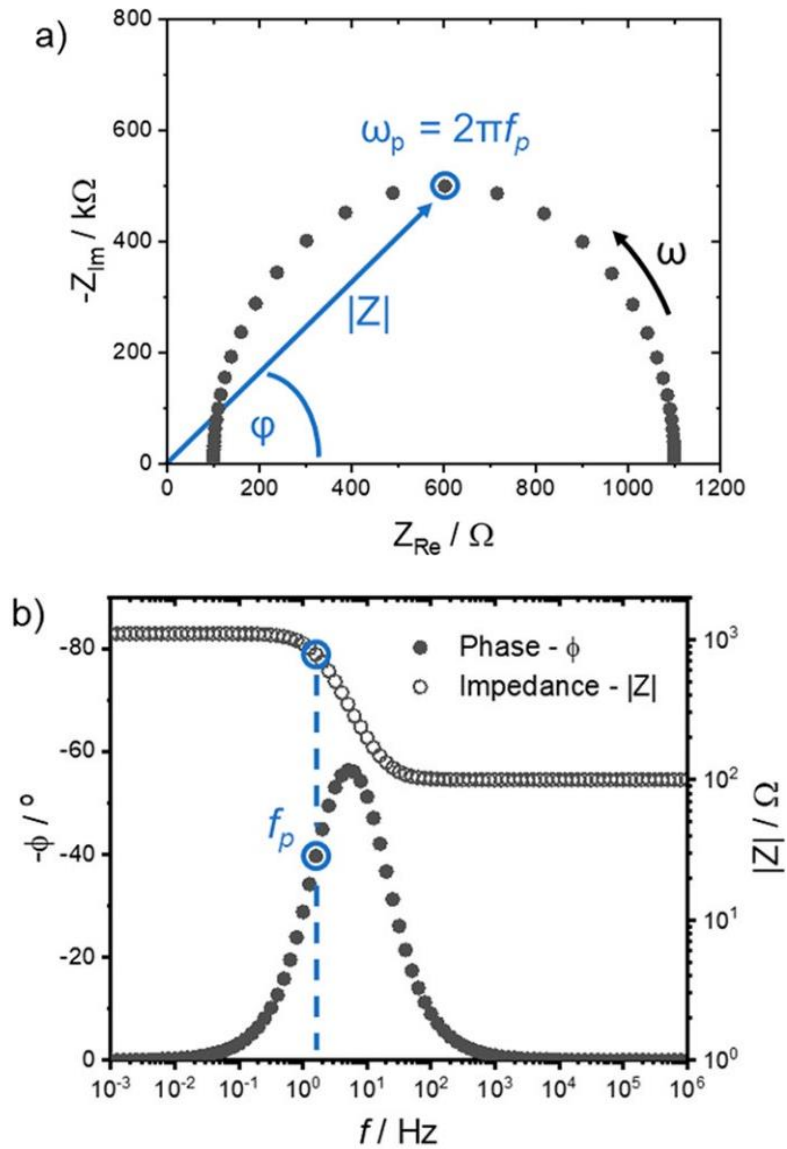


Figure 3.14 A simple a) Nyquist and b) Bode plot representing the Randles circuit in Figure 3.13, where $R_s = 100 \Omega$, $R_{ct} = 1000 \Omega$, and $C_{int} = 100 \mu\text{F}$ [181].

If a coating resistance increases during the test, the coating is becoming more protective, with the capacitance seeing the opposite effect and decreasing in value. For a coating that is becoming less protective, there will be a decrease in

the resistance values and an increase in the capacitance. Using the resistance and capacitance values, calculated from EIS, values such as corrosion rate, water uptake and delamination can be calculated.

The use of EIS expands much further than estimating the resistance and capacitance of a coated system and can also be used to detect any interfacial problems that may be occurring. If a coated sample exhibits defects or pinholes within the coating structure, the electrolyte is able to penetrate through to the substrate surface, which could lead to under film corrosion. This corrosion may alter the resistance of the coating during the EIS process, due to the formation of an oxide layer between the coating and substrate interface [182].

EIS has been utilised to study the corrosion resistance of SiO_x coatings on stainless steels substrates. For much of the literature, the coatings have been deposited using traditional sol-gel methods, with very few reports on the corrosion resistance of SiO_x coatings deposited using PECVD methods. SiO_x coatings deposited onto carbon steel, at plasma powers 200 and 300 W, provide a good protective barrier against corrosion. The resistance of the charge transfer (R_{ct}) gives a good indication of the protectiveness of the coating. Ribeiro et al [127] reported R_{ct} values of 1.51×10^6 and $3.60 \times 10^5 \Omega \cdot \text{cm}^2$ for 1 μm thick SiO_x layers deposited at plasma powers 200 and 300 W, respectively. At lower plasma powers of 10 and 15 W, the resultant coating was a more organic like SiO_xC_yH_z film, and provides lower R_{ct} values of 6.99×10^4 and $2.25 \times 10^5 \Omega \cdot \text{cm}^2$, respectively. Increasing the plasma power to 50 W resulted in a bilayer coating with a thin SiO_xC_yH_z at the coating surface, with an SiO_x top layer. The corrosion resistance proved to increase with this bilayer, and gave an R_{ct} value of $1.24 \times 10^7 \Omega \cdot \text{cm}^2$. The

degree of oxidation is therefore able to be controlled, and the addition of SiO_x inorganic layers enhances the corrosion resistance of carbon steels.

The EIS study of a SiO_x coating for medical devices has been undertaken by Walke et al [167]. Due to the chemical inertness and biocompatibility, SiO_x is of interest in the field of cardiac implants. The coating was deposited using a sol-gel method onto 316L stainless steel. The EIS experiments show that the resistance of the oxide layer reaches large values varying from 1.274×10^6 – $1.677 \times 10^6 \Omega \cdot \text{cm}^2$, suggesting the appropriate degree of protection. Another study by Delimi et al [170] reported the corrosion protection of a SiO_x coating on carbon steel, deposited using PECVD. The coated layers were deposited between 20 and 200 nm, and EIS measurements were taken using a 3% NaCl solution. The results from the study showed that the 20 nm thick layers did not provide a good corrosion protection for the carbon steel ($0.013 \text{ M} \Omega \cdot \text{cm}^2$), but coating thicknesses >100nm proved to efficiently protect the steel surface ($1.00\text{-}1.30 \text{ M} \Omega \cdot \text{cm}^2$), with the coating at 200 nm providing a 96% protection.

Fracassi et al [183] have deposited SiO_x coatings onto magnesium alloys, using PECVD. A 1.3 μm coating was deposited onto magnesium alloy substrates and EIS experiments were performed using a 0.1 M NaCl solution. The results showed that the addition of a SiO_x coating increased the corrosion protection, with the highest impedance modulus reported to be 8000 times higher than for the bare metal. A decrease in the corrosion protection of the coating was reported over time, which can be attributed to local corrosion mechanisms, starting at the sight of a defect. Pech et al [174] also reported an improved corrosion resistance of a 600 nm silica coating on 304 stainless steel, deposited using plasma assisted CVD (PACVD).

The addition of an inorganic silica coating has proven to provide an enhanced corrosion protection for stainless steel and metal substrates. The majority of the SiO_x coatings in the literature, studied by EIS have used traditional sol-gel methods. EIS data for PECVD and other plasma deposition methods has also been reported and proven to provide efficient corrosion protection. The use of MW-PECVD for depositing SiO_x coatings, on the corrosion protection of metals is limited and therefore opens the research gap. The corrosion protection of SiO_x coatings on high-speed steel substrates, deposited using MW-PECVD will be investigated further in this thesis.

3.7 Summary of chapter and rationale

The literature review has assessed the different deposition techniques for depositing SiO_x coatings. Each technique has its advantages and limitations and can all be used for a variety of different applications. RF-PECVD is the most commonly used method for depositing SiO_x coatings onto a variety of substrates, as discussed in section 3.3.2.3.

The use of MW-PECVD for deposition SiO_x has also been utilised, resulting in higher density, uniform coatings when compared with RF-PECVD. The deposition of SiO_x coatings onto steel substrates has not yet been fully established. The current literature mainly studies MW-PECVD as a deposition technique for depositing SiO_x onto polymeric substrates due to its lower temperatures and higher deposition rates.

Depositing SiO_x onto HSS proves a challenge as it involves the deposition of a non-conducting coating, onto a conducting substrate. RF and MW-PECVD methods are capable of depositing SiO_x coatings without the need for an interlayer. The addition of an interlayer may further affect the properties of a

coating, so the removal of this allows for more controllability of the deposited coating. MW-PECVD is a promising technique for depositing highly uniform, dense SiO_x coatings onto HSS substrates, and is favourable to RF methods due to the higher deposition rates.

The oxygen concentration during the deposition stage has a powerful effect on the properties of the coatings. Fine tuning the oxygen concentration by varying the HMDSO: O_2 ratios allows coatings to be deposited with different chemistries, microstructures and mechanical properties. The O_2 concentration affects the x values in the SiO_x and determining the appropriate x values may vary depending on the particular application of the coatings.

SiO_x -like coatings have proven to enhance the corrosion performance of a variety of metallic substrates. SiO_2 deposited onto stainless steels provide the best corrosion performance, which is closely followed by SiO_xC_y coatings onto carbon steel substrates. The deposition of inorganic SiO_x coating onto carbon steel substrates for corrosion protection provides a gap in the research and therefore a rationale for this thesis. This research will investigate the MW-PECVD process of depositing SiO_x coatings onto conductive substrates (such as HSS), using a HMDSO monomer in combination with O_2 . The chemistries of the SiO_x coatings will be explored, by varying the O_2 concentrations and differing thicknesses. HMDSO is the most commonly used monomer for depositing SiO_x coatings, due to its very high deposition rate, when using a microwave-excited plasma source.

Chapter 4 – Experimental procedures and analysis techniques

4.1 Introduction

This chapter details the experimental procedures used throughout this work. The microwave PECVD (MW-PECVD) technique used to deposit the SiO_x coatings is described in further detail, followed by the characterisation of the coatings. The analysis is split into three sections; the first relating to the mechanical properties of the coatings, the second relating to the chemical and structural composition, and the third relating to the electrochemical properties.

The main focus of this study will centre on the MW-PECVD technique, to deposit SiO_x coatings onto high-speed steel (HSS) substrates. This deposition method was chosen due to the enhanced capabilities of MW-PECVD in comparison to other deposition techniques. SiO_x is an insulating material being deposited onto a conducting substrate, which has proven to be difficult to deposit using certain deposition methods. This, however is overcome when using a microwave source.

4.2 Methods of Coating Deposition

All coating depositions were performed in the Advanced Materials laboratory, University of Leeds, using a bespoke Hauzer Flexicoat 850 coating system (Figure 4.1). The system is capable for the deposition of coatings with magnetron sputtering, high power impulse magnetron sputtering (HiPIMS), plasma nitriding, CARC+, microwave and more recently, a nanoparticle source . The machine also combines advanced plasma diagnostics due to the addition of Langmuir and optical probes. Figure 4.2 shows the system set up in the Advanced Materials Laboratory, and Figure 4.3 shows a schematic for the inside of the chamber. The internal dimensions of the chamber measure 800 x 800 x 900 mm (w x d x h) and the effective coating volume for the Flexicoat 850 system is Ø 500 x 500 mm.



Figure 4.1 The Hauzer Flexicoat 850 PVD machine.

The chamber is equipped with three circular arc evaporation targets, two 600 x 50 mm sputtering targets, and two 1200 W microwave antenna, stored inside parabolic reflectors. The back of the chamber is equipped with the microwave source and has the capability of being used as a door in order to clean the microwave sources. This is an important aspect, based on the deposition quality, as the microwave antennas may form a coated layer over time and may impede the quality of the coatings and become less effective during deposition.

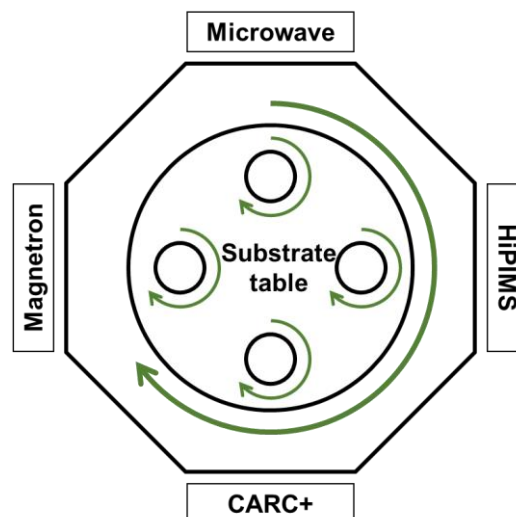
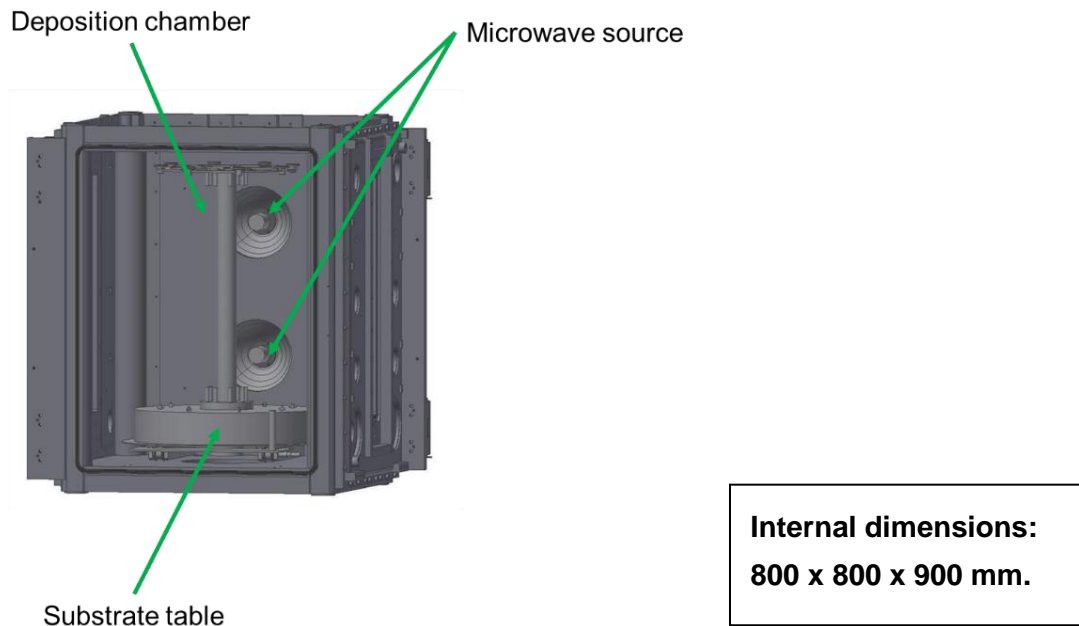
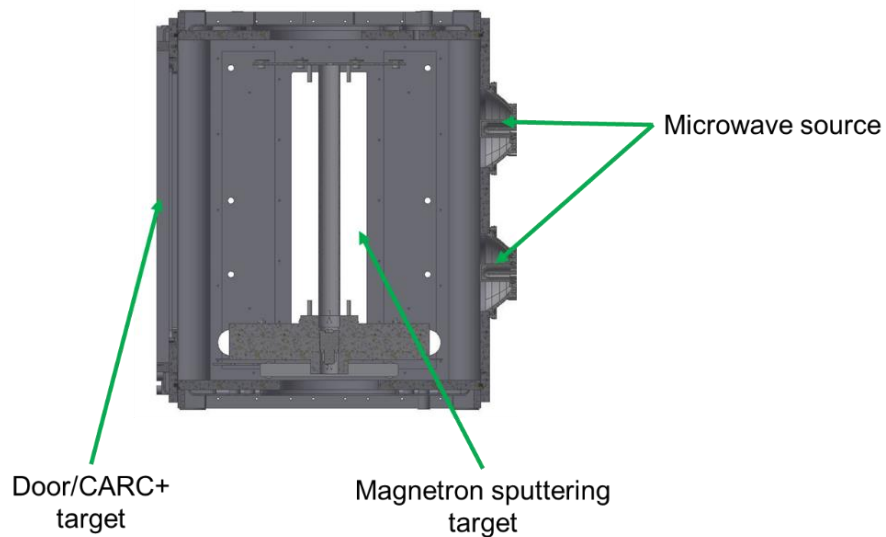


Figure 4.2 Schematic of the coating chamber in the Hauzer Flexicoat 850 PVD system, the microwave source will be the main focus for this study.



a) Front view of PVD chamber



b) Side view of the PVD chamber

Figure 4.3. Hauser Flexicoat 850 schematic of the deposition chamber, a) front view of PVD chamber and b) side view of PVD chamber, with internal dimensions of 800 x 800 x 900 mm.

4.2.1 Substrate and sample preparation

HSS is a type of carbon steel and has distinctive physical and mechanical properties, making it a suitable choice for many coating applications. There are a variety of different grades of HSS which can be divided into four categories;

molybdenum-cobalt, molybdenum-vanadium, tungsten and molybdenum. These alloy components within the steel, allow for different properties:

- Molybdenum – improves toughness.
- Tungsten – increases wear resistance and tempering.
- Cobalt – improves heat resistance and increases hardening temperatures.
- Vanadium – increase wear resistance.

There are a variety of grades of HSS, in which applications vary. The basic grades are summarised in Table 4.1.

Table 4.1. General grades of high-speed steel [184].

General description	ISO steel description	Material number (steel code)	Application
HSS	S 6-5-2 (DMo5/M2)	1.3343	Standard tool material for most common applications
HSS-Co	S 6-5-2-5 (Emo5Co/M35)	1.3243	High heat resistance, suited for roughening
HSS-E	S 6-5-3 (Ems5V3/M3)	1.3344	High friction resistance and cutting edge stability
HSS-E M 42	S 2-10-1-8 (M42)	1.3247	Increased resistance and hardness
P/M HSS-E	S 6-5-3-9	1.3207	High hardness, heat resistance and cutting edge stability

1.3343 HSS was chosen as the substrate for depositing the large matrix of silicon oxide coatings, due to the grade being the standard material for a variety of common applications. The HSS discs had a diameter of 25 mm, the mechanical characteristics and chemical composition can be found in Table 4.2 and Table 4.3, respectively.

Table 4.2. The mechanical characteristics of HSS 1.3343, DIN HS S-6-5-2.

Characteristics	1.3343 HSS
Density	8.16 g cm ⁻³
Melting point	1430°C
Elastic Modulus	190-210 GPa
Tensile strength	1200 MPa
Compressive Strength	3250 MPa
Thermal conductivity	41.5 W m ⁻¹ K ⁻¹
Hardness (as hardened)	832 HV or 8.2 GPa
Hardness (tempered at 620°C)	746 HV or 7.3 GPa

Table 4.3. The chemical composition of the high-speed steel (HSS) substrates used for the SiO_x coatings, from reference [185].

Chemical	Composition (at %)
Carbon (C)	0.86-0.94
Silicon (Si)	0.20-0.45
Manganese (Mn)	0.15-0.40
Chromium (Cr)	3.75-4.50
Molybdenum (Mo)	4.50-5.50
Vanadium (V)	1.75-2.20
Tungsten (W)	5.50-6.75
Iron (Fe)	83.29-79.26

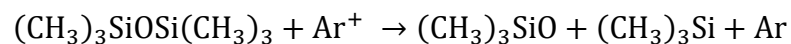
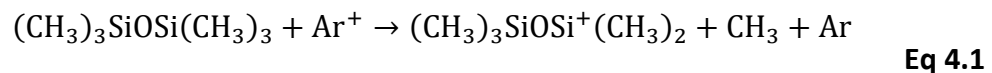
Firstly, HSS coupons, with a 25 mm diameter, were polished to a mirror finish ($R_a = 0.01 \mu\text{m}$) and cleaned with ethanol wipes. Once polished to the desired finish and roughness, the samples were fixed onto a rotational substrate table with a two folds rotation in the Hauzer Flexicoat 850 coatings platform based at the University of Leeds. The samples were then cleaned under vacuum to outgas. Following this, the samples were bombarded with argon ions (Ar^+) in order to atomically clean and etch the surface of any organic matter prior to the deposition

of the coatings – commonly known as plasma surface etching (PSE). The surface was etched for 90 minutes at 150°C, using a bias of -200 V.

4.2.2 Precursors

The precursors used for depositing the SiO_x coatings were hexamethyldisiloxane (HMDSO) ((CH₃)₃SiOSi(CH₃)₃) monomer, oxygen (O₂) and argon (Ar) gases. Ar is used as the excitation gas due to its inert behaviour and inability to react with other molecules or ions. A surplus of argon ions can lead to a higher deposition rate. HMDSO was the favourable monomer for the deposition of SiO_x coatings onto HSS substrates due to its very high deposition rates, when using a microwave-excited plasma source. HMDSO also benefits from being chemically inert, non-toxic, and having a high vapour pressure, as described in section 3.3.1.

HMDSO and O₂ are used in combination because when applied under vacuum and in the presence of plasma will deposit SiO_x onto a substrate. HMDSO is broken down by the plasma (Ar⁺ ions), and the ion-molecule reaction commences according to:



The HMDSO will continue to break down into smaller ions and radicals, without the addition of O₂ an organic-like SiO_x coatings will be deposited (e.g. PDMS, [(CH₃)₂SiO]_n). The addition of the O₂ gas will lead to recombination reactions, which in turn will lead to the deposition of an SiO_x coating onto the substrate.

4.2.3 MW-PECVD Coating Procedure

The main focus of this study was to characterise a matrix of SiO_x coatings using MW-PECVD. The PVD machine is equipped with two microwave components

(2.45GHz) that are equipped with stainless steel parabolic reflectors, in order to direct the plasma into the deposition chamber for irradiation of gases for plasma generation. The microwave antenna are protected with a quartz tube and borosilicate sleeve, which can be removed, the schematic is shown in Figure 4.4. It is important for these components to be easily accessible as the parabolic reflectors may become coated overtime, leading to the source becoming less effective and giving a poor coating quality.

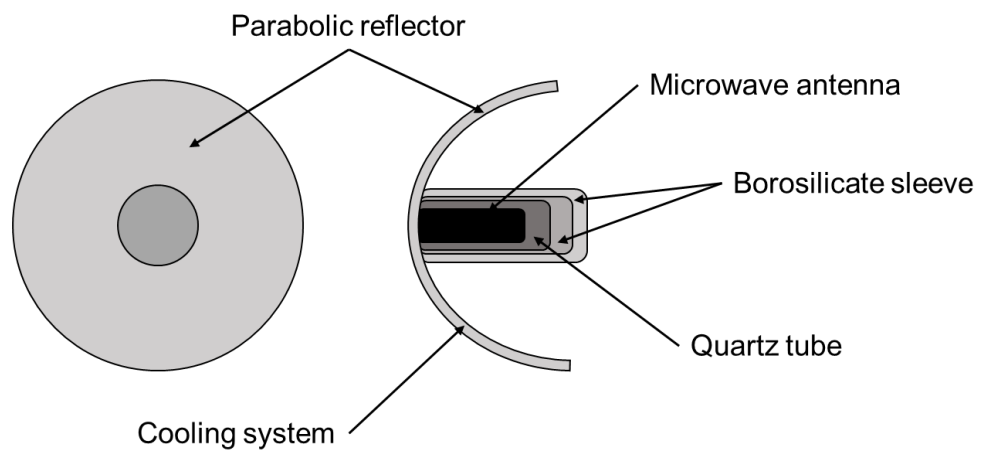


Figure 4.4 Schematic of the microwave antenna source.

A substrate table, is used to attach the substrates within the deposition chamber. The table houses cylindrical columns; allowing a two-fold rotation, whereby the cylinders are able to rotate independently to the table, or substrate holders, or a three-fold rotation, where the samples can be rotated separately to the table and the columns. The cleaned and polished HSS coupons were loaded onto the substrate table, with a two-fold rotation used throughout the deposition. This was then loaded into the PVD chamber, ready for deposition of the SiO_x coatings. The deposition steps are described in Table 4.4.

During the deposition, the substrate table can be biased, using a voltage from a DC power supply. The supply to the table can be pulsed, bi-polar or constant. A negative DC bias of -200 V was applied to the substrate, prior to deposition of the SiO_x coating. The application of a bias can increase the growth rate of the as-deposited coating, therefore increasing the deposition rate [186], [187]. The microwave was operated at a frequency of 2.54 GHz and a power of 1200 W for all coatings. The flow rates of the precursors were controlled throughout the deposition. Argon (Ar), hexamethyldisiloxane (HMDSO) and oxygen (O₂) were used as the precursor gases and the flow rates were varied throughout the depositions, dependent on the HMDSO:O₂ ratios that were being deposited. The design of experiments (DOE) parameters for all coatings and design thicknesses are detailed in section 4.3.

Table 4.4 Coating deposition step parameters.

Deposition step	Temperature (°C)	Pressure (10⁻⁵ mbar)	Bias (V)	Time (mins)
Chamber heating	200	7		35
Plasma Surface Etching (PSE)	150		-200	90
Heating	200			20
SiO_x coating			25	Described in section 4.3.

Following on from the deposition of the SiO_x coatings, the PVD chamber was cooled to room temperature and then vented to release the vacuum. The coated samples were removed from the substrate table and stored in a desiccator, to ensure the coatings were kept dry and away from moisture.

4.3 Deposition parameters

This section will discuss the deposition parameters for the two batches of coatings characterised in this research. Batch 1 and the first phase of coatings were deposited with varying HMDSO:O₂ ratios and a design of experiments (DOE) thickness of 2 µm. Batch 2 coatings were deposited with varying HMDSO:O₂ ratios and multiple DOE thicknesses (1 µm, 2 µm, 3.5 µm and 5 µm). The thicknesses are able to be controlled by controlling the Ar, O₂ and HMDSO flow rates, deposition power and pressures and the deposition times.

4.3.1 Batch 1 coatings – varying HMDSO:O₂ ratios.

The ratios of HMDSO and O₂ were varied in order to create surface coatings with different chemistries and topographies. All samples for Batch 1 were coated with a DOE thickness of 2 µm. The design thickness was determined experimentally by using differing deposition times, dependent on the HMDSO:O₂ ratio. The measured thickness of the samples varied slightly from the design values, ranging from 1.70 µm – 2.09 µm. Table 4.5 gives the required flow rates of Ar, HMDSO and O₂ and the deposition times for the corresponding HMDSO:O₂ ratios used.

Table 4.5. The argon, HMDSO and oxygen flow rates for the 1st batch of coated SiO_x samples, with varying HMDSO:O₂ ratios and a 2 µm design thickness.

HMDSO:O ₂ ratio	Ar flow rate (sccm)	HMDSO flow rate (sccm)	O ₂ flow rate (sccm)	Deposition Time
1:3	150	60	180	1 h 40
1:6	150	30	180	2 h 30
1:12	150	15	180	3 h 55 m
1:16	220	10	160	5 h 5 m
1:20	220	8	150	8 h
1:36	250	5	180	15 h 20 m

4.3.2 Batch 2 coatings – varying HMDSO:O₂ ratios and thicknesses.

Following on from the characterisation of batch 1 coated samples, a matrix of coatings were chosen to characterise their chemistries, microstructure and corrosion properties at varying HMDSO:O₂ ratios and thicknesses. Table 4.6 shows the argon, HMDSO and O₂ flow rates and the deposition times for each HMDSO:O₂ ratio and thickness.

Table 4.6. The argon, HMDSO and oxygen flow rates for the second batch of coated SiO_x samples, with varying HMDSO:O₂ ratios and different thicknesses.

DOE thickness (µm)	HMDSO:O ₂ ratio	Ar flow rate (sccm)	HMDSO flow rate (sccm)	O ₂ flow rate (sccm)	Deposition time
1	1:10	180	15	150	2 h 10 m
	1:12	150	15	180	2 h 22 m
	1:14	150	13	182	2 h 40 m
	1:16	220	10	160	3 h 15 m
	1:20	220	8	150	4 h 25 m
2	1:10	180	15	150	3 h 35 m
	1:12	150	15	180	3 h 55 m
	1:14	150	13	182	4 h 20 m
	1:16	220	10	160	5 h 5 m
	1:20	220	8	150	8 h
	1:24	200	8	180	7 h 20 m
	1:36	250	5	180	15 h 20 m
3.5	1:12	150	15	180	5 h 50 m
	1:14	150	13	182	6 h 50 m
	1:16	220	10	160	8 h 35 m
	1:20	220	8	150	12 h 55 m
5	1:12	150	15	180	7 h 45 m
	1:14	150	13	182	9 h 5 m
	1:16	220	10	160	12 h 3 m
	1:20	220	8	150	20 h

The second batch of coated samples focusses on the ratios that are close to stoichiometric SiO₂. This batch of coatings also focusses on a range of DOE thicknesses at 1 µm, 2 µm, 3.5 µm and 5 µm. The thicknesses of the samples were determined experimentally based on the deposition times, a higher deposition time resulted in a thicker coating.

4.4 Characterisation of the SiO_x coatings

There are a number of techniques available to characterise the surface of a particular coating. These techniques can range from analysing the surface topography to analysing the surface chemistry, the thicknesses and electrochemical properties of a particular coating. Techniques such as Calo® test, scratch test and nano-indenter are used to characterise the mechanical properties of a coating. The analysis techniques used to determine the surface topography and chemical composition of the coating include; scanning electron microscopy (SEM) with energy dispersive x-rays (EDX), transmission electron microscopy (TEM), Fourier transform infrared spectroscopy (FTIR) and x-ray diffraction (XRD). This section will detail the mechanical and chemical characterisation of the coatings.

4.5 Mechanical characterisation

4.5.1 Calo Test

The thicknesses of the silicon oxide coatings were determined using a Calo tester from TRIBOtechnic. The Calotest is used in accordance with Standard: ISO EN-1071-2 and VDI 3198. The Calo tester involves a holder and clamp for the surface of interest, in which a hardened steel sphere of a known diameter (d) is rotated against the surface. A diamond paste was applied to the surface and as the

sphere rotates a crater is formed through the coating down to the substrate. The speed of rotation and the length of time needed to abrade the surface are dependent on the surface coatings.

For the series of SiO_x coatings, a number of 3 measurements at different positions across the surface were taken for each sample and the average thickness was calculated. A speed of 200 rpm was used and time was varied from 2-10 minutes, depending on the design thickness of the coatings. Once the experiment had been performed, all samples were analysed using optical microscopy and the thickness was determined using the following Eq 4.2:

$$t = \frac{xy}{d} \quad \text{Eq 4.2}$$

Where t is the coating thickness, x and y are measured using the optical microscope and d is the sphere diameter. A schematic for the Calo test thickness measurement is shown in Figure 4.5.

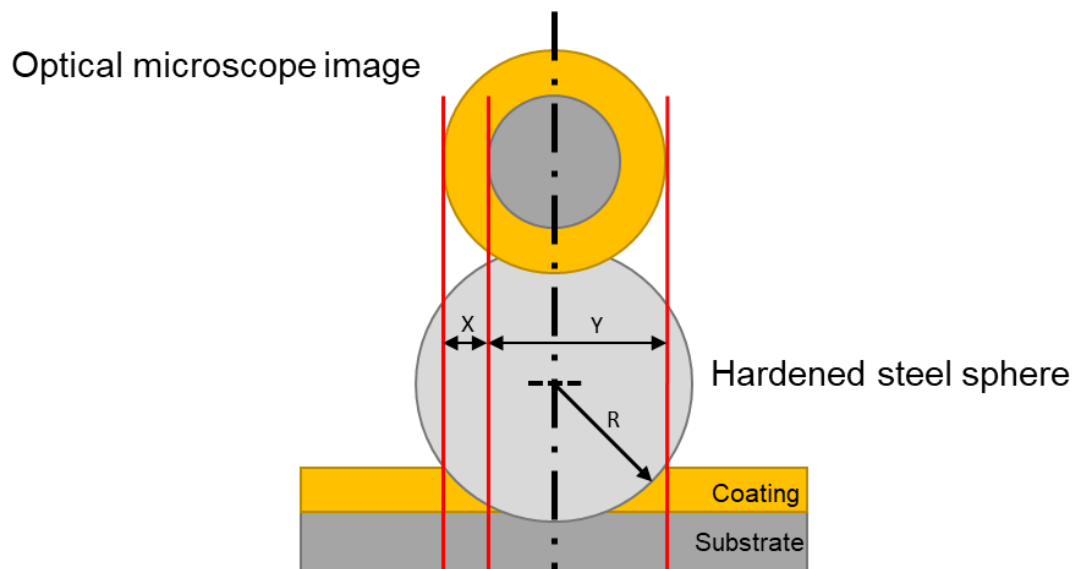


Figure 4.5. A schematic of the Calo test measurement and how the thickness is calculated. t =coating thickness, x and y =measurements determined using optical microscopy, d =diameter of the sphere.

4.5.2 Scratch Test

Scratch testing is a method used to determine the adhesion and scratch resistance for coatings and bulk materials. The method consists of scratching the surface of a sample with a diamond tip, in which a constant or progressive load can be applied. Using a Tribotechnic Milli Scratch Tester, in accordance with standard JIS 3255 and ISO 205 02, a video system allows the damage on the coating caused by the diamond tip to be examined, enabling a correlation with the applied load. This standard method allows for comparisons of different coatings, substrates, thicknesses of coatings and the scratch resistance of bulk materials.

The scratch testing method is a quantitative method in which critical loads (where failures begin to appear) are utilised in order to evaluate the adhesive or cohesive properties of a coating. When using a progressive load test, the critical load is determined to be the smallest load at which a failure may occur. There are multiple failure mechanisms which can occur throughout the duration of the scratch.

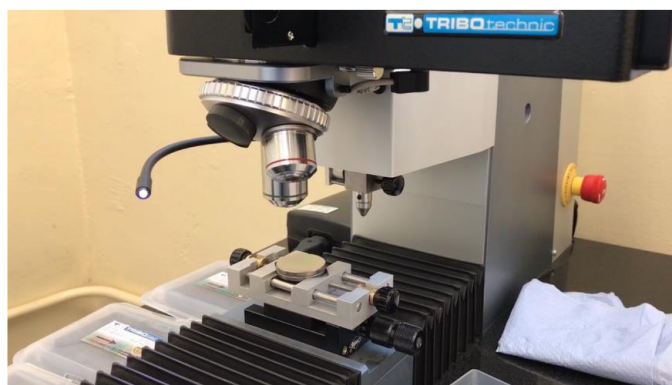


Figure 4.6. The Tribotechnic Scratch Tester Millennium 200 to characterise the adherence of the SiO_x coating onto the HSS substrate.

A diamond indenter Rockwell C tip with 200 μm radius was used for the scratch tests for each SiO_x coated sample. A series of 3 scratches were performed for each sample and the average critical load was calculated. The scratches were performed parallel to one another and spaced equally apart after each scratch was complete. The stylus was cleaned after each scratch with ethanol to ensure that any foreign materials from the coatings were removed. The table below gives the details for the scratch test conditions.

Table 4.7. The scratch test conditions for all SiO_x coated samples.



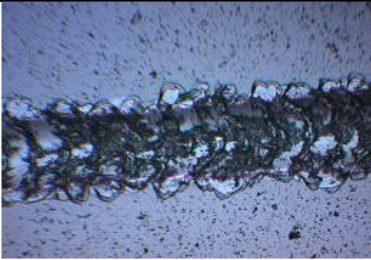
Progressive or Constant load?	Progressive
Initial load	0.9 N
Final load	50.0 N
Loading speed	100.0 N min^{-1}
Sample speed	10.0 mm min^{-1}
Scratch length	5.0 mm
Acoustic emission sensitivity	5.0 AE
Tip material	Diamond
Tip type	Rockwell C
Tip radius	200.0 μm
Coating	SiO_x
Substrate	HSS

Once the scratches had been formed on the surface, the optical microscope was used to examine the critical loads. Three critical loads (LC_1 , LC_2 and LC_3) were present for each sample. The critical loads can be categorised based on the type of failure event, in order for direct comparison of each sample. The failure events for the SiO_x coated samples are classified in Table 4.8 [188].

The LC_1 load is the point where cohesive failure occurs and is the minimum load at which cracking begins to occur within the coating. The LC_2 value is the load

where adhesive failures begin to occur, i.e. at the point where the crack reaches the coating substrate interface, causing coating delamination. This value shall then be used to determine the critical load of the coatings. The LC₃ value shall be taken at the first point at which the substrate can be seen and the coating begins to delaminate.

Table 4.8 Classifications of the scratch test results [188].

	Description of failure event	Optical microscope image
LC₁	Forward chevron cracks at the borders of the scratch track. LC ₁ is taken at the closest end of the event to the scratch start track.	
LC₂	Forward chevron cracks at the borders of the scratch, with the addition of interfacial spallation. LC ₂ is taken at the failure event that occurs first.	
LC₃	Gross interfacial spallation and delamination. LC ₃ shall be taken at the first point where the substrate can be seen.	

4.5.3 Nanoindentation

The most widely used technique to measure the mechanical properties of thin film coatings is nanoindentation, which is used to determine the elastic modulus, hardness and fracture toughness of various materials. The most common use for nanoindentation is for measuring hardness and elastic modulus, however it can also be used to measure other mechanical parameters, such as residual stress and creep. For nanoindentation, a specific load is applied to a sample through an indenter with a known geometry. A hard indenter tip (typically diamond) is compressed into the material, resulting in plastic and elastic deformation of the material. When the maximum load has been applied to the tip, it can be held at the maximum force in order to measure any creep within the material. The tip is then unloaded from the material, allowing some elastic recovery. For each indentation, a load displacement curve, shown in Figure 4.7, is generated and the mechanical properties can be calculated. The hardness can be determined using Eq 4.3 [189]:

$$H = \frac{P_{\max}}{A_c} \quad \text{Eq 4.3}$$

Where P_{\max} is the maximum load applied during indentation and A_c is the measured contact area.

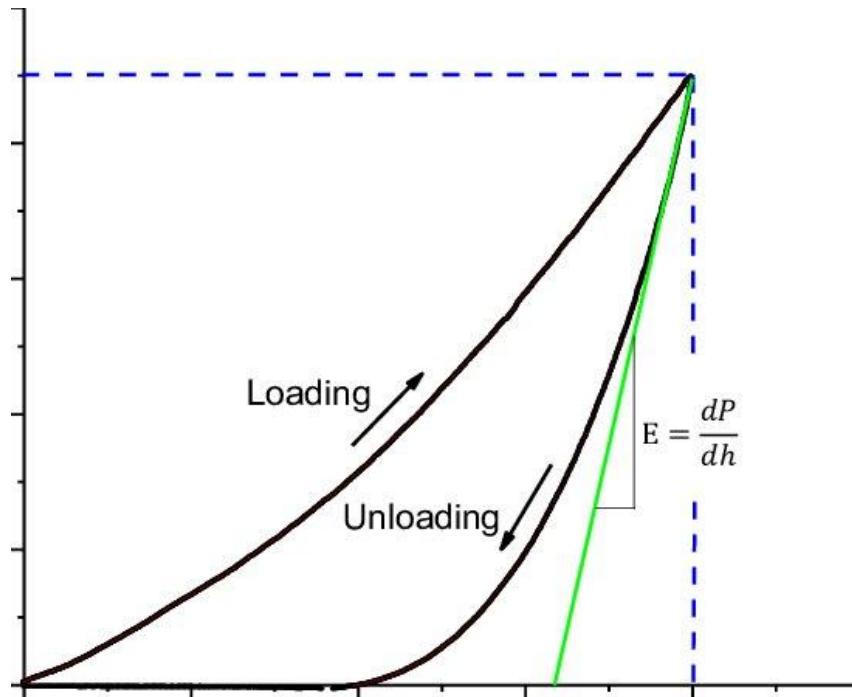


Figure 4.7. A typical load displacement curve for the nanoindentation process (E represents Young's modulus) [190].

It is recommended that the indentation depth is less than 10% of the coating thickness [191], to help avoid effects from substrate during the nanoindentation process [192]. This is feasible for coatings that are greater than 1 μm thick, those that are thinner present more of a challenge.

Nanoindentation tests were performed on SiO_x coated HSS, with a designed coating thickness of 2 μm , using a Micromaterials Nanotest platform and a Berkovich diamond indenter tip. The indentation was load controlled from a load of 0.1mN to a maximum load of 20 mN, with 10 indentations being applied to each sample. The offset of each indent was 50 μm , with a total surface area of 500 μm^2 covered. The loading and unloading rates applied were constant throughout the experiments at 0.1 mN s⁻¹. As the indentations were load controlled, the indentation depth was greater than 10%. The calculations for the hardness and elastic modulus used only the data for the indentations up to 10% on the coating depth. The reduced modulus was determined using the Oliver and

Pharr power law fitting method from the unloading curve [192]. The Young's modulus of the coating being measured was then calculated using:

$$\frac{1}{E_r} = \frac{(1 - \nu^2)}{E} + \frac{(1 - \nu_i^2)}{E_i} \quad \text{Eq 4.4}$$

Where E_r is the reduced modulus, ν_i and E_i are the Poisson's ratio and modulus of the indenter tip, respectively, and ν and E are the Poisson's ratio and modulus of the sample. The diamond Berkovich indenter tip has $E_i = 1140$ GPa and $\nu_i = 0.07$ for diamond.

For materials that are assumed to have a Young's modulus lower than that of diamond (orders of magnitude smaller), the indenter can be thought to be rigid. This allows the removal of the indenter terms from Eq 4.4, and allows the equation to be simplified to:

$$\frac{1}{E_r} = \frac{(1 - \nu^2)}{E} \quad \text{Eq 4.5}$$

The Poisson's ratio ν is estimated to be 0.17 for the SiO_x coating, taken from the Poisson's ratio of silicon dioxide (SiO_2). All calculations in the thesis use this assumed value throughout.

4.6 Chemical characterisation

4.6.1 Scanning electron microscopy with electron dispersive x-ray (SEM/EDX) spectroscopy

4.6.1.1 Background

Scanning electron microscopy (SEM) with energy dispersive x-ray (EDX) spectroscopy is one of the most commonly used surface analysis techniques. Scanning electron microscopy (SEM) involves a finely focused electron beam scanning the surface of a sample, with electron bombardment resulting in a series

of sample-beam interactions [193]. A simple schematic for a scanning electron microscope is shown in Figure 4.8.

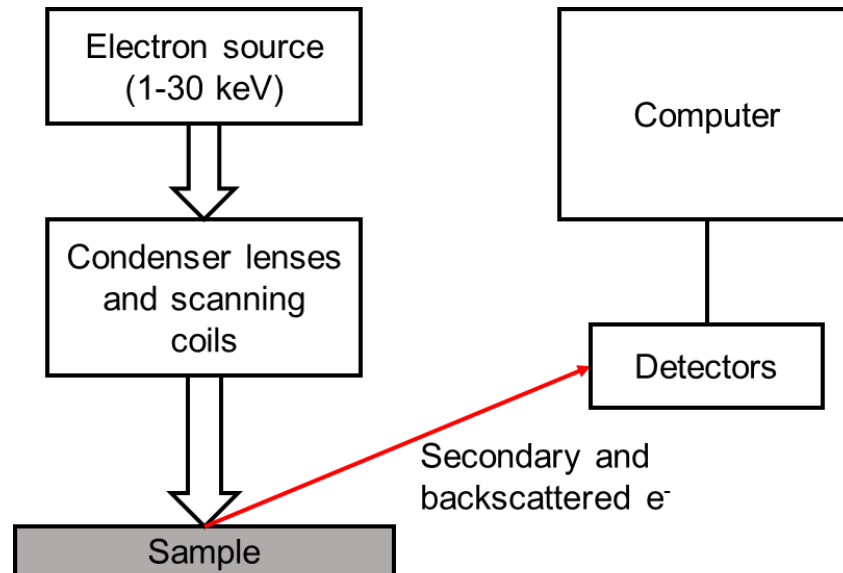


Figure 4.8 A simple schematic of the scanning electron microscope process adapted from reference [194].

EDX analysis is an analytical technique used to determine the chemical characterisation of a sample. EDX is usually coupled with SEM and can provide elemental analysis on samples areas in the nanometre (nm) range. The incident electron beam used in SEM analysis produces x-rays. The energy of the x-rays generated is characteristic of the elements that are found on the sample surface. The intensities of the measured x-rays give a quantitative analysis of the elemental composition and distribution throughout the sample.

4.6.1.2 Batch 1 and batch 2 analysis

SEM with EDX spectroscopy was used to characterise a plan-view of the surfaces of the SiO_x coatings. SEM imaging gives high resolution images by scanning the surface of a material with an incident beam of electrons. The electrons interact

with the atoms on the surface and produce low energy secondary electrons. The intensity of the secondary electrons can be measured, and their signals create an image of the surface composition and topography.

All SiO_x coated samples were analysed on a Carl Zeiss EVO MA15: variable pressure SEM with Oxford Instruments AZtecEnergy EDX system with 80 mm² X-Max Silicon Drift Detector (SDD) - secondary and backscattered imaging, EDX elemental mapping and line scans. The SDD hardware allows x-rays to be detected and measured, enabling them to be converted into signals used by the EDX software to provide accurate and reliable analysis. The sensitivity of the SDD allows accurate identification and characterisation of x-ray lines down to 72 eV and quantitative analysis at >400,000 cps.

Due to charging effects on the sample surface producing unwanted noise on the imaging signal, samples must be conductive to produce the best results. As the substrate and coatings are non-conductive, the SiO_x coatings must first be prepared to counteract these charging effects. The samples were mounted onto metallic holders using adhesive carbon pads, and a carbon paint which was applied to the coating edge to create a conductive pathway to the metallic holder. A carbon coating (~5 nm) was then applied to the surface of the SiO_x coated sample, using an evaporator. A series of five measurements were taken for each sample, spread evenly over the entire surface of each sample, as shown in Figure 4.9. An average of the five measurements was taken and plotted against HMDSO:O₂ ratio with error bars (standard deviation).

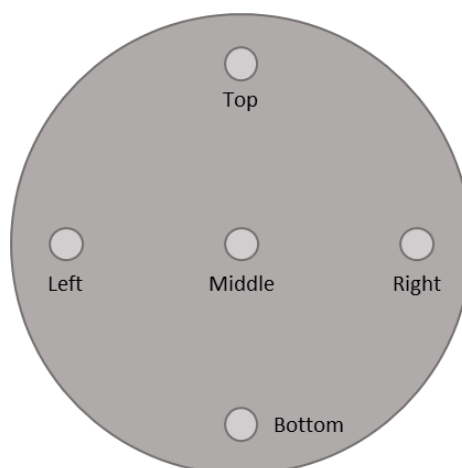


Figure 4.9. A schematic showing the plan-view positions of the five measurements taken for each sample.

The atomic concentrations for carbon, silicon and oxygen were analysed and the relative ratios were calculated in order to determine the silicon to oxygen ratios of all SiO_x coatings. Error bars were also calculated using the standard deviation of the five measured positions of each sample.

4.6.1.3 FIB cross sectional analysis of SiO_x coatings with SEM and EDX analysis

Focused ion beam with SEM and EDX analysis characterises the near surface elemental composition at an depth, produced by a Gallium (Ga^+) ion beam milling [6]. Samples were analysed on the Thermo Scientific™ Helios™ G4 CX DualBeam™. Cross sections were performed by removing a small area of the coating through to the substrate, using Ga^+ ion beam milling. FIB may be operated at low beam, for imaging the sample, or at high beam, for sputtering or milling the sample. FIB cross sectional analysis using SEM imaging and EDX was undertaken for each sample. EDX mapping and line scans were taken for each sample to investigate the composition of the coatings from substrate surface, through to the surface of the coating.

4.6.1.4 Transmission electron microscopy (TEM) of SiO_x coatings

FIB was used to prepare the SiO_x coated samples for TEM analysis. TEM was then used to obtain higher magnification and resolution images of the coatings, and for EDX mapping and line scan analysis. Thin sections were prepared from one SiO_x coated sample with HMDSO:O₂ ratio 1:24, using an FEI Helios G4 CX DualBeam. The site of interest was coated with a 200 nm platinum layer, deposited using a gallium ion beam. The surrounding material was further removed with the Ga⁺ beam, and was further thinned to desired dimension for TEM imaging. The TEM imaging was carried out using an FEI Titan Themis Cubed 300 TEM with high resolution images collected at magnifications of 593.0 kx, 419.3 kx and 37.0 kx. The instrument was fitted with a high angular annular dark field (HAADF) scanning TEM (STEM) detector and EDX system, allowing elemental mapping and line scan data to be obtained from the TEM sample.

4.6.2 Fourier Transform Infrared (FT-IR) spectroscopy

FT-IR analysis was performed to characterise the bonding present within the SiO_x coated samples. FT-IR measures the vibrations in bonds present in a sample. All samples were analysed using the attenuated total reflectance (ATR) technique with an FT-IR spectrometer. Measurements were taken for each sample and the main characteristic peaks were determined from the literature.

A Perkin Elmer Spectrum 100 was used to obtain the FTIR spectra. The spectra were acquired for each HMDSO:O₂ ratios and thicknesses, using attenuated total reflectance (ATR) from 4000 cm⁻¹ to 400 cm⁻¹. A total of 30 scans were taken for each sample. The Si-O bonding of the coatings will be studied based on the HMDSO:O₂ ratios. Typical bonding vibrations for SiO_x coatings are highlighted in Table 4.9

Table 4.9. The main FT-IR characteristic bonding vibrations for SiO_x coatings.

Main characteristic peaks	Wavenumber (cm⁻¹)
Si-O-Si bending [195]–[197]	~ 800 cm ⁻¹
Si₂O₃ [198], [199]	~880 cm ⁻¹
Si-O-Si asymmetric stretching (broad peak) [195]–[197]	~ 1000 cm ⁻¹
Si-O-Si asymmetric stretching (broad peak) [195]–[197]	~1150 cm ⁻¹

IR radiation measures the vibrational or rotational energy of atoms in a sample and can be used to determine functional groups within a molecule [200]. There are 2 different types of vibrations present within molecules, 1) stretching and 2) bending. Each functional group present in a molecule will have a different vibrational frequency, thus allowing for it to be specifically documented in the spectra. The infrared spectrum produces a graph showing the percentage transmittance with its corresponding frequency (wavenumber, cm⁻¹). A typical infrared spectrum will span from 4000-500 cm⁻¹. The region from 1500-500 cm⁻¹ is referred to as the fingerprint region, which usually contains a complicated series of adsorptions. These particular adsorptions are mainly due to bending vibrations and it is difficult to pick out bonds within this region due to the high uncertainty.

4.6.3 XPS analysis

X-ray photoelectron spectroscopy (XPS), or sometimes referred to as electron spectroscopy for chemical analysis (ESCA), is a quantitative technique for analysing the atomic composition and surface chemistry of a material. XPS data

can be obtained by irradiating a sample with x-rays and measuring the kinetic or binding energy of electrons that are emitted from the material. A simplified schematic for the XPS process is shown in Figure 4.10.

XPS analysis of the samples was performed at HarwellXPS, the EPSRC National Facility for X-Ray Photoelectron Spectroscopy. The instrument model used was a Thermo NEXSA. The x-ray source was Monochromatic Al K α with an energy of 1486.69 eV and source strength of 19.2 W. The charge control was a Thermo Scientific FG-03 dual-beam low energy electron/ion source with an ion gun current = 150 μ A and an ion gun voltage = 45 V. All samples analysed were under a pressure of < 10⁻⁸ mbar, a temperature of 300 K and used an analysis spot size of 200x100 μ m. All samples were affixed to the instrument using carbon tape. A survey spectrum pass energy of 150 eV and a region spectra pass energy of 40 eV was applied to each sample.

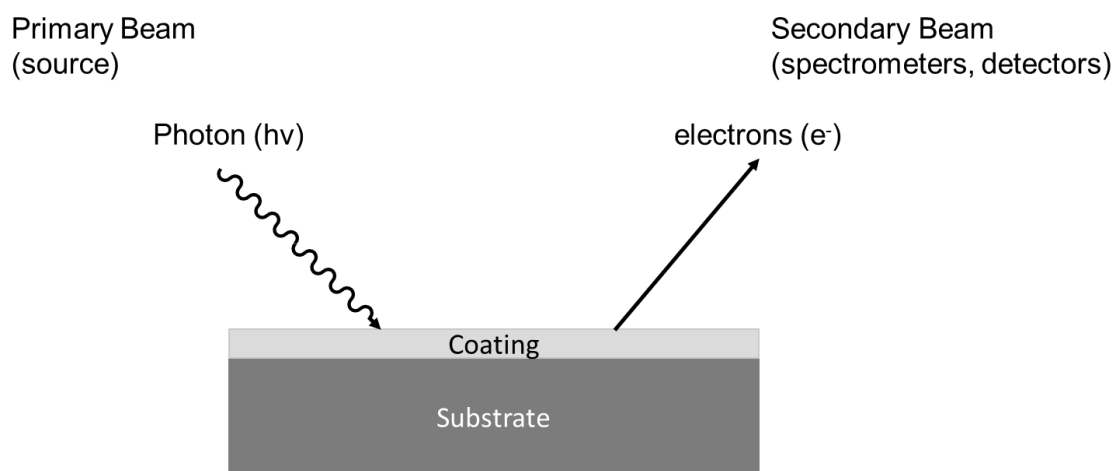


Figure 4.10. A simple schematic of the XPS analysis process, for a coated material. The primary beam emits a photon onto the surface of the sample, the secondary beam detects the electron that is lost.

Samples were first analysed without any surface preparation, however due to the large concentration of adventitious carbon, it was beneficial to clean and prepare

the surfaces. The samples were cleaned using an ion gun cluster source, with a cluster size of 75 Ar⁺, an energy of 3 keV for 300 seconds. The mono Ar ion source allowed layers of the surface to be etched to reveal the subsurface information of the SiO_x coatings. The surface preparation method allowed any adventitious carbon, dust or other particles to be eradicated from the sample. The samples 1:12, 1:14, 1:16, 1:20 and 1:36 analysed using XPS, with a DOE thickness of 2 μm. A survey spectra measuring from 1400 to 0 eV was recorded for each sample. The survey spectra allowed for further high resolution spectra to also be recorded. High resolution spectrums were acquired for Si 2p (110-95 eV), O 1s (545-526 eV) and C 1s (298-279 eV).

4.6.4 X-ray diffraction (XRD)

XRD is a commonly used non-destructive technique for structural characterisation of three-dimensional structures at the atomic level. X-rays are produced by accelerating an electron beam from a heated tungsten filament [201] towards a metal target (commonly Cu, Mo or Co) as shown in Figure 4.11.

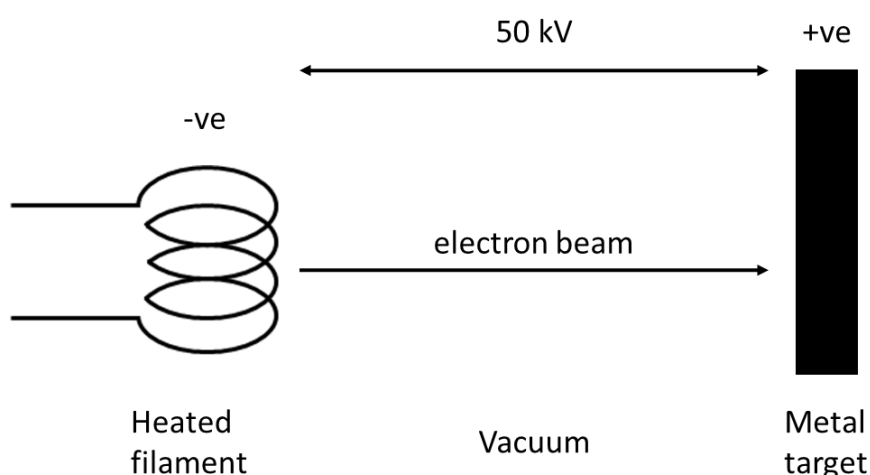


Figure 4.11 A schematic to show the production of x-rays using a heated filament, electron beam and a metal target (usually Cu, Mo or Co).

X-ray values are characteristic of the metal target that has been used to generate them. For example, for a copper target (Cu-K α), the wavelength is 1.54 Å and for a molybdenum target (Mo-K α) the wavelength is 0.707 Å. The target used in this thesis was a Cu-K α target with a wavelength of 1.54 Å.

X-rays are scattered by electron density and in crystals the x-rays are diffracted from the crystals. The diffraction pattern generated from the x-rays gives information about the arrangement of the electron density within the crystal. X-ray diffraction can be considered to be the reflection of x-rays from a family of parallel planes, Figure 4.12 shows a schematic of the diffraction of x-rays from a crystalline material.

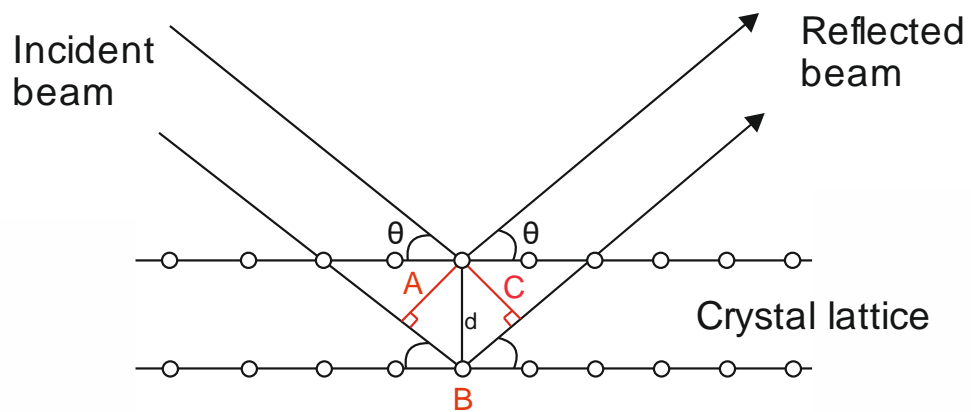


Figure 4.12 A schematic representation to show the process of the XRD technique.

From the above schematic, Bragg's law can be defined:

$$AB + BC = n\lambda \tag{Eq 4.6}$$

$$AB = BC = d\sin\theta \tag{Eq 4.7}$$

$$\text{Hence } n\lambda = 2d\sin\theta \tag{Eq 4.8}$$

$$\text{Bragg's law: } n\lambda = 2d\sin\theta \tag{Eq 4.9}$$

XRD is used to measure the average spacing between rows or layers of atoms. From the measured sample the orientation of a crystal or grain can be determined, the crystal lattice structure of an unknown material can be defined and the size, shape and internal stresses of a crystal system can be measured. There are seven different crystal systems as shown in Table 4.10.

From the measured sample the Miller indices can be determined, which specifies the directions and planes within a lattice or crystal. The Miller indices are denoted using three integers h, k and l (hkl values – Miller indices). h, k and l are the Miller index for the x-, y- and z-axis respectively. The distance between a family of planes with the same hkl values is d_{hkl} , or the d-spacing.

Table 4.10. A table to show the seven different crystal systems and their cell parameters.

Crystal System	Cell Parameters
Cubic	$a = b = c ; \alpha = \beta = \gamma = 90^\circ$
Tetragonal	$a = b \neq c ; \alpha = \beta = \gamma = 90^\circ$
Trigonal	$a = b = c ; \alpha = \beta = \gamma \neq 90^\circ$
Hexagonal	$a = b \neq c ; \alpha = \beta = 90^\circ, \gamma = 120^\circ$
Triclinic	$a \neq b \neq c ; \alpha \neq \beta \neq \gamma \neq 90^\circ$
Monoclinic	$a \neq b \neq c ; \alpha = \gamma = 90^\circ, \beta \neq 90^\circ$
Orthorhombic	$a \neq b \neq c ; \alpha = \beta = \gamma = 90^\circ$

Using the unit cell parameters from Table 4.10, the d-spacing and Miller indices for cubic SiO_2 can be characterised from the following:

- Cubic, tetragonal and orthorhombic cells give;

$$\frac{1}{d_{hkl}^2} = \frac{h^2}{a^2} + \frac{k^2}{b^2} + \frac{l^2}{c^2} \quad \text{Eq 4.10}$$

- Cubic, where $a = b = c$;

$$\frac{1}{d_{hkl}^2} = \frac{\Sigma}{a^2} \quad \text{Eq 4.11}$$

Where $d_{hkl}^2 = h^2 + k^2 + l^2$

The lattice constant (a) for the cubic phase of SiO_2 can be determined using the following expression:

$$a = d\sqrt{(h^2 + k^2 + l^2)} \quad \text{Eq 4.12}$$

Where the d -spacing is calculated using Bragg's law (Eq 4.9):

$$d = \frac{n\lambda}{2\sin\theta} \quad \text{Eq 4.13}$$

4.6.4.1 XRD analysis of batch 1 and batch 2 coatings

XRD was used to characterise all samples in order to determine the crystal lattice structure of the coatings. Firstly samples were cleaned with IPA to remove any contaminants from the surface, a polymeric sample holder was used to mount the SiO_x coated HSS samples onto the XRD Bruker D8 instrument. A glass slide was used to press the sample into position, to ensure it sat level with the sample holder. The process was repeated for all SiO_x coated samples with varying HMDSO: O_2 ratios and thicknesses. Once the sample was loaded into the Bruker D8, the conditions in Table 4.11 were applied to acquire the XRD diffractograms.

Table 4.11. A table to show the XRD conditions for all coated samples.

Measurement conditions	Parameters
Start position [2θ] (degrees)	5.000
End position [2θ] (degrees)	100.000
Step size (degrees)	0.033
Scan step time [s]	340.000
K-α1 [Å]	1.54
K-α2 [Å]	1.54443
K-β [Å]	1.39225

XRD diffractograms for each sample and thickness were collected and analysed to determine the 2θ values corresponding to the SiO_x coating, the full width at half maximum (FWHM) of the corresponding peaks, and the crystallographic planes. All XRD patterns for each coating with varying HMDSO: O_2 ratio showed an iron $\text{K}\alpha$ fluorescence peak, due to the iron containing HSS substrate. This behaviour is produced in iron samples when using $\text{Cu-K}\alpha$ radiation, due to $\text{Cu-K}\alpha$ having a higher energy than $\text{Fe-K}\alpha$ absorption. Therefore, the $\text{Cu-K}\alpha$ radiation will have sufficient energy for the Fe atoms to absorb and thus emitting as fluorescent radiation.

The XRD profiles were evaluated using X'PertHighscore Plus© software. Using the XRD data for each SiO_x coated sample, theoretical calculations can be used to calculate the crystallite size and the stress-strain of the coating. The Scherrer equation and Williamson-Hall (W-H) plots allow us to calculate these. The crystallite size can be determined from the Scherrer equation:

$$D = \frac{K\lambda}{\beta \cos\theta} \quad \text{Eq 4.14}$$

Where:

D = mean crystallite size, which may be smaller or equal to the grain size.

K = dimensionless shape factor, typically equal to 0.9.

λ = x-ray wavelength.

β = Full width at half maximum (FWHM), in radians.

θ = Bragg angle.

Using the crystallite size values, and the formula of Williamson and Smallman [202], the dislocation density, defined by the length of dislocation lines per unit volume of the crystal, can be determined.:

$$\delta = \frac{1}{D^2} \quad \text{Eq 4.15}$$

The crystallite size can also so be determined from Williamson-Hall plots, along with the strain of the coating, e.g. tensile or compressive. Using the uniform deformation method (UDM), a plot of $\beta \cos\theta$ vs $4\sin\theta$ can be used to determine the strain from the gradient of the slope and the crystallite size from the intercept.

The W-H equation can be written as:

$$\beta \cos\theta = \varepsilon(4\sin\theta) + \frac{K\lambda}{D} \quad \text{Eq 4.16}$$

Comparing this with the standard equation for a straight line, $y = mx + c$, the strain and size can be determined from the slope and intercept respectively.

Values for the crystallite size from the Scherrer equation and Williamson-Hall plots can then be compared.

4.7 Electrochemical techniques

Two different techniques were utilised to investigate the electrochemical responses of the SiO_x coatings on HSS for this study. These techniques included Tafel polarisation tests and electrochemical impedance spectroscopy. A three electrode electrochemical cell was employed, using a flat cell setup. The reference and counter electrode used was a silver/silver chloride (Ag/AgCl) InLab®, which uses an ARGENTHAL™ reference system with a silver ion tap bathing in 3 mol dm⁻³ potassium chloride (KCl) solution. The working electrode (WE) was coated HSS, and measurements were taken for samples with varying HMDSO:O₂ ratios and also differing thicknesses. The electrolyte solution used was 1 M NaCl at room temperature and pH 6.7, with the WE having an exposed area of 1 cm². This NaCl solution was chosen as a basic corrosive environment to understand the corrosion performance of the SiO_x coated HSS with varying HMDSO:O₂ ratios and varying thicknesses. As hydrogen fuel cells use a plethora of environments, the understanding of the SiO_x corrosion ability firstly needs to be understood, based on the HMDSO:O₂ ratios and thicknesses. Once this has been established further electrochemical testing can be developed for application specific environments, for example; alkaline fuel cells, phosphoric acid fuel cells and polymer electrolyte fuel cells. These environments involve the use of different electrolyte solutions and operating conditions e.g. temperatures and gas environments. Therefore, for the scope of this work, a 1 M NaCl electrolyte is used throughout.

The corrosion rate measurements were conducted using both direct current (DC) and alternating current (AC) methods with a Gill AC potentiostat.

Electrochemical impedance spectroscopy flat cell set-up

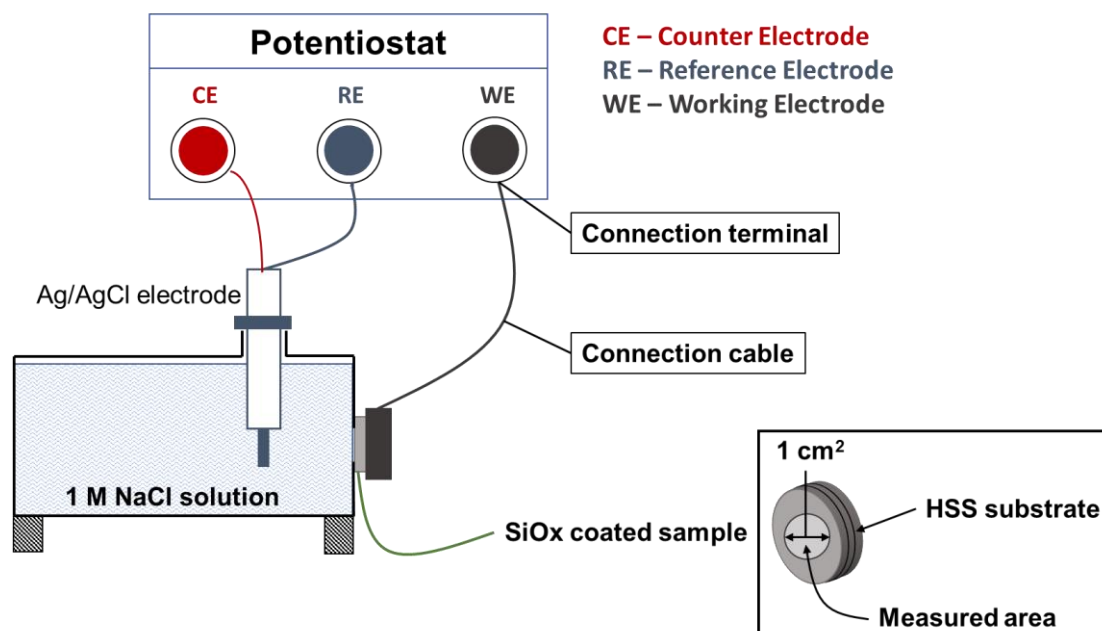


Figure 4.13. A schematic of the EIS set up for the SiO_x coated samples.

4.7.1 Polarisation curves for SiO_x coated HSS

Tafel polarisation curves were measured using a Gill AC potentiostat for all Batch 2 coated samples with varying HMDSO:O₂ ratios and a 2 μm DOE thickness. Firstly, an SiO_x coated sample was settled at an OCP of -500 mV, it was then polarised from -500 mV to -1200 mV for the cathodic curve vs the OCP. The cell was left to settle at the OCP for 10 minutes prior to starting the anodic sweep, which was measured between -500 mV and 200 mV for the anodic curve. Plotting both the cathodic and anodic curves on a plot of Potential (mV) versus log current density (mA cm⁻²) allows a theoretical value of the free corrosion potential (E_{corr}), corrosion current density (i_{corr}), cathodic Tafel slope (β_c) and anodic Tafel slope (β_a) to be determined. The cathodic and anodic curves are extrapolated using the

Tafel slopes extrapolation method. The Tafel extrapolation method uses a mathematical technique to estimate the E_{corr} and i_{corr} in an electrochemical cell. The extrapolation involves extending a known sequence of linear values within a Tafel plot usually between ± 50 -100 mV from the OCP. The intersection of the Tafel lines give the coordinates for the E_{corr} and i_{corr} values and the tangent slopes for the anodic and cathodic regions correspond to the anodic Tafel slope β_a and cathodic Tafel slope β_c , as shown in Figure 4.14.

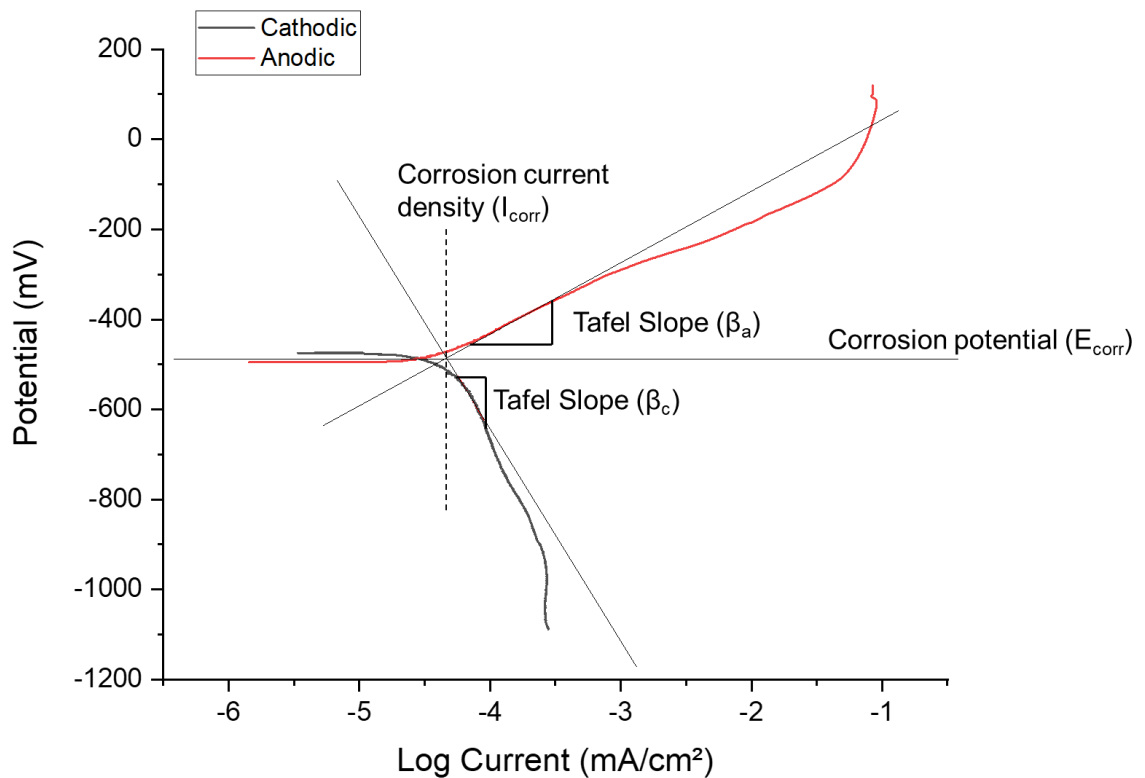


Figure 4.14. Tafel extrapolation example for the sample with HMDSO:O₂ ratio 1:12 and DOE thickness 2 μm .

Once both E_{corr} and i_{corr} have been determined, it is possible to determine the corrosion rate of the system. The cathodic Tafel slope (β_c) and the anodic Tafel slope (β_a) are defined from the slope of the linear extrapolations. The obtained

cathodic and anodic slopes are both extrapolated to find the E_{corr} , β_a , β_c , i_{corr} and the Stern-Geary coefficient of the SiO_x coated samples.

The results are calculated for E_{corr} vs. Ag/AgCl (mV), i_{corr} ($mA\ cm^{-2}$), Tafel constants - β_a ($mV\ dec^{-1}$) and β_c ($mV\ dec^{-1}$) and the Stern-Geary (S-G) coefficient (B) ($mV\ dec^{-1}$). The Stern-Geary equation can be used to obtain the polarisation resistance (R_p), using Eq 4.17:

$$R_p = \frac{B}{i_{corr}}$$

Where B is the Stern-Geary coefficient:

$$B = \frac{\beta_a \beta_c}{2.303(\beta_a + \beta_c)} \quad \text{Eq 4.17}$$

Once i_{corr} has been determined, the corrosion rate (CR) can be calculated in using one of the two following equations, **Error! Reference source not found.** or Eq 4.18. The equations can be used to calculate the corrosion rate in milli-inches per year and mm per year respectively. Corrosion is a fundamentally slow process with a typical corrosion rate being just 0.254 millimeters per year ($mm\ y^{-1}$) [203].

$$CR\ (mmpy) = \frac{3.27 \cdot I_{corr}\ (mA\ cm^{-2}) \cdot EW}{A \cdot \rho} \quad \text{Eq 4.18}$$

Where: CR = corrosion rate

i_{corr} = current density

EW = equivalent weight

A = corroded area

ρ = density of material






4.8 The Electrochemical Impedance Spectroscopy (EIS) of SiO_x coated high-speed steel

EIS is a highly sensitive characterisation technique used to establish the electrical response of a chemical system, through analysis of the interfacial properties related to electrochemical processes occurring at the electrode surface. Although Tafel constants are gathered prior to carrying out linear polarisation resistance (LPR), it was concluded to directly carry out EIS experiments instead. The reason for doing so was because the system is known to have a diffusion controlled mechanism due to the presence of the SiO_x coating, and therefore the system can be studied more accurately through the use of EIS experimentation.

The EIS data produces a Nyquist and Bode plot for each reading. Using these plots, an equivalent circuit can be fitted using ZView software, based on the structure of the coated sample. From this equivalent circuit, values for the capacitance and resistivity of the sample can be determined. The corresponding equivalent circuit for the SiO_x samples allowed the coating capacitance and resistance to be determined. The acceptance criteria used for the EIS fittings was chi-squared (χ^2) < 0.01, where a range of 0.003 to 0.01 shows an adequate good fit [204].

The equivalent circuits that are estimated using EIS can be made up of passive or active components. Passive elements are analogous to the system providing a model and discussion to the corrosion process, but are not components of the corrosion process itself. Passive elements include resistors (R), inductors (L), capacitors (C), constant phase elements (Q or CPE) and Warburg (W). Table 4.12 highlights the passive elements and their corresponding impedance.

Table 4.12 Passive elements which serve as components of an electrical circuit.

Circuit element	Symbol	Impedance
Resistor, R		$Z_R = R$
Inductor, L		$Z_L = j\omega L$
Capacitor, C		$Z_C = \frac{1}{j\omega C}$
Constant Phase Element, Q (or CPE)		$Z_{CPE} = \frac{1}{Q(j\omega)^n}$
Warburg, W		$Z_W = \frac{W}{(j\omega)^{0.5}}$

In EIS experiments, it is unlikely that the capacitor will behave ideally, therefore the capacitor is usually described as a constant phase element (CPE). A CPE is generally reported as an admittance (Y_o), with units of $\Omega^{-1} \text{ cm}^{-2} \text{ s}^n$ and can be described using the following equation (Eq 4.19):

$$Z_{CPE} = \frac{1}{Y_o(j\omega)^n} \quad \text{Eq 4.19}$$

When the value of $n = 1$, a CPE describes an ideal capacitor, when $n = 0$ the CPE signifies a pure resistor and when $n = 0.5$ the CPE is equivalent to the Warburg element. For $0.5 < n < 1$, the systems shows a behaviour that can be attributed to oxide films, surface heterogeneity or to charge transfer reactions [205].

For EIS the response of the system is presented using 2 different plots, a Nyquist plot and a Bode plot. The Nyquist plot, plots the imaginary impedance $-Z''$ versus

the real part of the impedance Z . A Nyquist plot uses the electrical components established by equivalent circuits to characterize the frequency dependence of impedance responses. An example of a Nyquist plot for a variety of equivalent circuits are presented in Figure 4.15.

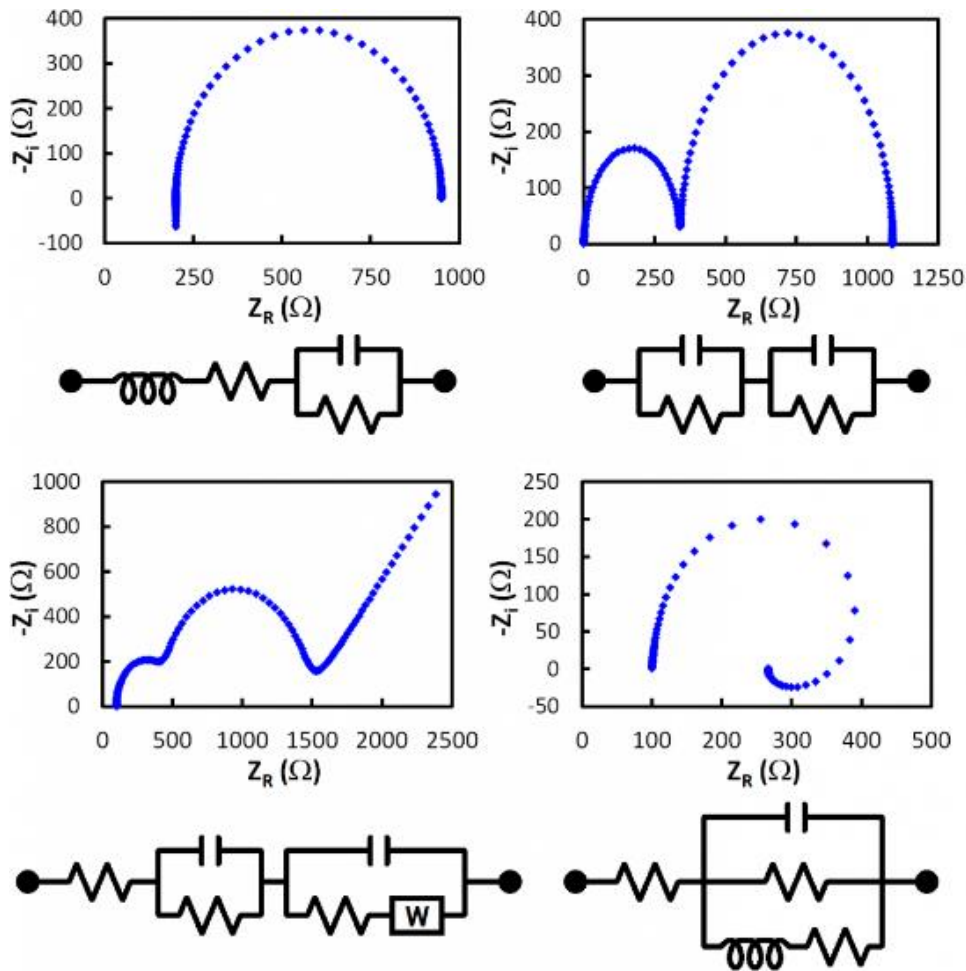


Figure 4.15 Nyquist plot examples with the corresponding equivalent circuits [206].

The Bode plot consists of two plots in one, the Bode impedance modulus ($|Z|$ vs. frequency (f)) and the Bode phase angle (degrees (ϕ) vs. frequency (f)). The x-axis is the logarithmic scale of the frequency (Hz) and the y-axis is 1) logarithm of the impedance and 2) the phase shift. The circuit behaviour of a coated sample can be determined from both the Nyquist and Bode plots. The resistance and

capacitance values can also be determined by fitting equivalent circuits to the corresponding plots.

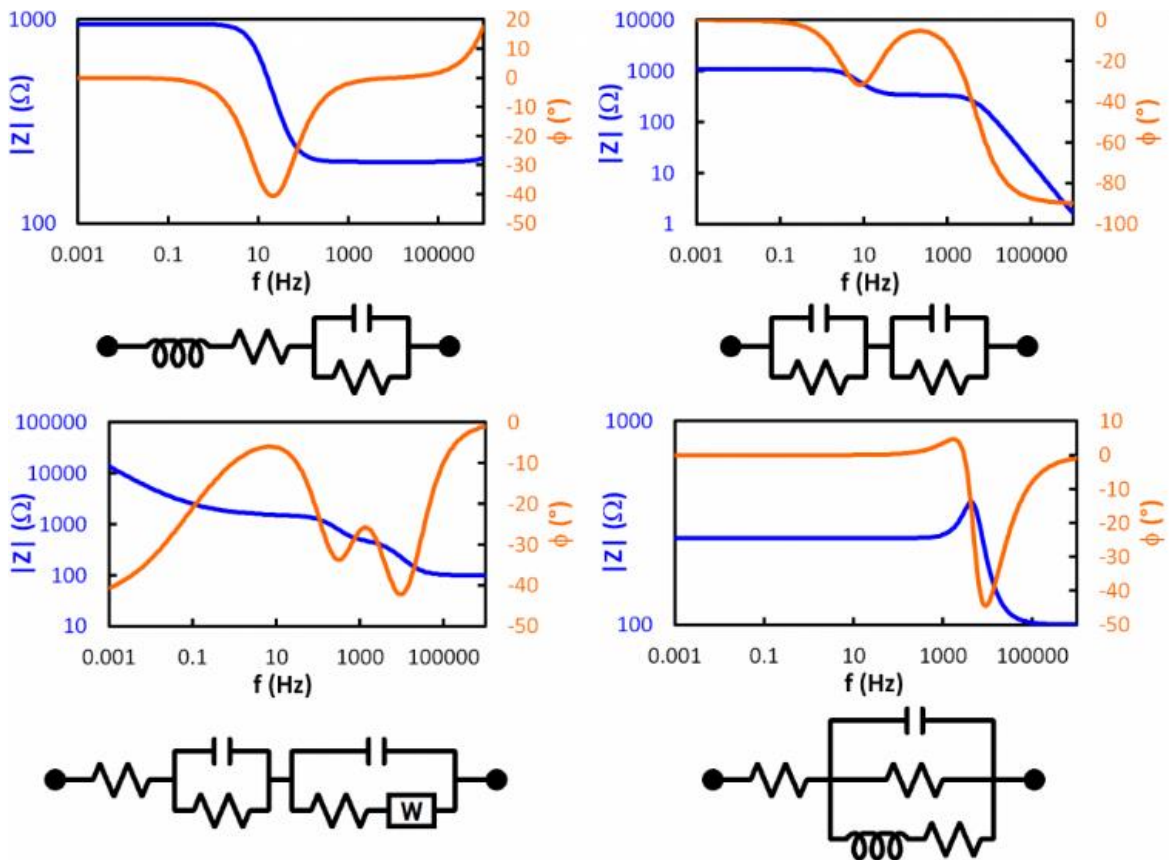


Figure 4.16 Bode plot examples with the corresponding equivalent circuits [206].

Generally, most coatings do not behave perfectly and will exhibit corrosion due to heterogeneity of the coating thickness or defects and pores within the coating structure. Utilising both the Nyquist and Bode plots, an equivalent circuit made up of passive elements can be fitted to the plots to understand the corrosion performance of a coating. The equivalent circuit depicted in Figure 4.17 and represents a real coating, where the coating is acting as a true capacitor (C_c). The circuit consists of the solution resistance (R_{sol}), the coating capacitance (C_c), the coating resistance (R_{por}) and a double layer capacitance (C_{dl}). The C_{dl} component represents the interface at which the electrolyte and reaches the

substrate surface. The coating resistance represents potential defects or pinholes within a coated structure, allowing the electrolyte to reach the substrate/metal surface and is in parallel with C_c , which may increase over time due to electrolyte uptake [207].

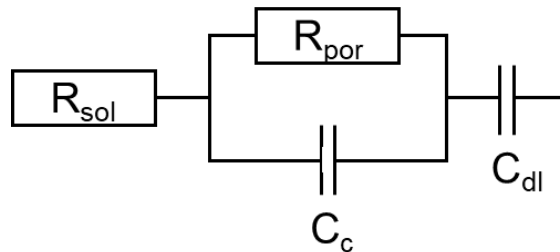


Figure 4.17 A simple equivalent circuit for a real coating. R_{sol} = resistance of the solution, R_{por} = pore resistance within the coating, C_c = coating capacitance, C_{dl} = capacitance at the double layer.

When corrosion at the electrolyte and substrate surface interface occurs, a more complex equivalent circuit can be used to depict the corrosion behaviour. Current can travel through a pore or defect within the coating, leading to the electrolyte being in contact with the metal. Figure 4.18 shows the equivalent circuit of a coating that exhibits corrosion, where the C_{dl} is parallel to the resistance of the charge transfer (R_{ct}), which is in series with R_{por} .

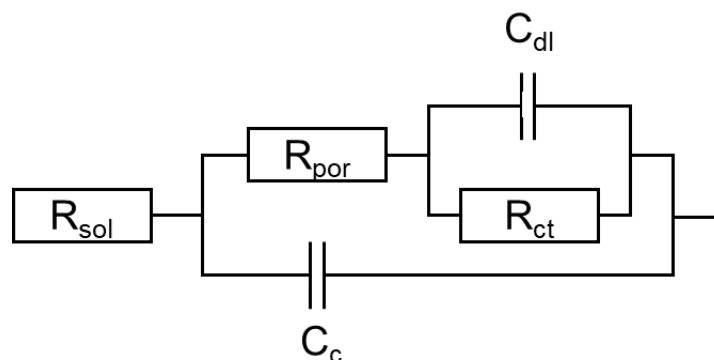


Figure 4.18 An equivalent circuit for a coating that exhibits corrosion. R_{sol} = resistance of the solution, R_{por} = pore resistance within the coating, C_c = coating capacitance, C_{dl} = capacitance at the double layer, R_{ct} = resistance of the charge transfer.

EIS is used for characterizing the dynamics of an electrochemical process. EIS is the response of an electrochemical system (coated metal) to an applied potential. The frequency dependence of the impedance can reveal chemical processes which may occur. Coatings from Batch 2 with a varying HMDSO:O₂ ratios and DOE thickness 2 μm were used to investigate the corrosion performance of SiO_x coatings. The dependence of the corrosion resistance on the HMDSO:O₂ ratio was investigated and also the dependence of the thickness. The frequency of the measurements ranged from 10,000 Hz to 0.005 Hz, with an AC excitation amplitude of 10 mV vs the OCP and a total of 50 points per decade. The frequency range was selected based on literature findings for SiO₂ coatings on a Ti-6Al-7Nb alloy [131] and SiO_x/SiO_xC_yH_z coatings on carbon steel substrates [127], [208], where the high frequency range started at 10 kHz. Due to the limitations of the Gill AC potentiostat, high frequency measurements were unable to be taken at 100 kHz due the instrument allowing frequencies up to 20 kHz. The experiment was run for a duration of 168 hours to characterise the

corrosion behaviour of the coatings over time, with each EIS measurement taking an estimated time of 26 minutes.

Table 4.13 details the samples used for the EIS experiments. The constant phase element (CPE) and resistance values for the different HMDSO:O₂ ratios were obtained through the fitting of the equivalent circuits, using the Nyquist and Bode plots. A complex equivalent circuit, containing 3 capacitive loops was determined for the SiO_x coatings. A CPE values are reported as an admittance (Y_0), where all values for n are $0.5 < n < 1$.

The experiments of the sample at ratio 1:12 were carried out at the DOE thicknesses 1, 2, 3.5 and 5 μm to investigate the dependence of the thickness on the resistance and capacitance of the coatings.

Table 4.13. The matrix of samples used for the determination of the resistivity and capacitance of SiO_x coated samples using EIS.

HMDSO:O ₂ ratio	DOE thickness (μm)
Uncoated	N/A
1:10	2
1:12	1, 2, 3.5, 5
1:14	2
1:16	2
1:20	2
1:24	2
1:36	2

Chapter 5 – Characterisation of SiO_x coatings with varying HMDSO:O₂ ratios

5.1 Introduction

This chapter comprises the results for the first batch of coatings, with varying HMDSO:O₂ ratios. The preliminary coatings were all coated with a DOE thickness of 2 µm and varying HMDSO:O₂ ratios. The ratios used for batch 1 included 1:1, 1:13, 1:6, 1:12, 1:16, 1:20 and 1:36. The ratios were chosen so that there was a broad range of oxygen concentrations used throughout the batch, to understand and compare the mechanical and structural properties of coatings with a small oxygen concentration (1:1 and 1:3) to those with a larger oxygen concentration (1:36).

Firstly in this chapter, there will be a review of the mechanical characteristics of the coatings by means of Calo® testing to determine the thickness and scratch testing to determine the adhesion and critical loads of the coatings. The results will be discussed, focussing on the HMDSO:O₂ ratios and how the oxygen concentration affects these properties. The second part of the chapter covers the characterisation of the chemistries and structural properties of the SiO_x coatings. The structure and chemistry of the coatings will be determined using scanning electron microscopy (SEM) with energy dispersive x ray (EDX) spectroscopy, x-ray diffraction (XRD) and Fourier transform infrared (FT-IR) analysis.

5.2 Mechanical characterisation of the first batch of coatings with varying HMDSO:O₂ concentrations

5.2.1 Calo® Test

The results for the Calo® test are provided in Table 5.1. The table consists of the sample name, the corresponding HMDSO:O₂ ratio, design of experiments

thickness (μm) (calculated from the flow rate and deposition rate of the gases in the chamber) and the actual thickness (μm) of the coating calculated using a Calo® test and optical microscopy.

Table 5.1. A list of the SiO_x coated samples with HMDSO: O_2 ratio, nominal thickness (μm) and actual thickness (μm) calculated using Calo® Test.

HMDSO:O_2 ratio	DOE thickness (μm)	Calculated thickness (μm)
1:1	2	0.26
1:3	2	1.80
1:6	2	1.70
1:12	2	2.09
1:16	2	1.72
1:20	2	2.07
1:36	2	2.21

The thickness measurements calculated from the Calo test and optical microscopy are shown in Figure 5.1. The thicknesses of the coatings deviate slightly when compared to the DOE thickness of the coating process. The sample with HMDSO: O_2 ratio 1:1 has a thickness considerably smaller than the design thickness. This may be due to having a lower concentration of oxygen present during the coating process, resulting in a more organic like coating. Wavhal et al proposed that at low concentrations of O_2 (<50%), the coatings produced are more polymer-like ($\text{SiO}_x\text{C}_y\text{H}_z$), with the presence of carbon and hydrogen [104].

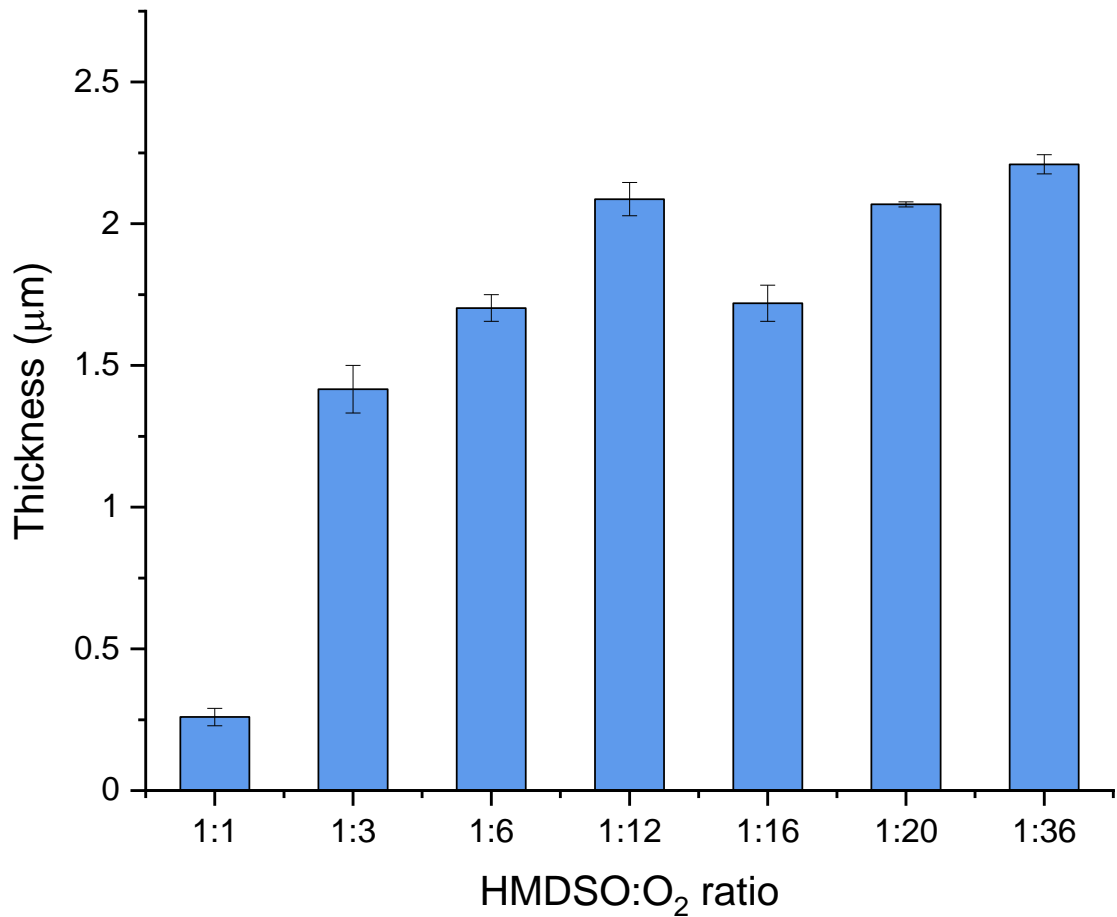


Figure 5.1. The average calculated thickness for the SiO_x coatings with varying HMDSO:O₂ ratios and a DOE thickness of 2 µm, including error bars.

The average thickness was calculated from 3 consecutive tests performed on different areas of the sample. The errors for each thickness were calculated using the standard deviation to consider any spatial variation across the surface of the coating. The error bars show that there is a slight spatial deviation for some of the samples. HMDSO:O₂ ratio 1:20 have minimal spatial deviation shown by the small error bars. The sample at 1:3 ratio has the largest error bar suggesting that there is a large spatial deviation across the whole sample and that the coating may not have deposited uniformly across the entire surface. The SiO_x coatings 1:12 and 1:20 give a good agreement with the design thickness, at 2.09 µm and 2.07 µm respectively. Three of the coatings - 1:3, 1:6 and 1:16 – have a thickness

that is under the 2 μm design thickness, 1.80 μm , 1.70 μm , 1.72 μm , respectively. The coating with ratio 1:36 has a thickness of 2.21 μm , slightly over the design thickness. Although some of the coatings did not meet the required design thickness, they all lie within $\pm 0.3 \mu\text{m}$. For the purpose of this research the thickness is satisfactory to further investigate the mechanical and chemical compositions of the coatings.

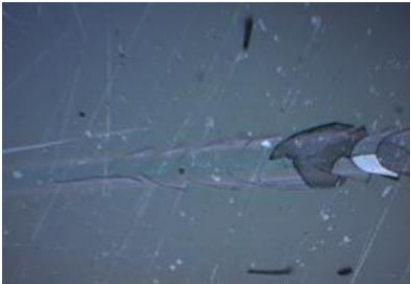
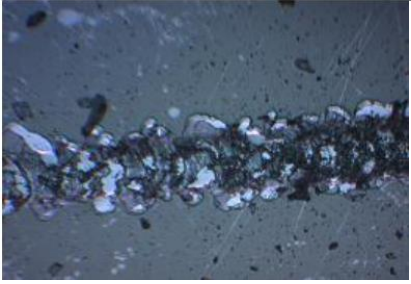
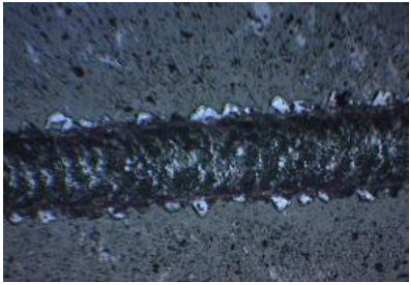
5.2.2 Scratch Test

A series of 3 scratches were performed for each sample and an average critical load was calculated. The critical loads presented in Table 5.2 shows the average values for the results from the scratch test, with the standard deviation. Each failure point occurs at a different critical load. There were three critical loads (LC_1 , LC_2 and LC_3) present for coated sample, and can be categorised based on the type of failure event, as described in section 4.5.2. Coating 1:12 exhibits the highest critical loads at all 3 points, 7.0, 23.0 and 35.5 N for LC_1 , LC_2 and LC_3 respectively. The lowest critical loads are from the coating 1:3, with a LC_1 at 4.2 N. These low values could be due to the lower oxygen concentration used during the deposition process. The lower O_2 rates may result in a coating with higher carbon concentration [209].

Table 5.2. Critical load values (LC_1 , LC_2 and LC_3) for the SiO_x coated HSS with varying HMDSO: O_2 ratios.

HMDSO: O_2 ratio	LC_1	LC_2	LC_3
1:3	4.2	15.9	32.1
1:6	6.6	18.1	33.3
1:12	7.0	23.0	35.5
1:16	4.7	16.9	33.9
1:20	5.6	16.2	32.0
1:36	5.5	15.7	33.7

As the HMDSO:O₂ ratio increases the LC₂ critical loads (N) increase up to the ratio 1:12, followed by a slight decrease as the ratio increases to 1:36. The increase in load up to the ratio 1:12 could be due to the decrease in carbon content throughout the coatings. A higher carbon content present in the coating, can result in the film having a higher porosity [209]. This higher porosity can result in poor adhesion of the coating onto the substrate surface and thus, lead to greater wear.

Critical load	Evidence of wear
<p data-bbox="501 757 560 790">LC₁</p> <p data-bbox="320 808 740 880">Coating begins to show signs of cracking.</p>	
<p data-bbox="501 1064 560 1097">LC₂</p> <p data-bbox="320 1120 740 1227">The coating shows cracking, with the addition of interfacial spallation.</p>	
<p data-bbox="501 1361 560 1395">LC₃</p> <p data-bbox="355 1417 703 1489">Delamination of coating, resulting in a wear track.</p>	

The poor adhesion of the coating can then lead to delamination, cracking, spalling and then finally, failure. The results from the scratch test support the work published by Yang et al [209], showing that a decrease in the carbon content of the film leads to higher critical loads due to a better adhesion to the substrate.

Sahli et al [210] proposed that introducing an oxygen source during the deposition process lead to the production of SiO₂-like films, therefore reducing the effects that carbon may have on the properties of the coatings. The decrease in the critical loads for HMDSO:O₂ ratios >1:12 may be due to the increased oxygen concentration, leading to a higher concentration of oxygen present in the coatings. The literature suggests [106] that the coating reaches stoichiometry at HMDSO:O₂ ratio 1:13, ratios greater than this may have excess oxygen present, which in turn may result in a reduced adhesion of the coatings to the substrate.

5.3 Chemical characterisation of the first batch of coatings with varying HMDSO:O₂ concentrations

5.3.1 Energy dispersive x ray spectroscopy

EDX spectra and elemental mapping were used to characterise the elemental composition of the SiO_x coatings. The atomic concentrations of C, O and Si were analysed and calculated based on their relative ratios, as described in section 4.6.1.2.

5.3.1.1 Atomic concentration of carbon present in SiO_x coatings

All samples were analysed using SEM with EDX analysis, in order to characterise the chemical composition of the coatings. Figure 5.2 shows the graph of the atomic % of carbon present in the coatings as a function of the HMDSO:O₂ ratio. It can be seen that as the HMDSO:O₂ ratio increases, there is a decrease in the content of carbon present in the coatings. The carbon content reaches zero at ratio 1:16 and results in minimal error bars for the samples 1:16, 1:20 and 1:36. The sample with HMDSO:O₂ ratio 1:1 had the highest concentration of carbon present and a large error due to delamination of the coating. However, due to the delamination of the coating, the carbon, oxygen and silicon concentrations of the

coating are complicated due to interference from the substrate. The low concentration of oxygen present during the coating deposition can lead to the incomplete oxidation of HMDSO and therefore leads to a highly organic coating, with poor adhesion.

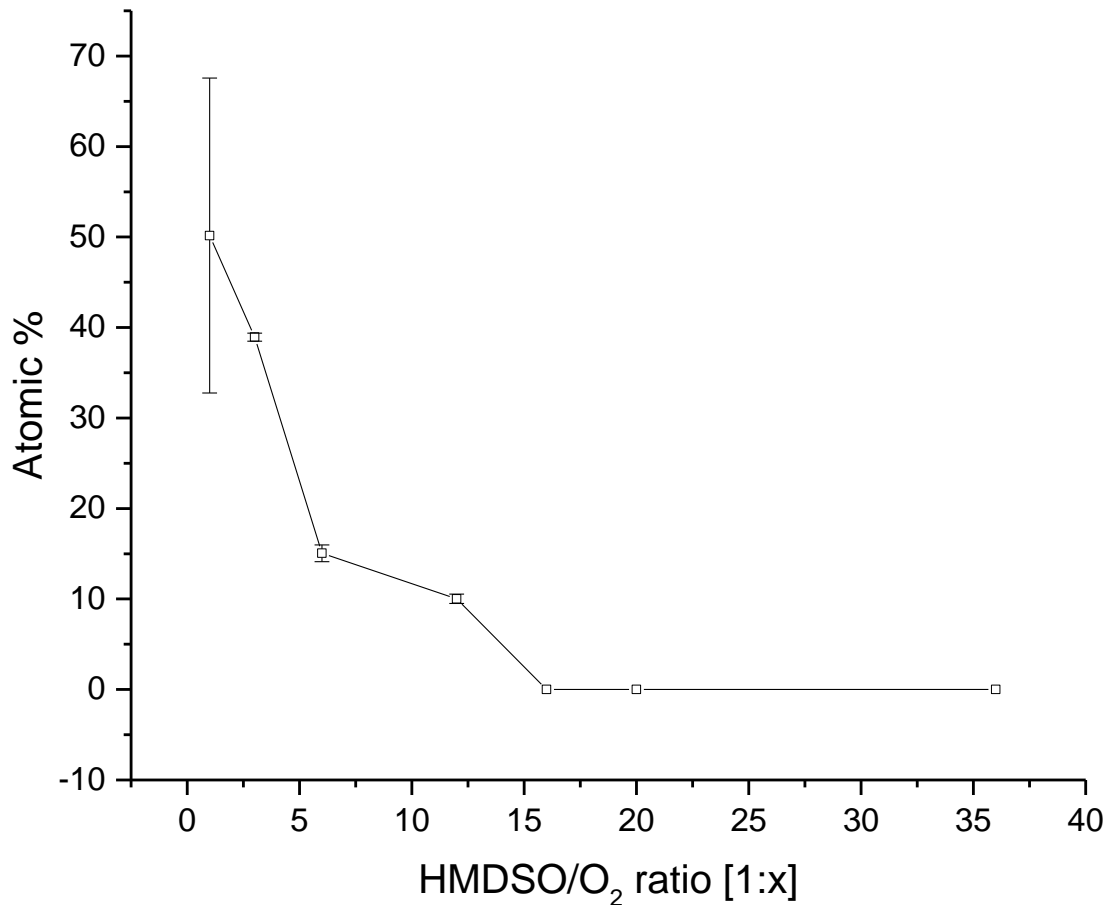


Figure 5.2 The atomic concentration (%) of carbon present in the SiO_x coatings with increasing HMDSO:O₂ ratio and DOE thickness 2 μm.

The results for the atomic concentration of carbon in the coatings with a comparison to the atomic concentration of carbon present within the HMDSO and O₂ mixture added to the chamber are depicted in Figure 5.3. At HMDSO:O₂ ratios greater than 1:6, there was a good agreement with the amount of carbon present in the coatings as there was with the precursor mixture. At low oxygen

concentration however, there is a larger amount of carbon present in the coating. This may be due to the incomplete oxidation of HMDSO within the chamber, prior to the deposition of SiO_x onto the substrate surface, thus depositing a more organic polymer-like film ($\text{SiO}_x\text{C}_y\text{H}_z$) instead of an inorganic-like SiO_2 film [104].

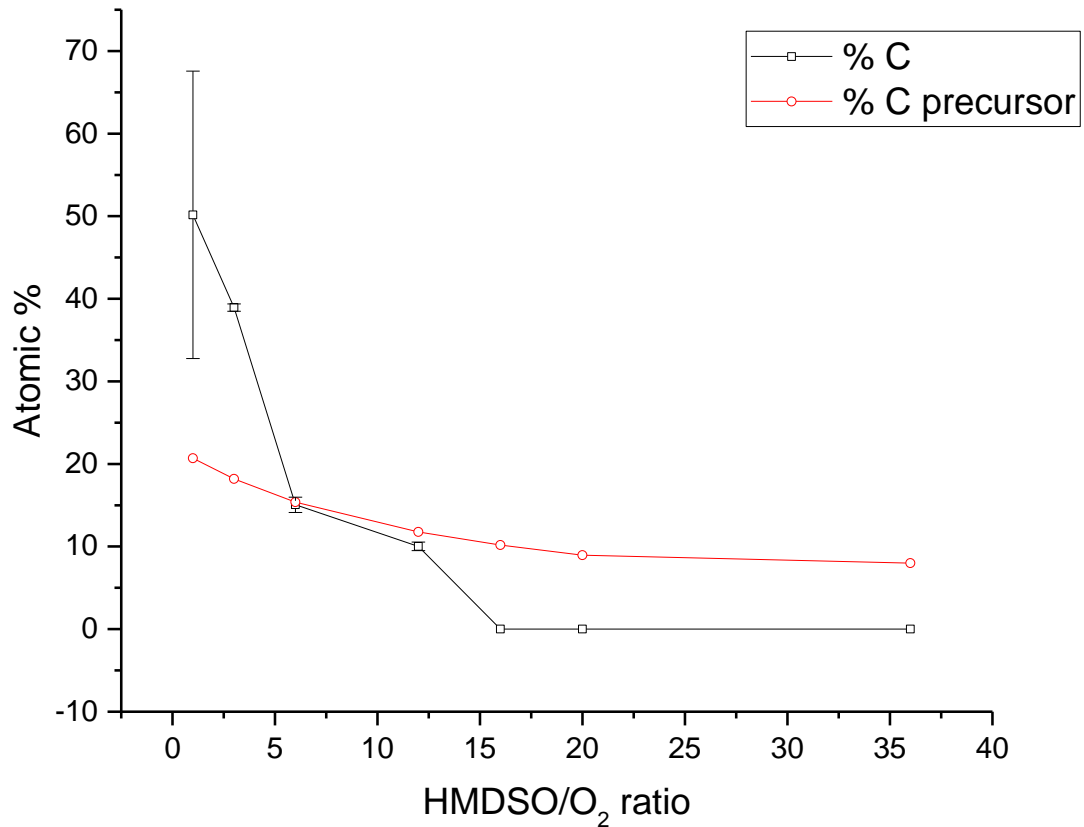


Figure 5.3 The atomic concentration (%) of carbon present in the SiO_x coatings with increasing HMDSO: O_2 ratio and DOE thickness $2\ \mu\text{m}$, and the atomic concentration of carbon present in the HMDSO and O_2 precursor mixture present within the PVD chamber.

As the HMDSO: O_2 ratio increases the amount of carbon present within the SiO_x coating decreases. The carbon concentration appears to reach zero between HMDSO: O_2 ratio 1:12 and 1:16. However, due to the sensitivity of EDX spectroscopy, any element with a concentration below 5% may not be accurately measured.

5.3.1.2 Atomic % of oxygen (O) and silicon (Si) in relation to HMDSO:O₂ ratio

The atomic concentration of elemental oxygen (O) and silicon (Si) were also characterised for each sample. Figure 5.4 shows the graph of the atomic concentrations of O and Si plotted as a function of the HMDSO:O₂ ratio. As the concentration of O₂ is decreased there is an increase in the amount of both oxygen and silicon present in the coatings. The coating with HMDSO:O₂ ratio 1:1 gives a large error.

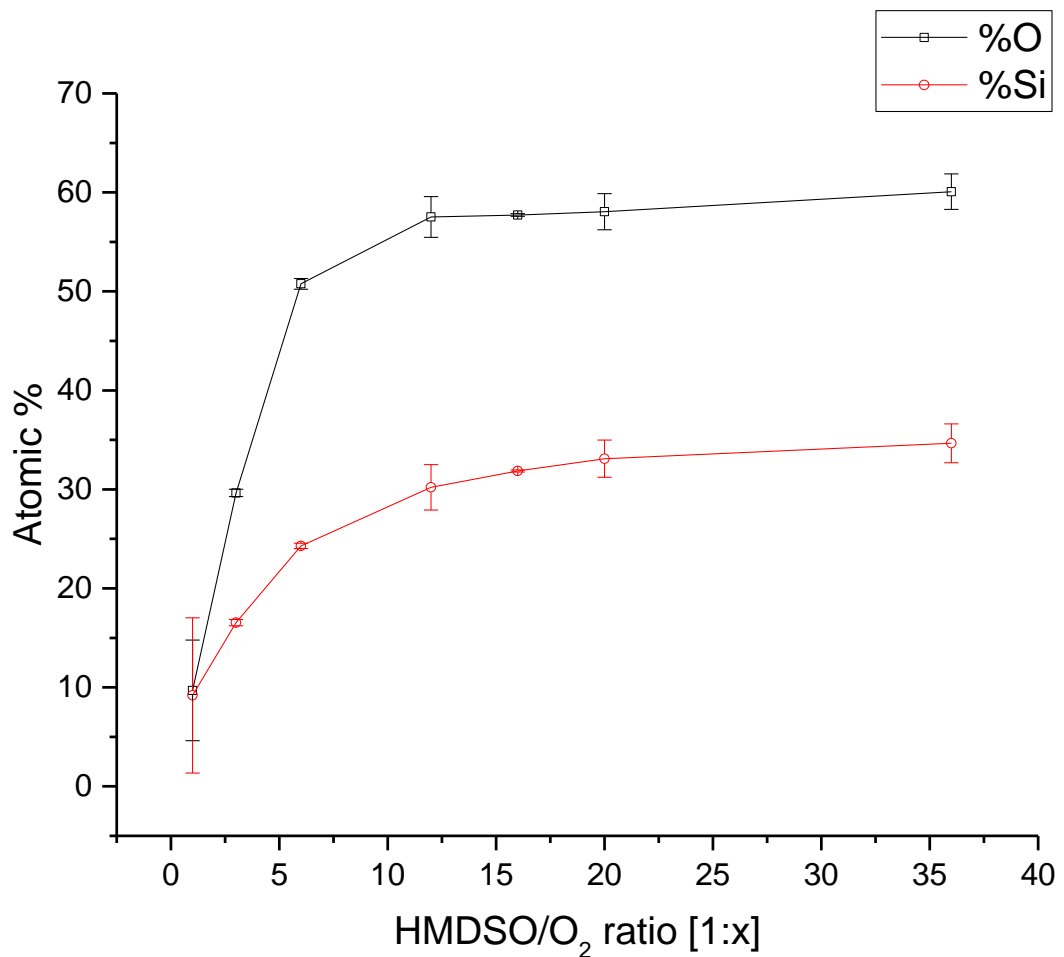


Figure 5.4 The atomic concentration (%) of both silicon and oxygen present in the SiO_x coatings with increasing HMDSO:O₂ ratio and DOE thickness 2 μm, including error bars.

The data from the EDX analysis is displayed in Table 5.3 and shows the oxygen, silicon and carbon concentrations (atomic %) for each sample at differing

HMDSO:O₂ ratios. This data has been utilised to calculate the silicon to oxygen (Si:O) ratios for each sample, as shown in Figure 5.5.

Table 5.3. The oxygen, silicon and carbon concentrations for the samples with varying HMDSO:O₂ ratios, acquired from EDX analysis.

Atomic %	1:1	1:3	1:6	1:12	1:16	1:20	1:36
% O	51.3	64.2	67.6	65.6	64.4	63.7	63.4
% Si	48.7	35.8	32.4	34.4	35.6	36.3	36.6
% C	50.2	38.9	15.0	10.0	0	0	0

The graph displayed in Figure 5.5 shows that the Si:O ratio increased with an increase in the HMDSO:O₂ ratio from 1:1 to 1:6. This is then followed by a decrease in the Si:O ratio as the HMDSO:O₂ ratio increased up to 1:36.

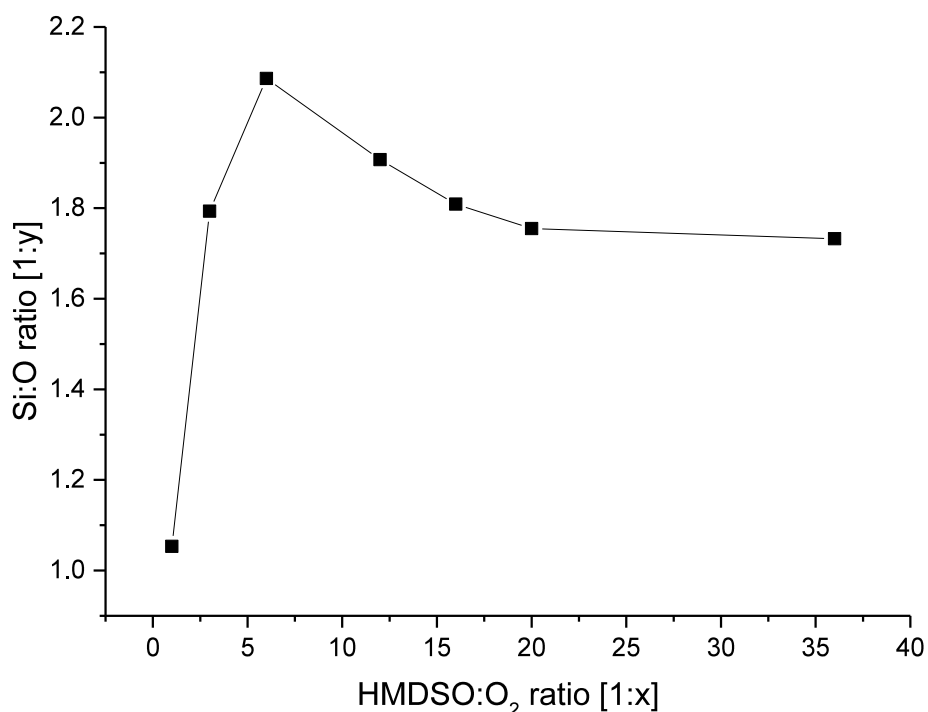


Figure 5.5 The Si:O ratio calculated from the EDX atomic concentrations of silicon and oxygen for SiO_x coatings with varying HMDSO:O₂ ratios and DOE thickness 2 μm.

The results for the atomic concentration of oxygen and silicon with a comparison to the atomic concentration of oxygen and silicon present in the HMDSO and O₂ precursor mixture added into the chamber are presented in Figure 5.6.

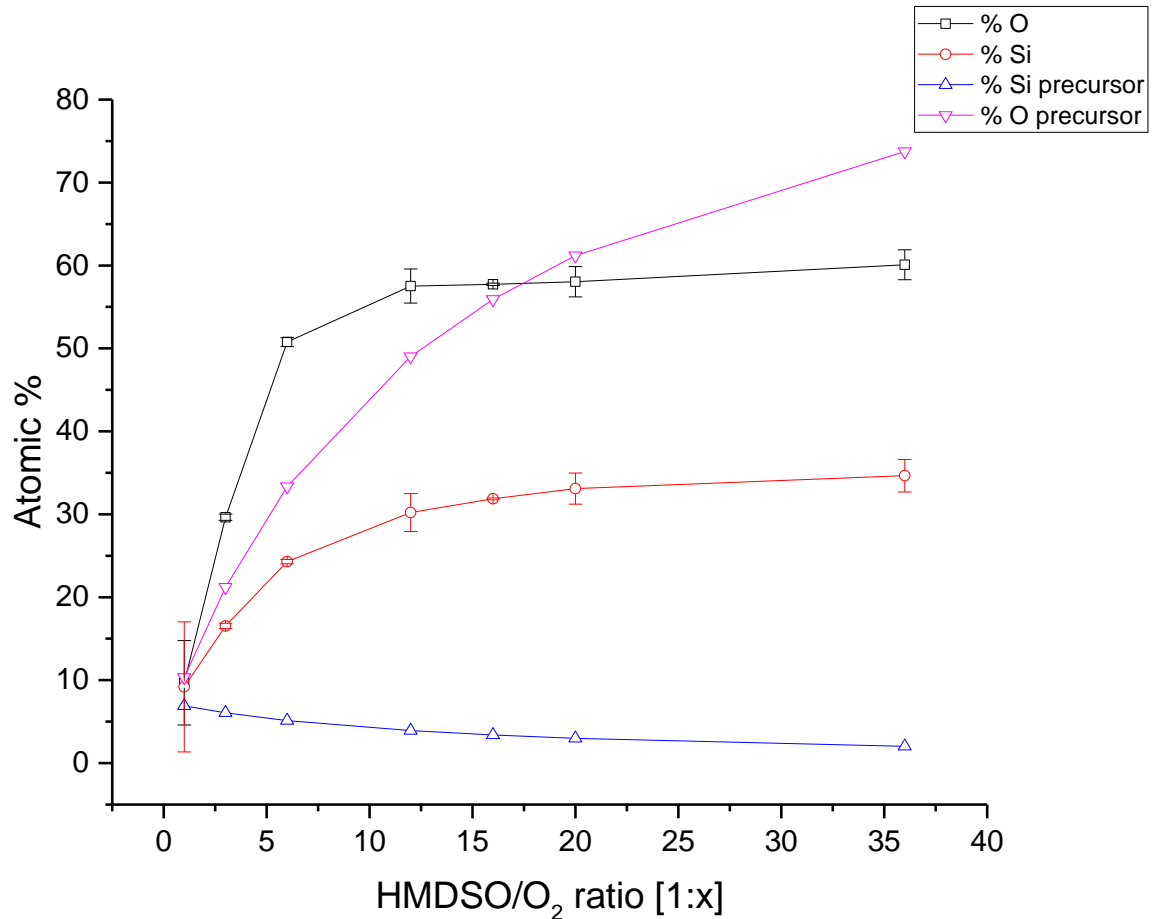
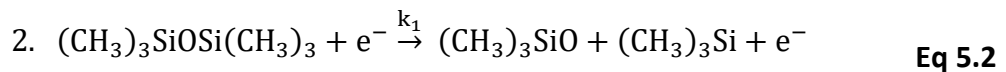
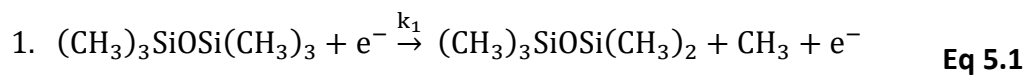


Figure 5.6 The atomic concentration (%) of both silicon and oxygen present in the SiO_x coatings and the atomic % of silicon and oxygen present in the precursors with increasing HMDSO:O₂ ratio.

As the oxygen concentration during the deposition process is increased, there is an increase in the oxygen content in the coatings. Surprisingly, the amount of silicon in the coating also increases with increasing oxygen content. This increase could be due to the decrease in carbon content of the coatings. As the HMDSO:O₂ ratio reaches 1:16, the oxygen and silicon content in the films begins

to plateau and there is only a small increase in the O and Si content from 1:16 ratio to 1:36 ratio. In comparison to the atomic % of O and Si in the precursors we see slightly different trends when the SiO_x coating is deposited. The atomic % of silicon in the precursor mixture decreases very slightly with an increase in oxygen, however we see the opposite effect when the SiO_x coating has been deposited. Moreover, the atomic % of O in the precursor mixture increases more dramatically than on the as deposited coating. This may be to do with the reaction kinetics and how the bonds are cleaved within the PECVD chamber. The atomic % of Si and O within the precursor mixtures assumes that all the silicon and oxygen available is reacted and deposited onto the surface of the substrate, thus giving a slightly different trend to that from SEM/EDX analysis.

Sonnenfeld et al [105] have researched the chemical kinetics of the reaction that takes place during dielectric barrier discharge at atmospheric pressure for the deposition of silicon oxide coatings. The chemical plasma process was analysed using gas chromatography (GC) in order to study the chemical conversion of the precursor in either a helium or argon environment [105]. Two reaction schemes based on the species detected in GC have been proposed:



Where k_1 and k_2 are the reaction rates for the proposed reaction schemes.

A reaction mechanism scheme has been proposed and proposes some of the smaller fragments that HMDSO may be converted into prior to adsorption onto the substrate surface.

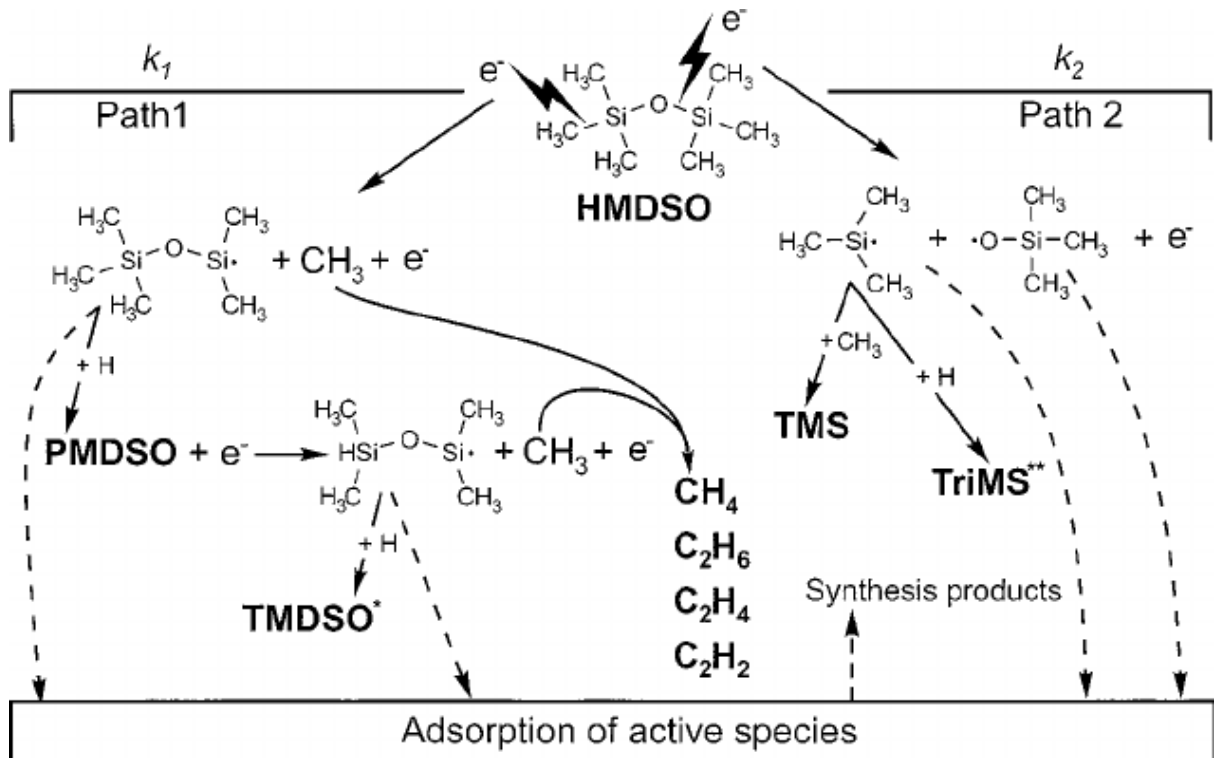


Figure 5.7. The reaction scheme for the plasma process of the breakdown of HMDSO into its smaller constituents during the deposition process of SiO_x . Figure taken from reference [105].

From the reaction mechanism scheme in Figure 5.7 it is assumed that the polymerisation processes that lead to the deposition of SiO_x take place on the surface of the substrate that is exposed to the plasma [105]. The by-products from the synthesis are desorbed back into the gas phase and do not take part in polymerisation. As most of the by-products are organic radicals, there will be a lower carbon content in the coating than in the precursor mixture. Reaction path 1 shows to dominate the conversion of HMDSO, therefore the rate of reaction is higher ($k_1 > k_2$), and can be assumed to be the critical step in the plasma polymerisation of SiO_x coatings. Therefore, it can be assumed that at the

beginning of the deposition process, the microwave energy is used to form the plasma which breaks the Si-CH₃ bond in the HMDSO precursor. This is followed by a cascade of further fragmentations into smaller radicals, which in turn react with the O₂ in the chamber. The higher HMDSO:O₂ ratios increases the amount of O₂ available to react with the fragments and therefore resulting in complete oxidation of HMDSO to form SiO₂-like inorganic coatings [87].

This may also explain why the silicon concentration increases as we increase the concentration of oxygen. Higher levels of oxygen present will lead to HMDSO being completely oxidised, with the stoichiometric ratio of HMDSO:O₂ for complete oxidation being 1:13 [106]. This explains why at ratio 1:16, the carbon content is assumed to reach zero. Based on the atomic concentration data from the EDX analysis, the coating reaches stoichiometric SiO₂ between ratios 1:6 and 1:12.

The EDX results agrees with Lamendola et al [145], who proposed that at high concentrations of oxygen there is a high content of oxygen atoms which promotes the consumption of C, Si and CH radicals. Thus, suggesting that at high HMDSO:O₂ ratios there is a negligible concentration of complex fragments such as SiO_xCH_z and SiC_xH_y, and the dominating film precursors are SiO radicals which lead to the formation of SiO₂-like films.

5.3.2 X-ray diffraction (XRD)

XRD patterns were carried out for each sample, following the procedure stated in section 4.6.4. From the XRD patterns shown in Figure 5.8, it can be seen that each sample gives the same diffraction pattern, with no shift in 2θ values and comparable intensities. The sample at HMDSO:O₂ ratio 1:1 has been excluded from the dataset due to inconclusive data. The largest peak at 2θ = 44.6° has

been assigned to an iron peak, from the high-speed steel (HSS) substrate. This peak increases in height as the HMDSO:O₂ ratio increases. The peaks at 2θ = 39.4°, 46.4°, 72.5° and 82.0° have all been assigned as silicon oxide peaks.

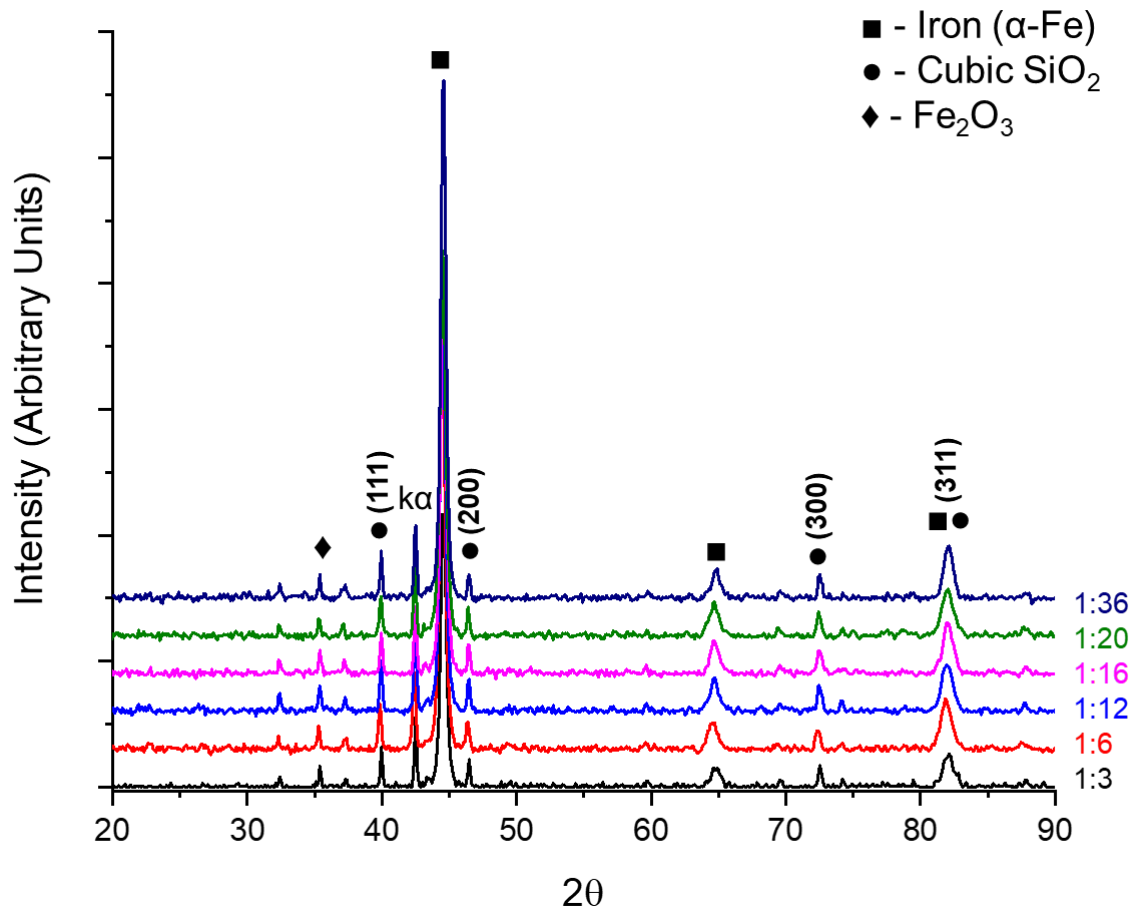


Figure 5.8. The stacked diffractograms of the SiO_x coatings with varying HMDSO:O₂ ratios and DOE thickness 2 μm.

Figure 5.8 shows the stacked diffractograms for the SiO_x coated HSS samples. The peaks at 82.0° is relatively broad, potentially due to a crossover of peaks from both the silicon oxide coating and iron from the HSS. The peaks at 2θ = 39.4, 46.4, 72.5 and 82.0° can be assigned to pure cubic silicon dioxide (SiO₂), reference 01-076-6230 from the ICDD database. The sharp silicon oxide peaks shown on the diffractogram indicates that the coatings showed some crystallinity. The crystallinity of the coatings was calculated using the Scherrer equation. The

peaks at $2\theta = 42.5^\circ$ ($K\alpha$), 44.6° , 64.5° and 82.0° can be assigned to cubic α -iron (α -Fe), reference 01-080-3817 from the ICDD database. The broader peak at 82.0° has been assigned to both iron and silicon dioxide, due to a crossover. The peak at 42.5° is a $K\alpha$ sister peak from fluorescence of the large iron peak at $2\theta = 44.6^\circ$, the $K\alpha$ peak is described in further detail in section 4.6.4. The average crystallite sizes for the SiO_x coatings with DOE thickness $2 \mu\text{m}$ are shown in Table 5.4.

Table 5.4. The average crystallite sizes (nm) of the SiO_x coatings with varying HMDSO: O_2 ratios and DOE thickness $2 \mu\text{m}$.

HMDSO: O_2 ratio	Average crystallite size (nm)	Average error (nm)
1:3	18.0	0.3
1:6	17.1	0.5
1:12	16.8	0.6
1:16	16.6	0.3
1:20	16.8	0.3
1:36	19.9	0.4

As the HMDSO: O_2 ratio increases from 1:1 to 1:12, there is a decrease in the average crystallite size (nm) of the silicon dioxide coating. However, when the HMDSO: O_2 ratio reaches 1:16, there is an increase in the average crystallite size (nm), which then continues to increase up to HMDSO: O_2 ratio 1:36. Bhoraskar et al. reported that the crystallite size decreases with increasing porosity [211], suggesting that as the crystallite size decreases with an increase in HMDSO: O_2 ratio up to 1:12, there may be a decrease in the porosity of the coating. It would also suggest that for HMDSO: O_2 ratios 1:16-1:36, there may be an increase in the porosity. Other literature has also suggested that as the carbon content in the

films decreases, there is a decrease in the porosity [209], agreeing with the results of Bhoraskar et al. As it has been established that the carbon content in the films decreases with an increase in the HMDSO:O₂ ratio according to the EDX analysis.

The small peak at $2\theta \sim 32.5^\circ$ was unable to be identified. This peak may be due to some contamination on the surface of the SiO_x coating, or some contamination within the coating structure. Contamination within the coating structure may occur during the deposition of the SiO_x coating. Increasing the O₂ concentration is thought to have an increase in the deposition rate, however it may also result in particulate contamination of the thin film [87]. These particles may be a result of debris in the chamber from previous PECVD depositions, i.e. excess carbon maybe left in the chamber from the deposition of diamond-like carbon (DLC) coatings. However, this is unlikely to take place due to the plasma surface etching to clean the HSS surface prior to the SiO_x deposition. Therefore, the peak could be due to small amounts of contamination on the top surface of the coating.

5.3.3 FT-IR

FT-IR measurements were taken for each sample with varying HMDSO:O₂ ratio. Figure 5.9 shows the absorbance (a.u.) plotted against the wavenumber (cm⁻¹) for each sample. Typical characteristic peaks for SiO_x coatings are described in section 4.6.2.

Table 5.5 The main characteristic peaks present in the SiO_x coated samples.

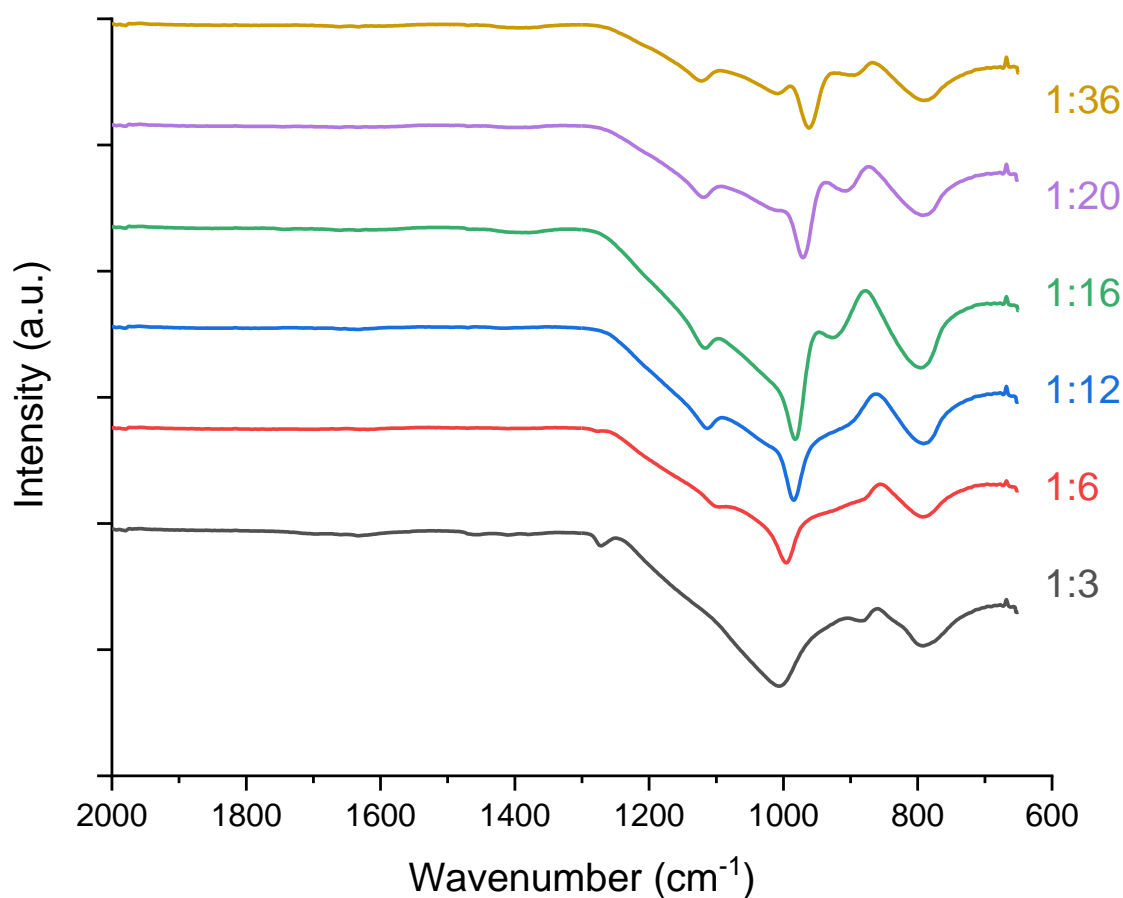


Figure 5.9. A graph to show the FT-IR spectra for the samples with increasing HMDSO:O₂ ratio. Plotted as a function of wavenumber (cm⁻¹) against absorbance (a.u.).

From the literature [212], a peak at 2100 cm⁻¹ has been reported as a Si-H stretch, however for the current samples there is no peak present in the FT-IR spectra for the films deposited under these conditions. The FT-IR peaks were assigned as follows, the peak at ~800 cm⁻¹ has been assigned to Si-O-Si asymmetric bending and the broad peak at ~1000-1150 cm⁻¹ has been assigned to Si-O-Si asymmetric stretching. The intensity of the Si-O-Si asymmetric stretching band at 1000 cm⁻¹ increases from HMDSO:O₂ ratios 1:3 – 1:16. However, as the HMDSO:O₂ ratio continues to increase there is a decrease in the intensity of this band for samples 1:20 and 1:36.

The peak at $\sim 800\text{ cm}^{-1}$ assigned to a Si-O-Si bending shows that the intensity of the band shows a similar trend to that of the Si-O-Si asymmetric stretching band. There is an increase in the intensity of the band of samples with HMDSO:O₂ ratios 1:3-1:16, corresponding with the increase in the O₂ concentration. At the higher levels of O₂ concentration there was a decrease in the intensity of the band for samples 1:20 and 1:36. As the O₂ concentration reaches higher levels and surpasses the HMDSO:O₂ ratio 1:16 we begin to see non stoichiometric SiO₂-like films and the excess oxygen in the chamber may lead to reactions with the species that are not adsorbed onto the surface of the substrate, e.g. radicals and ions.

As the HMDSO:O₂ ratio increases, a new band at $\sim 880\text{ cm}^{-1}$ is becoming visible. This band has been attributed to Si₂O₃ and is associated with sub-oxidised silicon species, with oxygen interstitials within the coating. The coatings with HMDSO:O₂ ratio 1:6 and 1:12 do not have this peak present, however the other coatings do. The ratio 1:3 could be due to the incomplete oxidation of the HMDSO during the deposition.

Table 5.6. FT-IR data for the peak positions of the Si-O-Si asymmetric stretching peaks, with varying HMDSO:O₂ ratios.

HMDSO:O ₂ ratio	Peak position (cm ⁻¹)	
	Si-O-Si asym. Stretching in phase ($\sim 1000\text{ cm}^{-1}$)	Si-O-Si asym. Stretching out of phase ($\sim 1150\text{ cm}^{-1}$)
1:3	1004	1272
1:6	995	1102
1:12	985	1113
1:16	982	1117
1:20	971	1119
1:36	962	1123

The peak positions of the SiO_x coatings for the asymmetric Si-O-Si stretching peak are shown in Table 5.6. There are two peaks observed for the Si-O-Si stretching, the main peak at ~1000 cm⁻¹ and the shoulder at ~1150 cm⁻¹. The peak ~100 cm⁻¹ decreases in wavenumber with an increase in the HMDSO:O₂ ratio,. This shift in the wavenumber are indicative of the change in the stoichiometry of the SiO_x coatings and the increase in oxygen concentration [213]. The peak also becomes sharper with an increase in the HMDSO:O₂ ratio, suggesting that the coating may be getting denser with the increased oxygen concentration [214].

5.4 Summary of chapter

- EDX spectroscopy and FT-IR have been used successfully to characterise the composition of the SiO_x coated surfaces.
- EDX showed that as the O₂ concentration was increased, the amount of carbon present in the film was decreased, leading to a more inorganic coating. FT-IR showed that sample 1:3 did not contain any Si-CH₃ bonds, contradicting with the results from EDX that show that there is carbon present in the coating.
- The FT-IR data also shows that there is an increase in the intensity of the Si-O-Si bonding with increasing HMDSO:O₂ ratios.
- XRD has been used successfully to analyse HSS samples coated with a SiO_x coating with varying HMDSO:O₂ ratios. It is apparent that the SiO_x coating is crystalline, contrary to the typical amorphous silica. The average crystallite sizes of the coatings vary with HMDSO:O₂ ratios and are calculated from the Scherrer equation.

- The XRD pattern shows a peak at $\sim 32.5^\circ$ that is unable to be identified and may be due to some contamination on the surface of the coating. The contamination can affect the surface layer by disrupting and decreasing the compactness and density of the thin film.
- The increase in the amount of oxygen present in the chamber may also affect the HMDSO, by diluting its concentration within the gas mixture [215]. Thus, resulting in a lower amount of silicon being deposited onto the substrate surface.

Chapter 6 – Characterisation of SiO_x coatings with a comparison of the HMDSO:O₂ ratio and thickness.

6.1 Introduction to the chapter

Following on from the chemical and mechanical analyses of the first batch of coatings, a second batch of coatings were deposited. The second batch of coatings focuses on the HMDSO:O₂ ratios closer to that of stoichiometric SiO₂, with the matrix including ratios 1:10, 1:12, 1:14, 1:16, 1:20, 1:24 and 1:36. All the coatings were deposited with a design thickness of 2 μm, with coatings 1:12, 1:14, 1:16 and 1:20 coated with varying thicknesses of 1 μm, 3.5 μm and 5 μm. The coatings with ratios 1:1, 1:3 and 1:6 were not included in this section as the oxygen concentrations are not sufficient enough to produce inorganic-like SiO₂ coatings, having a more organic nature due to the presence of carbon.

The aim of this chapter is to review the mechanical, chemical and microstructural characteristics of the SiO_x coatings with a comparison to the HMDSO:O₂ ratios and also the thickness. The microstructure of the coatings will be further analysed in this chapter, with a focus on the XPS and XRD analysis of the coatings, with theoretical calculations for crystallite sizes and the strain of the coatings.

6.2 Mechanical characterisation of the second batch of coatings

6.2.1 Nanoindentation

In order to further study the mechanical characterisation of the SiO_x coatings, nanoindentation was used to quantify the mechanical properties. The basic properties gained from the nanoindentation results were the hardness (H) and Young's modulus (E). The hardness is a measure of the resistance of a material to plastic deformation, whereas Young's modulus is the resistance to elastic

deformation. The combination of mechanical properties from the SiO_x coating and the substrate, means that a maximum depth of 10% would be suitable to determine the Young's modulus of the coating [216].

The hardness and Young's modulus of the coatings was determined for all HMDSO:O₂ ratios at a 10% penetration depth, and a DOE thickness of 2 μm. The results are displayed in Table 6.1.

Table 6.1. The hardness (*H*) and young's modulus (*E*) values of the SiO_x coatings.

HMDSO:O ₂ ratio	Hardness (GPa)	Young's modulus (GPa)
HSS substrate	8.2	200
1:10	5.9 ± 1.0	100.4 ± 1.7
1:12	5.1 ± 0.5	93.3 ± 1.7
1:14	4.6 ± 0.2	82.0 ± 1.3
1:16	5.0 ± 0.4	83.6 ± 1.6
1:20	5.9 ± 0.8	97.4 ± 1.4
1:24	5.9 ± 0.5	99.3 ± 1.3
1:36	5.7 ± 0.5	93.1 ± 1.9

The nanoindentation results show that the coating with HMDSO:O₂ ratio 1:24 has the highest hardness at 5.9 GPa and ratio 1:14 gives the lowest hardness at 3.6 GPa. The difference in hardness between the HMDSO:O₂ ratios varies by 1.3 GPa. Taking into consideration the errors, the hardness values overlap slightly, thus suggesting that the hardness of the SiO_x coatings are similar. When compared to the uncoated HSS substrate, the coatings have a reduce hardness and elastic modulus. The nanomechanical characterisation of the SiO_x coatings relies on the hardness assessment of SiO₂-like coatings, with SiO₂ values of

hardness reported between 4-8 GPa [217], [218] and Young's modulus ranging from 24 to 120 GPa [217], [219], [220]. The hardness values for the SiO_x coatings are slightly higher than those reported in the literature, but the Young's modulus values lie within the higher end of the ranges that have been reported.

The oxygen concentration during the deposition can influence the hardness of the SiO_x coating. Benítez et al [218] reported that plasma polymerised HMDSO thin films, using DC glow discharge produced coatings with increasing hardness with the addition of O₂. A 0% oxygen content (100% HMDSO) produced a coating with 1.2 GPa hardness, which increased to 3.7 GPa at 35% O₂ and 6.6 GPa at 60% O₂. The hardness of the SiO_x coatings in Table 6.1 are higher than those reported by Benítez due to the increase in O₂ concentration during the deposition process (O₂ ≥ 90% for all coatings). The effect of the hardness and Young's modulus on the SiO_x coatings will be explored further throughout this chapter, comparing with the structural characteristics of the coatings. The hardness increases with an increase in the HMDSO:O₂ ratio from 1:14 through to 1:24. The hardness at ratio 1:12 is higher than that of coatings 1:14 and 1:16, and the coating at ratio 1:36 has a slight decrease in the hardness. Thus, it can be concluded that the hardness does increase with the oxygen concentration to a degree. The hardness values will be considered throughout this chapter when characterising the composition and microstructure of the coatings.

6.3 Compositional analysis of the second batch of coatings with varying HMDSO:O₂ concentrations and varying thickness

The chemistry of the coatings will be explored using SEM imaging with EDX analysis. A focused ion beam (FIB) cross section has also been analysed to investigate the structural integrity and chemistry of the coating, from the top

surface, through to the substrate. XPS analysis will further enhance the characterisation of the SiO_x coatings, and will be used to understand the bonding structure of the coatings.

6.3.1 Scanning Electron Microscopy imaging of the surface of SiO_x coated HSS.

SEM imaging was used to study the surface microstructure and topography of the coated samples. The SEM images are presented in Appendix A. All coatings show good homogeneity of the coatings across the surface, however there are no discernible features. The coating at HMDSO:O₂ ratio 1:12 shows a slightly rough surface, in comparison to the other coated samples. The coating with ratio 1:16 indicates slight crater-like defects on the top surface which may affect the properties of the coating. The image of the sample 1:20 shows a very smooth top surface, with some possible contamination, however this should not affect the overall performance of the coating. Sample 1:24 also shows signs of defects, with a risen area on top of the coating. Both sample 1:14 and 1:36 show a relatively smooth top surface, with some visible scratch like marks on sample 1:36.

6.3.2 Atomic concentration (%) of silicon and oxygen of the SiO_x coatings from EDX analysis

The atomic concentration of silicon and oxygen was determined using EDX point and elemental mapping analyses. The sensitivity of EDX is relatively low, so coatings with < 5% atomic concentration are difficult to characterise. However, a comparison with x-ray photoelectron spectroscopy (XPS) is also established later in this chapter. EDX is a useful tool to characterise the composition of a coated sample at the submicron level, but for the SiO_x coating with a thickness < 1 μm, it is difficult to conclude the true Si to O ratio of the coatings as the substrate will also produce elemental characterisation. Table 6.2 presents the oxygen and

silicon atomic concentrations for all HMDSO:O₂ coated samples at the 4 different thicknesses. Table 6.3 presents the Si:O ratios of all coated samples, calculated from the silicon and oxygen atomic concentrations from the EDX data.

Table 6.2 – The atomic concentration of oxygen and silicon from the EDX analyses.

		Thickness (µm)			
HMDSO:O ₂ ratio		1	2	3.5	5
% O	1:10	52.5±0.2	56.4±1.4		
	1:12	49.9±0.8	59.9±0.03	63.2±0.1	63.8±0.02
	1:14	50.5±1.2	59.5±2.1	58.7±0.3	59.1±0.05
	1:16	50.7±0.3	57.9±0.01	61.9±0.2	63.4±0.1
	1:20	50.3±0.3	57.8±0.3	62.7±0.03	63.6±0.1
	1:24		56.7±0.1		
	1:36		58.5±1.9		
	% Si	1:10	23.0±0.3	29.0±1.5	
1:12		19.5±0.2	33.0±0.0	35.6±0.2	35.7±0.1
1:14		21.5±1.2	33.0±1.7	32.2±0.1	32.0±0.3
1:16		20.9±0.3	30.7±0.1	36.5±0.1	36.1±0.1
1:20		20.7±0.1	31.6±0.2	35.5±0.1	36.0±0.1
1:24			31.5±0.2		
1:36			33.2±1.6		

The concentration of oxygen and silicon varies with a change in HMDSO:O₂ ratios. For the coating with a ratio of 1:12, the oxygen concentration is the lowest at 1 µm thickness when compared to the other ratios. However, at 2 µm, 3.5 µm and 5 µm the concentration of oxygen is the highest compared to the other HMDSO:O₂ ratios. Even though the oxygen concentration of sample 1:12 at 1 µm is the lowest, the silicon concentration is also lower and gives Si:O ratio of 2.56 (x=2.56, therefore SiO_{2.56}).

As mentioned in Chapter 5.3.1 it is expected that the Si:O ratio will increase with an increase in oxygen concentration during the deposition. The higher O₂ concentration during the deposition process, the more inorganic-like the coating and therefore reduces the number of organic contaminants, such as hydrogen and carbon. The addition of oxygen during the deposition process can also affect the coating properties. The coatings can range from hydrophobic poly(dimethyl siloxane)-like, to more hydrophilic and nanoporous, and finally towards inorganic-like, hard films with only a trace of hydrocarbons [221]. Using this theory, the SiO_x coated samples can be described as inorganic-like hard films due the minimal presence of hydrocarbons within the coating structure.

For the samples coated at 2 μm, the HMDSO:O₂ ratio 1:10 has the largest Si:O ratio of 1.95 (i.e. x=1.95, so, SiO_{1.95}). This value is very close to that of stoichiometric SiO₂. This somewhat contradicts some of literature which suggests that stoichiometric SiO₂ is achieved at ratios 1:12 or 1:13. However, one study by Michaeli agrees with this and found that a 1:10 ratio produced a very hard quartz-like and crystalline SiO_x coating [108] when deposited onto a methyl methacrylate substrate. Another study by Hegemann et al. [153] contradicts previous research and states that a more quartz-like film is evident at ratios greater than 1:6, with their coatings reaching stoichiometry at Si:O ratio 1:6.7. Both Michaeli and Hegemann used microwave plasma techniques to deposit the coatings, both on to polymeric materials, and both giving different ratios of Si:O for stoichiometric SiO₂. Blanchard et al., [221] reported that using HMDSO in combination with O₂ at a fixed ratio of 1:10 results in a significantly reduced carbon content and a Si:O ratio of 1.91. The deposition method by Blanchard did not use a microwave source to deposit the coatings, but used an RF driven reactor, and Si wafers were used as the substrate. The 1:10 HMDSO:O₂ ratio reported by Michaeli and

Blanchard to give a more inorganic- like coating, agrees with the Si:O ratio found in the EDX analysis of the SiO_x coated HSS. It is evident from the literature that the difference in HMDSO:O₂ ratios, to deposit stoichiometric SiO₂ is largely dependent on the method of deposition and the substrate the coating is being deposited.

Table 6.3 Si:O ratio calculated from the EDX analyses.

HMDSO:O ₂ ratio	Si:O ratio			
	1 μm	2 μm	3.5 μm	5 μm
1:10	2.29±0.03	1.95±0.00	-	-
1:12	2.56±0.02	1.81±0.00	1.81±0.01	1.79±0.00
1:14	2.36±0.07	1.78±0.01	1.83±0.01	1.85±0.02
1:16	2.43±0.02	1.89±0.00	1.69±0.00	1.76±0.01
1:20	2.43±0.00	1.83±0.00	1.77±0.01	1.77±0.01
1:24	-	1.80±0.01	-	-
1:36	-	1.76±0.03	-	-

All coatings deposited with a design thickness of 1 μm have a Si:O ratio that is over stoichiometry. Due to the sensitivity of EDX analysis, it is unlikely that the Si:O ratio calculated is a true representation of the actual ratio because of the lower thickness. The HMDSO:O₂ ratios at 1:12, 1:16 and 1:20 have a decrease in their Si:O ratio, 1.81 to 1.79, 1.89 to 1.76 and 1.83 to 1.77 respectively, as the thickness increases from 2 μm to 5 μm. In contrast, the ratio 1:14 sees an increase in the Si:O ratio from 1.78 to 1.85, with an increase in the thickness from 2 μm to 5 μm.

6.3.3 Focused ion beam (FIB) cross sectional analysis

The FIB cross sectional analysis was carried out on one sample with HMDSO:O₂ ratio 1:20 and a DOE thickness of 2 μm. The uniformity of the coating was analysed from the top surface of the coating through to the substrate. EDX elemental mapping also allowed the composition of the coating to be assessed from the top surface, through to the substrate surface. Figure 6.1 shows the FIB cross sectional analysis of the coating and the corresponding EDX elemental mapping is shown in Figure 6.2.

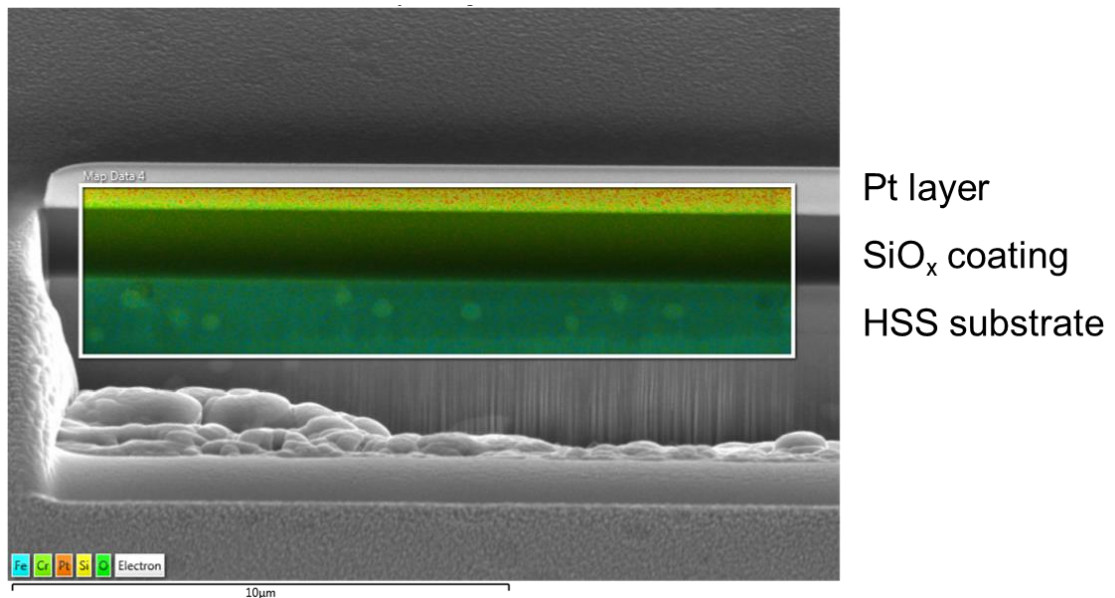


Figure 6.1 Focused ion beam (FIB) cross section of the SiO_x coating with HMDSO:O₂ ratio 1:20 and DOE thickness 2 μm. The EDX elemental mapping area is highlighted.

The EDX analysis shows that the coating is characteristically made up of silicon and oxygen, however there may be some contamination of chrome at the coating and substrate interface. There is also some carbon contamination on the top surface of the coating, however this may be residue from the thin carbon coating applied to the top surface, to ensure there are no charging effects during analysis.

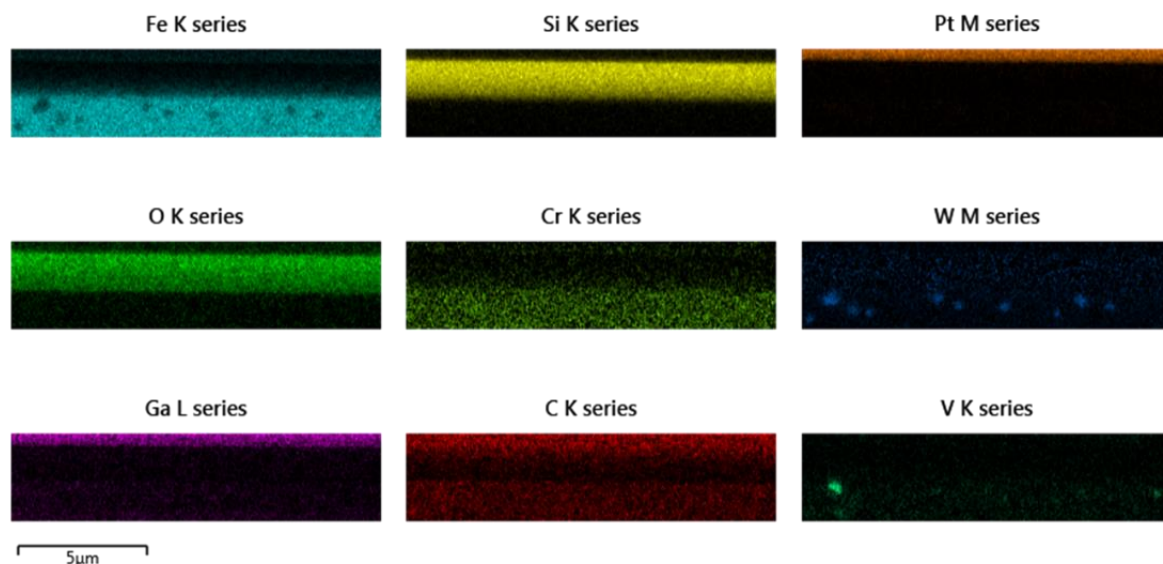


Figure 6.2. Elemental mapping for the FIB cross section of the coating with HMDSO:O₂ ratio 1:20 at 2 μm thickness.

6.3.4 FT-IR analysis

The infrared absorption spectra of the SiO_x coatings was measured using FT-IR spectroscopy. The spectra for the coatings with varying HMDSO:O₂ ratios and a DOE thickness of 2 μm are displayed in Figure 6.3. The oxidised states of the SiO_x coatings have been compared and the peak positions of the Si-O bonds are shown in Table 6.4. The main vibration modes for the Si-O bonding are bending and stretching, both in phase and out of phase, at ~800, 1000 and 1150 cm⁻¹, respectively. The spectra presented show no clear characteristics of silicon oxycarbide (SiO_xC_y) features, most notably at the Si-CH₃ band around 1260 cm⁻¹ [222].

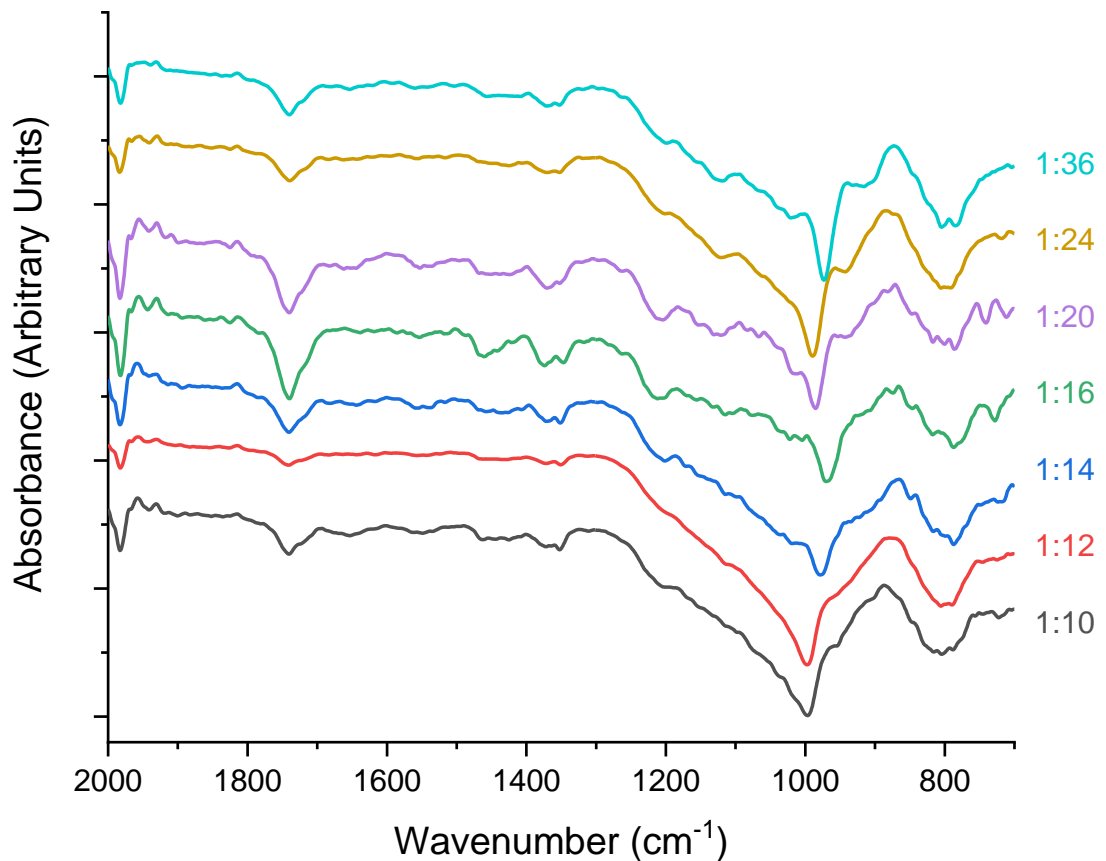


Figure 6.3 FT-IR spectra for the SiO_x coatings with varying HMDSO:O₂ ratios and a DOE thickness of 2 μm. Plotted as a function of wavenumber (cm⁻¹) against absorbance (a.u).

The FT-IR spectra vary with a change in the HMDSO:O₂ ratios. Both coatings 1:20 and 1:36 have a lower intensity when compared to the other HMDSO:O₂ ratios. The dominant peak at around 1000 cm⁻¹, with a shoulder around 1200 cm⁻¹ can be assigned to the asymmetric stretching of siloxane (Si-O-Si). The peak positions for the asymmetric stretching vary with HMDSO:O₂ ratios. Both coatings 1:10 and 1:12 exhibit the same peak position, both in phase and out of phase, whereas the other coatings exhibit a shift towards lower frequency. As discussed in section 4.6.2, the shift in the wavenumber are indicative of the change in the stoichiometry of the SiO_x coatings and the increase in oxygen concentration [213]. Stoichiometric silica (SiO₂) gives an asymmetric peak at around 1080 cm⁻¹ [136] in phase, which is a higher frequency than the observed

frequencies for the SiO_x coatings. However, the out of phase position is around 1203 cm⁻¹, which is similar to the SiO_x coatings, suggesting that the coatings are not purely stoichiometric.

Table 6.4 FT-IR vibration modes for SiO_x coated HSS with varying HMDSO:O₂ ratios at a DOE thickness of 2 μm.

HMDSO:O ₂ ratio	Peak position (cm ⁻¹)		
	Si-O bending (cm ⁻¹)	Si-O-Si asym. Stretching in phase (cm ⁻¹)	Si-O-Si asym. Stretching out of phase (cm ⁻¹)
1:10	806	1000	1209
1:12	799	1000	1209
1:14	794	979	1207
1:16	791	964	1219
1:20	796	984	1204
1:24	804	992	1209
1:36	794	974	1209

A change in the peak position of the Si-O-Si stretching band to higher frequency and a shift of the Si-O-Si bending band to lower frequency can be indicative of a decrease in the stress of the coating [223]. The Si-O bending band decreases with an increase in the HMDSO:O₂ ratio from 1:10-1:16, and then increases slightly with a continued increase in HMDSO:O₂ ratio for samples 1:20 and 1:24. The peaks at around 1720 cm⁻¹ corresponds to C=O stretching for an aliphatic ketone. The peaks are observed for each coating due to residual acetone from the cleaning of the coating surface prior to the FT-IR analysis.

6.3.5 XPS analysis

Atomic concentrations for Si, O and C and the atomic ratio of Si:O have been measured using XPS analysis. SiO_x samples at a thickness of 2 μm were

analysed using with and without argon bombardment. A survey spectrum and three high resolution spectra of O 1s, C 1s and Si 2p, were recorded for each HMDSO:O₂ ratio. The high resolution spectra were fitted using a Gaussian fitting and a U 2 Tougaard background.

The data without the argon ion bombardment gives a large adventitious carbon peak, therefore it was necessary to use argon cluster ions to etch and clean the surface of the sample to remove any contamination. Cleaning the surface allowed for a more accurate calculation of the Si:O ratios, as the carbon within the SiO_x coating was negligible. The survey spectra for the XPS analysis before surface cleaning were used to calculate the atomic concentration of Si, O and C (Table 6.5). The atomic concentration for carbon is extremely high, therefore the Si:O ratio cannot be determined accurately from this data.

Table 6.5. The Si, O and C concentrations of the SiO_x coatings from XPS data analyses before Ar cluster bombardment, with respect to the HMDSO:O₂ ratio.

HMDSO:O ₂ ratio	% Si	% O	% C
1:12	18.2	27.7	52.5
1:14	17.2	26.0	54.9
1:16	22.2	33.4	43.2
1:20	12.0	18.2	63.6
1:36	20.6	31.2	46.0

This analysis was repeated using Ar bombardment.

Figure 6.4 shows the survey spectrum for the samples 1:12, 1:14, 1:16, 1:20 and 1:36 at a 2 μm thickness. The high resolution spectra for the three elements are shown in Figure 6.5, Figure 6.6 and Figure 6.7, with component fittings. The

highest Si:O ratio is sample 1:12, and the lowest is from sample 1:14. The lowest Si:O ratio agrees with the results from EDX, with 1:14 having the lowest ratio, whereas, the highest ratio is from sample 1:16. The values for the Si:O ratios from both XPS and EDX analysis are comparable to one another allowing the EDX values to be accepted. The only difference between the two analysis techniques is the sensitivity with EDX able to look at submicron layers, and XPS focussing in the nanometre range.

The binding energy (eV) for the Si 2p peak varies slightly with a change in HMDSO:O₂ ratio. There is a single, symmetrical Si 2p peak for all ratios. Curve fitting of the peaks using CasaXPS software was used to determine the bonding present within the coating. A single Gaussian curve was fitted to the symmetric peaks for the Si 2p and O 1s high resolution spectra, using a U2 Tougaard background. This fitting shows that the bonding nature of the coatings suggest that Si and O is predominantly in the form Si(-O)₄, and indicates the presence of an O-Si-O network. This is also in agreement with the O 1s high resolution spectra, as there is a single peak which also indicates the presence of the O-Si-O network.

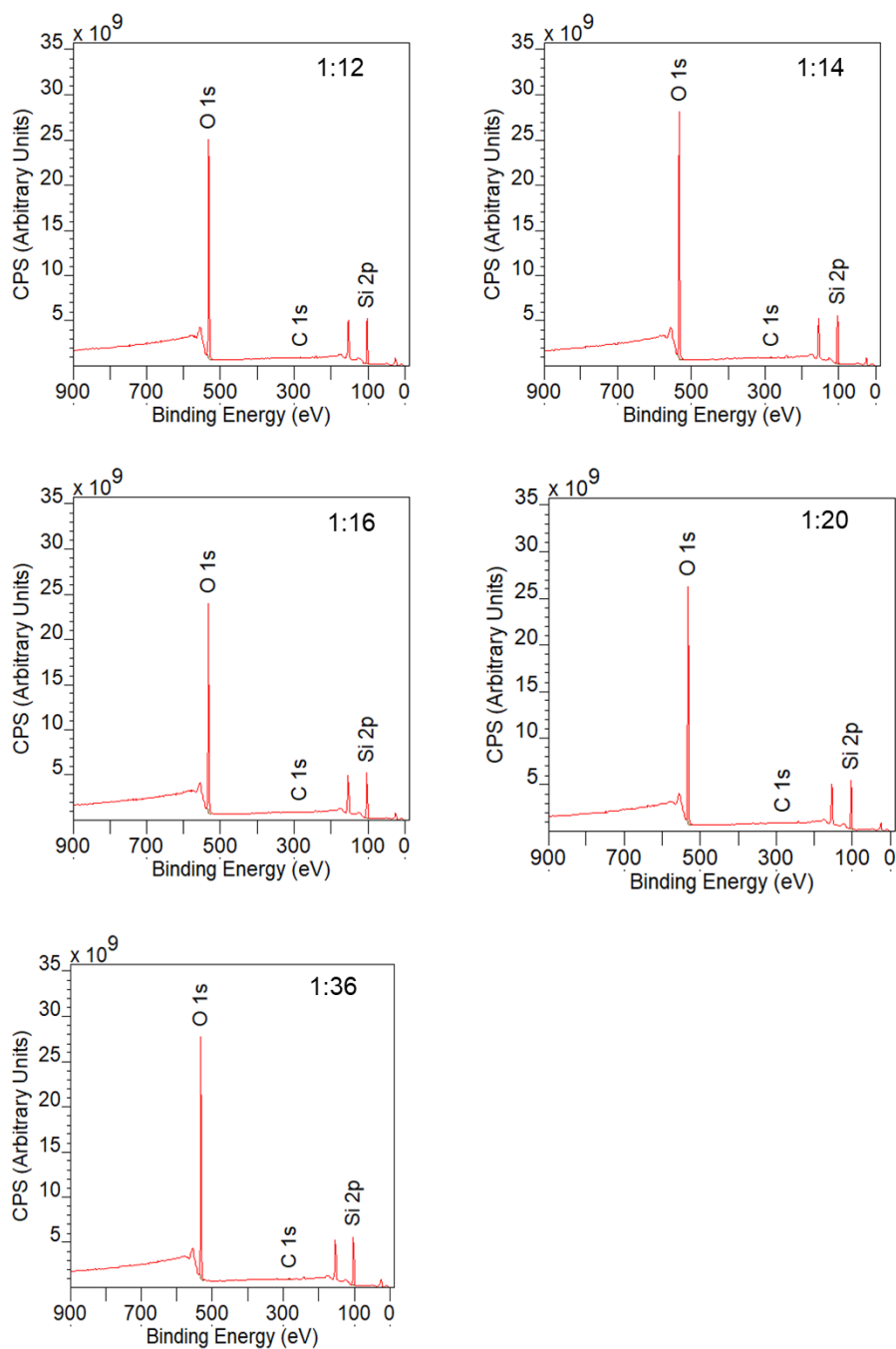


Figure 6.4 XPS survey spectra for the SiO_x coated samples at varying HMDSO:O₂ ratios. The undefined peak is Si 2s and is not included in the high resolution spectra.

The sharp peaks from the XPS survey spectra suggest that there may be some crystallinity within the coatings [224]. This crystallinity may arise from the SiO₂-like structure formed during the coating process. The microstructure and crystallinity of the coating is explored further in the XRD section 6.4.1.

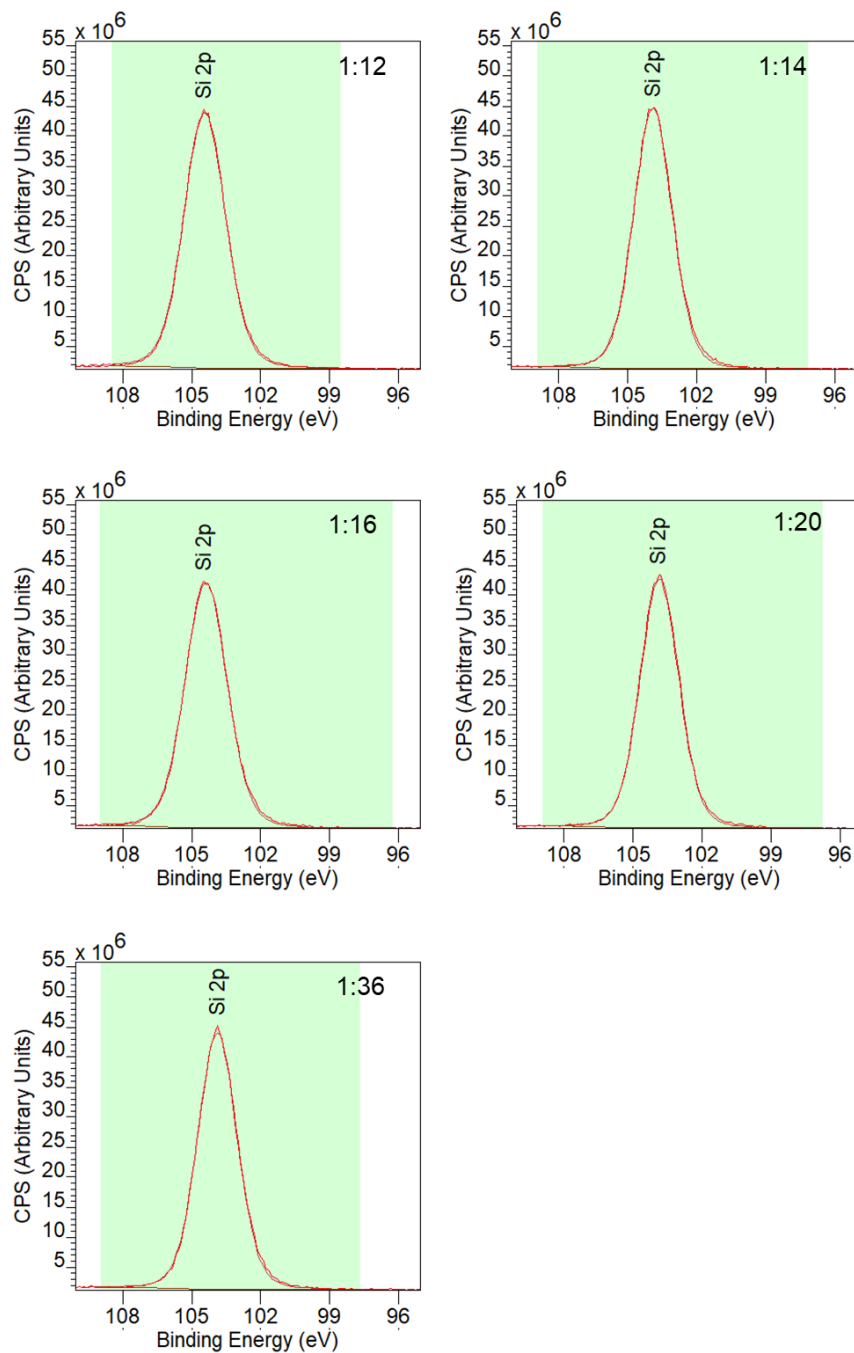


Figure 6.5 The XPS Si 2p high resolution spectra for the SiO_x coated samples at varying HMDSO:O₂ ratios. The spectra are fitted with Gaussian curves using a U2 Tougaard background.

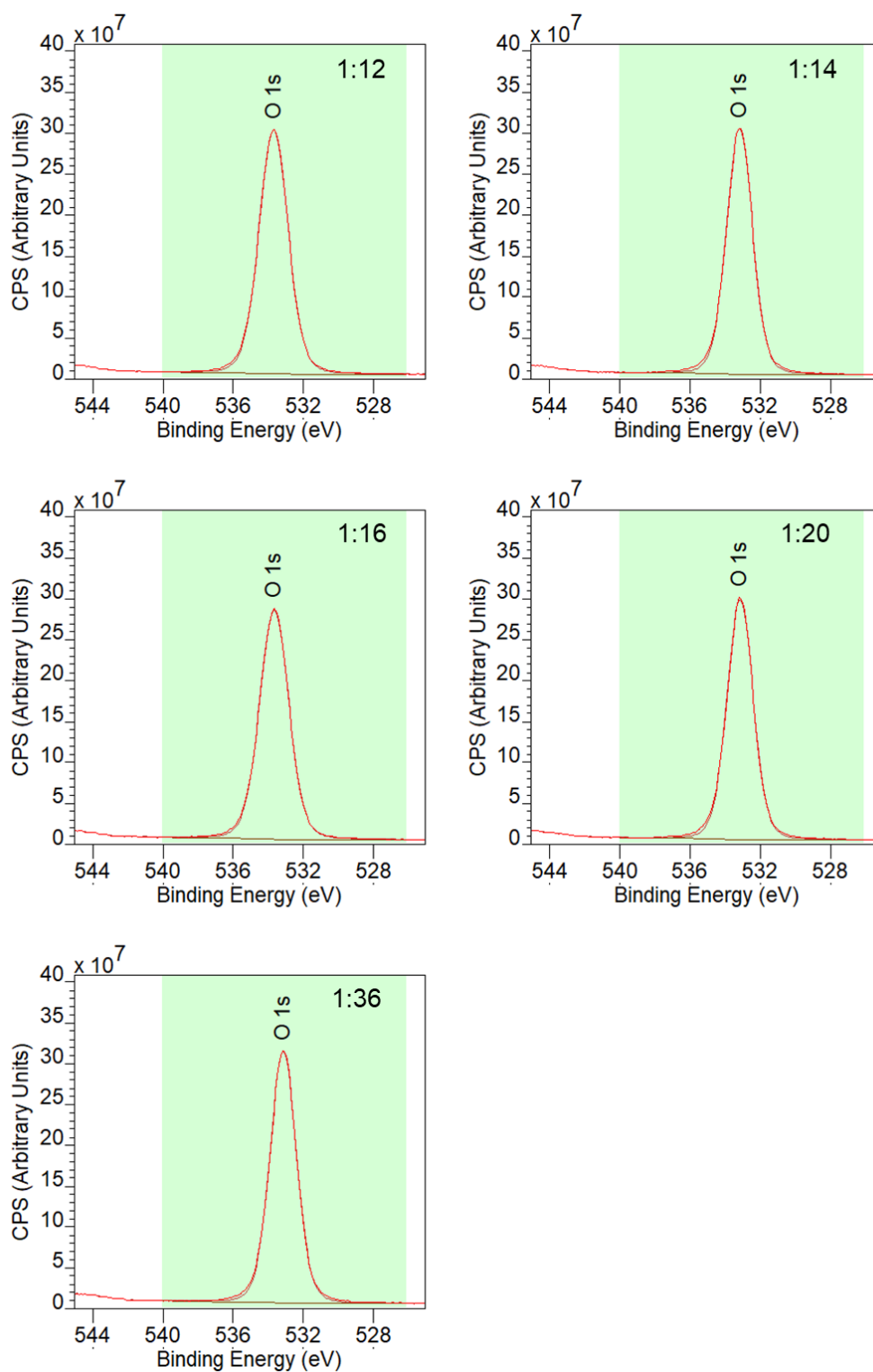


Figure 6.6 The XPS O 1s high resolution spectra with fittings for the SiO_x coated samples at varying HMDSO:O₂ ratios. The spectra are fitted with Gaussian curves using a U2 Tougaard background.

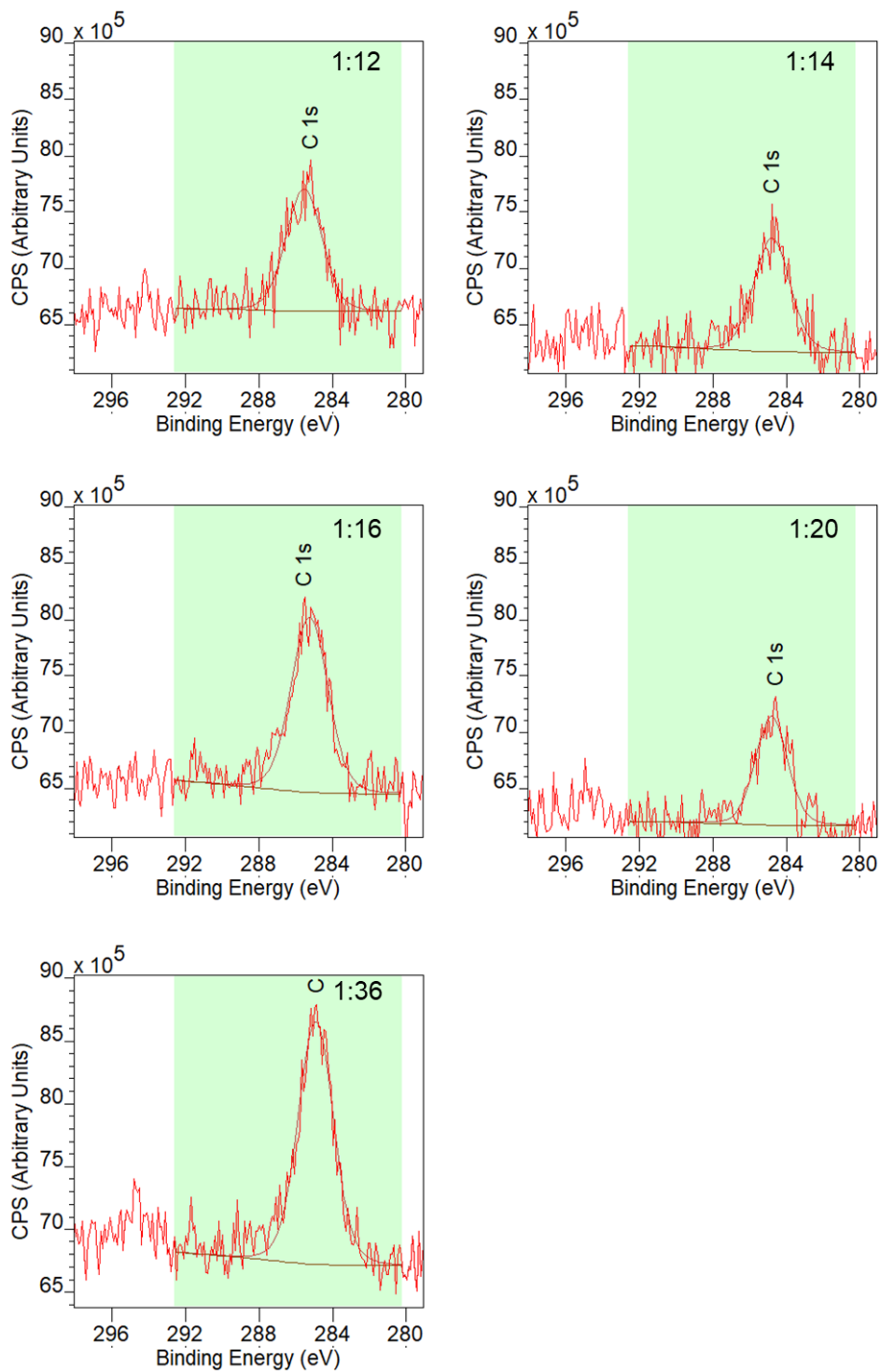


Figure 6.7 The XPS C 1s high resolution spectra with fittings for the SiO_x coated samples at varying HMDSO:O₂ ratios. The spectra are fitted with Gaussian curves using a U2 Tougaard background.

The binding energies and FWHM are presented in Table 6.6. For stoichiometric SiO₂, the Si is bonded to four neighbouring oxygen atoms in a tetragonal structure [143]. The Si 2p position for quartz has a binding energy of 103.4 eV

[225]. The binding energy (eV) of the Si 2p peak for the coating with HMDSO:O₂ ratios 1:12 and 1:16 shift to a higher binding energy (104.4 eV), when compared to the other HMDSO:O₂ ratios. This peak can be assigned to the Si-O bond (SiO₂). For the five samples analysed, the high resolution spectra peak for Si 2p gives a symmetrical single peak, allowing just one sub-peak to be fitted (Figure 6.5). Similarly, with the O 1s high resolution spectra, a single symmetrical peak is analysed for all the samples (Figure 6.6). This allows one sub peak fitting, centred around the binding energies listed above. The samples with HMDSO:O₂ ratio 1:12 and 1:16, have a binding energy of 533.7 eV, and the samples 1:14, 1:20 and 1:36 have binding energies 533.2, 533.1 and 533.1 eV, respectively. When comparing the Si 2p and O 1s peaks, it is found that the binding energies present the same variation tendency in all the samples.

Table 6.6 The binding energies and full width at half maximum (FWHM) of Si 2p and O1s high resolution spectra for SiO_x coatings with design thickness 2 µm.

HMDSO:O ₂ ratio	Binding Energy (eV)		FWHM	
	Si 2p	O 1s	Si 2p	O 1s
1:12	104.4	533.7	2.13	1.94
1:14	103.9	533.2	1.98	1.73
1:16	104.4	533.7	2.16	1.94
1:20	103.9	533.1	1.99	1.74
1:36	103.9	533.1	2.01	1.77

Ma et al [226] reported that increasing the oxygen content, increased the binding energies for both the Si 2p and O 1s peaks. A shift of the Si:O ratio from 2 to 1.6 saw a shift in binding energies from 104.4 eV to 104.2 eV. When the stoichiometry

is close to that of SiO₂, the component of Si 2p high resolution peak represents almost all of the signal [227]. Ma et al, also reported that the sub-peak from the Si 2p component for the sample with Si:O ratio of 2, is predominantly at binding energy 533.3 eV. This binding energy is comparable to the ones observed from the XPS samples in Table 6.6. However, although the binding energies are comparable to those of stoichiometric SiO₂, the observed Si:O ratios for samples 1:14, 1:16, 1:20 and 1:36 are slightly lower, with sample 1:12 having a ratio of 2. The sample with ratio 1:20, gives a Si:O ratio of 1.80 and Si 2p and O 1s binding energies of 103.9 eV and 533.1 eV, respectively. This shift towards a lower binding energy, agrees with the results reported by Ma et al [226].

The difference in binding energies, compared to that of tetragonal quartz may be due to the crystalline structure of the coatings. The higher shift of binding energy for the Si 2p peak may be a result of the coating being crystalline in nature, and therefore more similar to silica quartz, where c-silica is made up of repeating patterns of silicon and oxygen [99]. The downfield shift from Si 2p quartz (103.4 eV) is due to Si bonding with a methyl group (Si-CH₃), due to carbon having a lower electronegativity than oxygen [228]. As there is no downward shift of binding energies to lower than 103.9 eV for the Si 2p peak, it can be confirmed that there is little to no Si-CH₃ or Si-C bonding.

The FWHM values for the Si 2p peaks vary, with samples 1:12 and 1:16 having similar values of 2.13 and 2.16 respectively. Samples 1:14, 1:20 and 1:36 have slightly lower FWHM values of 1.98, 1.99 and 2.01, respectively.

The amount of carbon present in the coatings, after argon ion bombardment, is negligible. The sample with the highest carbon content is 1:16. It would be expected that the coating with the highest oxygen concentration during the

deposition process would result in a coating with the least amount of carbon. C 1s peaks and component fittings are shown in Figure 6.7.

The oxygen, silicon and carbon concentrations were calculated from the high resolutions fittings and are presented in Table 6.7, with the Si:O ratios. The silicon concentration increase with an increase in HMDSO:O₂ ratio from 33.2% for coating 1:12 to 33.9% for coating 1:36. The oxygen concentration decreases with an increase in HMDSO:O₂ ratio, therefore leading to a decrease in the Si:O ratios.

Table 6.7 The Si, O and C concentrations and Si:O ratio of the SiO_x coatings from XPS survey spectra after Ar bombardment, with respect to HMDSO:O₂ ratio.

HMDSO:O ₂ ratio	% Si	Std Dev	% O	Std Dev	% C	Std Dev	Si:O ratio
1:12	33.2	0.001	66.5	0.002	0.3	0.001	2.00
1:14	33.3	0.001	66.4	0.002	0.3	0.001	1.99
1:16	33.6	0.002	65.5	0.002	0.9	0.002	1.95
1:20	33.9	0.001	65.8	0.002	0.7	0.001	1.94
1:36	33.9	0.002	65.7	0.002	0.4	0.002	1.94

6.4 Microstructural analysis of the SiO_x coatings

The microstructure of the coatings was investigated using XRD and Raman spectroscopy. XRD allowed the apparent crystalline structure to be explored further and the crystallite size and microstructure strain to be theoretically calculated. It is important to study the microstructure of the coatings as it can differ from that of the bulk material, with the same chemical composition. XRD can be applied to characterise the crystalline properties of a coating, and also to determine any residual stresses.

6.4.1 X-ray diffraction (XRD)

The microstructural characteristics were investigated using XRD analyses for each sample with varying HMDSO:O₂ ratio and different thicknesses. The XRD diffractograms for each sample are almost identical in nature and vary only by the intensity of the peaks. Typically, SiO_x coatings are predominantly amorphous [229]–[231] (except for SiO₂ in the quartz form which is crystalline), however the spectra give sharp peaks with low noise suggesting that the SiO_x coatings deposited using MW-PECVD are crystalline.

The XRD data, including 2θ values, d -spacing and lattice constant are displayed in Table 6.8. The XRD diffraction patterns for the SiO_x coatings with varying HMDSO:O₂ ratios, with DOE thicknesses of 1 μm , 2 μm , 3.5 μm and 5 μm are shown in Figure 6.8, Figure 6.9, Figure 6.10 and Figure 6.11, respectively. From the diffraction patterns there are intense and broad peaks corresponding to the iron (Fe) present within the HSS substrate. The predominant phase of the SiO_x coating is from cubic SiO₂ (ICDD 01-076-6230), characterised from the ICDD database. From the presence of sharp, well-defined peaks in the XRD patterns for all HMDSO:O₂ ratios and DOE thicknesses, it is evident that the coatings are crystalline in nature.

Table 6.8 Calculated lattice constant (a) from XRD diffraction data at varying HMDSO:O₂ ratios and a DOE thickness of 2 μm.

HMDSO:O ₂ ratio	SiO _x (DOE 2 μm)			ICDD reference 01-076-6230		
	2θ (°)	hkl planes	d- spacing (Å)	Lattice constant, a (Å)	Lattice constant (Å)	2θ (°)
1:10	39.98	111	2.253	3.902	a = 3.930	39.69
	46.46	200	1.953			46.16
	72.51	300	1.303			72.03
	82.07	311	1.173			81.10
1:12	40.10	111	2.247	3.894		
	46.60	200	1.947			
	72.66	300	1.300			
	82.18	311	1.172			
1:14	39.69	111	2.269	3.912		
	46.19	200	1.964			
	72.33	300	1.305			
	81.90	311	1.175			
1:16	39.80	111	2.263	3.909		
	46.34	200	1.958			
	72.49	300	1.303			
	82.01	311	1.174			
1:20	39.93	111	2.256	3.903		
	46.44	200	1.954			
	72.56	300	1.302			
	82.09	311	1.173			
1:24	39.99	111	2.253	3.900		
	46.50	200	1.952			
	72.57	300	1.302			
	82.12	311	1.173			
1:36	39.96	111	2.254	3.903		
	46.47	200	1.953			
	72.50	300	1.303			
	82.05	311	1.174			

Comparing the experimental results, and the data taken from ICDD reference 01-076-6230 there are slight differences between the positions of the peaks and also the calculated lattice constant, a . These differences may be caused by the manifestation of a defect in the cell of the crystal, which in turn leads to local changes within the lattice parameters. The peak positions of the XRD spectra are shifted to slightly higher 2θ values. The shift to higher angles can be caused by numerous changes within the crystal structure including; interstitial sites, vacancies, local structure transformations, which can have an effect on the lattice parameters. However, a shift to higher 2θ angles may also be due to instrumental errors and the height position of the sample within the sample holder. As the shift in 2θ is consistent with all coatings, it can be concluded that it is due to a sample height issue.

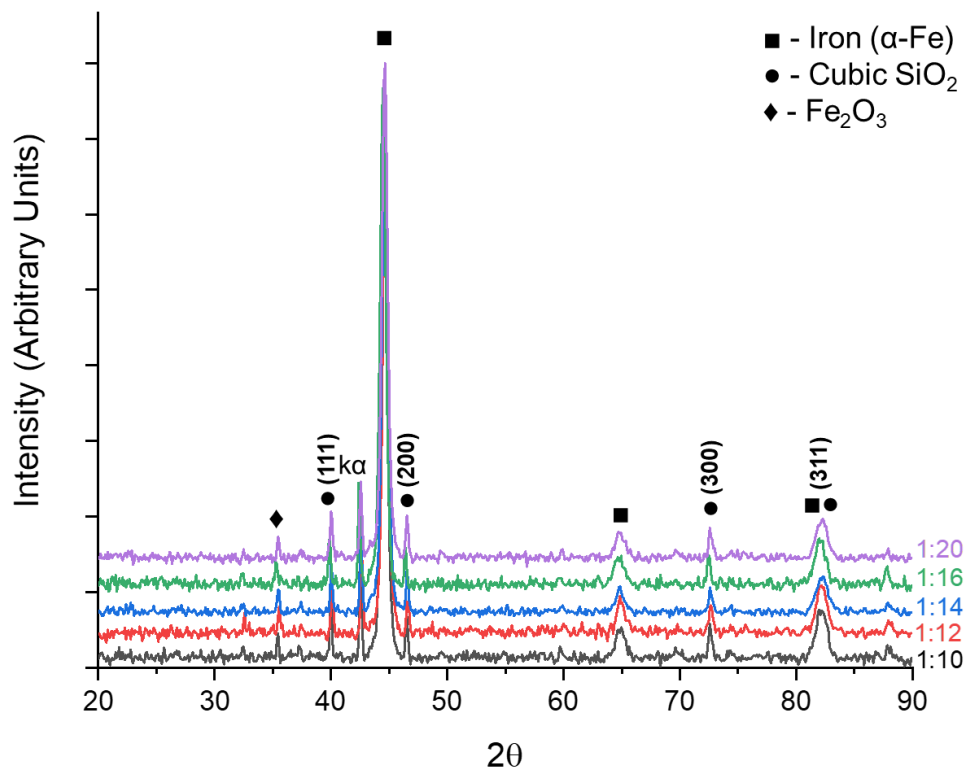


Figure 6.8 The stacked XRD diffractograms for samples with HMDSO:O₂ ratios 1:10, 1:12, 1:14, 1:16 and 1:20, with a DOE thickness of 1 μm.

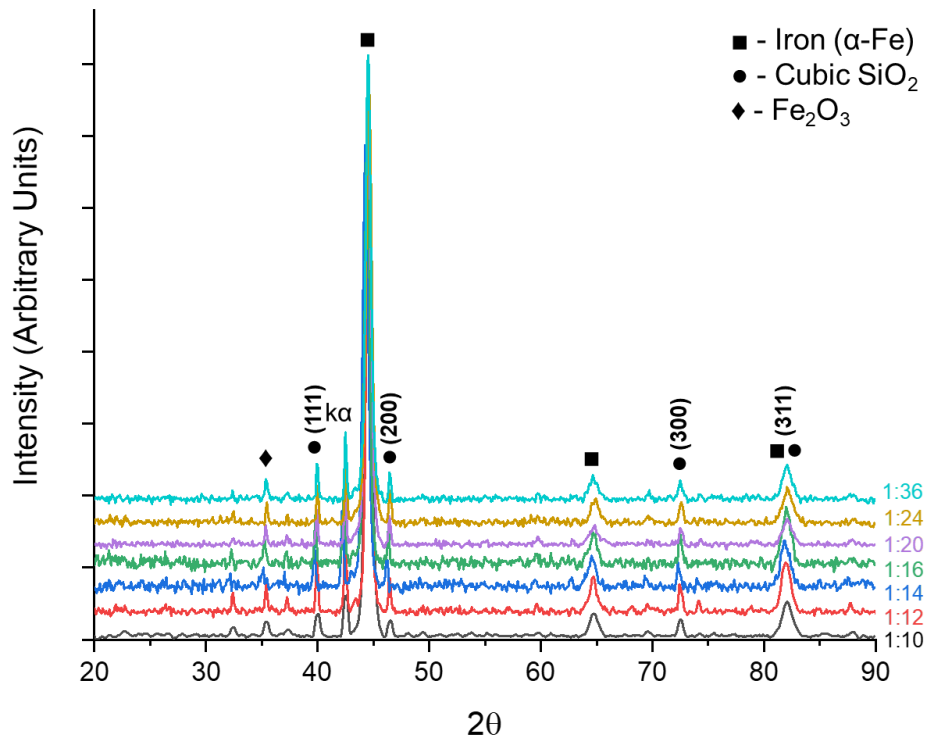


Figure 6.9 The stacked XRD diffractograms for samples with HMDSO:O₂ ratios 1:10, 1:12, 1:14, 1:16, 1:20, 1:24 and 1:36 with a DOE thickness of 2 μm.

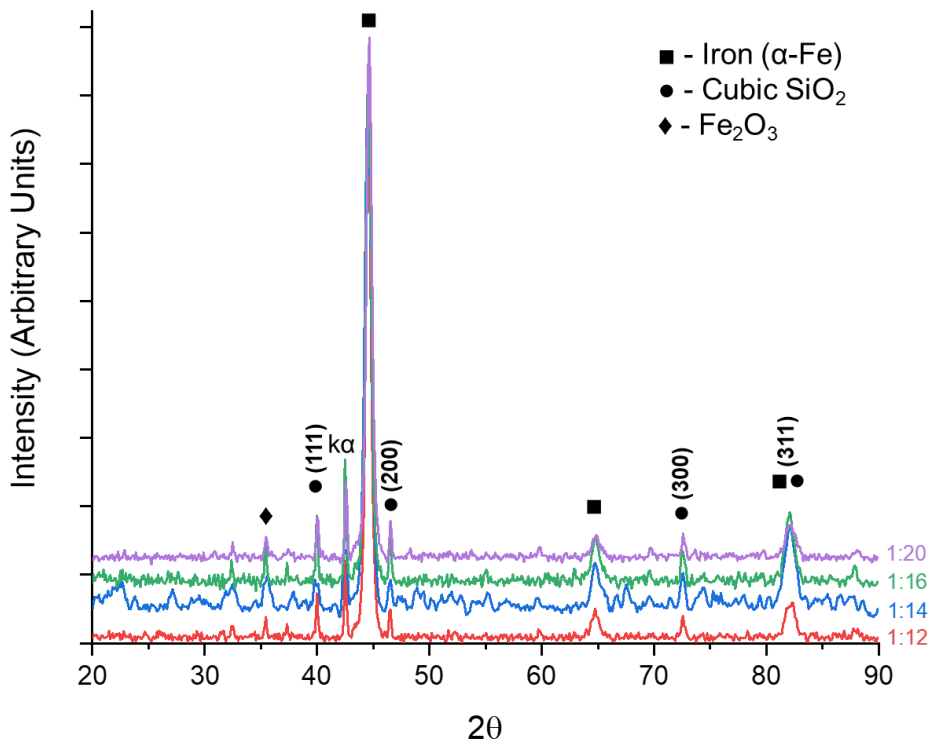


Figure 6.10 The stacked XRD diffractograms for samples with HMDSO:O₂ ratios 1:12, 1:14, 1:16 and 1:20, with a DOE thickness of 3.5 μm.

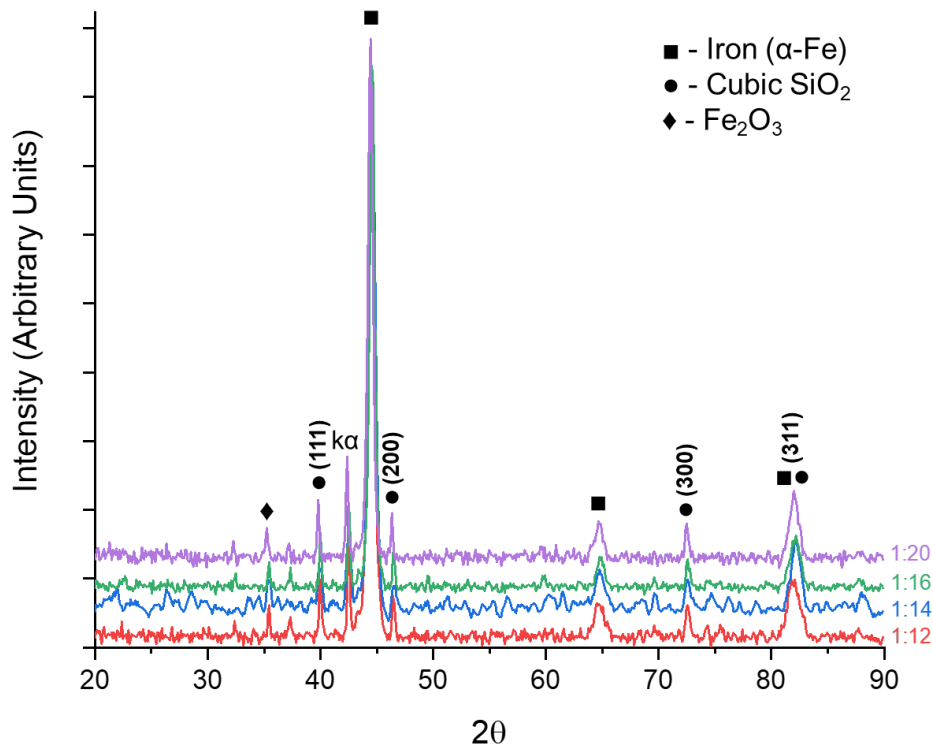


Figure 6.11 The stacked XRD diffractograms for samples with HMDSO:O₂ ratios 1:12, 1:14, 1:16 and 1:20, with a DOE thickness of 5 μ m.

The peaks at $2\theta = 44.5^\circ$, 64.8° and 82.1° are assigned to α -Fe in the cubic phase (ICDD 01-080-3817). The SiO_x peaks at $2\theta = 40.0^\circ$, 46.5° , 72.6° and 82.1° can be assigned to cubic SiO_2 (ICDD 01-076-6230) and indexed as the (111), (200), (300) and (311) plane diffractions. For the broad peak at 82.1° , there is a crossover from the Fe and SiO_x , which leads to the peak broadening. The peak at 42.5° has been assigned as a $K\alpha$ peak, which is produced from a transition of an electron, caused by the Fe peak at 44.5° . The peak at around $2\theta = 32.5^\circ$ has been unable to be identified. This extra peak may be due to contamination of the coating surface and is explained in further detail in section 5.3.2.

The small peak at $2\theta = 35.5^\circ$ has been assigned to iron oxide (Fe_2O_3), which may be present due to the formation of iron oxide at the surface of the substrate. This iron oxide may be formed on the surface pre-deposition, through exposure of the HSS substrate to air and moisture or could be a resultant corrosion product

at the surface of the substrate. The iron oxide may form due to defects or imperfections within the coatings, which in turn allow moisture and air through to the surface of the substrate and therefore resulting in oxidation of the iron within the HSS. This is explored further in Chapter 7.

Due to the nature of the diffractograms, with sharp peaks given for the SiO_x coating, and no presence of amorphous SiO_2 reported to be around $2\theta=20-25^\circ$ [232], [233], the coatings show a crystalline structure. These findings, however, largely disagree with the literature. Jeong et al [234] reported that a chemically processed SiO_x coating material gave broad XRD peaks, showing an amorphous structure with low levels of crystallinity. Similarly, Hernandha [235] reported strong XRD peaks relating to a cubic-structure Si, but no distinct diffraction data from the SiO_x coatings, due to having low crystallinity.

Cao et al, [236] have reported a similar finding, with a 2-phase, nanocrystalline and amorphous Si peak, which was dispersed throughout an amorphous SiO_x matrix. The diffraction patterns from the SiO_x coatings suggest that they have a crystalline structure, contradicting much of the literature. The crystallinity of the coatings can be further investigated by using the 2θ values from the diffraction patterns, and the full width at half maximum (FWHM) values. Using these values, it is possible to calculate the SiO_x crystallite sizes, using the Scherrer equation. The crystallite size can also be determined using a Williamson-plot, which also provides information on the stress-strain of the coatings. Calculating the crystallite sizes and the strain of the coatings provides a theoretical approach to the microstructure of the coatings.

6.4.2 Calculation of the crystallite size using the Scherrer equation

It is important to understand the crystallite size within a coating structure as it can affect the structural, mechanical, electrical and corrosion properties of a coating. The crystallite size can be affected by the deposition parameters, including temperature, pressure and plasma conditions. One of the major effects that the crystallite size has on a coating is its photoactivity.

The structure of SiO_x coatings from the XRD diffractograms have shown that the coatings, have a crystalline nature and do not have the presence of an amorphous SiO₂ peak. The XRD spectra 2θ values, and the FWHM for the SiO_x coatings are used to calculate the average crystallite sizes within the SiO_x microstructure. Due to the growth of polycrystalline clusters, the crystallite size of a particle is not the same as the particle size [237]. The crystallite size is the smallest undistorted region in a crystal and is different to the particle size and in some cases, may differ from the grain size.

6.4.2.1 A comparison of the average crystallite size with the HMDSO:O₂ ratios

Table 6.9 gives the theoretically calculated values of the average crystallite sizes (nm), strain and dislocation densities for all HMDSO:O₂ ratios and thicknesses. The 2θ values and FWHM values, assigned to SiO_x and indexes of (111), (200), (300), and (311) are used to calculate the average crystallite sizes.

The average crystallite size varies with the HMDSO:O₂ ratio and also the thickness of the coatings. For coatings deposited at 1 μm, 2 μm, 3.5 μm and 5 μm respectively. For the coatings deposited at a design thickness of 1 μm, the largest average crystallite size is from the SiO_x coating with HMDSO:O₂ ratio 1:20, with a size of 30.3 nm. The smallest average crystallite size is from the

sample 1:12 with a size of 25.7 nm. There is an increase in the crystallite size from ratio 1:12 to 1:20, however the ratio at 1:10 exhibits a larger crystallite size of 29.2 nm, when compared to coatings 1:12 and 1:14 (28.5 nm).

Table 6.9. Average crystallite sizes (nm), strain and dislocation densities of the SiO_x coatings with varying HMDSO:O₂ ratios and varying DOE thicknesses, calculated from the Scherrer equation.

HMDSO: O₂ ratio	Average crystallite size (nm)	Error (nm)	Strain ϵ ($\times 10^{-3}$)	Dislocation density (10^{15} lines/m²)
1 μm				
1:10	29.2	0.6	1.7	3.6
1:12	25.7	0.7	1.7	3.3
1:14	28.5	0.6	1.8	4.1
1:16	30.0	0.6	1.6	3.2
1:20	30.3	0.6	1.8	3.9
2 μm				
1:10	24.2	0.5	1.8	3.5
1:12	25.9	0.5	1.7	3.2
1:14	28.0	1.0	1.6	3.1
1:16	31.5	0.6	1.5	2.9
1:20	28.1	0.7	1.7	3.3
1:24	26.7	0.6	1.8	3.6
1:36	27.9	0.7	1.7	3.2
3.5 μm				
1:12	28.9	0.8	1.6	2.9
1:14	30.8	1.2	1.6	3.3
1:16	26.7	0.6	1.6	2.9
1:20	30.7	0.8	1.6	3.2
5 μm				
1:12	23.7	0.7	2.0	4.8
1:14	29.4	1.1	1.5	2.7
1:16	28.5	0.6	1.7	3.5
1:20	29.3	0.6	1.5	2.7

The coatings with a DOE thickness of 2 μm exhibit a similar pattern, however there is now an increase in the crystallite size from ratio 1:10 through to 1:16, varying from 24.2 nm to 31.5 nm. The 1:20 coating decreases in crystallite size when compared to 1:16, with a size of 28.1 nm. There is also a decrease in the crystallite size of this sample with coating thickness varying from 1 μm to 2 μm . The coatings at ratio 1:24 and 1:36 have an average crystallite size of 26.7 nm and 27.9 nm, respectively.

The coatings deposited with a design thickness of 3.5 μm and 5 μm show a slightly different trend in the crystallite size when comparing the HMDSO:O₂ ratios. For both thicknesses there is an increase in the crystallite size from ratio 1:12 to 1:14, from 28.9 nm to 30.8 nm, and 23.7 nm to 29.4 nm, for thickness 3.5 μm and 5 μm respectively. The crystallite size then decreases with an increase in ratio to 1:16, to 26.7 nm at 3.5 μm and 29.3 nm at 5 μm , which then sees another increase in crystallite size at ratio 1:20. The ratios 1:12, 1:14 and 1:20 all see a reduction in the crystallite size, with an increase in thickness from 3.5 μm to 5 μm . The coating at 1:16, however sees a slight increase in the crystallite size.

Overall, all HMDSO:O₂ ratios and thicknesses have a variation in the crystallite sizes, but there is no distinct trend from the current dataset. The crystallite size is further explored and calculated from Williamson-Hall plots in the subsequent section.

The coatings with a DOE thickness of 2 μm exhibit a similar pattern, however there is now an increase in the crystallite size from ratio 1:10 through to 1:16, varying from 24.2 nm to 31.5 nm. The 1:20 coating decreases in crystallite size when compared to 1:16, with a size of 28.1 nm. There is also a decrease in the crystallite size of this sample with coating thickness varying from 1 μm to 2 μm .

The coatings at ratio 1:24 and 1:36 have an average crystallite size of 26.7 nm and 27.9 nm, respectively.

The coatings deposited with a design thickness of 3.5 μm and 5 μm show a slightly different trend in the crystallite size when comparing the HMDSO:O₂ ratios. For both thicknesses there is an increase in the crystallite size from ratio 1:12 to 1:14, from 28.9 nm to 30.8 nm, and 23.7 nm to 29.4 nm, for thickness 3.5 μm and 5 μm respectively. The crystallite size then decreases with an increase in ratio to 1:16, to 26.7 nm at 3.5 μm and 29.3 nm at 5 μm , which then sees another increase in crystallite size at ratio 1:20. The ratios 1:12, 1:14 and 1:20 all see a reduction in the crystallite size, with an increase in thickness from 3.5 μm to 5 μm . The coating at 1:16, however sees a slight increase in the crystallite size.

Overall, all HMDSO:O₂ ratios and thicknesses have a variation in the crystallite sizes, but there is no distinct trend from the current dataset. The crystallite size is further explored and calculated from Williamson-Hall plots in the subsequent section.

The strain of the coatings varies between 1.5 and 2.0 $\times 10^{-3}$ for all SiO_x coatings, and a dense array of dislocations are shown to be present within the coating structure. The dislocation densities also vary between 2.7 $\times 10^{15}$ and 4.8 $\times 10^{15}$ lines m⁻², which is below the upper limit of dislocation density (10^{16} m⁻²) [238]. Dislocations within distorted crystals may lead not only to the peak broadening of the XRD spectra, but also to anisotropy in peak width [239]. A comparison of the dislocation densities and the strain of the coatings, suggests that there is a direct correlation and that a higher strain may lead to a higher dislocation density, as shown in Figure 6.12.

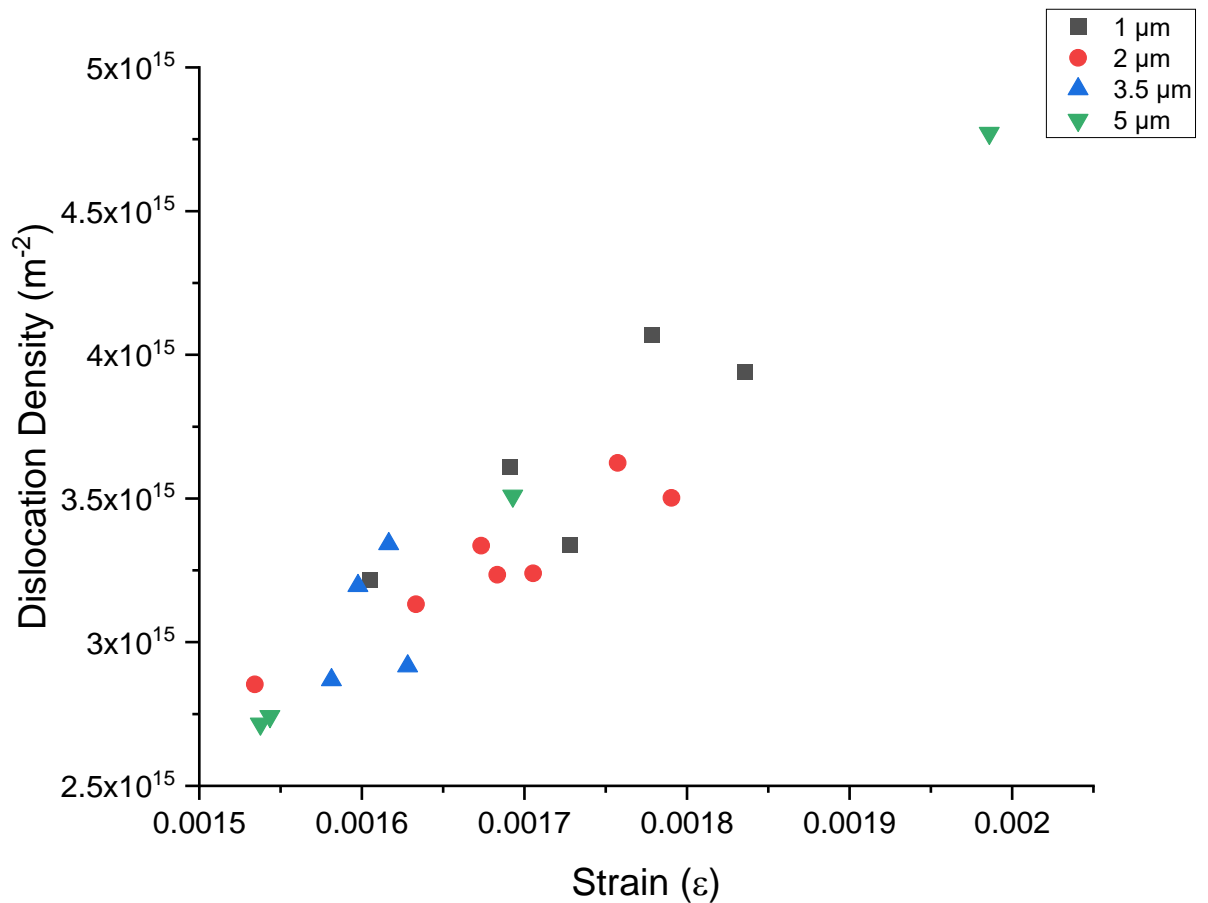


Figure 6.12 The micro strain (ϵ) of the coatings calculated from the Scherrer equation increases with an increase in the dislocation density (m^{-2}) of the SiO_x coatings, with DOE thicknesses of $1 \mu\text{m}$, $2 \mu\text{m}$, $3.5 \mu\text{m}$ and $5 \mu\text{m}$.

The increase of dislocation density with an increase in the micro strain is present for all DOE thicknesses of the SiO_x coatings. The coatings deposited with a DOE thickness of $3.5 \mu\text{m}$ show the smallest strain compared to the coatings at other deposition thicknesses. The largest strain of 4.8×10^{-3} and dislocation density of 2.0×10^{-3} is exhibited by the SiO_x coating with ratio 1:12 at a thickness of $5 \mu\text{m}$.

The average crystallite sizes of the coatings at DOE thickness of $2 \mu\text{m}$ has been compared with the nanoindentation results to explore whether the hardness and elastic modulus are dependent on the size of the crystallites. The results are displayed in Table 6.10.

Table 6.10 A comparison of the average crystallite sizes of the HMDSO:O₂ ratio with a DOE thickness of 2 μm, with the hardness and elastic modulus from nanoindentation results.

HMDSO:O ₂ ratio	Average crystallite size (nm)	Hardness (GPa)	Young's modulus (GPa)
HSS	-	8.4	
1:10	24.2	5.8 ± 0.9	100.4 ± 1.7
1:12	25.9	5.1 ± 0.5	93.3 ± 1.7
1:14	28.0	4.6 ± 0.2	82.0 ± 1.3
1:16	31.5	5.0 ± 0.4	83.6 ± 1.6
1:20	28.1	5.9 ± 0.8	97.4 ± 1.4
1:24	26.7	5.9 ± 0.5	99.3 ± 1.3
1:36	27.9	5.7 ± 0.5	93.1 ± 1.9

The relationship between average crystallite size and the hardness of the SiO_x coatings, there was no identifiable trend between the hardness (GPa) of the coatings and the crystallite sizes (nm). The increase in the crystallite size from 24.2 nm to 31.5 nm sees a slight decrease in the hardness of the coatings. However, the crystallite sizes at 27.9 nm, 28.0 nm and 28.1 nm all have a different hardness, even though the crystallite sizes are comparable. Thus, the crystallite size of the SiO_x coatings does not have an impact on the hardness.

6.4.2.2 A comparison of the average crystallite sizes with varying thicknesses

The average crystallite sizes of the samples with HMDSO:O₂ ratio 1:12, 1:14, 1:16 and 1:20 were all selected for comparison of the samples with differing thicknesses. These samples were chosen as they have been deposited at 1 μm, 2 μm, 3.5 μm and 5 μm. The comparison of the average crystallite sizes and the DOE thicknesses are displayed in Table 6.9. The coatings with ratios 1:14 and 1:20 follow a very similar trend, with a decrease in the average crystallite size

from 1 μm to 2 μm , followed by an increase with an increase in thickness to 3.5 μm , and then a further decrease. The coating at ratio 1:16 has an inverse trend, and exhibits an increase in crystallite size with an increase in thickness from 1 to 2 μm , followed by a large decrease when the thicknesses increases to 3.5 μm and lastly and increase in size with an increase to 5 μm . The coating 1:12, has a completely different trend and exhibits a gradual increase in the crystallite size with the increase in thickness from 1 μm to 3.5 μm , and is then followed by a large decrease, when increasing the thickness to 5 μm .

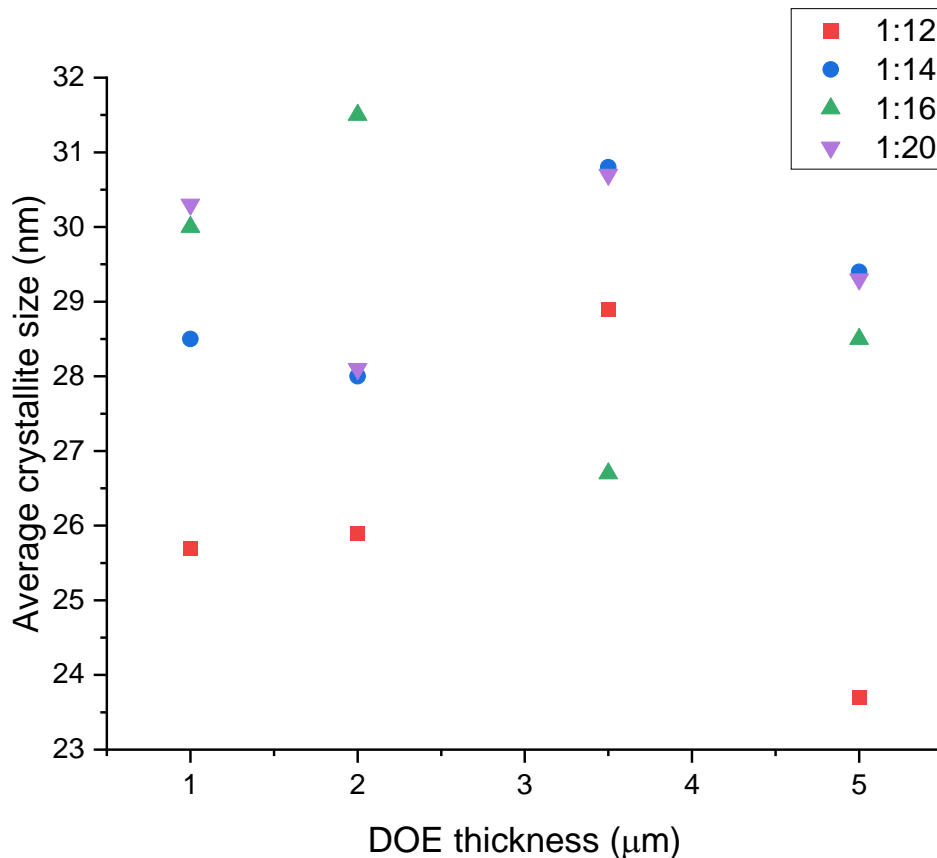


Figure 6.13 A comparison of the average crystallite sizes (nm) with the DOE thickness (μm) of the SiO_x coatings with HMDSO: O_2 ratios 1:12, 1:14, 1:16 and 1:20.

6.4.3 Williamson-Hall analysis

Williamson-Hall (W-H) plots can be utilised to theoretically calculate the crystallite size and micro strain of a coated sample from complex XRD data. Diffraction

peaks should ideally be sharp, however no matter how sharp a peak maybe it will have its own ideal shape, which can be attributed to peak broadening. This broadening can arise from:

1. Instrumental contributions: from the source of radiation, radiation not perfectly monochromatic, misalignment of the diffractometer.
2. Sample contributions: from crystallite size, crystal lattice distortion (micro-strain) due to dislocations or defects.

The micro strain contribution may be caused by deviations from an ideal crystalline lattice, which are most often produced by grain boundaries, residual stresses, and other defects which may cause a non-uniform lattice distortion. These deviations are mainly observed as peak broadening of the Bragg peak, and also a shift the 2θ peak. The crystallite size varies as a function of $\frac{1}{\cos\theta}$ and strain varies as a function of $\tan\theta$, calculated from the peak width, or full width at half maximum (FWHM). Curve fitting of the XRD spectra for the corresponding SiO_x peaks was carried out using Origin Pro software. A Gaussian function was used for the peak fittings, and a value of 2θ and FWHM was distinguished, with the associated errors of the curve fitting.

Using the relationship between peak broadening varying with micro strain, the following Williamson-Hall equation is observed:

$$\beta \cos\theta = \varepsilon(4\sin\theta) + \frac{K\lambda}{D} \quad \text{Eq 6.1}$$

Where, β = FWHM, ε = strain, θ = Bragg angle, λ = x – ray wavelength,

K = dimensionless shape factor, 0.9 and D = crystallite size.

A plot of $\beta\cos\theta$ vs $4\sin\theta$ can be produced from Eq 6.1. From this plot, the theoretical uniform stress can be calculated from the slope of the line and a theoretical value of the crystallite size can be determined from the intercept.

Using:

$$y = mx + c \quad \text{Eq 6.2}$$

$$\beta\cos\theta = 4\varepsilon \sin\theta + \frac{K\lambda}{D} \quad \text{Eq 6.3}$$

Where:

$$m = \varepsilon \quad \text{Eq 6.4}$$

$$c = \frac{K\lambda}{D} \quad \text{Eq 6.5}$$

This method is the uniform deformation model (UDM) [240], assuming that strain is uniform in all crystallographic directions. The Williamson-Hall plots for all HMDSO:O₂ ratios and thicknesses are shown in Figure 6.14, Figure 6.15, Figure 6.18 and Figure 6.19 for the design thicknesses 1 μm , 2 μm , 3.5 μm and 5 μm , respectively. The average crystallite sizes, calculated using the UDM Williamson-Hall method are displayed in Table 6.11, Table 6.12, Table 6.14 and Table 6.15, for thicknesses 1 μm , 2 μm , 3.5 μm and 5 μm , respectively. Values calculated using the Scherrer equation are also included for comparison.

6.4.3.1 W-H plots for the coatings deposited at DOE thickness 1 μm

The W-H plots for the SiO_x coatings with varying HMDSO:O₂ ratios, deposited at a DOE thickness of 1 μm are presented in Figure 6.14. From the graph, the slope

of the lines for the samples 1:10, 1:12, 1:14 and 1:20 are all similar in nature. The micro strain is calculated from the value of the slopes, and are presented in Table 6.11.

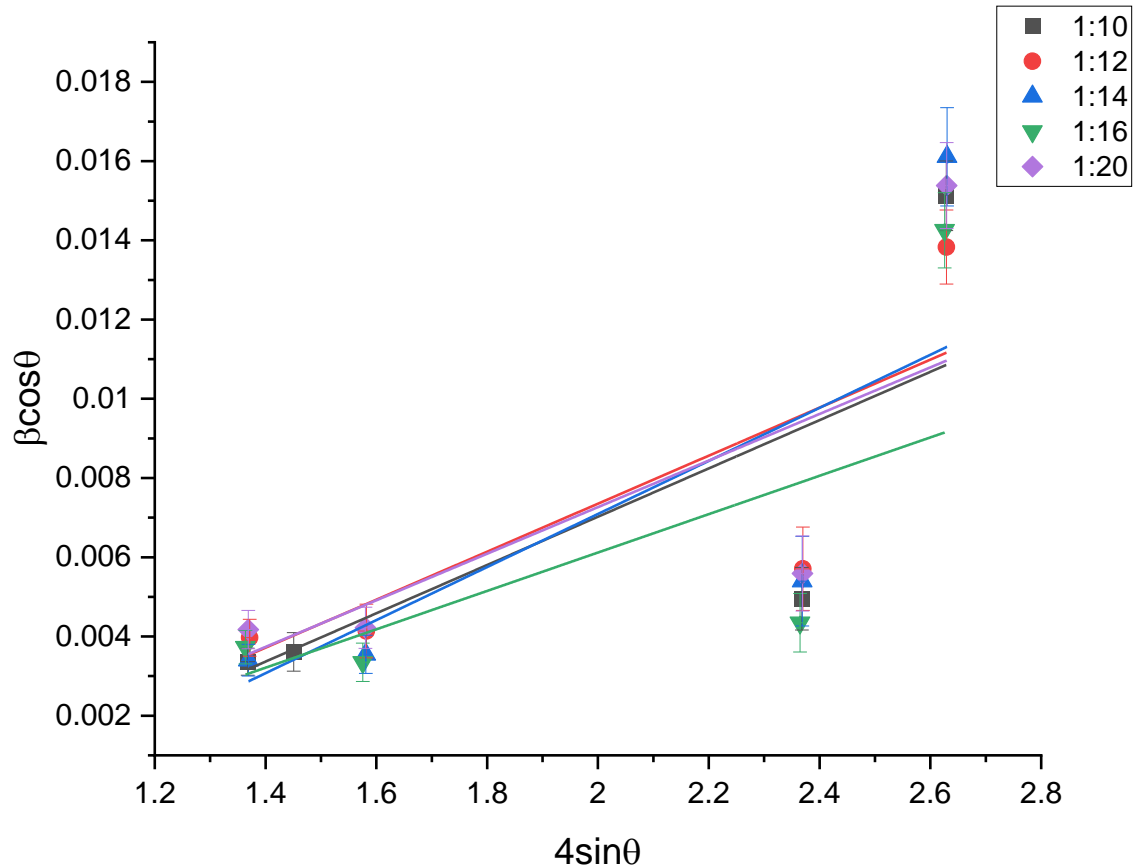


Figure 6.14 Williamson-Hall plot for SiO_x coated samples with varying HMDSO: O_2 ratios and a DOE thickness of $1\ \mu\text{m}$, with error bars calculated from the Gaussian peak fittings using OriginPro software.

The strain of sample 1:16 is 4.8×10^{-3} , which is considerably lower than the strain of the other samples coated at the same thickness. The same sample (1:16) exhibits the largest crystallite size of 38.8 nm and sample 1:14 has the smallest crystallite size, at 22.0 nm and the largest micro strain at 6.7×10^{-3} . The values for the crystallite size vary in comparison to those calculated from the Scherrer equation. Using the W-H method the sample 1:10 gives a lower crystallite size of 26.8 nm and 1:12 gives a larger size of 29.1 nm. The crystallite sizes calculated

from both methods for the coating at ratio 1:20, give comparable sizes, with the W-H plot method giving 30.9 nm and the Scherrer equation giving 30.3 nm.

Table 6.11 Geometric parameters of the SiO_x coatings, with a design thickness of 1 μm.

HMDSO:O ₂ ratio	Williamson-Hall Method (UDM)		Scherrer Equation	
	D (nm)	ε (x10 ⁻³)	D (nm)	ε (x10 ⁻³)
1:10	26.8	6.1	29.2±0.6	1.7
1:12	29.1	6.1	25.7±0.7	1.7
1:14	22.0	6.7	28.5±0.6	1.8
1:16	38.8	4.8	30.0±0.6	1.6
1:20	30.9	5.9	30.3±0.6	1.8

6.4.3.2 W-H plots for the coatings deposited at DOE thickness 2 μm

The W-H plots of the coatings deposited at a design thickness of 2 μm give gradients of a similar nature for all samples at varying HMDSO:O₂ ratios (Figure 6.15), with the exception of sample 1:10. Sample 1:10 gives a steeper slope, and in turn relates to a higher micro strain of the coating at 7.5x10⁻³. The geometric parameters calculated from the W-H plots and Scherrer equations are displayed in Table 6.12.

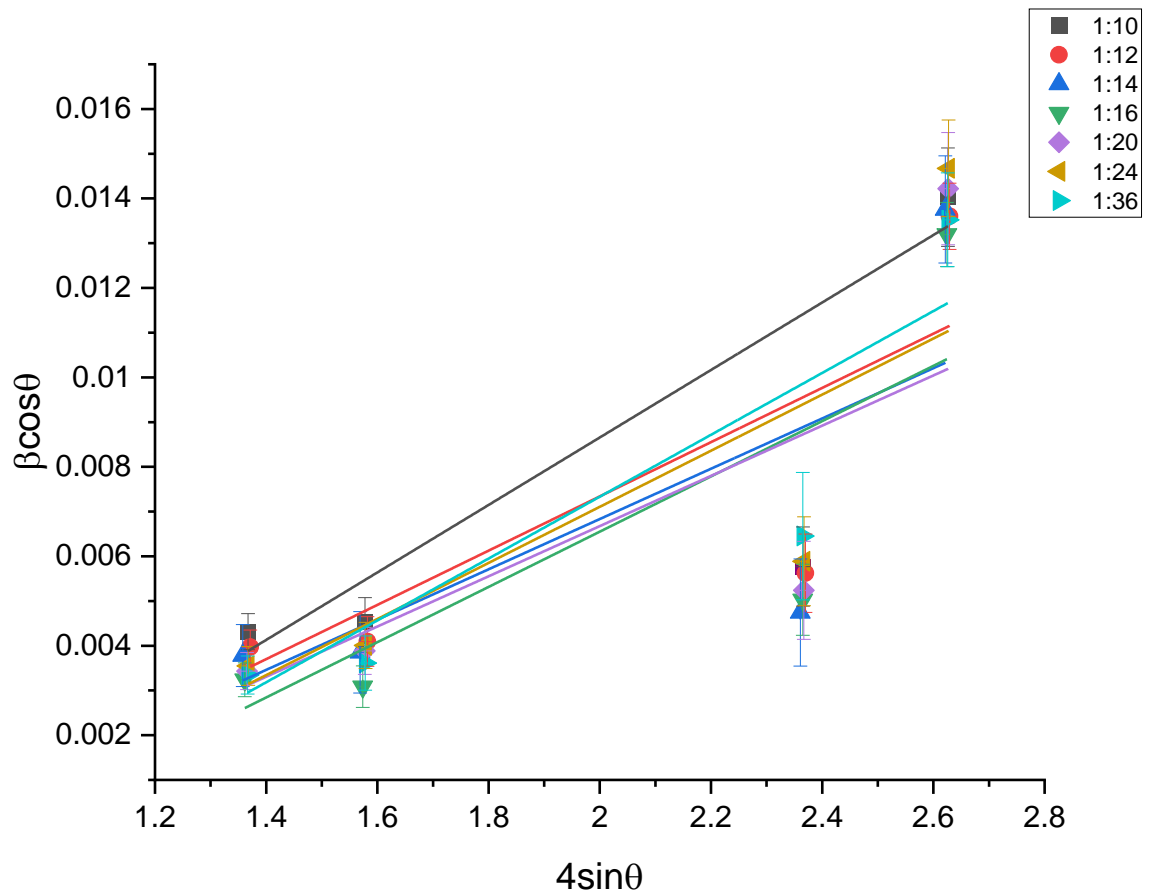


Figure 6.15 Williamson-Hall plots for the SiO_x coated samples with varying HMDSO:O₂ ratios and a DOE thickness of 2 μm. Error bars are calculated from Gaussian peak fitting using Origin Pro.

The sample with ratio 1:10 also gives one of the lowest crystallite sizes at 21.6 nm, agreeing with the values calculated from the Scherrer equation. The sample 1:36 gives the lowest crystallite size of 21.3 nm and a micro strain of 6.9×10^{-3} , falling just behind the strain of sample 1:10. The smallest strain of the samples coated at 2 μm is found in the ratios 1:14 and 1:20 with a value of 5.6×10^{-3} . Sample 1:14 has the largest crystallite size (31.4 nm) calculated from the W-H method, with sample 1:20 having a slightly smaller crystallite size of 30.4 nm. From these results, there is a slight correlation between the crystallite size and the micro strain. The coatings that have a lower crystallite size calculated from W-H, have a larger strain and vice versa. This is not valid for all samples, but begins to show a minor trend.

Table 6.12 Geometric parameters, calculated from the UDM method and Scherrer equation, of the SiO_x coatings with a design thickness of 2 μm

HMDSO:O ₂ ratio	Williamson-Hall Method (UDM)		Scherrer Equation	
	D (nm)	ε (x10 ⁻³)	D (nm)	ε (x10 ⁻³)
1:10	21.6	7.5	24.2±0.5	1.8
1:12	25.9	6.1	25.9±0.5	1.7
1:14	31.4	5.6	28.0±1.0	1.6
1:16	23.8	6.2	31.5±0.6	1.5
1:20	30.4	5.6	28.1±0.7	1.7
1:24	25.5	6.3	26.7±0.6	1.8
1:36	21.3	6.9	27.9±0.7	1.7

The coating at ratio 1:12 gives the same calculated crystallite size using both methods. Coatings 1:10, 1:16, 1:24 and 1:36 give a smaller crystallite size when calculated from W-H, and the coatings 1:14 and 1:20 give a larger crystallite size from the W-H calculations. The micro strain values calculated for the SiO_x coatings from the Scherrer equation are much lower in comparison to the strain calculated from the W-H method.

A comparison of the W-H method using the UDM, with the hardness values is shown in Table 6.13 and Figure 6.16. As the crystallite size increases, the hardness varies, with a small decrease in the hardness from the smallest crystallite size (21.6 nm), to the largest (31.4 nm).

Table 6.13 A comparison of the average crystallite size calculated from the Williamson-Hall method, with the hardness values from nanoindentation.

HMDSO:O ₂ ratio	W-H method (UDM)		Hardness (GPa)	Young's modulus (GPa)
	D (nm)	ϵ ($\times 10^{-3}$)		
1:10	21.6	7.5	5.8 ± 0.9	100.4 ± 1.7
1:12	25.9	6.1	5.1 ± 0.5	93.3 ± 1.7
1:14	31.4	5.6	4.6 ± 0.2	82.0 ± 1.3
1:16	23.8	6.2	5.0 ± 0.4	83.6 ± 1.6
1:20	30.4	5.6	5.9 ± 0.8	97.4 ± 1.4
1:24	25.5	6.3	5.9 ± 0.5	99.3 ± 1.3
1:36	27.9	6.9	5.7 ± 0.5	93.1 ± 1.9

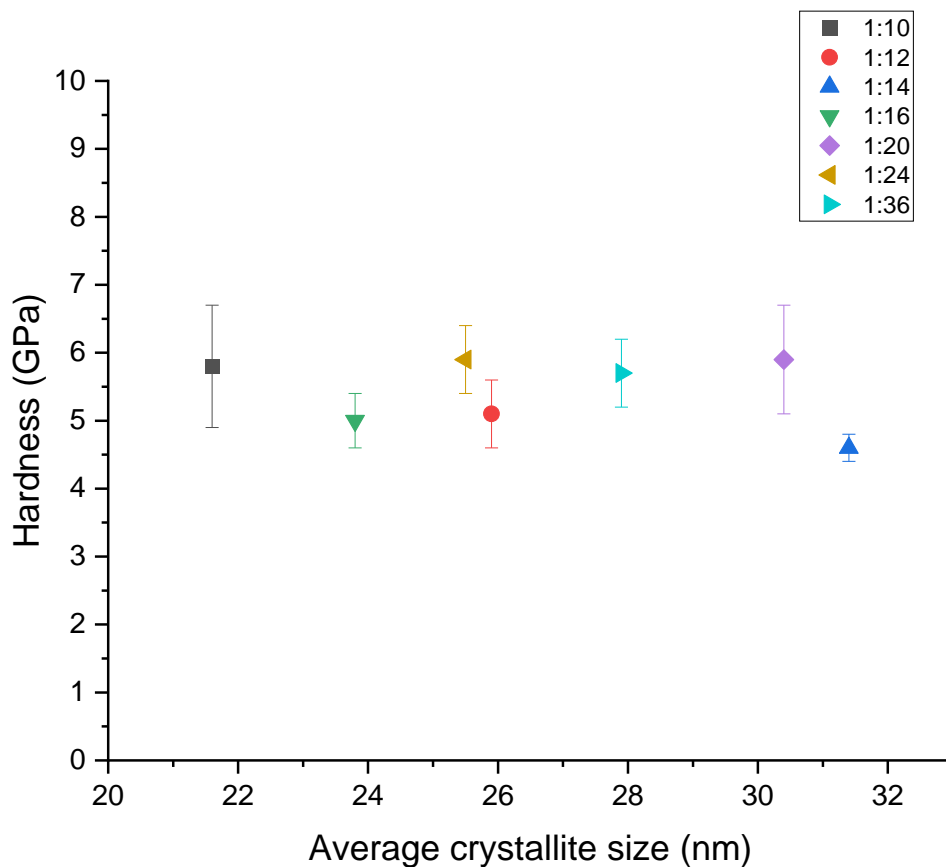


Figure 6.16 The average crystallite sizes (nm) calculated from the Williamson Hall UDM method versus the hardness (GPa), for SiO_x coatings with varying HMDSO:O₂ ratios and a DOE thickness 2 μ m.

There is no definite correlation between the hardness of the SiO_x coatings and their average crystallite size comparison, therefore assuming that the crystallite size calculated from the UDM does not affect the overall hardness of the SiO_x coatings. However, it has been reported that a reduction in the crystallite size can increase the hardness [241], but not directly for an SiO_x coating. Another study using nanocrystalline nickel reported that the hardness increased with an increase in the grain size, therefore contradicting the previous statement [242]. For the SiO_x coatings, it is difficult to draw a conclusion as there is no definitive trend, but from the observed data the hardness and crystallite size are independent of one another.

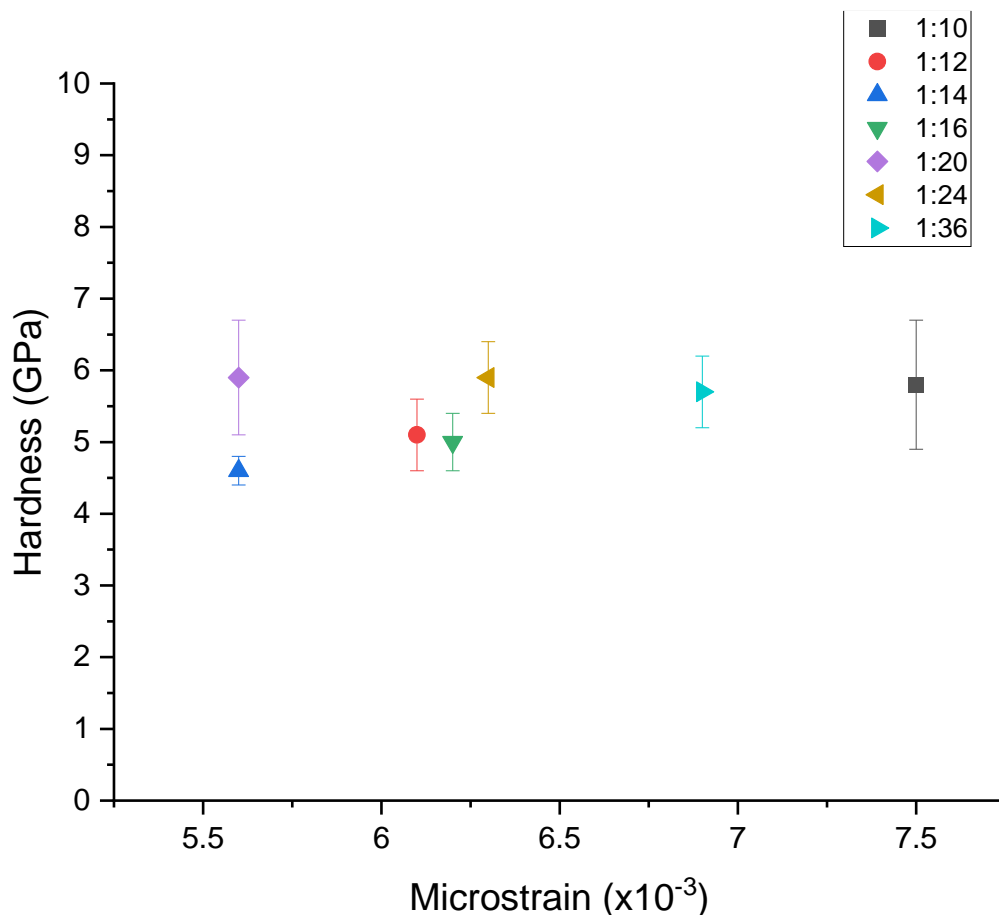


Figure 6.17 The microstrain of the SiO_x coatings calculated from the Williamson Hall UDM method versus the hardness (GPa), for SiO_x coatings with varying HMDSO:O₂ ratios and DOE thickness 2 μm.

Similarly, the micro strain of the coating also does not appear to have an effect on the hardness of the SiO_x coatings. It is observed that there may be a slight increase in the hardness of the coatings with an increase in the strain, if sample 1:20 were not taken into consideration. The coating 1:10 gives the highest strain and the smallest crystallite size, whereas coating 1:14 gives the highest crystallites size and the lowest strain, therefore suggesting that the strain of the coating is dependent on the crystallite size.

6.4.3.3 W-H plots for the coatings deposited at DOE thickness 3.5 μm

For the coatings deposited at a design thickness of 3.5 μm, the plots show a very similar trend in gradients, but with different intercepts. The value calculated from the gradients for the micro strain vary from 5.6x10⁻³ for sample 1:20 to 6.0x10⁻³ for sample 1:16. The calculated values for both the crystallite size and micro strain, using the W-H method do not show much of a trend. The largest calculated value for the crystallite size (29.4 nm) is found from coating 1:12 and the lowest crystallite size (24.4nm) is found from coating 1:14. Sample 1:14 also exhibits the smallest crystallite size at a design thickness of 1 μm.

Table 6.14 Geometric parameters, calculated from the UDM method and Scherrer equation, of the SiO_x coatings with a design thickness of 3.5 μm

HMDSO:O ₂ ratio	Williamson-Hall Method (UDM)		Scherrer Equation	
	D (nm)	ε (x10 ⁻³)	D (nm)	ε (x10 ⁻³)
1:12	29.4	5.7	28.9±0.8	1.6
1:14	24.4	5.9	30.8±1.2	1.6
1:16	28.6	6.0	27.0±0.6	1.6
1:20	28.5	5.6	30.7±0.8	1.6

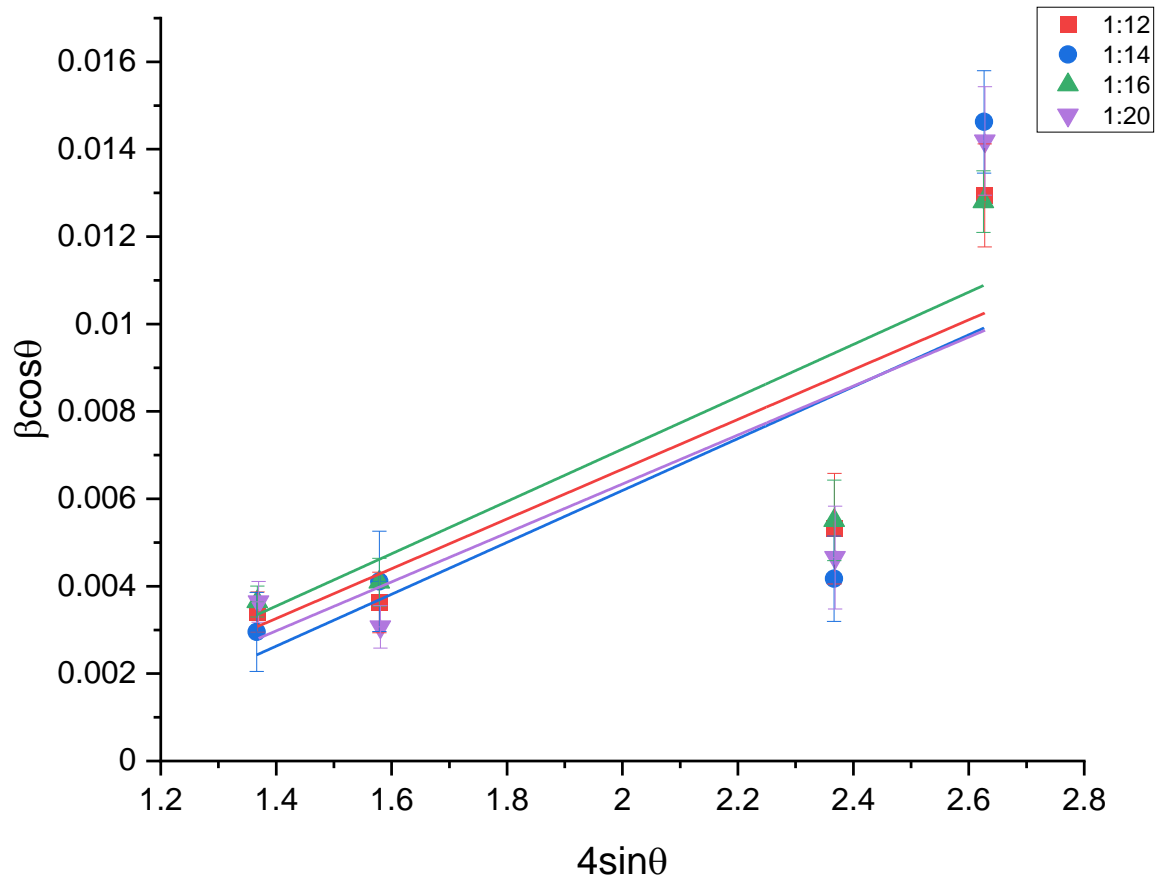


Figure 6.18 Williamson-Hall plots for the SiO_x coated samples with varying HMDSO:O₂ ratios and a DOE thickness of 3.5 μm, using the UDM method. Error bars are calculated from Gaussian peak fitting using Origin Pro.

The difference in the micro strain of the coatings is minimal, with a small difference of 0.4×10^{-3} . The strain sizes calculated from sample 1:20, decrease slightly with an increase in thickness, from 5.9×10^{-3} at 1 μm to 5.3×10^{-3} at 5 μm. The strain also decreases with an increase in thickness for the coating 1:14, varying from 6.7×10^{-3} at 1 μm to 5.3×10^{-3} at 5 μm.

6.4.3.4 W-H plots for the coatings deposited at DOE thickness 5 μm

The coatings 1:12 and 1:16 deposited at a thickness of 5 μm, show similar gradients, with different intercepts (Figure 6.19). The gradients are higher in comparison to the coatings 1:14 and 1:20. The larger gradients lead to a larger micro strain at 7.0×10^{-3} for coating 1:12 and 6.6×10^{-3} for coating 1:16. The

coatings 1:14 and 1:20 both have a lower micro strain of 5.3×10^{-3} . The coatings with the higher micro strain, result in a crystallite size and the coatings with the lower micro strain result in larger crystallite sizes (Table 6.15).

Table 6.15 Geometric parameters, calculated from the UDM method and Scherrer equation, of the SiO_x coatings with a design thickness of $5 \mu\text{m}$

HMDSO: O_2 ratio	Williamson-Hall Method (UDM)		Scherrer Equation	
	D (nm)	ϵ ($\times 10^{-3}$)	D (nm)	ϵ ($\times 10^{-3}$)
1:12	23.9	7.0	23.7 ± 0.7	2.0
1:14	33.0	5.3	29.4 ± 1.0	1.5
1:16	23.4	6.6	28.5 ± 0.6	1.7
1:20	34.0	5.3	29.3 ± 0.6	1.5

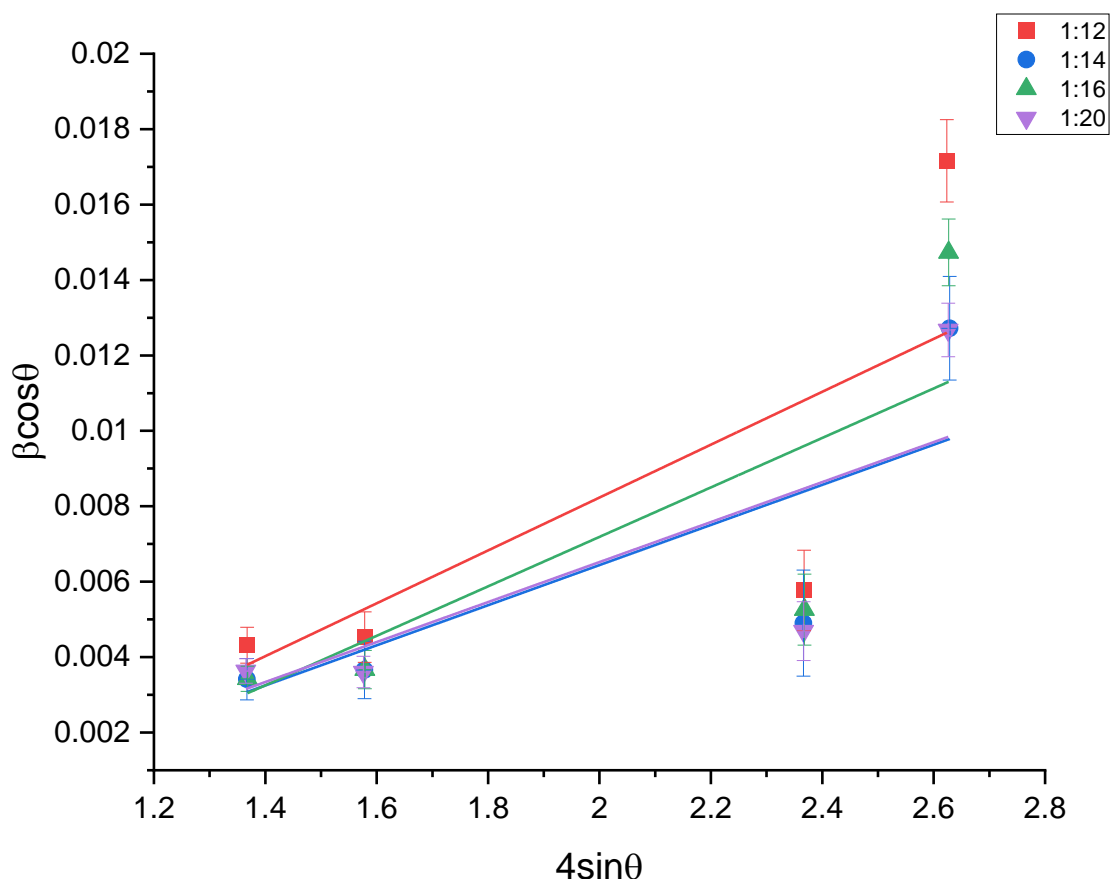


Figure 6.19 Williamson-Hall plots for the SiO_x coated samples with varying HMDSO: O_2 ratios and a DOE thickness of $5 \mu\text{m}$, using the UDM method. Error bars are calculated from Gaussian peak fitting using Origin Pro.

For the coatings deposited at 5 μm , it can be concluded that the crystallite size has an effect on the micro strain. The larger the micro strain, the smaller the crystallite size, and vice versa. Comparing the values of the crystallite size from the W-H method, to those calculated from the Scherrer equation, the trend is similar between the two methods. Both coatings 1:12 and 1:16 give the lowest crystallite sizes (23.9 and 23.4 nm) from the W-H method, and also the lowest sizes from the Scherrer equation, 23.7 nm and 28.5 nm. The major difference is that the size calculated from WH for sample 1:16 is considerably lower than that calculated from the Scherrer equation. The coatings 1:14 and 1:20, also give the highest crystallite sizes, when using both methods.

6.4.3.5 A comparison of the average crystallite size with the thickness of the coatings

A comparison of the average crystallite sizes calculated from the Williamson-Hall method and the thickness of the coatings are shown in Table 6.16 and Figure 6.20.

Table 6.16 The average crystallite size calculated from the Williamson Hall method, for samples 1:12, 1:14, 1:16 and 1:20, with a comparison to the DOE thicknesses.

HMDSO:O ₂ ratio	Average crystallite size (nm)			
	1 μm	2 μm	3.5 μm	5 μm
1:12	29.1	25.9	29.4	23.9
1:14	22.0	31.4	24.4	33.0
1:16	38.8	23.8	28.6	23.4
1:20	30.9	30.4	28.5	34.0

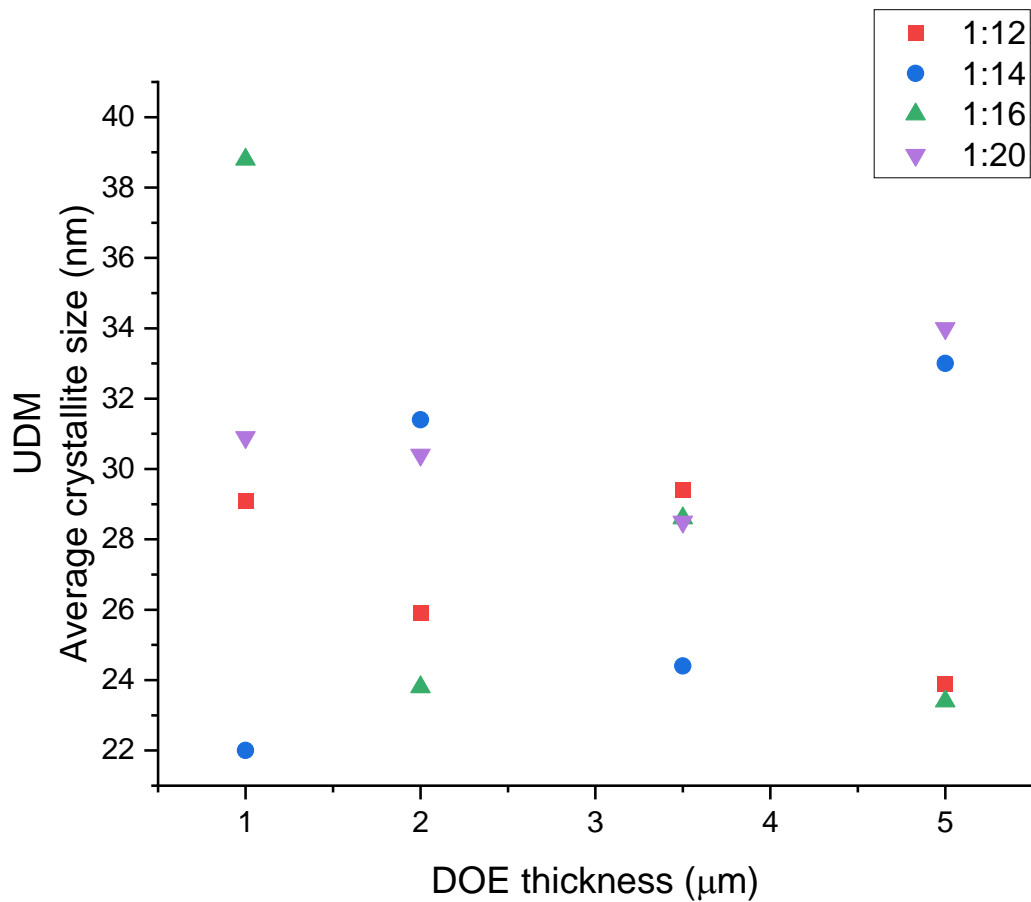


Figure 6.20 A graph showing the comparison of the average crystallite size (nm) calculated from the Williamson Hall method versus the thickness μm of the coatings.

The average grain sizes calculated using atomic force microscopy in the literature have been reported for SiO_2 films. The grain size and crystallite size are considered to be the same, however this is not always true. Zhang et al [243] reported that an increase in the film thickness. Increases the average grain size. The coatings with ratios 1:12 and 1:16 both have a general decrease in the hardness with an increase in the DOE thickness of the coatings from 1 μm through to 5 μm . On the other hand, coatings 1:14 and 1:20 show an overall increase in the hardness with an increase in the DOE thickness. This is in agreement with the results reported by Zhang, however the average grain size is

higher for their coatings at 60.7 nm, 64.2 nm and 66.9 nm for thickness 500 nm, 1000 nm and 2000 nm respectively.

6.5 Summary of chapter

In summary, a large matrix of SiO_x coatings with varying HMDSO: O_2 ratios and varying thicknesses have been successfully deposited using MW-PECVD, with HMDSO and O_2 precursors. The XRD patterns showed that the SiO_x coatings deposited using this method have a crystalline structure, contrary to the literature where SiO_x coatings have a reported amorphous structure with low levels of crystallinity.

- The nanomechanical results calculated from nanoindentation vary with HMDSO: O_2 ratio, however, there are no discernible trends as the errors of each nanoindentation overlap for each coating. Therefore, the increase in oxygen concentration does not affect the mechanical properties of the coatings.
- The binding energies (eV) for the samples coated with a 2 μm thickness vary with HMDSO: O_2 ratio. Coatings 1:12 and 1:16 gave binding energies comparable to those found in the literature for stoichiometric SiO_2 .
- The Si:O ratios calculated from the XPS survey spectra also vary with HMDSO: O_2 ratio, with coating 1:12 giving the highest ratio of 2 (almost stoichiometric) and gradually reducing to 1.94 at coating 1:36.
- Curve fittings for the high-resolution spectra of Si 2p and O 1s, both gave single peaks which are attributed to Si – O bonding for tetrahedral SiO_2 .
- The XRD results have allowed the microstructure of the coatings to be explored. From the XRD diffractograms, the coatings give very similar spectra, with little variation between HMDSO: O_2 ratios. Due to the

crystalline nature of the coatings, the microstructure was able to be investigated further based on peak broadening.

- The average crystallite size of the coatings was successfully calculated using both the Scherrer equation and Williamson-Hall, using the uniform deformation method (UDM). The calculation of the crystallite sizes, using both the Scherrer equation and the W-H method have given variations with HMDSO:O₂ ratios and thicknesses. However, there are no clear trends to suggest that varying the oxygen concentration during the deposition influences the crystallite size.
- The micro strain of the coatings, using both the Scherrer equation and Williamson Hall plots, was calculated successfully. The micro strain also varies throughout the SiO_x coatings, both with the HMDSO:O₂ ratio and the thickness of the deposited coating.
- The comparison of the average crystallite size using both methods, with the thickness of the coatings shows slightly different trends for coatings with the different HMDSO:O₂ ratios.
 - From the Scherrer equation method, all of the coatings exhibited an overall decrease in the average crystallite, with an increase in the film thickness from 1 μm through to 5 μm.
 - On the other hand, the Williamson-Hall method showed that sample 1:12 and 1:16 agreed with the Scherrer trend, as there was an overall decrease in the crystallite size with increasing film thickness. The coatings with ratios 1:14 and 1:20 however showed an overall increase in the film thickness, agreeing with the finding reported by Zhang et al [243].

- To conclude, the MW-PECVD method for depositing SiO_x coatings allows the formation of crystalline coatings.

Chapter 7 – Electrochemical behaviour of SiO_x coatings with varying HMDSO:O₂ ratios and thicknesses

7.1 Introduction

This chapter encompasses the corrosion behaviour of the SiO_x coated samples, to establish the electrochemical performance of the coatings with varying HMDSO:O₂ ratios. The corrosive environment used was a 1 M NaCl solution at room temperature, using a three-electrode flat cell set up, as described in section 4.7. The use of a 1M NaCl solution, pH 6.7, as the corrosive environment was chosen in order to first understand the corrosion behaviour of the coatings. As hydrogen fuel cells use a plethora of environments, the understanding of the SiO_x corrosion ability needs to be understood, based on the HMDSO:O₂ ratios and thicknesses. The effect of the DOE thickness of the coatings on the corrosion resistance and the capacitance of the coatings will also be investigated.

7.2 Corrosion performance of the SiO_x coatings with varying HMDSO:O₂ ratio

7.2.1 Potentiodynamic analysis

Tafel extrapolation of polarisation curves is a widely used method for measuring the corrosion current density (i_{corr}) of a coated sample [244]. From the determination of i_{corr} , it is possible to calculate the corrosion rate [245]. Tafel extrapolation is widely utilised as it is a faster experimental method when compared with weight loss estimation also allows the determination of the anodic and cathodic Tafel constants, which are valuable when assessing the corrosion rates of a coated sample and to also understand the kinetics of the corrosion reactions.

Tafel extrapolation tests were performed using a three-electrode flat cell for all HMDSO:O₂ ratios at a DOE thickness of 2 μm. This thickness was chosen for the polarisation experiments due to having the largest matrix of HMDSO:O₂ ratios with this thickness. Therefore, it is possible to understand the corrosion performance of the coatings over a widespread range of HMDSO:O₂ ratios.

Tafel polarization curves were recorded for both the anodic and cathodic sweeps, as described in section 4.7 of the experimental chapter. Both data were combined to produce a Tafel polarisation curve. Figure 7.1 shows the Tafel polarisation curves for all HMDSO:O₂ ratios coated with a DOE thickness of 2 μm, with a comparison to an uncoated HSS sample. The aim of the potentiodynamic measurements was to determine the free corrosion potential (E_{corr}) of the coated samples, corrosion current density (i_{corr}) and the anodic and cathodic Tafel constants.

From the graph shown in Figure 7.1, the polarisation curves for the SiO_x coated samples a shift towards the left is observed and therefore show decreasing in current, when compared to the uncoated sample. This is in agreement with the known properties of all coatings, including silicon oxide, in order to reduce material degradation by playing the role of a barrier to water ingress. The potential (mV) of all of the SiO_x coated samples shift to more electropositive values, when comparing to the uncoated HSS sample, which has a value of -535 mV.

Using both the anodic and cathodic Tafel polarization curves for all samples, both the anodic (β_a) and cathodic (β_c) Tafel constants can be determined, through extrapolation of the anodic and cathodic curves respectively. Figure 4.14 shows the extrapolation technique for evaluating the β_a and β_c Tafel constants and the

E_{corr} and i_{corr} components. The extrapolation procedures are further detailed in the Experimental chapter, section 4.7.1.

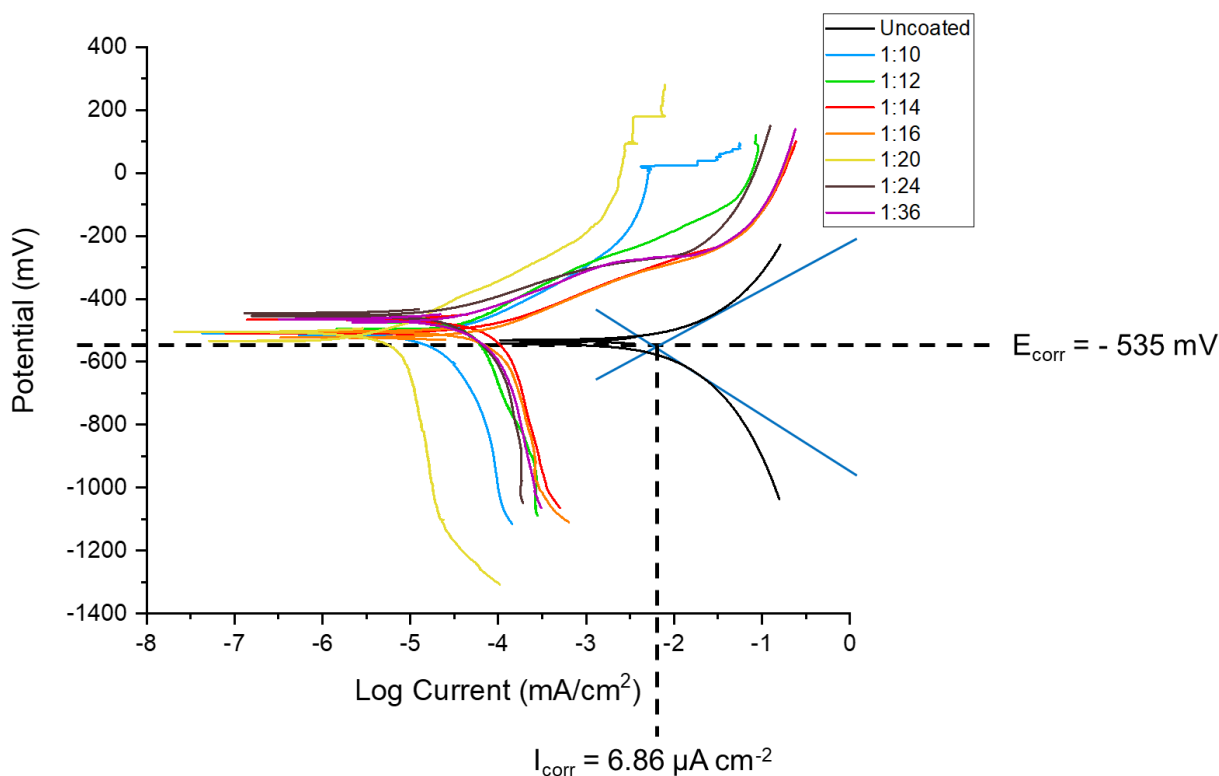


Figure 7.1. The Tafel extrapolation curves for SiO_x coated HSS with a DOE $2 \mu\text{m}$ thickness with varying HMDSO: O_2 ratios. The annotation on the graph is for the uncoated HSS with a E_{corr} value = -535 mV and $i_{\text{corr}} = 6.86 \mu\text{A cm}^{-2}$.

The open circuit potential (OCP), or E_{corr} , of the uncoated HSS was measured to be -534 mV . The corresponding values for the SiO_x coated samples ranged between -451 and -515 mV , as shown in Figure 7.1. The corrosion current density for the uncoated sample was determined to be $6.58 \mu\text{A cm}^{-2}$ and the corresponding values for the coated samples ranged between 0.02 and $0.08 \mu\text{A cm}^{-2}$. The increase in E_{corr} and decrease in i_{corr} values for the coated samples indicates a better corrosion resistance, when compared with the uncoated HSS [246].

Table 7.1. Tafel extrapolation results related to the polarization curves from Figure 7.1, for samples coated to a 2 μm thickness with varying HMDSO:O₂ ratios.

HMDSO:O ₂ ratio	E_{corr} vs. Ag/AgCl (mV)	βa (mV dec ⁻¹)	$-\beta c$ (mV dec ⁻¹)	i_{corr} ($\mu\text{A cm}^{-2}$)	Stern-Geary coefficient (B) / mV dec ⁻¹
Uncoated	-535	171	343	6.86	49.5
1:10	-515	98	488	0.02	35.3
1:12	-487	148	498	0.05	49.5
1:14	-494	105	452	0.08	37.0
1:16	-516	116	424	0.07	39.5
1:20	-518	153	666	0.01	54.3
1:24	-451	93	275	0.03	30.2
1:36	-474	107	266	0.04	33.1

The cathodic polarization curves presented for the SiO_x coatings vary in shape to that of their respective anodic polarisation curves. This difference suggests that there are different electrochemical processes occurring. The driving force for the potentiodynamic experiment is controlled (through the applied potential) and the change in the reaction rate is observed from the current values. For the anodic polarisation curves, the voltage-current response varies with HMDSO:O₂ ratio. For the samples 1:12, 1:14, 1:16, 1:24 and 1:36, the curve is of a similar shape and the increase in current when the voltage is applied, also follows a similar trend and demonstrating that the coatings are presenting a pseudo-passive behaviour [247] – the point at which the current remains almost the same for a short period of time, and only shows a small increase. The anodic curves for samples 1:10 and 1:20 behave in a similar manner, however show a larger increase in the current density. It is observed that the SiO_x coating shows active,

uniform dissolution at lower potentials leading into a pseudo-passivation behaviour. Several metals and alloys including Fe, Cr, and stainless steels are known to show an active to passive transition during the anodic polarisation [248]. For all SiO_x coatings, the cathodic polarisation curves are comparable and shows an oxygen reduction reaction [249]. The presence of the SiO_x coating may result in the reduction of the coating into SiO(OH)₃⁻ and SiO₂(OH)₂²⁻ [250]. However, this phenomena has been demonstrated to occur at high pH ~ 11 and can therefore not be comparable to the polarisation curves presented here due to the pH level being ~7.

The corrosion potential (E_{corr}) does not vary significantly between the uncoated HSS and the SiO_x coated samples. The corrosion current (i_{corr}), on the other hand, is much greater for the uncoated HSS sample at 6.86 $\mu\text{A cm}^{-2}$ than for the SiO_x coated HSS samples, which vary between 0.01 and 0.08 $\mu\text{A cm}^{-2}$. The decrease in i_{corr} of SiO_x coated mild steel has been reported by Gangan et al. [177] It was found that the uncoated mild steel gave an i_{corr} value of 12.001 $\mu\text{A cm}^{-2}$ and the SiO_x coated samples gave i_{corr} values between 6.932 and 0.325 $\mu\text{A cm}^{-2}$. The coated samples were deposited using different deposition powers, and found that increasing the plasma power decreased the corrosion current of the samples. Kirtay, S [251] also reported that the addition of a silica coating onto a mild steel substrate resulted in a small decrease in the E_{corr} and a large decrease in the i_{corr} values, ranging from 11.7 $\mu\text{A cm}^{-2}$ for mild steel, to 0.35 $\mu\text{A cm}^{-2}$ for silica sol-gel coated mild steel. The SiO_x coatings investigated in this study showed a large decrease in the corrosion current, when compared to the uncoated sample.

Samples 1:10, 1:16 and 1:20 have the lowest corrosion potentials, -515 mV, -516 mV and -518 mV respectively, when compared with the other SiO_x coated

samples. With an insignificant difference when compared to the uncoated HSS sample. Sample 1:24 exhibits the highest corrosion potential of -451 mV, a change of $+84$ mV when compared to bare HSS. Although some samples showed a small increase in the corrosion potential when compared to the bare HSS, all samples increased and therefore show a slightly enhanced corrosion resistance. The lowest corrosion current is from sample 1:20, with the highest corrosion current exhibited by sample 1:14.

The threshold for the corrosion current density for use of a coating in a PEMFCs is to be less than 0.016 mA cm⁻². Based on the measurements for the SiO_x coated HSS, all HMDSO:O₂ ratios would make a suitable coating for their use as coatings in bipolar plates within a PEMFC due to the corrosion current density of all the SiO_x coatings falling within the range of $0.01 - 0.08$ μ A cm⁻², 3 orders of magnitude smaller than the PEMFC threshold.

7.2.2 Electrochemical impedance spectroscopy of the SiO_x coatings

Electrochemical impedance spectroscopy (EIS) has been utilised in this thesis to investigate the electrochemical response of SiO_x coated HSS. Using EIS, the resistivity and capacitance of the SiO_x coatings can be calculated. This section will focus on the corrosion behaviour of the coatings, using EIS, with respect to the HMDSO:O₂ ratios and also the dependence of the thickness.

The chemistry of a coating can have an effect on the corrosion properties, and therefore barrier protection of a coated sample. A series of EIS tests were performed for a selection of SiO_x coated samples, with varying HMDSO:O₂ ratios. The ratios analysed were 1:10, 1:12, 1:14, 1:16, 1:20 and 1:24, all with a coated thickness of 2 μ m. The aim of these experiments was to characterise the

electrochemical behaviour of the coatings, which in turn allows a theoretical value for the resistance and capacitance of the coatings to be calculated.

Each sample was tested for 1 week (168 hours), using a flat cell setup as shown in section 3.5.1, in a sodium chloride (NaCl) 1M solution. EIS spectra were recorded throughout the period of the experiment and analysed at specific time points, through fitting equivalent circuits of both the Nyquist and Bode plots produced through the use of ZView software. The Nyquist and Bode plots for the sample with HMDSO:O₂ ratio 1:20 are presented in Figure 7.2 and Figure 7.3, respectively. The plots show the corresponding data after 1 hour, 72 hours and 168 hours. The Nyquist and Bode plots for the other sample ratio can be found in Appendix A.

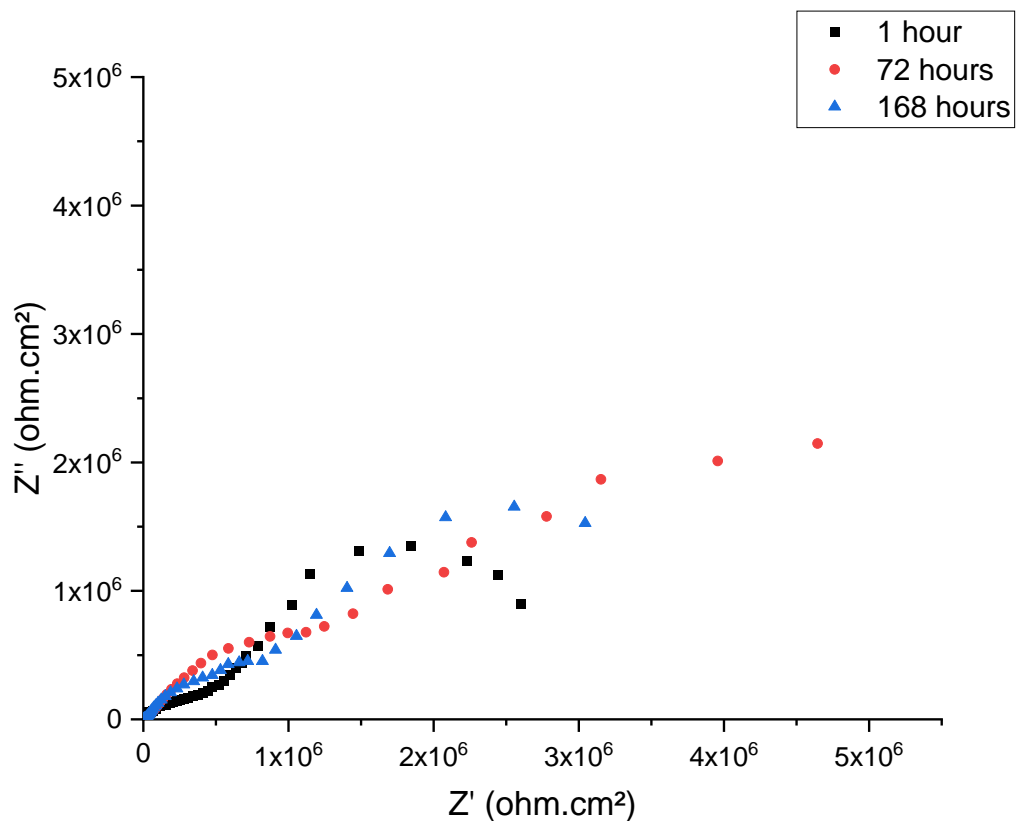


Figure 7.2. Nyquist plot for the SiO_x coated sample with HMDSO:O₂ ratio 1:20 and a DOE thickness of 2 μm, at 1 h, 72 h and 168 h.

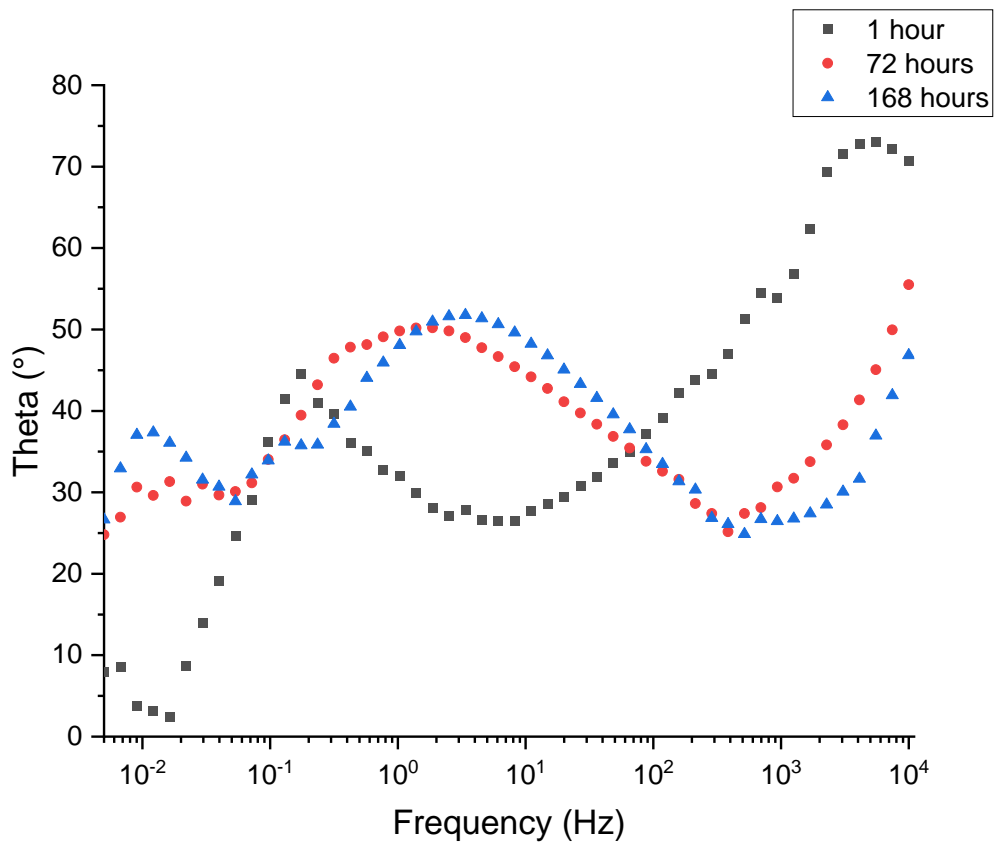
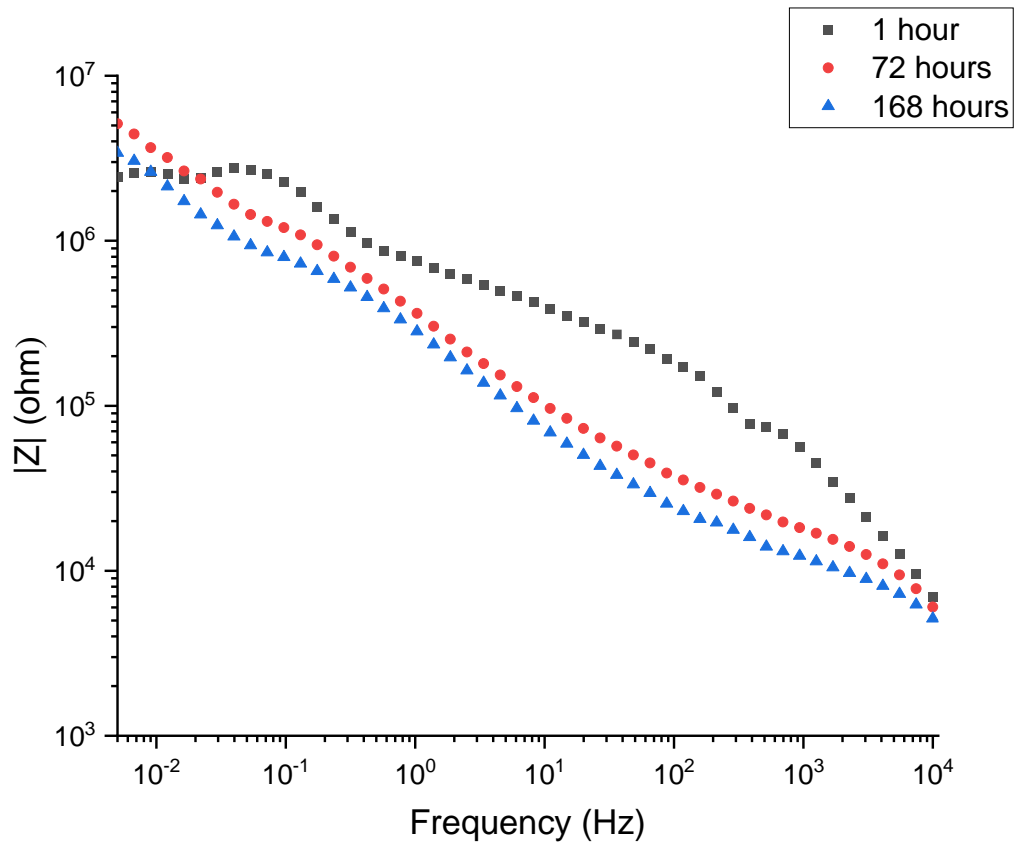


Figure 7.3. Bode plots for the SiO_x coated sample with HMDSO: O_2 ratio 1:20 and a DOE thickness of $2 \mu\text{m}$, at 1 h, 72 h and 168 h.

The impedance value, Z' (ohm cm^2), from the Nyquist plot increases from 1 hour to 72 hours, but then decreases from 72 hours to 168 hours. This trend will be further explored throughout this chapter.

Using both the Nyquist and Bode plots, an equivalent circuit can be fitted to evaluate the capacitance and resistance of the coating. The equivalent circuits were fitted to both the Nyquist and Bode plots for each sample using ZView software. An equivalent circuit with three capacitive loops, each made up of a constant phase element (CPE) and resistance, can be fitted to the plots to determine the capacitance and resistance of; the substrate, the coating and the electrical double layer. The three time constants for the SiO_x coatings can be defined as:

1. Constant phase element (CPE) and resistance of the electrical double layer.
2. Constant phase element (CPE) and resistance of the coating – at high frequency resulting from the penetration of the NaCl electrolyte through a pore or defect in the coating [252].
3. Constant phase element (CPE) and resistance of the oxide layer – at lower frequency.

A constant phase element (CPE) was used for each capacitive loop instead of an “ideal” capacitor, due to the coatings having a certain degree of inhomogeneity within the coating surface [176]. The CPE values of each coating were in the range $0.5 < n < 1$, therefore suggesting that the coating is not acting as an ideal capacitor and is not a resistor.

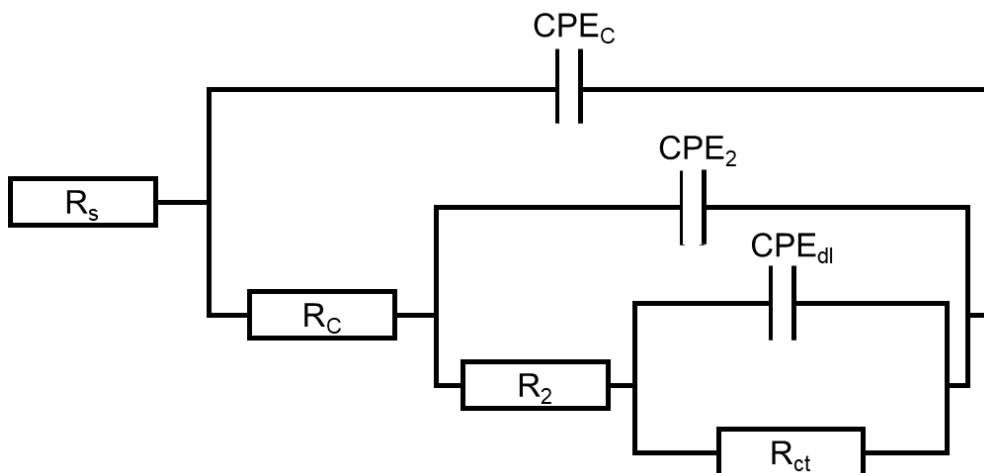


Figure 7.4. Equivalent circuit for the SiO_x coatings, with the following components: R_s = solution resistance, CPE_C = coating capacitance, R_C = coating resistance, CPE_2 = corrosion layer capacitance, R_2 = corrosion layer resistance, CPE_{dl} = double layer capacitance, R_{ct} = charge transfer resistance.

The equivalent circuit for the SiO_x coatings is shown in Figure 7.4, is made up of a solution resistance (R_s) – in this case, the resistance of 1M NaCl in the presence of high speed steel (HSS). The solution resistance values of the NaCl solution were considerably higher in some coatings, when compared to the solution resistance of NaCl solution ($\sim 70 \Omega \text{ cm}^2$). Rowlands and Chuter proposed that the solution resistance measured during EIS is essentially a measure of the ionic film resistance, due to the resistance of seawater being negligible [253]. This is also supported by the fact that a coated metal will give higher R_s values, when compared to an uncoated metal [254].

There are also 3 capacitive loops consisting of; a constant phase element (CPE_C) and resistance (R_C) of the coating, a constant phase element (CPE_2) and resistance (R_2) of a corrosion layer and a constant phase element (CPE_{dl}) and resistance (R_{ct}) of the electrical double layer. Angelini et al [183] reported an equivalent circuit with two capacitive loops for a SiO_x coating on Q-panel steel, however, using the same equivalent circuit for the coatings in this thesis did not result in a good fitting. It has been proposed that the 3rd capacitive loop may be

due to an additional oxide layer forming throughout the EIS experiment, or prior to deposition of the SiO_x coating.

Figure 7.5 shows the equivalent circuit fittings for the HMDSO:O₂ ratio sample 1:20 at 1 h, 72 h and 168 h, using the ZView software. The equivalent circuit fittings for all other SiO_x coatings are presented in the Appendix B.

Fitting equivalent circuits for the series of SiO_x coatings at 2 μm gives values for the resistance and capacitance of the coatings at different time points (1 hour, 72 hours and 168 hours). The results for the coating resistance and capacitance values are given in Table 7.2. All CPE values are given as an admittance (Y_0), as described in section 4.8. In general, most coatings showed an increase in the resistance of the charge transfer (R_{ct}) over the period of the experiment. Samples 1:10, 1:12, 1:14, 1:24 and 1:36 all had an increase in the resistance from 1 hour to 168 hours, from: $2.53 \times 10^5 \Omega \text{ cm}^2$, $2.79 \times 10^5 \Omega \text{ cm}^2$, $9.22 \times 10^6 \Omega \text{ cm}^2$, $1.66 \times 10^5 \Omega \text{ cm}^2$ and $1.22 \times 10^5 \Omega \text{ cm}^2$ to $6.28 \times 10^6 \Omega \text{ cm}^2$, $3.42 \times 10^5 \Omega \text{ cm}^2$, $1.16 \times 10^7 \Omega \text{ cm}^2$, $6.37 \times 10^6 \Omega \text{ cm}^2$ and $9.00 \times 10^5 \Omega \text{ cm}^2$, respectively. Demonstrating an increase in the amount of protection from the coating to the substrate.

Samples 1:16 and 1:20, saw a decrease in the resistance throughout the duration of the experiment, falling from $9.18 \times 10^6 \Omega \text{ cm}^2$ and $3.36 \times 10^6 \Omega \text{ cm}^2$, respectively, to $7.20 \times 10^6 \Omega \text{ cm}^2$ and $2.59 \times 10^6 \Omega \text{ cm}^2$. Although decreasing in resistance, the order of magnitude remains the same and therefore shows that their protective performance is not largely affected throughout. Figure 7.6 shows a graphical representation of the resistance values. Samples 1:12, 1:16, and 1:24 increase in resistance from 1 to 72 h, and then decrease between 72 h and 168 h, with sample 1:14 having the highest overall resistance of all the SiO_x coatings of $4.86 \times 10^7 \Omega \text{ cm}^2$ after 72 h.

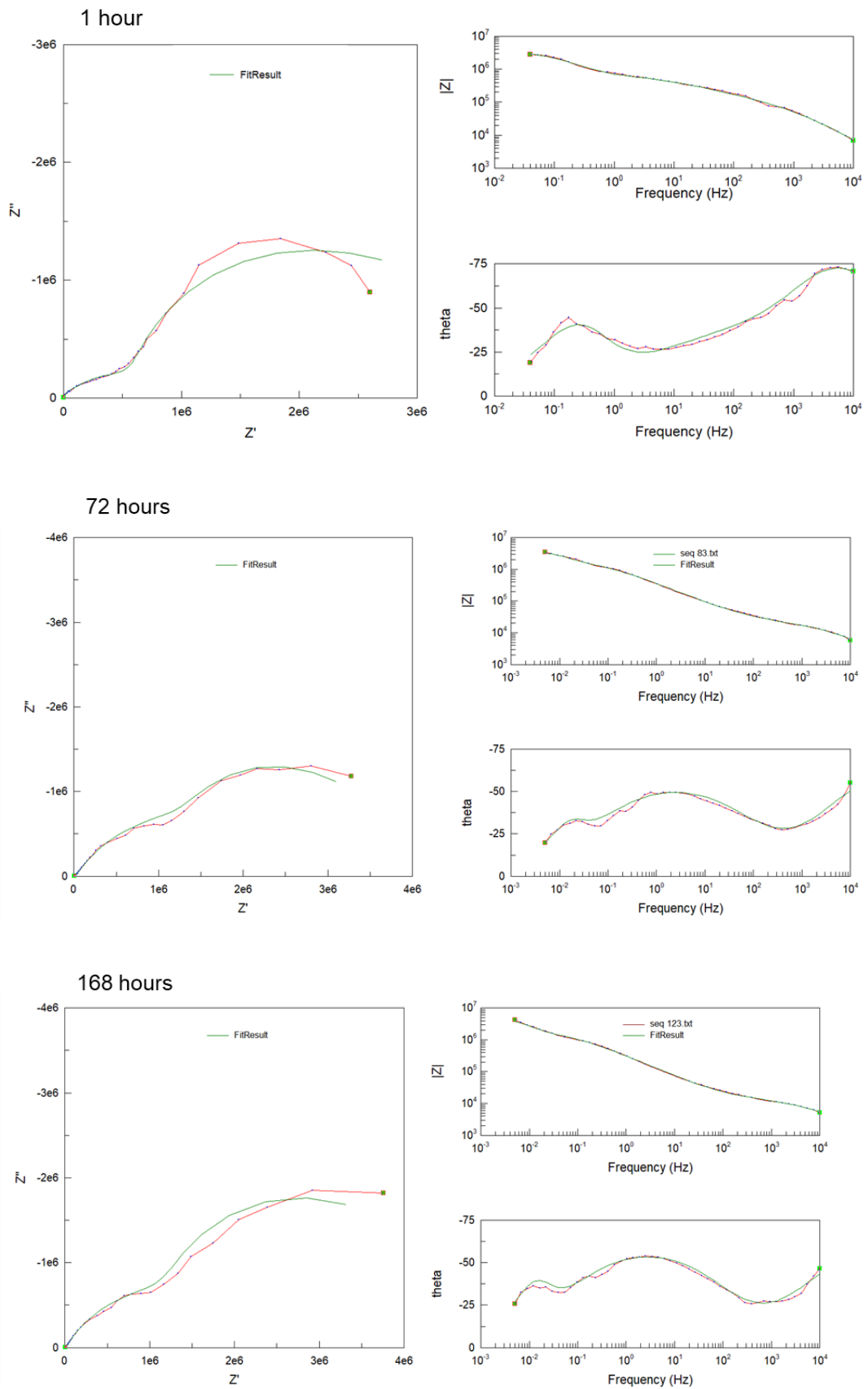


Figure 7.5. Nyquist and Bode equivalent circuit fits for the SiO_x coated sample with HMDSO: O_2 ratio 1:20 and a DOE thickness of 2μ , at 1 h, 72 h and 168 h.

Table 7.2. The coating resistance and capacitance values for the SiO_x coated samples, with varying HMDSO:O₂ ratios and a DOE thickness of 2 μm, calculated from EIS spectra.

HMDSO:O ₂ ratio	R _s (Ω cm ²)	R _c (Ω cm ²)x10 ⁵	CPE _c		R ₂ (Ω cm ²) x10 ⁵	CPE ₂		R _{ct} (Ω cm ²) x10 ⁵	CPE _{dl}	
			Y _o Ω ⁻¹ cm ⁻² s ⁿ	n		Y _o Ω ⁻¹ cm ⁻² s ⁿ	n		Y _o Ω ⁻¹ cm ⁻² s ⁿ	n
1 Hour										
1:10	1450	1.59	2.94x10 ⁻⁹	1.0	7.46	9.72x10 ⁻⁸	1.0	2.53	4.70x10 ⁻⁶	0.7
1:12	437	0.27	1.71x10 ⁻⁸	0.8	0.47	1.33x10 ⁻⁶	0.6	2.79	2.37x10 ⁻⁷	0.8
1:14	3340	1.54	3.94x10 ⁻⁹	1.0	4.92	1.40x10 ⁻⁷	0.8	92.2	2.31x10 ⁻⁷	0.8
1:16	5990	0.05	3.31x10 ⁻¹²	1.0	5.99	1.23x10 ⁻⁸	0.8	91.8	4.09x10 ⁻⁸	0.9
1:20	1740	0.63	2.44x10 ⁻⁹	1.0	8.55	2.15x10 ⁻⁷	0.5	33.6	3.89x10 ⁻⁷	0.9
1:24	480	0.28	4.18x10 ⁻⁸	0.8	0.008	4.07x10 ⁻⁷	1.0	1.66	6.25x10 ⁻⁶	0.8
1:36	6450	0.15	2.11x10 ⁻¹¹	1.0	4.64	1.57x10 ⁻⁸	0.9	1.22	1.21x10 ⁻⁶	1.0
72 Hours										
1:10	994.5	0.27	1.96x10 ⁻⁹	1.0	5.27	2.42x10 ⁻⁸	0.6	62.7	1.93x10 ⁻⁶	0.9
1:12	145.2	0.12	2.41x10 ⁻⁸	0.8	1.25	1.79x10 ⁻⁶	0.6	4.02	1.64x10 ⁻⁵	0.8
1:14	3275	2.76	1.62x10 ⁻⁹	1.0	6.24	1.08x10 ⁻⁷	0.8	486	2.08x10 ⁻⁷	0.8
1:16	4489	0.14	1.35x10 ⁻¹⁰	1.2	33.6	4.54x10 ⁻⁸	0.6	118	4.26x10 ⁻⁷	0.9
1:20	996.44	0.24	4.12x10 ⁻⁸	0.7	36.7	7.90x10 ⁻⁷	0.6	24.2	8.60x10 ⁻⁶	1.2
1:24	433.4	0.39	2.04x10 ⁻⁸	0.8	48.6	2.03x10 ⁻⁷	0.7	76.8	2.72x10 ⁻⁶	0.9
1:36	4273	2.44	1.39x10 ⁻⁹	1.0	0.95	1.76x10 ⁻⁷	0.7	5.93	2.39x10 ⁻⁶	0.8
168 Hours										
1:10	1185	0.12	1.92x10 ⁻⁹	1.0	4.06	2.84x10 ⁻⁷	0.6	62.8	4.79x10 ⁻⁶	0.8
1:12	345.3	0.19	1.77x10 ⁻⁷	0.7	1.69	1.54x10 ⁻⁶	0.5	3.42	4.73x10 ⁻⁵	1.0
1:14	1896	2.24	2.79x10 ⁻⁹	1.0	3.49	6.64x10 ⁻⁷	0.8	116	1.52x10 ⁻⁶	0.9
1:16	3442	0.80	2.48x10 ⁻⁹	0.9	1.41	3.77x10 ⁻⁸	0.7	72.0	1.16x10 ⁻⁶	0.9
1:20	1084.8	0.15	7.59x10 ⁻⁸	0.7	1.57	9.01x10 ⁻⁷	0.7	25.9	8.30x10 ⁻⁶	1.1
1:24	951.6	0.18	6.14x10 ⁻⁹	0.9	15.9	3.22x10 ⁻⁷	0.6	63.7	1.61x10 ⁻⁶	0.8
1:36	4628	3.53	1.29x10 ⁻⁹	1.0	1.55	5.15x10 ⁻⁸	0.9	9.00	4.88x10 ⁻⁶	0.9

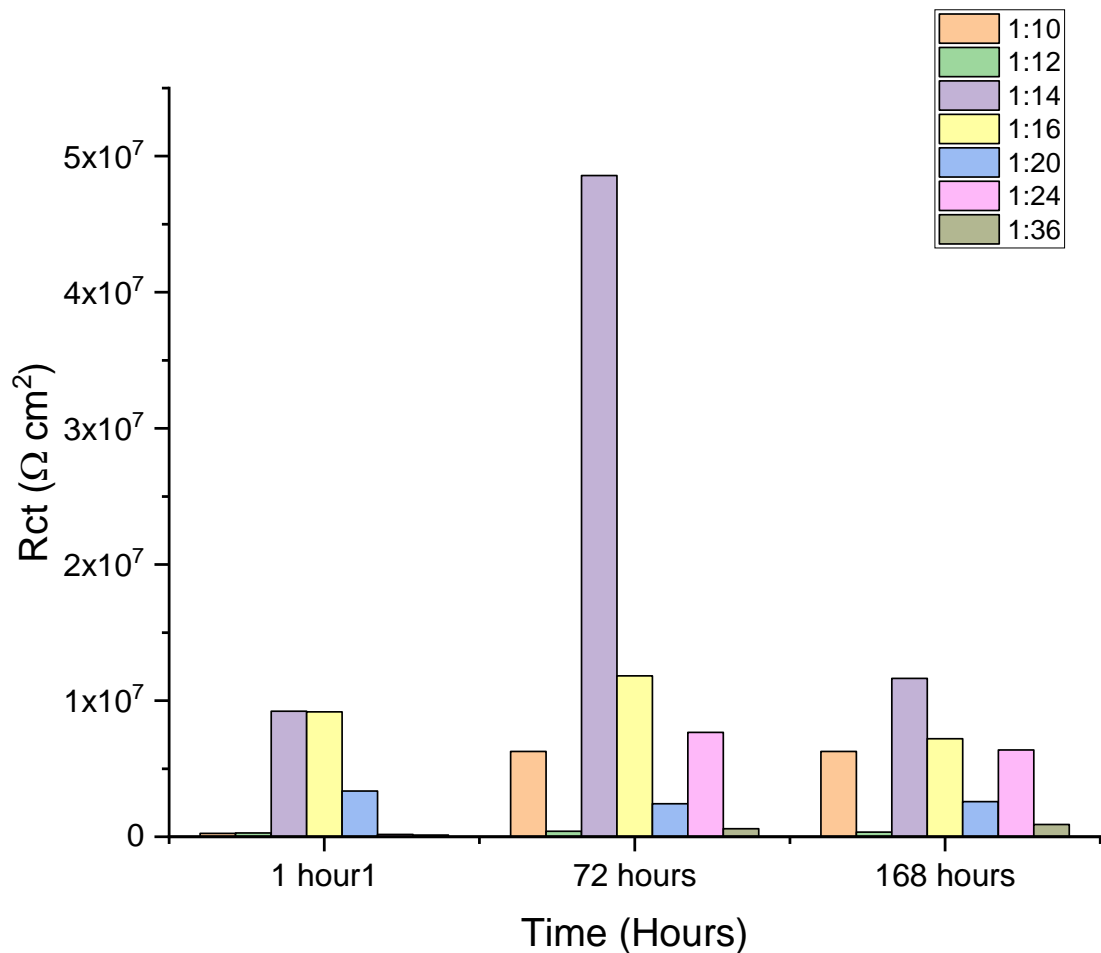


Figure 7.6 The R_{ct} ($\Omega \text{ cm}^2$) of the SiO_x coated samples with varying HMDSO: O_2 ratios and a DOE thickness of $2 \mu\text{m}$, calculated from the EIS data after 1 h, 72 h and 168 h.

The increase in resistance throughout the experiment suggests that the coating is becoming more protective. Both samples 1:14 and 1:16 see an increase in R_{ct} by one order of magnitude, suggesting that the coatings are becoming highly protective throughout the first 72 h. Both samples then see a decrease in the R_{ct} values, with sample 1:16 having a resistance lower at 168 h ($7.2 \times 10^6 \Omega \text{ cm}^2 \text{ s}^n$) compared to after 1 h ($9.18 \times 10^6 \Omega \text{ cm}^2$). On the other hand, sample 1:14 increases in resistance from $9.22 \times 10^6 \Omega \text{ cm}^2$ after 1 hour, to $4.86 \times 10^7 \Omega \text{ cm}^2$ after 72 h, and decreases after 168 h to $1.16 \times 10^7 \Omega \text{ cm}^2$ however has a higher R_{ct} at the end of the experiment. Sample 1:14 shows the best protective ability

compared to the other SiO_x coatings, and gives the highest resistance value, suggesting that the coating itself is providing the HSS with the highest protection from the electrolyte.

The R_{ct} values for SiO_x coatings are lower than those reported by Delimi et al [170], that reported R_{ct} values of SiO_x-like coated carbon steel to be 1.00 and 1.30 MΩ cm², for coatings thicknesses 100 nm and 200 nm respectively. These values are 3 orders of magnitude larger than the values with varying HMDSO:O₂ ratios, suggesting that the MW-PECVD coatings are less protective than those deposited by PECVD. The coatings deposited by Delimi, however are 10 times thinner and the corrosive environment was a 3% NaCl aqueous solution.

The increase in R_{ct} from 1 hour to 72 hours of the experiment, may indicate that a secondary protective layer is being formed, through a diffusion-controlled corrosion mechanism, thus leading to the formation of an extra barrier layer to the substrate [182]. One potential mechanism may be through the penetration of dissociated Cl⁻ ions, from the NaCl electrolyte [255], [256]. The anion migration of chloride ions may be due to the small diameter of the ions, enabling permeation through the protective passive film. The Cl⁻ ions will move from the electrolyte/SiO_x coating interface, through to the metal/SiO_x coating interface. Once the aggressive Cl⁻ anion has reached the metal surface, breakdown of the passive coating will occur. Chloride ions within the SiO_x matrix will alter the internal structure of the coating and form a more conduction oxide. In the passive film, the chloride ions which have migrated will replace the bound water, which in turn increases the conductivity of the passive film and will eventually lead to breakdown.

The Cl⁻ ions will also penetrate through the coatings where defects and pinholes may occur and cause adsorption through the oxide film [257], [258], leading to thinning, and destruction of the oxide barrier layer. The anions will also form pits which develop at sites where oxygen that is adsorbed onto the metal surface will be replaced by the Cl⁻ ions. These chloride ions will begin to form clusters and consume the oxide, resulting in thinning, and will begin to form complexes with the metallic ions. Once this film has been destroyed, the corrosion process of the HSS begins through electrochemical processes [259], the anodic and cathodic reactions are shown in Eq 7.1 and Eq 7.2. A corrosion mechanism for the electrolyte penetration and destruction of the oxide layer is shown in Figure 7.7.

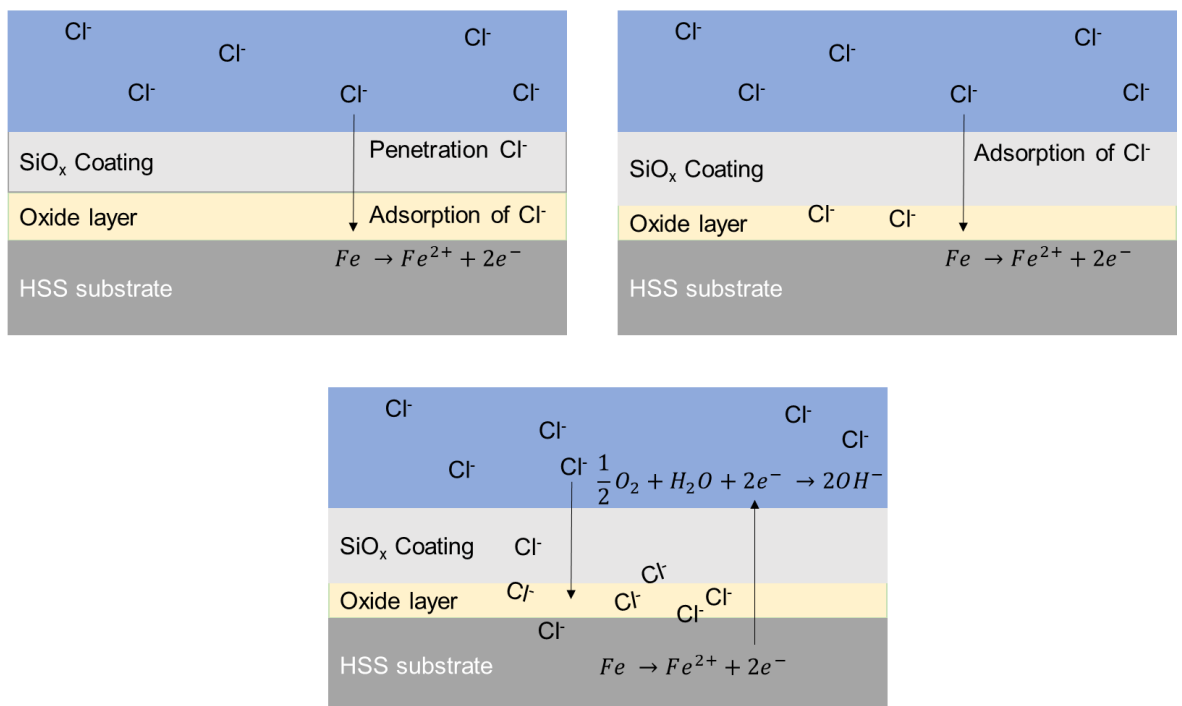
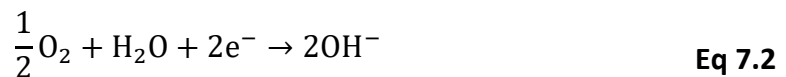


Figure 7.7 A corrosion mechanism for the reaction of NaCl with HSS, adapted from [255].

This behaviour could also be linked to the anodic polarisation curves which demonstrate some pseudo-passivation behaviour from the coatings. The decrease in resistance after the 72 h, may suggest that this barrier layer is corroding or that the SiO_x coated layer may be becoming more porous to the corrosive media throughout the duration of the experiment. The SiO_x coatings that have an overall increase in the R_{ct} from 1 h to 168 h may still have the extra barrier layer present at the end of the experiment.

The coating 1:20 shows a different behaviour compared to the other coatings within the matrix. The R_{ct} decreases within the first 72 h from $3.36 \times 10^6 \Omega \text{ cm}^2$ to $2.42 \times 10^6 \Omega \text{ cm}^2$, however, the resistance then increases from 72 h to 168 h to $2.59 \times 10^6 \Omega \text{ cm}^2$. The protective ability of the coating demonstrates an increase after 72 h, suggesting that the electrolyte may have penetrated and disturbed the coating, which then later leads into a corrosion reaction at the HSS surface, coating interface.

The crystallite sizes calculated from both the Scherrer equation, and the Williamson-Hall methods have been compared with the R_{ct} values to understand the relationship between the crystallite size and the electrochemical resistance of the SiO_x coatings. The resistance values of the coatings after the duration of the test (168 h) were used for the comparison, and are presented in Table 7.3

Table 7.3 A comparison of the coating resistance values after 168 hours, with the average crystallite sizes calculated from the Scherrer equation and Williamson-Hall plots of the SiO_x coated HSS samples at DOE thickness 2 μm.

Coating (HMDSO:O ₂)	Crystallite Size	Crystallite Size	<i>R</i> _{ct} (Ω cm ²) x10 ⁵
	(nm) Scherrer Equation	(nm) Williamson-Hall	
1:10	24.2	21.5	62.8
1:12	25.9	28.9	3.42
1:14	28.0	31.4	116
1:16	31.5	23.9	72.0
1:20	28.1	30.5	25.9
1:24	26.7	25.5	63.7
1:36	27.9	21.3	9.0

The sample with the lowest resistance after 168 hours is 1:12, at 3.42x10⁵ Ω cm². From the Scherrer calculation, it also has one of the lowest crystallite sizes (25.9 nm). A linear regression fit for the *R*_{ct} values vs the average crystallite sizes (nm) calculated from both the Scherrer equation and Williamson-Hall plots are shown in Figure 7.8 and Figure 7.9 respectively. Samples 1:20 and 1:24 have the highest resistance values after 168 h at 1.57 x10⁵ Ω cm² and 1.59x10⁶ Ω cm². The comparison of their respective crystallite sizes calculated from the Scherrer equation are also similar at 28.1 nm and 26.7 nm for samples 1:20 and 1:24 respectively. However, further comparison of the crystallite sizes with the resistance values does not account for a trend with the values for the *R*_{ct}. Therefore, the average crystallite sizes of the SiO_x coatings does not have an effect on the corrosion performance of the coatings. This is also shown from the regression fits with fitted with a line of best fit. There is no clear trend to suggest

that the resistance of the coatings is dependent on the crystallite sizes of the SiO_x coatings.

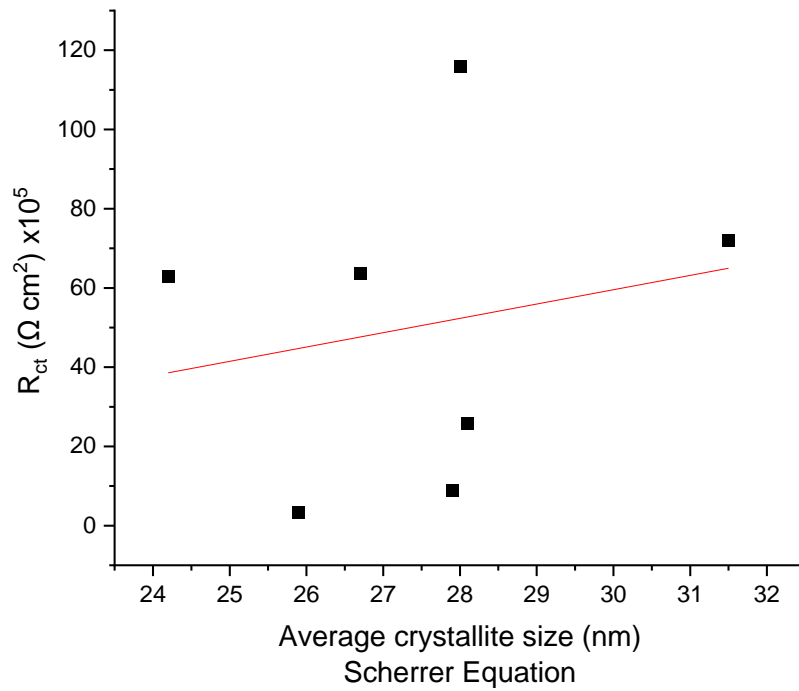


Figure 7.8. Regression fit of the average crystallite sizes (nm) calculated from the Scherrer equation vs the R_{ct} ($\Omega \text{ cm}^2$) $\times 10^5$.

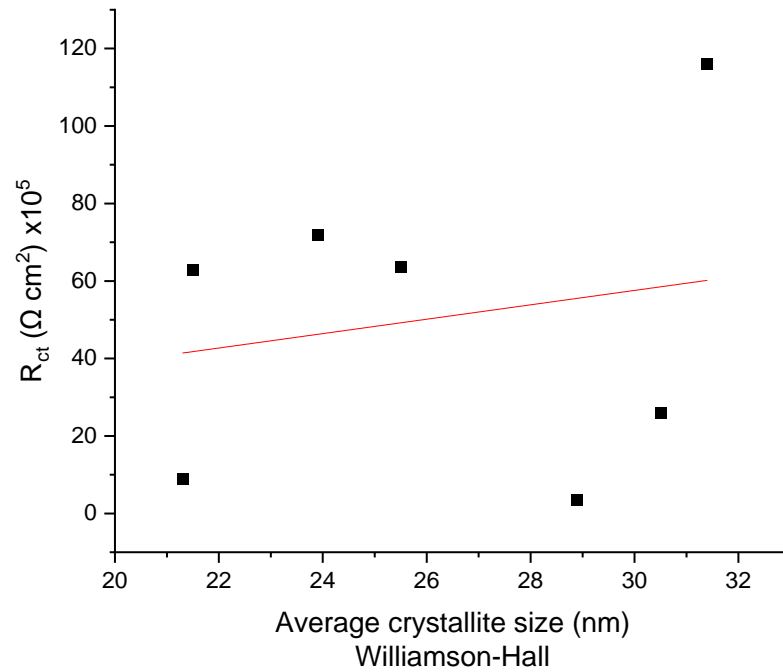


Figure 7.9 Regression fit of the average crystallite sizes (nm) calculated from the Williamson-Hall plots vs the R_{ct} ($\Omega \text{ cm}^2$) $\times 10^5$.

The capacitance values at the double layer for the SiO_x samples can be found in Table 7.2 and Figure 7.10. A lower capacitance value for a coating indicates that the coating has more protective abilities, and a higher capacitance value indicates the coating will be less protective.

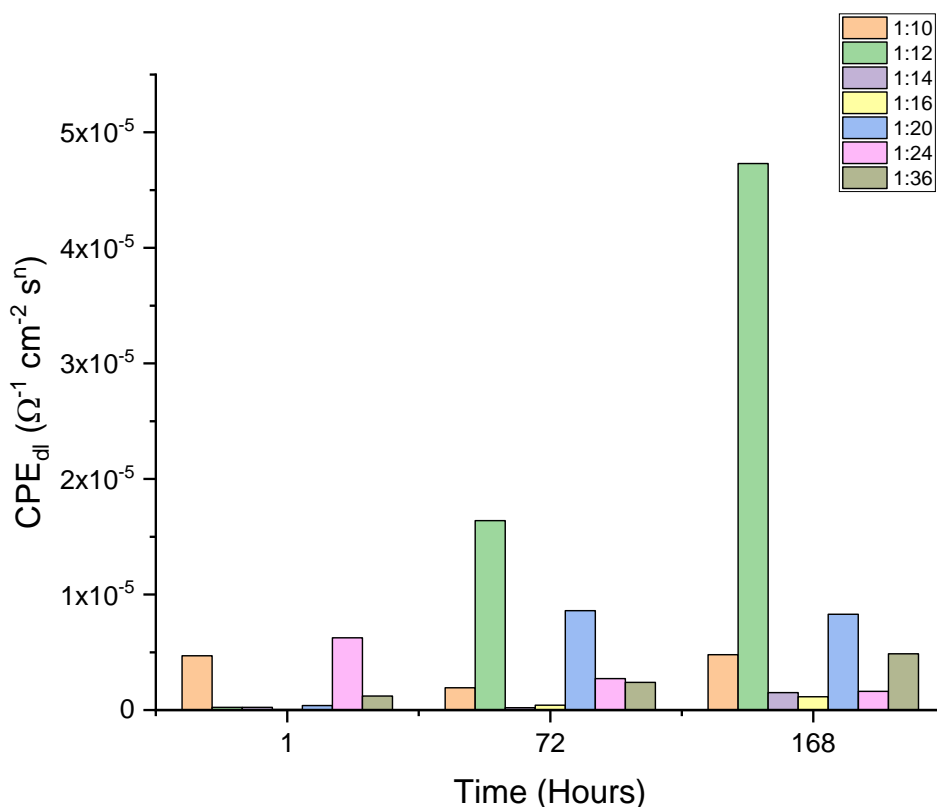


Figure 7.10. A comparison of the CPE_{dl} (Ω⁻¹ cm⁻² sⁿ) values of the SiO_x coated samples with varying HMDSO:O₂ ratios and a DOE thickness of 2 μm, calculated from the EIS data at 1 h, 72 h and 168 h.

The sample with ratio 1:12 has the largest capacitance, peaking at 4.73x10⁻⁵ Ω⁻¹ cm⁻² sⁿ after 72 h. This is in line with the corresponding resistance values, as coating 1:12 has the lowest resistance when compared to the other coatings. Sample ratio 1:16 has the lowest capacitance at the start of the experiment with a value of 4.09x10⁻⁸ Ω⁻¹ cm⁻² sⁿ, however, this value increases through the duration of the experiment to 4.26x10⁻⁶ Ω⁻¹ cm⁻² sⁿ at 72 h and to 1.16x10⁻⁶ Ω⁻¹ cm⁻² sⁿ after 168 h. These capacitance values suggest that the coating is

becoming less protective throughout the experiment, and shows some agreement with the resistance value which also decreases from the start to the end of the EIS duration.

Based on both the resistance and capacitance values of the coatings, the least protective coatings are 1:12 and 1:36 as they both exhibit a decrease in resistance over time, and an increase in their capacitance. Therefore, both coatings are becoming less protective and will lead to failure over longer periods of time. The most protective coating is 1:14 as it increases in resistance throughout the experiment and decreases in the capacitance. It also exhibits the highest resistance value at 168 hours. Thus, showing the best corrosion protection of all the coatings.

The CPE_{dl} values have been compared with the average crystallite sizes calculated from both the Scherrer equation and the Williamson-Hall method, in order to understand further the trend in resistance values. The values are shown in Table 7.4, Figure 7.11 for the Scherrer equation method and Figure 7.12 for the Williamson-Hall method.

Table 7.4 A comparison of the average crystallite sizes with the capacitance values from the EIS data at 168 hours.

Coating (HMDSO:O ₂)	Crystallite Size (nm)		CPE_{dl} (F cm ⁻²)
	Scherrer Equation	Williamson-Hall	
1:10	24.2	21.5	4.79x10 ⁻⁶
1:12	25.9	28.9	4.73x10 ⁻⁵
1:14	28.0	31.4	1.52x10 ⁻⁶
1:16	31.5	23.9	1.16x10 ⁻⁶
1:20	28.1	30.5	8.30x10 ⁻⁶
1:24	26.7	25.5	1.61x10 ⁻⁶
1:36	27.9	21.3	4.88x10 ⁻⁶

The graphs of the CPE_{dl} values versus the crystallite sizes calculated from both the Scherrer equation and Williamson-Hall methods are presented in Figure 7.11 and Figure 7.12, respectively. Both graphs show that there is no correlation between the average crystallite sizes and the CPE_{dl} . As the average crystallite size increases, the graphs show that the CPE values remain similar and do not increase nor decrease with size. A study by Qi et al found that a reduced crystallite size of nickel-graphene oxide nano-composite coatings can effectively improve the corrosion resistance of the coatings [260]. Based on this research, as the crystallite sizes increase, a decrease in the CPE_{dl} value would be expected. The only sample that would somewhat fit this hypothesis would be the coating 1:12 as it has the lowest corrosion resistance of all the coatings, and from the W-H method, has a larger crystallite size (28.9 nm).

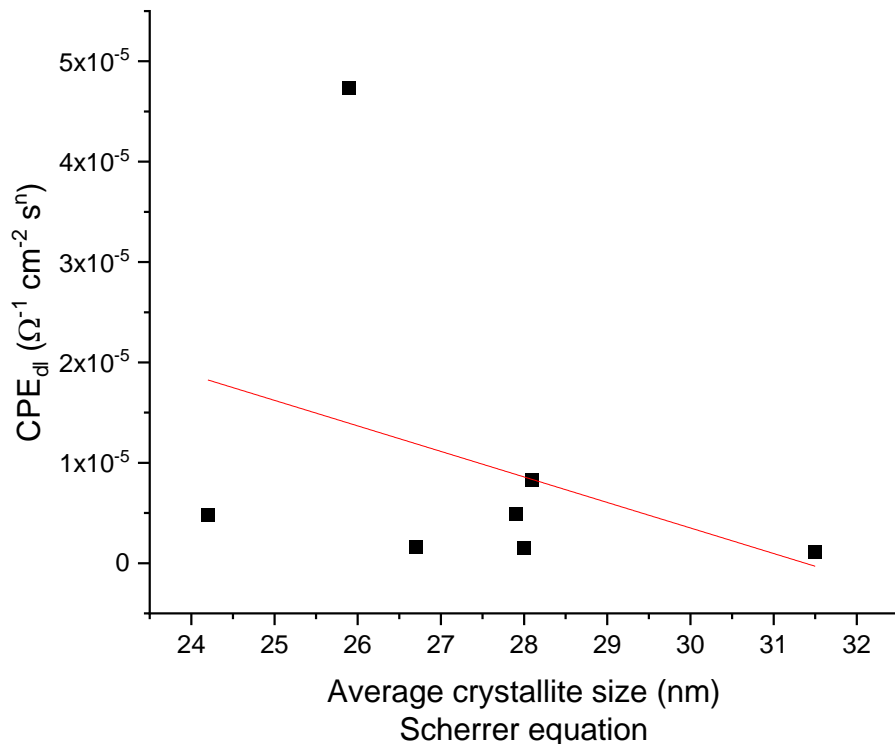


Figure 7.11 A comparison of the average crystallite sizes (nm) of the SiO_x coatings calculated from the Scherrer equation, versus the CPE_{dl} values ($\Omega^{-1} \text{ cm}^2 \text{ s}^n$).

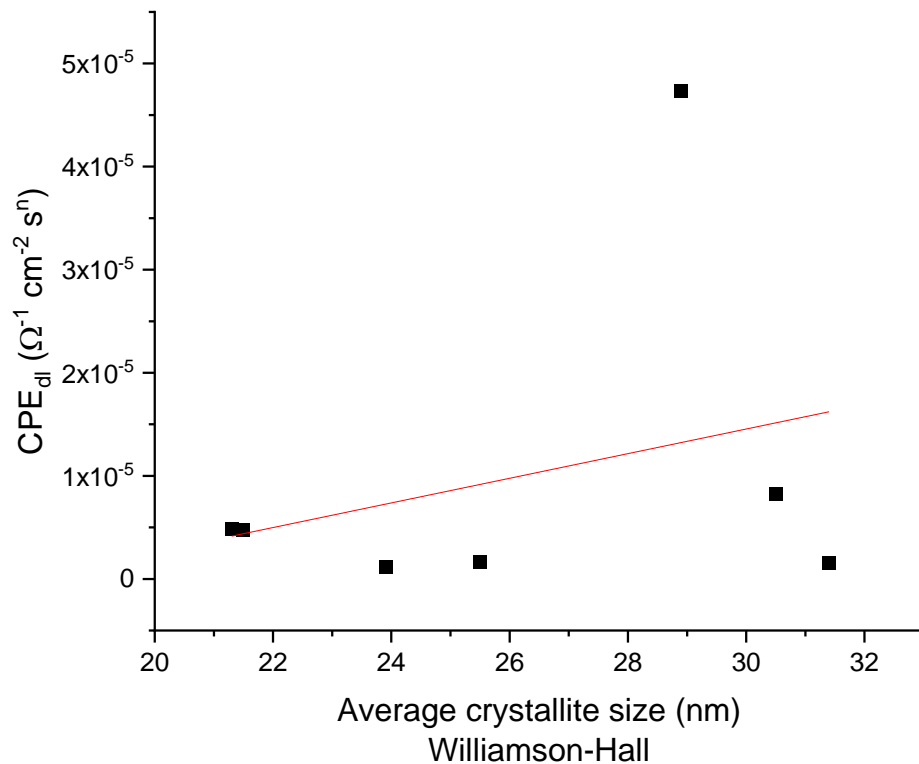


Figure 7.12 A comparison of the average crystallite sizes (nm) of the SiO_x coatings calculated from the Williamson-Hall plots, versus the CPE_{dl} values (Ω⁻¹ cm⁻² sⁿ) determined from the EIS data.

7.2.2.1 Corrosion mechanisms based on resistance and capacitance values

The increase in resistance values of the coatings 1:14, 1:16, 1:20 and 1:24 from 1 hour to 72 h, followed by a decrease in the resistance from 72 h to 168 h has been hypothesised to be due to the formation of an extra corrosion layer, which then decomposes throughout the duration of the experiment. The formation of this layer may lead to the increased corrosion resistance, thus increasing the barrier properties of the coating during the first 72 h. Another possibility for the increase in the corrosion resistance may be due to the chloride ions filling any pores and defects within the coating. This will in turn lead to less electrolyte penetrating through to the metal surface and therefore lead to an increase in resistance. A schematic highlighting a mechanism for the formation of the barrier

coating, and increased resistance values between 1 and 72 h is shown in Figure 7.13. The electrolyte may penetrate through pinholes or defects within the coating structure, through to the substrate surface. This may then lead to cracks forming within the coating, allowing the HSS to react with the electrolyte. Due to the nature of high-speed steel (HSS), the corrosion barrier layer could be formed from a reaction with iron [261] or from a reaction with the chromium (Cr) content.

The reaction of iron with water or oxygen is a slow process, especially at room temperature, therefore for this reaction to occur a considerable amount of heat is needed. As the EIS experiments were performed at room temperature, it is unlikely that the corrosion layer formed is iron oxide. The oxidation of chromium (Cr), on the other hand, has been reported to be enhanced in the presence of NaCl, with the main reaction product being Cr_2O_3 [262]. Mori et al [263] also reported the formation of chromium containing corrosion products during the reaction of steel with NaCl and H_2O .

The corrosion layer shown in the schematic can be hypothesised to be Cr_2O_3 from the reaction of oxygen with the HSS. The mechanism for this corrosion layer depositing on the surface of the substrate could be due to the defects or pores within the coating. Cracks will begin to form, allowing the transportation of NaCl to the surface, and also the transportation of excess oxygen, which may further react with the Cr in the HSS. Further investigation to determine whether a corrosion mechanism and product is formed on the substrate/coating interface is determined in section 7.4.

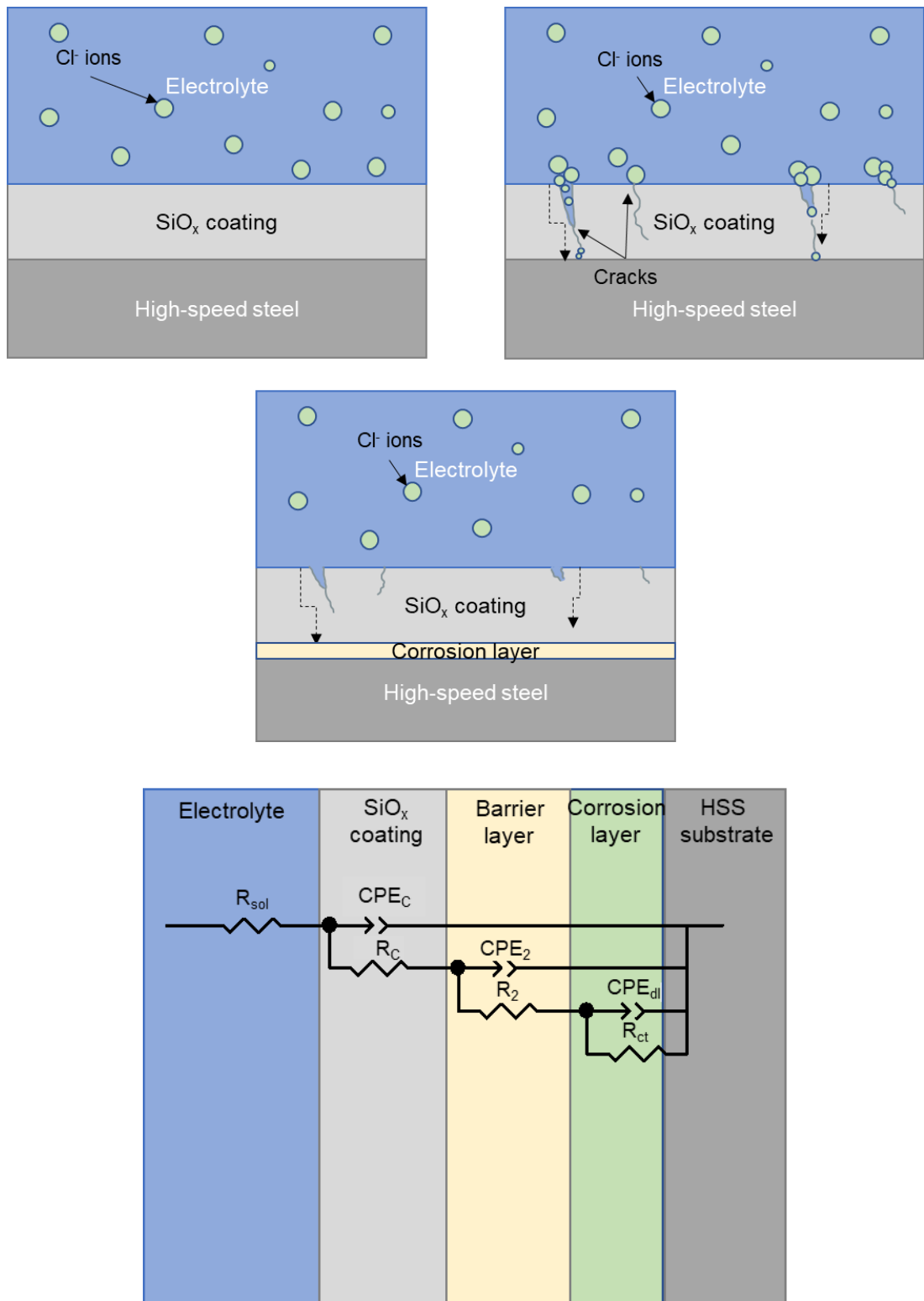
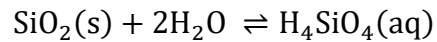


Figure 7.13. A schematic highlighting the three capacitive loops – CPE_C for the coating, CPE_2 for the corrosive layer, and CPE_{dl} for the double layer, determined from fitting equivalent circuits to Nyquist and Bode plots.

A second avenue for the increase in the resistance of the coatings at 72 hours may be due to the SiO_x coating being involved, through dissolution of the coating. The reaction of SiO₂ with water leads to the formation of silicic acid [264], shown in Eq 7.3. This reaction can be accelerated by the sodium chloride solution.



Eq 7.3

Unlike quartz, amorphous silica dissolution rates are 10 times faster and enhanced even further with the introduction of NaCl at near neutral pH [265]. The rate at which dissolution occurs is dependent on the SiO₄ tetrahedral network [266]. Due to the SiO_x coatings being of amorphous nature with some crystallinity present, the dissolution rates will be slower than those of amorphous silica. Therefore, the increase in corrosion resistance for the SiO_x coatings 1:10, 1:12, 1:14, 1:24 and 1:36 could be due to the formation of the corrosion barrier layer, followed by the dissolution of the SiO_x coating into silicic acid.

7.3 The effect of the corrosion resistance of SiO_x coated HSS with varying thickness

The thickness of a coated surface can influence the corrosion resistance of a coating. Increasing the coating thickness can improve the corrosion resistance of the coated surface. This section will look at the EIS results of the sample coated at HMDSO:O₂ ratio 1:12, at different coating thicknesses. The sample 1:12 was chosen due to being the closest to that of stoichiometric SiO₂, and to investigate whether the low resistance values at DOE 2 μm, resonate throughout the different thicknesses. The coating thicknesses studied in this section are DOE thickness

1 μm , 2 μm , 3.5 μm and 5 μm . The coating resistance and capacitance values for the 1:12 coatings with different thicknesses at 1 hour, 72 hours and 168 hours are presented in Table 7.5, and the R_{ct} values are plotted in the graph shown in Figure 7.14.

The coating with the highest resistance is the coating with DOE thickness 5 μm , peaking at $1.45 \times 10^7 \Omega \text{ cm}^2$ after 72 hours. The coating with the lowest resistance throughout the whole experiment has a 2 μm thickness, by one order of magnitude difference. The coating with the lowest thickness (1 μm), shows good corrosion protection when compared with the 2 μm coating. However, the R_{ct} of the 1 μm coating decreases throughout the experiment from $6.83 \times 10^6 \Omega \text{ cm}^2$ after 1 h, to $2.36 \times 10^6 \Omega \text{ cm}^2$ after 72 h then $1.30 \times 10^6 \Omega \text{ cm}^2$ after 168 h. Surprisingly, the R_{ct} after 1 hour is the highest for the 1 μm coating. The higher R_{ct} may be due to the electrolyte penetrating through the coating at a faster rate, due to having a lower thickness and therefore a shorter pathway for the electrolyte to reach the HSS surface. The coatings with a thickness of 2, 3.5 and 5 μm , increase in resistance throughout the experiment. This increase suggests that the coatings are becoming more protective throughout, and it is expected that the coating with the highest resistance would have a thicker coating. The 5 μm coating has the largest resistance value after 168 h ($9.71 \times 10^6 \Omega \text{ cm}^2$), when compared to the other coatings – so proves to have the best corrosion resistance.

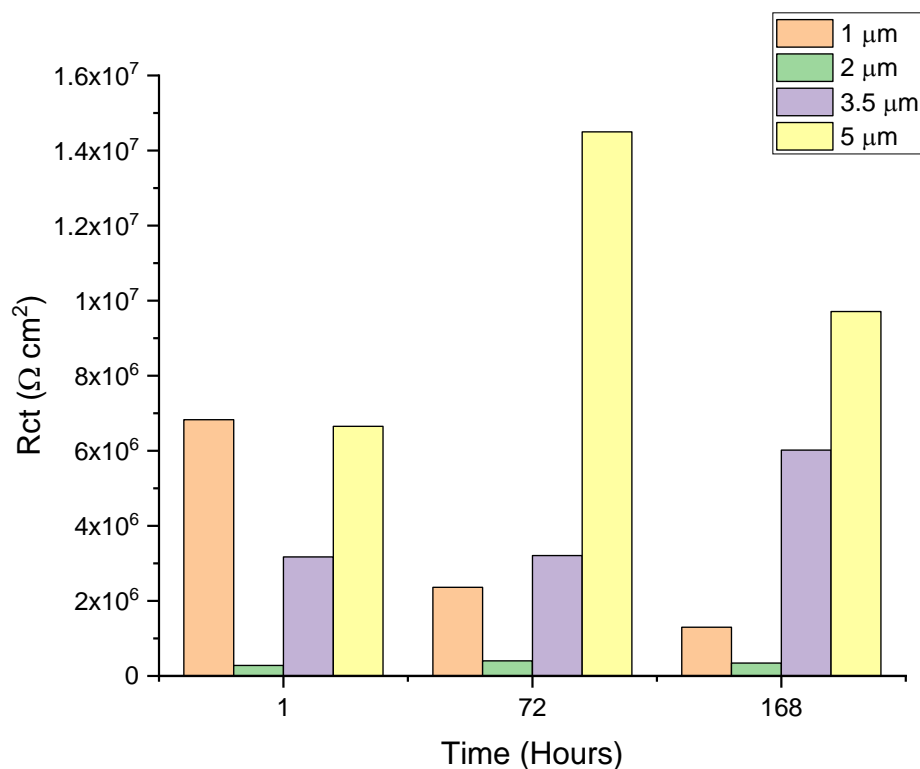


Figure 7.14. A comparison of the coating resistance (R_{ct}) over time for the SiO_x coatings with a HMDSO: O_2 ratio 1:12 and varying thicknesses.

R_{ct} values reported by Ning et al. [24] are comparable to the R_{ct} measurements after 1 hour. Ning et al reported values of $3.077 \times 10^6 \text{ } \Omega \text{ cm}^2$, $5.365 \times 10^6 \text{ } \Omega \text{ cm}^2$ and $1.898 \times 10^7 \text{ } \Omega \text{ cm}^2$ for silica coating with a thickness of 188.6 nm, 267.9 nm and 322.7 nm, respectively. The measurements were taken after a 0 hour immersion time, and show an increased R_{ct} with an increase in the thickness of the coating. The coating deposited at 1 μm , after 1 hour immersion does not follow this trend, and has the highest resistance when compared to the thicker coatings. The data reported by Ning, uses a corrosive environment of geothermal water and a temperature of 90°C , however, the corrosion protection trend of the coatings is comparable to that of the SiO_x coated HSS.

Table 7.5. Resistance and capacitance values for HMDSO:O₂ sample 1:12, at different coating thicknesses (1 μm, 2 μm, 3.5 μm and 5 μm). Values are evaluated at 1 hour, 72 hours and 168 hours.

Thickness (μm)	R_s (Ω cm ²)	R_{SiO_x} (Ω cm ²)x10 ⁵	CPE_{SiO_x}		R_{corr} (Ω cm ²) x10 ⁵		CPE_{corr}		R_{ct} (Ω cm ²) x10 ⁵		CPE_{dl}	
			Y_o Ω ⁻¹ cm ⁻² s ⁿ	n	Y_o Ω ⁻¹ cm ⁻² s ⁿ	n	Y_o Ω ⁻¹ cm ⁻² s ⁿ	n	Y_o Ω ⁻¹ cm ⁻² s ⁿ	n		
1 hour												
1	6637	0.49	4.25x10 ⁻⁸	0.8	1.54	7.54x10 ⁻⁸	0.9	68.3	1.84x10 ⁻⁷	0.9		
2	437.2	0.27	1.71x10 ⁻⁸	0.8	0.47	1.33x10 ⁻⁶	0.6	2.79	2.37x10 ⁻⁷	0.8		
3.5	2782	3.19	2.9x10 ⁻⁹	0.9	17.4	2.62x10 ⁻⁸	0.7	31.7	1.07x10 ⁻⁷	1.0		
5	6637	0.94	8.48x10 ⁻¹¹	1.1	6.11	8.31x10 ⁻⁸	0.5	66.5	1.04x10 ⁻⁷	1.0		
72 hours												
1	4619	0.095	8.55x10 ⁻⁹	0.9	0.91	2.82x10 ⁻⁶	0.5	23.6	3.39x10 ⁻⁵	0.9		
2	145.2	0.12	2.41x10 ⁻⁸	0.7	1.25	1.79x10 ⁻⁶	0.6	4.02	1.64x10 ⁻⁵	1.0		
3.5	3612	2.43	9.58x10 ⁻¹⁰	1.0	10.8	1.58x10 ⁻⁸	0.8	32.1	3.25x10 ⁻⁶	0.9		
5	4619	0.54	3.18x10 ⁻¹⁰	1.1	4.23	1.45x10 ⁻⁷	0.6	145	1.15x10 ⁻⁶	0.9		
168 hours												
1	5858	0.092	4.87x10 ⁻⁷	0.5	0.096	5.62x10 ⁻⁶	0.7	13.0	4.52x10 ⁻⁵	0.9		
2	345.3	0.19	1.77x10 ⁻⁷	0.7	1.69	1.54x10 ⁻⁶	0.5	3.42	4.73x10 ⁻⁵	1.0		
3.5	4479	0.28	1.19x10 ⁻¹⁰	1.2	7.22	1.40x10 ⁻⁸	0.7	60.2	4.75x10 ⁻⁶	0.9		
5	5858	0.26	5.52x10 ⁻¹¹	1.3	3.83	1.23x10 ⁻⁷	0.6	97.1	1.69x10 ⁻⁶	0.9		

The capacitance (CPE_{dl}) of the coatings with different thicknesses varies over time, as shown in Table 7.5 and Figure 7.15. All coating thicknesses present an increase in the capacitance values throughout the experiment, with coatings deposited at 1 μm and 2 μm exhibiting an increase in capacitance by 2 orders of magnitude from $1.18 \times 10^{-7} \Omega^{-1} \text{cm}^{-2} \text{s}^n$ and $2.3 \times 10^{-7} \Omega^{-1} \text{cm}^{-2} \text{s}^n$ to $4.52 \times 10^{-5} \Omega^{-1} \text{cm}^{-2} \text{s}^n$ and $4.73 \times 10^{-5} \Omega^{-1} \text{cm}^{-2} \text{s}^n$, respectively. The coatings deposited at 3.5 μm and 5 μm saw an increase in capacitance values by 1 order of magnitude from, $1.07 \times 10^{-7} \Omega^{-1} \text{cm}^{-2} \text{s}^n$ and $1.04 \times 10^{-7} \Omega^{-1} \text{cm}^{-2} \text{s}^n$ to $4.75 \times 10^{-6} \Omega^{-1} \text{cm}^{-2} \text{s}^n$ and $1.69 \times 10^{-6} \Omega^{-1} \text{cm}^{-2} \text{s}^n$, respectively. The increases in the capacitance values shows that the coatings are becoming less protective throughout the experiment, and coatings with thicknesses 1 and 2 μm are the least protective.

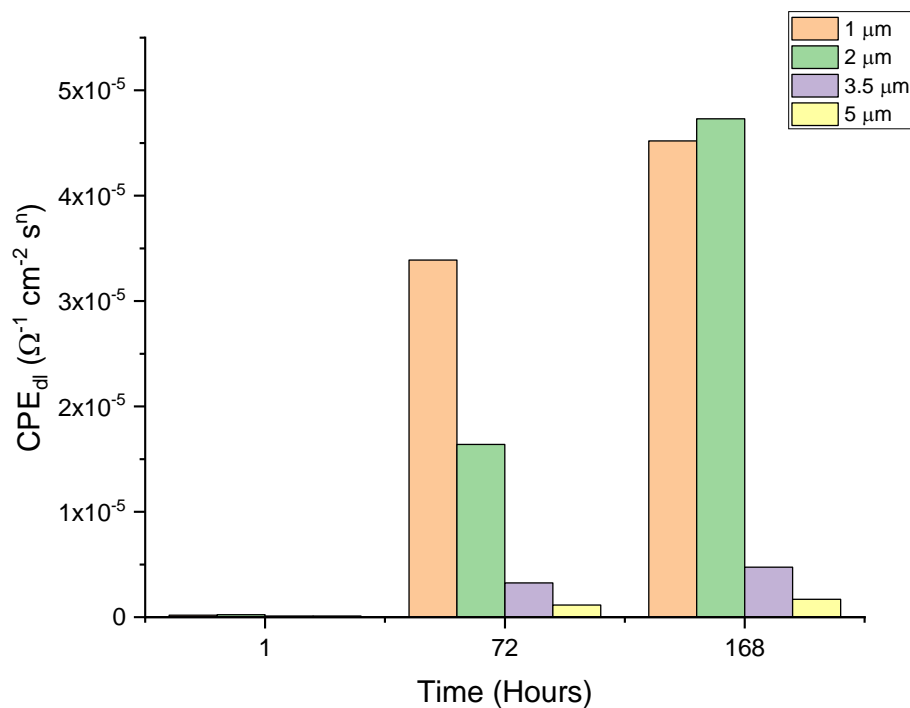


Figure 7.15. A comparison of the CPE_{dl} values over time (1 h, 72 h and 168 h) for the SiO_x coatings with HMDSO: O_2 ratio 1:12 and varying thicknesses.

The lowest capacitance is exhibited from the sample coated at 5 μm , and remains the lowest throughout the experiment. This coating thickness shows the best

corrosion performance due to having the largest R_{ct} after 168 hours and the smallest capacitance. The coating with a thickness of 2 μm shows the least corrosion protection due to the low and decreasing resistance values, and the high and increasing capacitance values.

7.4 Analysis of samples after corrosion tests

Following the EIS experiments to determine the resistance and capacitance of the coatings, a sample was chosen to be analysed using SEM with EDX and also TEM. As the results from the analysis of the EIS data with varying HMDSO:O₂ ratios showed an increase in resistance from 1-72 hours, followed by a decrease, the sample with ratio 1:20 with a thickness of 2 μm was chosen to assess the behaviour of the coatings. With sample 1:20 having one of the highest resistance values, but also showing the trend of increasing resistance between 1 and 72 hours, it was chosen to determine the hypothesis proposed with regards to the corrosion layer formation.

7.4.1 Mechanical characterisation of the SiO_x coatings after the EIS experiments

The impact of the SiO_x coatings being exposed to the NaCl solution for 168 h can lead to the mechanical properties of the coatings being changed. The hardness values for the post-EIS coatings are given in Table 7.6, with a comparison to the hardness values prior to EIS. The hardness of the coatings at HMDSO:O₂ ratios 1:14, 1:16, 1:20 and 1:24 decrease after the EIS experiments. The reasoning for the decrease may be due to the electrolyte and the corrosion test weakening the coating structure through electrolyte penetration of the coatings, leading to the formation of an oxide layer due to reaction of the electrolyte with the HSS. The hardness of the coatings 1:10 and 1:12 remains the same prior to EIS and after.

Table 7.6 A comparison of the hardness of the SiO_x coatings with varying HMDSO:O₂ ratios and a DOE thickness of 2 μm, prior to EIS and after EIS (168 h).

HMDSO:O₂ ratio	Post-EIS Hardness (GPa)	Pre-EIS Hardness (GPa)
1:10	4.7 ± 1.2	5.9 ± 1.0
1:12	5.2 ± 0.5	5.1 ± 0.5
1:14	1.7 ± 0.1	4.6 ± 0.2
1:16	2.2 ± 0.1	5.0 ± 0.4
1:20	2.3 ± 0.1	5.9 ± 0.8
1:24	1.3 ± 0.1	5.9 ± 0.5

7.4.2 SEM cross sectional analysis with EDX analysis

Following the corrosion tests, the appearance of the coating remained unchanged, with no visible signs of cracking or delamination. Therefore, focused ion beam (FIB) cross sectional analysis was carried out to study the chemistry of the coating at the coating/substrate interface, after the 168 hour EIS experiment. The SEM images are shown in Figure 7.16, and are shown for sample with HMDSO:O₂ ratio 1:20 with a DOE thickness of 2 μm, both before and after EIS experiments and at different magnifications.

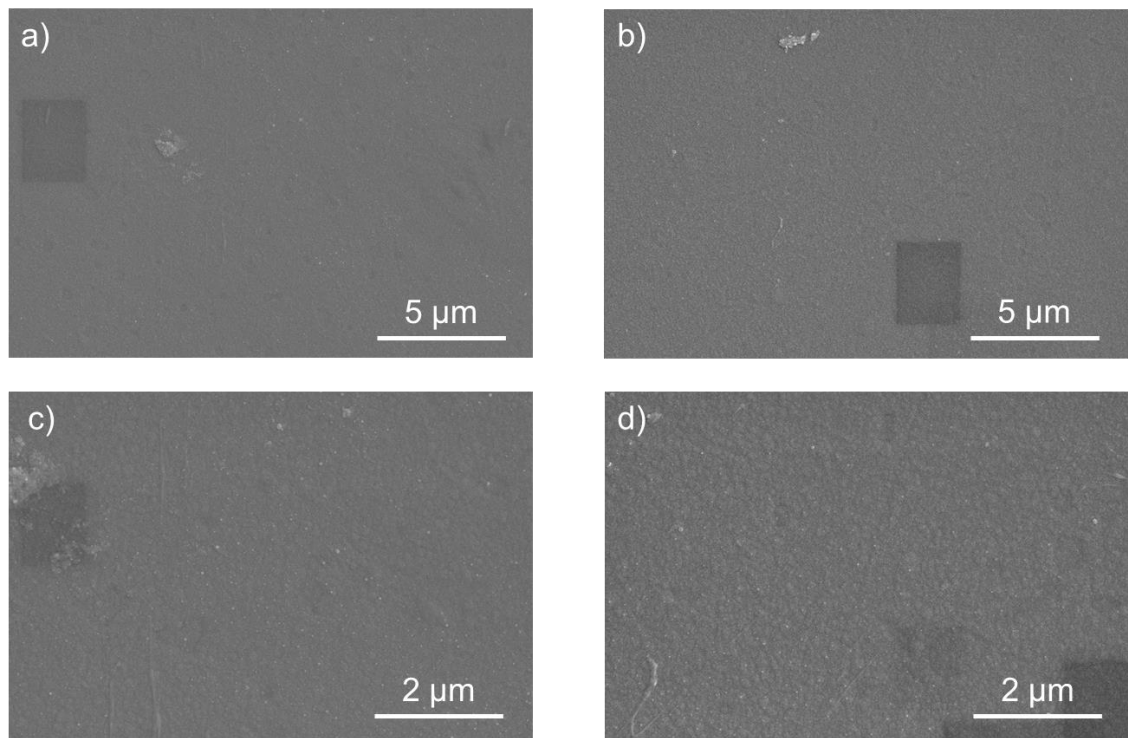


Figure 7.16. SEM images for the sample with HMDSO:O₂ ratio 1:20, and DOE thickness of 2 μm, pre and post EIS experiments at different magnifications. a) 1:20 before EIS and b) 1:20 after EIS at 20 000x magnification, c) 1:20 before EIS and d) 1:20 after EIS at 50 000x magnification.

From the images, there is a clear change in the surface texture and roughness when comparing the images before EIS and after EIS experiments. The images show no clear signs of delamination after the experiment, but due to the change in surface texture and the water uptake values for sample 1:20, the electrolyte may have penetrated the coating and created swelling. Figure 7.17 shows the FIB cross sections of the sample 1:20 at DOE thickness 2 μm. The thickness of each sample has been applied, with a thickness of 1.76 μm before EIS and 1.80 μm after EIS. The slight change in the thickness could be from the penetration of the electrolyte through the coating, resulting in some water uptake by the coatings.

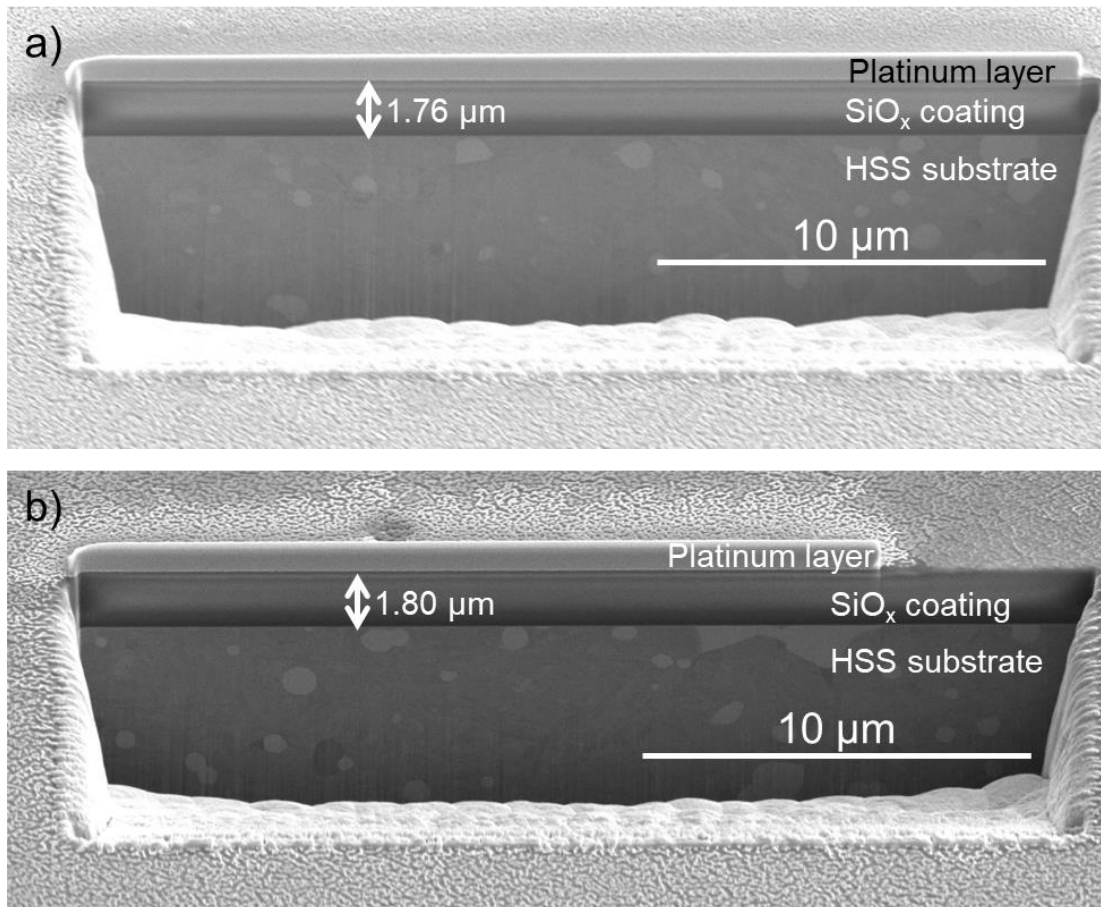


Figure 7.17 FIB cross section of the SiO_x coated sample with HMDSO:O₂ ratio 1:20 and DOE thickness 2 μm, a) before EIS and b) after EIS.

A series of line scans were recorded using EDX, after the experiment. The line scans for both samples and 1:20 are shown in Figure 7.18. Lines scans for the elements of oxygen (O), silicon (Si), iron (Fe) and chromium (Cr) are shown for both samples. From the line scans, both samples are showing a trace of Cr in the SiO_x coating. This may suggest that the Cr or CrO₂/Cr₂O₃ from the HSS is being adsorbed through the coating during the experiment. This could be due to the NaCl solution getting through the pores in the SiO_x coating, which could have been exacerbated during the experiment.

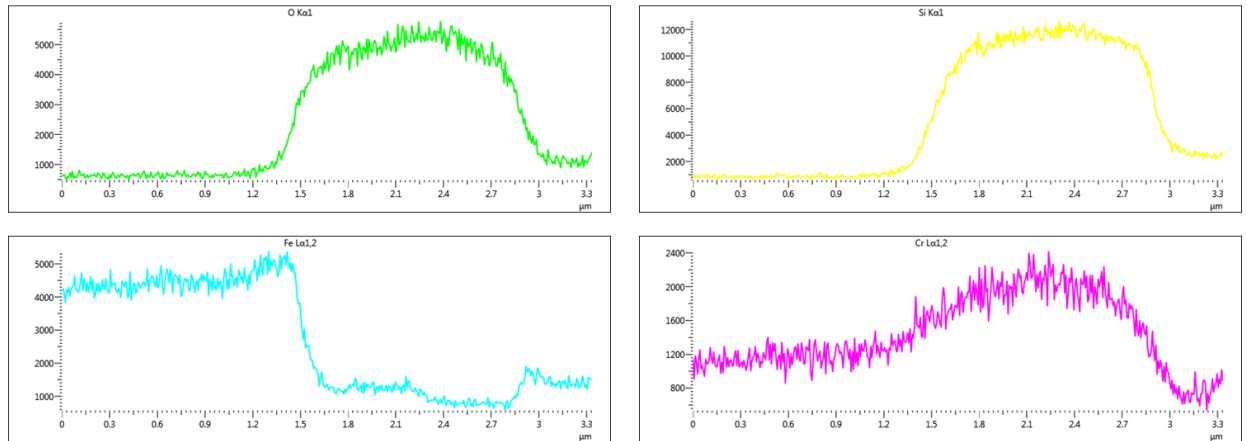
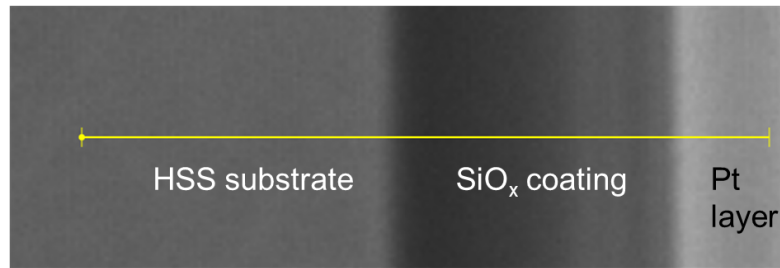


Figure 7.18. EDX line scans for SiO_x coating with HMDSO:O₂ ratio 1:20 and a DOE thickness 2 μm after 168 h EIS experiment.

Due to the sensitivity of the SEM and EDX analysis, it is not clear to fully understand the trend that is being seen during the experiment and there is no clear solution to the proposed phenomena that is leading to the increased resistance. Therefore, it is useful to study a TEM image, with higher sensitivity, to propose a conclusion to the increased resistance and reduced capacitance.

7.4.3 TEM analysis of sample 1:20

The resistance values of the coatings at different HMDSO:O₂ ratios show a trend that can only be determined through further investigation of the coatings. The hypothesised trend discussed in section 7.2.2.1 suggests the formation of a Cr₂O₃ corrosion layer between the HSS substrate and the SiO_x coating, or the dissolution of the SiO_x coated layer at the substrate coating interface. The EIS data suggest that this barrier layer may have been formed during the first 72 hours of the experiment, due to the increase of resistance. Once formed, this

layer may have started to corrode after the 72 hours, as a reduction in the R_{ct} values of the samples 1:14, 1:16, and 1:24. The sample with ratio 1:20 shows a slightly different trend, with a decrease in the R_{ct} from 1 to 72 hours, followed by an increase. Figure 7.19 shows a theoretical mechanism of the reaction or process that may be occurring during the timeframe where the increase in R_{ct} occurs. The Cl^- ions from the NaCl may enhance the corrosion and the formation of a chromium oxide layer.

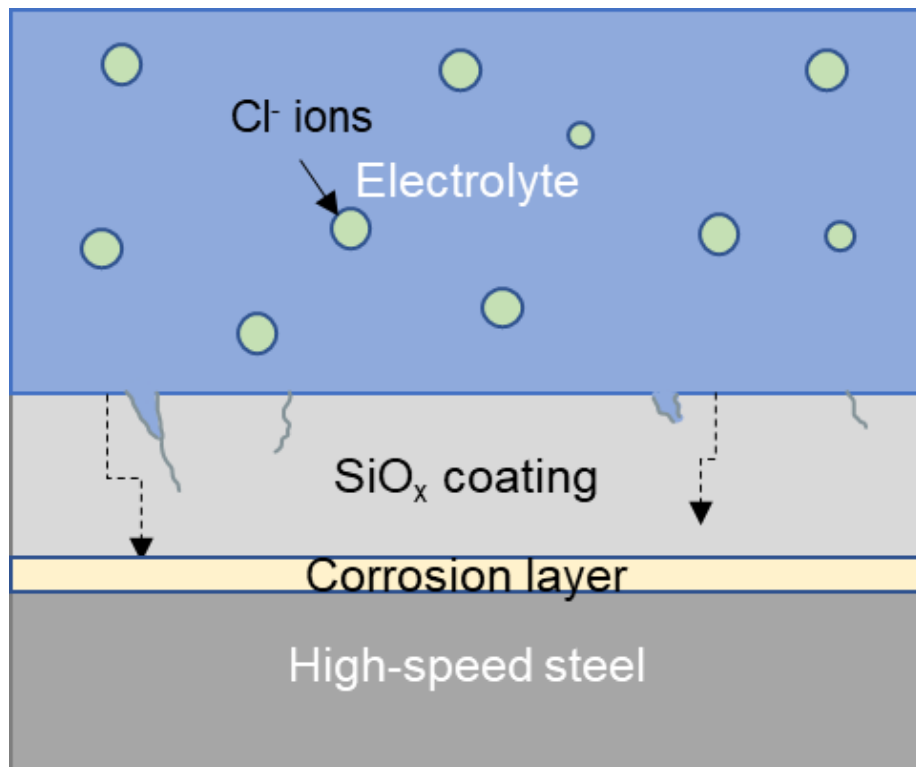


Figure 7.19. Theoretical mechanism for the trends occurring in the resistance values of the SiO_x coatings with HMDSO: O_2 ratio 1:16, 1:20 and 1:24, and a DOE thickness of 2 μm .

The sample with ratio 1:20 and a DOE thickness of 2 μm , was selected for TEM preparation, imaging and EDX analysis. The reason for choosing this particular sample was due to the increase in the resistance values between 72 and 168 hours, suggesting that the formed corrosion layer would still be present. TEM

imaging and EDX analysis has provided one possible avenue to theorise the increased resistance values of the SiO_x coated HSS samples.

One avenue, may be due to the formation of a corrosive layer during the EIS process. The TEM sample was prepared, as described in section 4.6.1.4 of the experimental chapter. The TEM image presented in Figure 7.20, shows a potential, small delamination area creating a pore or gap between the substrate surface and the coating. The image also, shows there is an additional, thin layer between the HSS substrate and the SiO_x coating, measuring at ~5 nm.

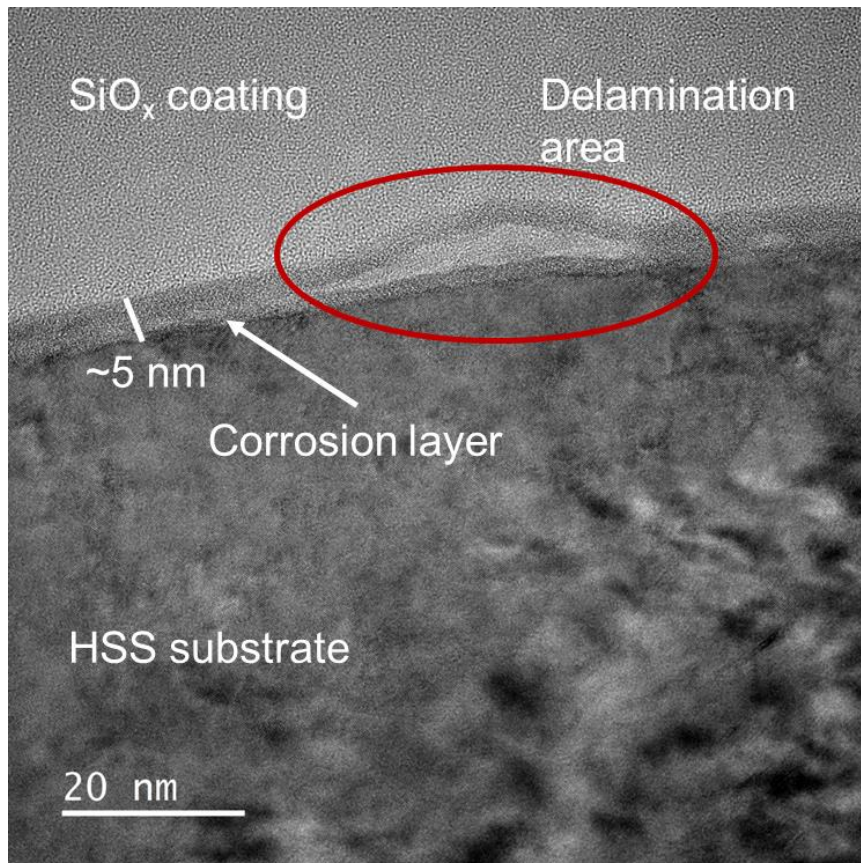


Figure 7.20 TEM imaging of SiO_x coating with HMDSO:O₂ ratio 1:20 with a DOE thickness 2 μm showing the SiO_x coating and HSS interface with a ~5 nm corrosion layer, after 168 h.

EDX analysis allowed the TEM sample to be explored further and to investigate the additional layer that is shown in the TEM image. Elemental mapping and line scan data from the TEM image are shown in Figure 7.21 and Figure 7.22 respectively.

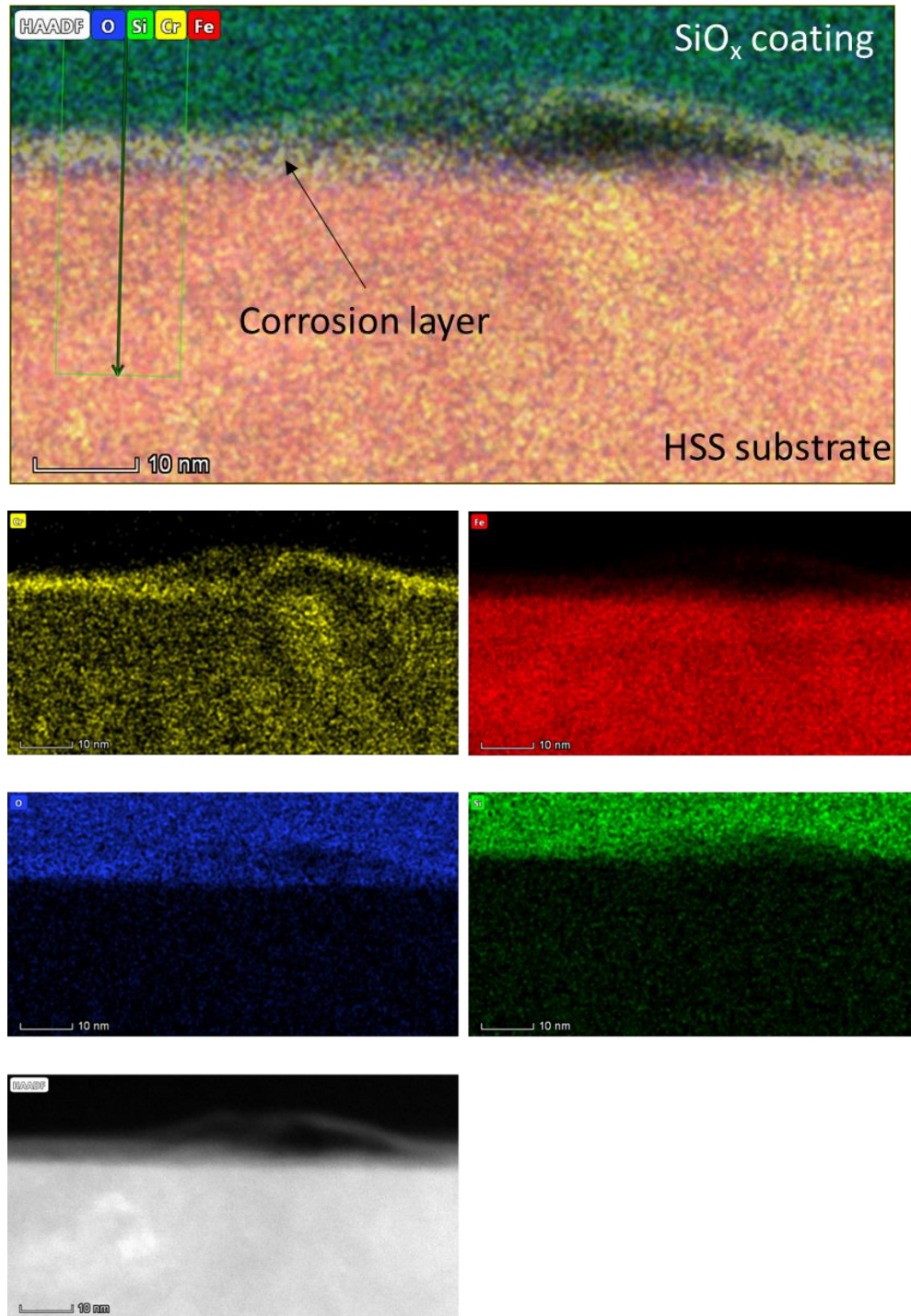


Figure 7.21 The EDX elemental mapping of SiO_x coating with HMDSO:O₂ ratio 1:20 and a DOE thickness 2 μm, from the TEM image, after 168 h.

From the elemental mapping analysis, Cr is present throughout the HSS substrate and also shows a considerable amount present at the coating, substrate interface. A small amount of iron also shows to be present, as well as oxygen. Suggesting that the corrosion layer could be chromium oxide, with iron a some iron oxide content as well.

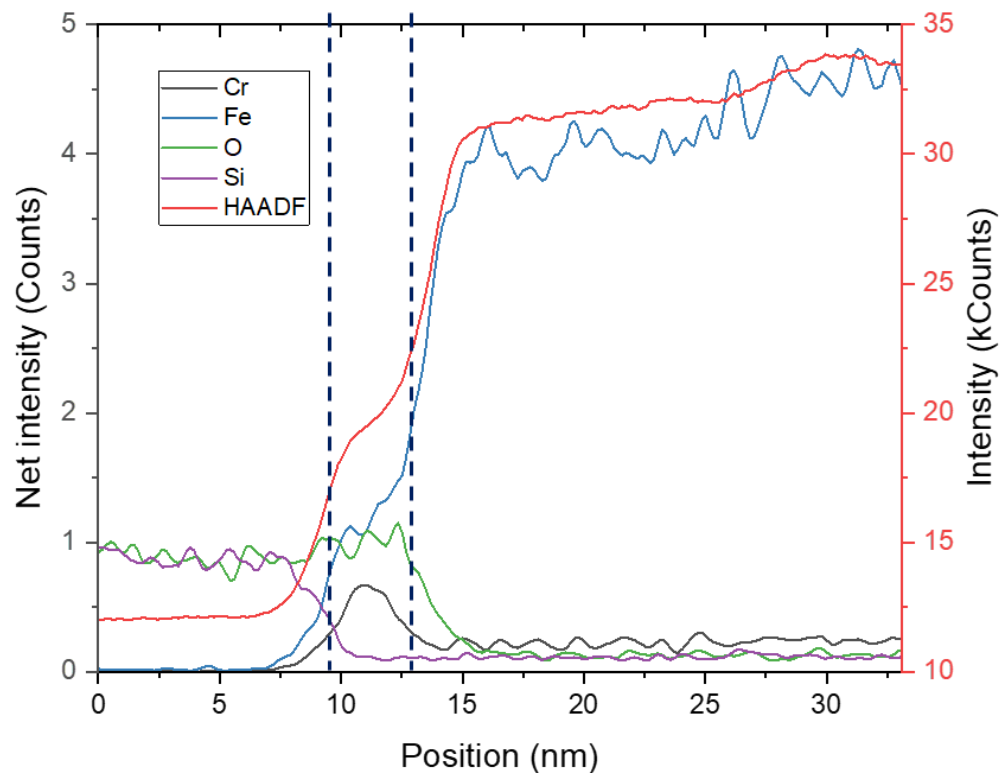


Figure 7.22. Line scan data from the TEM sample, 1:20 after the 168 hour EIS experiment.

Furthermore, the line scan data also supports the elemental mapping data and suggests a chromium oxide layer is present between 10 and 15 nm, as shown in Figure 7.22. This ~ 5 nm layer, is consistent with the layer shown in the TEM image in Figure 7.20. Therefore, the formation of a corrosive layer during the EIS experiments may be due to the formation of a chromium oxide layer, through the penetration of chloride ions through the SiO_x coatings. This potentially leads to

the adsorption of Cl^- ions through the coating, leading to degradation of the and corrosion of the HSS, thus resulting in the release of Cr to react with O_2 .

The increase in resistance values and the decrease in capacitance values between 1 and 72 hours for samples 1:14, 1:16 and 1:24 can be determined to be from the formation of a Cr_2O_3 corrosive layer. The decrease of the R_{ct} values from 72 hours to 168 hours may be due to this corrosive layer slowly dissipating, however still maintaining a layer small layer of Cr_2O_3 and providing an extra corrosion protection due to the overall increase in resistance throughout the duration of the experiment.

7.5 Summary of chapter

In summary, this chapter has shown the experimental data from the potentiodynamic results, electrochemical impedance spectroscopy and analysis of the samples post-EIS analysis. The use of inorganic SiO_x coatings for their use a protective layer against corrosion has proven to be promising. The addition of an SiO_x layer provides the HSS substrate with an increase in the corrosion resistance.

7.5.1 The effect of the HMDSO: O_2 ratio on the corrosion properties of SiO_x coated HSS

- From the potentiodynamic results, extrapolation of the Tafel curves has shown that all coated samples are more protective than that of an uncoated HSS sample. The corrosion current values (i_{corr}) for the SiO_x coated samples with a DOE thickness of 2 μm are lower than those proposed in the literature, indicating a better corrosion resistance.
- The EIS data has shown that the most protective sample is 1:14 at the DOE thickness of 2 μm , as it gives the highest increase in resistance from

1 hour to 168 hours and decreases in capacitance throughout the experiment.

- The least protective coating is shown to be 1:12, due to the lower resistance values and higher capacitance values, compared to all other samples. However, the coating 1:12 with a DOE thickness of 2 μm shows a different trend in the resistance and capacitance values, when compared to the other ratios. Sample 1:12 exhibits a slight increase in R_{ct} throughout the duration of the experiment, suggesting that the sample is becoming more protective.
- The samples 1:16, 1:20 and 1:24 exhibit a particular trend throughout the duration of the EIS experiment. The samples increase in resistance overall but have a larger increase in resistance between 1 and 72 hours, followed by a slight decrease between 72 and 168 hours.
- A proposed theory for these phenomena is the formation of a corrosive layer during the first 72 hours of the experiment, followed by the destruction of the layer after 72 hours, shown from the decrease in resistance values.
- SEM/EDX and TEM imaging were used to understand the proposed theory. The SEM imaging showed that the texture and roughness of the surface remains largely unchanged, and there are no visible pores on the coating surface.
- EDX analysis suggests that chromium is being adsorbed through the SiO_x coating. The TEM imaging with elemental mapping and line scans showed that an additional layer is present between the surface of the HSS substrate and the SiO_x coating, measuring ~ 5 nm. This elemental mapping and line scan data also show that a layer has formed between

the coating and substrate. The layer is shown to be a chromium oxide layer, as shown in the line scan data between 10 and 15 nm. This is also in agreement with the TEM image, with the layer measuring ~ 5 nm, thus concluding that a chromium oxide layer is formed during the experiment, allowing for extra corrosion protection and increasing the resistance of the coating.

7.5.2 The effect of the thickness on the corrosion properties of SiO_x coated HSS

- The sample coated with HMDSO:O₂ ratio 1:12 was used for the determination of corrosion resistance and capacitance at different thicknesses.
- The corrosion resistance of the coating increases when the thickness is increased from 1 μm through to 3.5 μm. The coating with a thickness of 5 μm has a lower corrosion resistance compared to the coating at 3.5 μm.
- The coating with the least protection has a coating thickness of 1 μm. The corrosion resistance of this coating also decreases with the duration of the experiment, suggesting that it is becoming less protective. This is also backed up by the increase in the capacitance values for this coating.

Overall, both the HMDSO:O₂ ratio and the thickness have an effect on the corrosion performance of the SiO_x coated HSS. The sample 1:24 at a DOE thickness of 2 μm has the highest coating resistance, and is therefore the most protective coating. With respect to the thickness, the coating with ratio 1:12 and a DOE thickness of 3.5 μm gives the highest coating resistance and lowest coating capacitance. Therefore suggesting that a coating thickness of 3.5 μm, provides a more corrosion resistant coating.

Chapter 8 – Conclusions and Further Work

8.1 Conclusions

This study has provided an insight into the MW-PECVD method for depositing SiO_x coating onto a HSS substrate using a MW-PECVD technique for the deposition. The mechanical, chemical and microstructural properties were analysed with respect to the HMDSO: O_2 ratios and the coating thickness. The corrosion properties of the coatings were also explored, again focussing on the HMDSO: O_2 ratios and the thickness of the coatings. The conclusions for the work are explored in further detail in this chapter.

A large matrix of coatings have successfully been developed using the MW-PECVD coating technique. Varying the precursor HMDSO: O_2 ratios allowed a thorough comparative study of the mechanical, chemical and microstructural properties. The SiO_x coatings deposited using this coating method were found to be crystalline in nature, unlike many other SiO_x coatings which have been found to be largely amorphous. The MW-PECVD method enables coatings with a different microstructure to be deposited and thus changes the characteristics and properties of the SiO_x coatings.

8.1.1 The effect of the HMDSO: O_2 ratio on the properties of SiO_x coatings

- The HMDSO: O_2 ratio has an effect on the chemical structure of the SiO_x coatings. Increasing the ratio, and therefore the oxygen concentration results in an increase in the O_2 concentration, and the amount of carbon present in the film was decreased. This leads to a more inorganic coating, SiO_2 -like coating, whereas the lower oxygen concentration resulted in a more organic-like coatings due to the presence of carbon.

- The increase in the oxygen concentration during the depositions result in varying Si:O ratios. The coating deposited at ratio 1:12 and a DOE thickness of 2 μm resulted in a purely stoichiometric coating, where $x = 2$, therefore $1:12 = \text{SiO}_2$.
- The microstructure of the coatings is also affected by the oxygen concentration during the deposition, resulting in the coatings having different crystallite sizes. There is, however, no distinct trend that can be distinguished from the crystallite size and HMDSO:O₂ ratio dependence.
- The nanomechanical results calculated from nanoindentation vary with HMDSO:O₂ ratio. However, there are no clear trends to conclude whether the increase in oxygen concentration affects the mechanical properties of the coatings. The hardness of the coatings is greater than 5 GPa, with the exception of coating 1:14.
- The polarisation measurements showed that the SiO_x coatings provide the HSS substrate with some corrosion protection. This is observed with a decrease in the corrosion current density and an increase in the corrosion potential, when compared to that of an uncoated HSS substrate.
- The curves also present a pseudo-passivation behaviour of the coatings, as shown by the anodic polarisation curve.
- The corrosion resistance of the coatings varies with the HMDSO:O₂ ratios, but there is no discernible trend observed to suggest that increasing the oxygen concentration has an effect on the corrosion resistance. The coating with the highest corrosion resistance is sample 1:14 with DOE thickness 2 μm , however this coating demonstrates a large decrease in the hardness after EIS testing. The reduction in hardness may be indicative of the water uptake exhibited by the coating.

- The sample with ratio 1:12 saw an increase in the hardness of the coating after the EIS test. This is the only sample to exhibit this behaviour. It is also the only coating to have a steady increase of the corrosion resistance throughout the duration of the experiment. This concludes that the coating is becoming more protective over time and may be the result of a corrosion oxide layer forming between the coating and substrate interface.
- Some of the coatings (1:10, 1:14, 1:16 and 1:24) exhibited a behaviour in which the corrosion resistance increased from 1 to 72 hours, and was followed by a decrease from 72 to 168 hours. The increase in resistance suggests that the coating is becoming more protective, and may be due to the formation of an extra oxide layer. This hypothesis was investigated through further analysis after the electrochemical experiments.
- TEM imaging with EDX analysis proved the formation of ~5 nm chromium oxide layer between the coating and the substrate interface. Thus, supporting the hypothesis.

8.1.2 The effect of the thickness of the SiO_x coatings

- The comparison of the average crystallite size using both methods, with the thickness of the coatings shows slightly different trends for coatings with the different HMDSO:O₂ ratios. Using the Scherrer method, all of the coatings exhibited an overall decrease in the average crystallite, with an increase in the film thickness from 1 μm through to 5 μm. On the other hand, the Williamson-Hall method showed that sample 1:12 and 1:16 agreed with the Scherrer trend, as there was an overall decrease in the crystallite size with increasing film thickness. The coatings with ratios 1:14

and 1:20 however showed an overall increase in the film thickness, agreeing with the finding reported by Zhang et al [243].

- The corrosion resistance of the coatings is also affected by the thickness. Sample 1:12 was used to carry out EIS experiments on the different thicknesses. There was an increase in the corrosion resistance with increasing thickness from 1 μm through to 3.5 μm , however the 5 μm thickness then saw a decrease. Therefore, concluding that the SiO_x coating with ratio 1:12 and a DOE thickness of 3.5 μm provides the best coating resistance.

Overall, the most promising SiO_x coating based on the corrosion properties has a HMDSO: O_2 ratio 1:14, as it has the highest corrosion resistance. However, it could be argued that the coating with ratio 1:12 could be one of the best coatings due to being purely stoichiometric at DOE thickness 2 μm , and great microstructural properties. The corrosion resistance of this coating, although an order of magnitude lower in comparison to the other coatings, has proven to perform the best during the EIS experiment. The water uptake is the lowest when compared with the other coatings, and it is the only coating to demonstrate an increased hardness after the EIS experiment. It can be concluded from these results that the formation of the oxide layer during the electrochemical tests, enhances the properties of the SiO_x coating.

8.2 Further Work

The work in this thesis has provided a great insight into the chemical, microstructural and corrosion properties of SiO_x coatings. There is great potential to further enhance the current study and build upon the knowledge within this

area and to work towards a particular application. The opportunities identified for the further avenues of work could be:

- Further development of the coating procedure and parameters, with the avenue of investigating the breakdown of the HMDSO within the deposition chamber and the deposition chemistry. The use of optical emission spectroscopy (OES) during the deposition can be used to study the trace elements within the chamber, and therefore allows the breakdown of HMDSO to be observed and how it reacts with O₂. Understanding the species present within the chamber will be able to help further control the deposition of SiO_x coatings.
- To carry out further electrochemical tests using EIS for more prolonged periods of time and to study the long term impact on the corrosion resistance of the coatings, as well as defining the breakdown of the coatings. A small matrix of coatings would be further investigated including 1:12, 1:14, 1:16 and 1:24, due to the corrosion behaviour of the coatings. The experiments could be performed over a 1 and 6 month period.
- For more application specific SiO_x coatings, perform EIS experimentation using different corrosive media, for example; acidic solutions – phosphoric acid (H₃PO₄) for use in a phosphoric acid fuel cell, alkaline solution – KOH for alkaline fuel cells.
- To further characterise the corrosion layer formed during the EIS tests. This could be studied through:
 - Examining the corroded area of the SiO_x coatings, using TEM and EDX analysis, at 24 hour intervals to study how and when the layer is formed over time.

- Utilising FTIR and Raman analysis to examine the Si-O bonding both prior to EIS experiments and after the experiments to see if the corrosive media affects the chemistry and bonding of the SiO_x coating.

References

- [1] A. Leiden, P. J. Brand, F. Cerdas, S. Thiede, and C. Herrmann, "Transferring life cycle engineering to surface engineering," *Procedia CIRP*, vol. 90, pp. 557–562, 2020, doi: 10.1016/j.procir.2020.02.132.
- [2] G. Koch, "Cost of corrosion," in *Trends in Oil and Gas Corrosion Research and Technologies: Production and Transmission*, A. M. El-Sherik, Ed. Boston: Woodhead Publishing, 2017, pp. 3–30.
- [3] M. Woydt *et al.*, "Tribologie in Deutschland Querschnittstechnologie zur Minderung von CO₂-Emissionen und zur Ressourcenschonung," *Gesellschaft für Tribol. eV, Jülich*, pp. 1–33, 2019.
- [4] B. Wang, Z. Mi, I. Nistor, and X. C. Yuan, "How does hydrogen-based renewable energy change with economic development? Empirical evidence from 32 countries," *Int. J. Hydrogen Energy*, vol. 43, no. 25, pp. 11629–11638, 2018, doi: 10.1016/j.ijhydene.2017.03.059.
- [5] J. Wang, H. Wang, and Y. Fan, "Techno-Economic Challenges of Fuel Cell Commercialization," *Engineering*, vol. 4, no. 3, pp. 352–360, 2018, doi: 10.1016/j.eng.2018.05.007.
- [6] A. Hermann, T. Chaudhuri, and P. Spagnol, "Bipolar plates for PEM fuel cells: A review," *Int. J. Hydrogen Energy*, vol. 30, no. 12, pp. 1297–1302, 2005, doi: 10.1016/j.ijhydene.2005.04.016.
- [7] V. Mehta and J. S. Cooper, "Review and analysis of PEM fuel cell design and manufacturing," *J. Power Sources*, vol. 114, no. 1, pp. 32–53, 2003, doi: 10.1016/S0378-7753(02)00542-6.
- [8] R. L. Borup and N. E. Vanderborgh, "Design and testing criteria for bipolar plate materials for PEM fuel cell applications," *Mater. Res. Soc. Symp. - Proc.*, vol. 393, pp. 151–155, 1995, doi: 10.1557/proc-393-151.
- [9] P. Sharma and O. P. Pandey, "Proton exchange membrane fuel cells: fundamentals, advanced technologies, and practical applications," in *PEM Fuel Cells*, G. Kaur, Ed. Elsevier, 2022, pp. 1–24.
- [10] H. Wang and J. A. Turner, "Ferritic stainless steels as bipolar plate material for polymer electrolyte membrane fuel cells," *J. Power Sources*, vol. 128, no. 2, pp. 193–200, 2004, doi: 10.1016/j.jpowsour.2003.09.075.
- [11] Y. Wang and D. O. Northwood, "An investigation into polypyrrole-coated 316L stainless steel as a bipolar plate material for PEM fuel cells," *J. Power Sources*, vol. 163, no. 1 SPEC. ISS., pp. 500–508, 2006, doi: 10.1016/j.jpowsour.2006.09.048.
- [12] L. Wang *et al.*, "Electrochemical behaviour and surface conductivity of niobium carbide-modified austenitic stainless steel bipolar plate," *J. Power Sources*, vol. 246, pp. 775–782, 2014, doi: 10.1016/j.jpowsour.2013.08.025.
- [13] P. Odetola, P. Popoola, O. Popoola, and D. Delpont, "Electrodeposition of Functional Coatings on Bipolar Plates for Fuel Cell Applications – A Review," in *Electrodeposition of Composite Materials*, A. M. A. Mohamed and T. D. Golden, Eds. Rijeka: IntechOpen, 2016.

- [14] T. Bohackova, J. Ludvik, and M. Kouril, "Metallic material selection and prospective surface treatments for proton exchange membrane fuel cell bipolar plates—a review," *Materials (Basel)*, vol. 14, no. 10, 2021, doi: 10.3390/ma14102682.
- [15] R. Taherian, "A review of composite and metallic bipolar plates in proton exchange membrane fuel cell: Materials, fabrication, and material selection," *J. Power Sources*, vol. 265, pp. 370–390, 2014, doi: 10.1016/j.jpowsour.2014.04.081.
- [16] D. Kalliopi K. Aligizaki, "Surface Engineering for Corrosion and Wear Resistance," *Anti-Corrosion Methods Mater.*, vol. 51, no. 1, p. 62, Feb. 2004, doi: 10.1108/acmm.2004.12851aae.001.
- [17] W. Tillmann and E. Vogli, "Selecting Surface-treatment Technologies," in *Modern Surface Technology*, Weinheim, FRG: Wiley-VCH Verlag GmbH & Co. KGaA, 2006, pp. 1–10.
- [18] C. M. Hansson, "The impact of corrosion on society," *Metall. Mater. Trans. A Phys. Metall. Mater. Sci.*, vol. 42, no. 10, pp. 2952–2962, 2011, doi: 10.1007/s11661-011-0703-2.
- [19] A. Royani *et al.*, "Corrosion of carbon steel after exposure in the river of Sukabumi, West Java," *IOP Conf. Ser. Mater. Sci. Eng.*, vol. 541, no. 1, 2019, doi: 10.1088/1757-899X/541/1/012031.
- [20] L. Körner, A. Sonnenfeld, and P. R. von Rohr, "Silicon oxide diffusion barrier coatings on polypropylene," *Thin Solid Films*, vol. 518, no. 17, pp. 4840–4846, 2010, doi: <https://doi.org/10.1016/j.tsf.2010.02.006>.
- [21] S. R. Kim, M. H. Choudhury, W. H. Kim, and G. H. Kim, "Effects of argon and oxygen flow rate on water vapor barrier properties of silicon oxide coatings deposited on polyethylene terephthalate by plasma enhanced chemical vapor deposition," *Thin Solid Films*, vol. 518, no. 8, pp. 1929–1934, 2010, doi: 10.1016/j.tsf.2009.07.147.
- [22] M. Atik, P. de Lima Neto, L. A. Avaca, M. A. Aegerter, and J. Zarzycki, "Protection of 316L stainless steel against corrosion by SiO₂ coatings," *J. Mater. Sci. Lett.*, vol. 13, no. 15, pp. 1081–1085, 1994, doi: 10.1007/BF00633520.
- [23] I. Stambolova, S. Yordanov, L. Lakov, S. Vassilev, V. Blaskov, and B. Jivov, "Preparation of sol-gel SiO₂ coatings on steel and their corrosion resistance," *MATEC Web Conf.*, vol. 145, p. 05011, Jan. 2018, doi: 10.1051/matecconf/201814505011.
- [24] C. Ning, L. Mingyan, and Z. Weidong, "Fouling and corrosion properties of SiO₂ coatings on copper in geothermal water," *Ind. Eng. Chem. Res.*, vol. 51, no. 17, pp. 6001–6017, 2012, doi: 10.1021/ie202091b.
- [25] H. A. Aboubakr, "Decontamination of food and food-processing surfaces from norovirus by cold atmospheric-pressure gaseous plasma," University of Minnesota, 2017.
- [26] D. A. Gurnett and A. Bhattacharjee, *Introduction to plasma physics: With space and laboratory applications*, vol. 9780521364. Cambridge University Press, 2005.
- [27] T. J. M. Boyd and J. J. Sanderson, *The Physics of Plasmas*, vol. 74, no.

5. Cambridge University Press, 2003.
- [28] M. G. Kivelson and C. T. Russell, Eds., *Introduction to Space Physics*. Cambridge University Press, 1995.
- [29] T. H.-B. York Thomas M., "1.1 Introduction," in *Introduction to Plasmas and Plasma Dynamics - With Reviews of Applications in Space Propulsion, Magnetic Fusion and Space Physics*, Elsevier, 2015.
- [30] C. Cardinaud, "Fluorine-based plasmas: Main features and application in micro-and nanotechnology and in surface treatment," *Comptes Rendus Chim.*, vol. 21, no. 8, pp. 723–739, 2018, doi: 10.1016/j.crci.2018.01.009.
- [31] C. L. da Silva, R. G. Sonnenfeld, H. E. Edens, P. R. Krehbiel, M. G. Quick, and W. J. Koshak, "The Plasma Nature of Lightning Channels and the Resulting Nonlinear Resistance," *J. Geophys. Res. Atmos.*, vol. 124, no. 16, pp. 9442–9463, 2019, doi: 10.1029/2019JD030693.
- [32] B. Fotovvati, N. Namdari, and A. Dehghanghadikolaei, "On coating techniques for surface protection: A review," *J. Manuf. Mater. Process.*, vol. 3, no. 1, p. 28, Mar. 2019, doi: 10.3390/jmmp3010028.
- [33] J. Kurose and K. Ross, "Chapter 1 Introduction Chapter 1 : Introduction Chapter 1 : roadmap," in *Handbook of Physical Vapor Deposition (PVD) Processing (2nd Edition)*, United States of America: Elsevier, 2004, pp. 1–35.
- [34] A. Inspektor and P. A. Salvador, "Architecture of PVD coatings for metalcutting applications: A review," *Surf. Coatings Technol.*, vol. 257, pp. 138–153, 2014, doi: 10.1016/j.surfcoat.2014.08.068.
- [35] A. Baptista, F. Silva, J. Porteiro, J. Míguez, and G. Pinto, "Sputtering physical vapour deposition (PVD) coatings: A critical review on process improvement and market trend demands," *Coatings*, vol. 8, no. 11, 2018, doi: 10.3390/COATINGS8110402.
- [36] H. Hoche, S. Groß, and M. Oechsner, "Development of new PVD coatings for magnesium alloys with improved corrosion properties," *Surf. Coatings Technol.*, vol. 259, no. PA, pp. 102–108, 2014, doi: 10.1016/j.surfcoat.2014.04.038.
- [37] R. Gouveia, F. Silva, P. Reis, and A. Baptista, "Machining Duplex Stainless Steel: Comparative Study Regarding End Mill Coated Tools," *Coatings*, vol. 6, no. 4, p. 51, 2016, doi: 10.3390/coatings6040051.
- [38] V. Nunes, F. J. G. Silva, M. F. Andrade, R. Alexandre, and A. P. M. Baptista, "Increasing the lifespan of high-pressure die cast molds subjected to severe wear," *Surf. Coatings Technol.*, vol. 332, pp. 319–331, 2017, doi: 10.1016/j.surfcoat.2017.05.098.
- [39] K. S. Sree Harsha, "Chapter 2 - Evaporation," in *Principles of Vapor Deposition of Thin Films*, Oxford: Elsevier, 2006, pp. 11–143.
- [40] Gianni Monaco, "Coating Technology : Evaporation Vs Sputtering," *AR coating technologies*. Satisloh Italy, pp. 1–8, 2016, [Online]. Available: http://www.satisloh.com/fileadmin/contents/Whitepaper/Coating_Technology_final.pdf.
- [41] A. Behera, P. Mallick, and S. S. Mohapatra, "Nanocoatings for

- anticorrosion,” in *Corrosion Protection at the Nanoscale*, S. Rajendran, T. A. N. H. Nguyen, S. Kakooei, M. Yeganeh, and Y. Li, Eds. Elsevier, 2020, pp. 227–243.
- [42] M. B. Tahir, M. Rafique, M. S. Rafique, T. Nawaz, M. Rizwan, and M. Tanveer, “Photocatalytic nanomaterials for degradation of organic pollutants and heavy metals,” in *Nanotechnology and Photocatalysis for Environmental Applications*, M. B. Tahir, M. Rafique, and M. S. Rafique, Eds. Elsevier, 2020, pp. 119–138.
- [43] H. Gekonde and R. Aharanov, “Chemical Vapor Deposition of Wear Resistant Coatings Onto Piston Ring Running Face, Side Face, and Inner Diameter in One Coating Run,” EP2906738B1, 2018.
- [44] H. Holzschuh, “Chemical-vapor deposition of wear resistant hard coatings in the Ti-B-C-N system: Properties and metal-cutting tests,” *Int. J. Refract. Met. Hard Mater.*, vol. 20, no. 2, pp. 143–149, 2002, doi: 10.1016/S0263-4368(02)00013-6.
- [45] K. V. Madhuri, “Thermal protection coatings of metal oxide powders,” in *Metal Oxide Powder Technologies*, Y. Al-Douri, Ed. Elsevier, 2020, pp. 209–231.
- [46] J. O. Carlsson and P. M. Martin, “Chemical Vapor Deposition,” in *Handbook of Deposition Technologies for Films and Coatings*, P. M. B. T.-H. of D. T. for F. and C. (Third E. Martin, Ed. Boston: William Andrew Publishing, 2010, pp. 314–363.
- [47] H. Xiao, “Chemical Vapor Deposition and Dielectric Thin Films,” in *Introduction to Semiconductor Manufacturing Technology, Second Edition*, vol. 2, Bellingham, Washington: Society of Photo-Optical Instrumentation Engineers, 2013, pp. 369–450.
- [48] S. Eränen *et al.*, “Thin Films on Silicon,” in *Handbook of Silicon Based MEMS Materials and Technologies: Second Edition*, Second Edi., M. Tilli, T. Motooka, V.-M. Airaksinen, S. Franssila, M. Paulasto-Kröckel, and V. Lindroos, Eds. Boston: William Andrew Publishing, 2015, pp. 124–205.
- [49] P. Laube, “Deposition,” 2017. https://www.halbleiter.org/pdf/pdf_en/Deposition/Deposition - Chemical vapor deposition.pdf.
- [50] R. G. Gordon, S. Barry, J. T. Barton, and R. N. R. Broomhall-Dillard, “Atmospheric pressure chemical vapor deposition of electrochromic tungsten oxide films,” *Thin Solid Films*, vol. 392, no. 2, pp. 231–235, 2001, doi: 10.1016/S0040-6090(01)01033-1.
- [51] P. Therm, “PECVD,” 2014. <http://www.plasma-therm.com/pecvd.html>.
- [52] K. Gupta, N. K. Jain, and R. Laubscher, “Surface Property Enhancement of Gears,” in *Advanced Gear Manufacturing and Finishing*, K. Gupta, N. K. Jain, and R. Laubscher, Eds. Academic Press, 2017, pp. 167–196.
- [53] A. Kashyap, N. K. Singh, M. Soni, and A. Soni, “Deposition of thin films by chemical solution-assisted techniques,” in *Chemical Solution Synthesis for Materials Design and Thin Film Device Applications*, S. Das and S. Dhara, Eds. Elsevier, 2021, pp. 79–117.
- [54] J. Long *et al.*, “Doped microcrystalline silicon layers for solar cells by

- 13.56 MHz plasma-enhanced chemical vapour deposition,” *Energy Procedia*, vol. 15, pp. 240–247, 2012, doi: 10.1016/j.egypro.2012.02.028.
- [55] S. S. Asad *et al.*, “Deposition of thin SiO_x films by direct precursor injection in atmospheric pressure microwave torch (TIA),” *Plasma Process. Polym.*, vol. 6, no. SUPPL. 1, pp. S508–S513, 2009, doi: 10.1002/ppap.200931104.
- [56] I. Levin and D. Brandon, “Metastable alumina polymorphs: Crystal structures and transition sequences,” *J. Am. Ceram. Soc.*, vol. 81, no. 8, pp. 1995–2012, 1998, doi: 10.1111/j.1151-2916.1998.tb02581.x.
- [57] J. Pesti and G. L. Larson, “Tetramethyldisiloxane: A Practical Organosilane Reducing Agent,” *Org. Process Res. Dev.*, vol. 20, no. 7, pp. 1164–1181, 2016, doi: 10.1021/acs.oprd.6b00124.
- [58] S. Thongrom, Y. Tirawanichakul, N. Munsit, and C. Deangngam, “One-step microwave plasma enhanced chemical vapor deposition (MW-PECVD) for transparent superhydrophobic surface,” *IOP Conf. Ser. Mater. Sci. Eng.*, vol. 311, no. 1, p. 12015, Feb. 2018, doi: 10.1088/1757-899X/311/1/012015.
- [59] W. Ahmed *et al.*, “Surface Engineering of Dental Tools with Diamond for Improved Life and Performance,” in *Emerging Nanotechnologies in Dentistry*, K. Subramani and W. Ahmed, Eds. Boston: William Andrew Publishing, 2012, pp. 239–272.
- [60] Y. Liu, J. He, N. Zhang, W. Zhang, Y. Zhou, and K. Huang, “Advances of microwave plasma-enhanced chemical vapor deposition in fabrication of carbon nanotubes: a review,” *J. Mater. Sci.*, vol. 56, no. 22, pp. 12559–12583, 2021, doi: 10.1007/s10853-021-06128-1.
- [61] G. Lucovsky and D. V. Tsu, “Plasma enhanced chemical vapor deposition: Differences between direct and remote plasma excitation,” *J. Vac. Sci. Technol. A Vacuum, Surfaces, Film.*, vol. 5, no. 4, pp. 2231–2238, 1987, doi: 10.1116/1.574963.
- [62] J. E. Stevens, “Electron Cyclotron Resonance Plasma Sources,” in *High Density Plasma Sources*, O. A. Popov, Ed. Park Ridge, NJ: William Andrew Publishing, 1995, pp. 312–379.
- [63] W. L. Johnson, “Electrostatically-Shielded Inductively-Coupled RF Plasma Sources,” in *High Density Plasma Sources*, O. A. Popov, Ed. Park Ridge, NJ: William Andrew Publishing, 1995, pp. 100–148.
- [64] E. A. Irene, “SiO₂ Films,” in *Handbook of Ellipsometry*, H. G. Tompkins and E. A. Irene, Eds. Norwich, NY: William Andrew Publishing, 2005, pp. 569–636.
- [65] S. M. Rossnagel, “Physical vapor deposition,” in *Handbook of Semiconductor Manufacturing Technology, Second Edition*, Boston, MA: Springer US, 2007, pp. 15-1-15–27.
- [66] C. Grèzes-Besset and G. Chauveau, “Optical coatings for large facilities,” in *Optical Thin Films and Coatings: From Materials to Applications*, A. Piegari and F. Flory, Eds. Woodhead Publishing, 2013, pp. 695–717.
- [67] S. Achanta, D. Drees, and J.-P. Celis, “Nanocoatings for tribological applications,” in *Nanocoatings and Ultra-Thin Films*, A. S. H. Makhlof

and I. Tiginyanu, Eds. Woodhead Publishing, 2011, pp. 355–396.

- [68] R. B. Darling, “Physical Vapor Deposition Physical Vapor Deposition (PVD),” *Met. Finish.*, vol. 97, no. 1, pp. 417–430, 2013, doi: [https://doi.org/10.1016/S0026-0576\(01\)85301-0](https://doi.org/10.1016/S0026-0576(01)85301-0).
- [69] Y. Hamedani, P. Macha, T. J. Bunning, R. R. Naik, and M. C. Vasudev, “Plasma-Enhanced Chemical Vapor Deposition: Where we are and the Outlook for the Future,” 2016, doi: 10.5772/64654.
- [70] D. M. Mattox, “Physical Sputtering and Sputter Deposition (Sputtering),” in *Handbook of Physical Vapor Deposition (PVD) Processing*, Second Edi., D. M. Mattox, Ed. Boston: William Andrew Publishing, 2010, pp. 237–286.
- [71] M. Aliofkhazraei and N. Ali, “Fabrication of Micro/Nanostructured Coatings by CVD Techniques,” in *Comprehensive Materials Processing*, vol. 7, S. Hashmi, G. F. Batalha, C. J. Van Tyne, and B. Yilbas, Eds. Oxford: Elsevier, 2014, pp. 85–117.
- [72] A. Kumar and D. Nanda, “Methods and fabrication techniques of superhydrophobic surfaces,” in *Superhydrophobic Polymer Coatings: Fundamentals, Design, Fabrication, and Applications*, S. K. Samal, S. Mohanty, and S. K. Nayak, Eds. Elsevier, 2019, pp. 43–75.
- [73] L. F. Pochet, P. Howard, and S. Safaie, “CVD coatings: From cutting tools to aerospace applications and its future potential,” *Surf. Coatings Technol.*, vol. 94–95, pp. 70–75, 1997, doi: 10.1016/S0257-8972(97)00478-7.
- [74] W. Chen *et al.*, “Influence of PECVD deposition temperature on phosphorus doped poly-silicon passivating contacts,” *Sol. Energy Mater. Sol. Cells*, vol. 206, p. 110348, 2020, doi: 10.1016/j.solmat.2019.110348.
- [75] E. Y. Gusev, J. Y. Jityaeva, A. A. Geldash, and O. A. Ageev, “Effects of PECVD temperature and RF power on surface structure and refractive index of amorphous and polycrystalline silicon films,” *J. Phys. Conf. Ser.*, vol. 917, no. 3, p. 32029, Nov. 2017, doi: 10.1088/1742-6596/917/3/032029.
- [76] Y. Shi, L. He, F. Guang, L. Li, Z. Xin, and R. Liu, “A review: Preparation, performance, and applications of silicon oxynitride film,” *Micromachines*, vol. 10, no. 8, p. 552, 2019, doi: 10.3390/mi10080552.
- [77] I. P. Fulfillment, “Development of Plasma Enhanced Chemical Vapor Deposition (PECVD) Gate Dielectrics for TFT Applications By Development of Plasma Enhanced Chemical Vapor Deposition (PECVD) Gate Dielectrics for TFT Applications,” in *Structure*, 2010, no. June 2010.
- [78] S. B. Jin, Y. S. Choi, I. S. Choi, and J. G. Han, “Surface energy modification of SiO_xC_yH_z film using PECVD by controlling the plasma processes for OMCTS (Si 4O4C8H24) precursor,” *Thin Solid Films*, vol. 519, no. 20, pp. 6763–6768, 2011, doi: 10.1016/j.tsf.2011.01.214.
- [79] F. Jiang *et al.*, “Research progress of optical fabrication and surface-microstructure modification of SiC,” *J. Nanomater.*, vol. 2012, 2012, doi: 10.1155/2012/984048.
- [80] K. Wasa, M. Kitabatake, and H. Adachi, “Sputtering Systems,” in *Thin Film Materials Technology*, K. Wasa, M. Kitabatake, and H. Adachi, Eds.

Norwich, NY: William Andrew Publishing, 2004, pp. 115–189.

- [81] A. Barranco *et al.*, “Synthesis of SiO₂ and SiO_xCyHz thin films by microwave plasma CVD,” *Thin Solid Films*, vol. 401, no. 1–2, pp. 150–158, 2001, doi: 10.1016/S0040-6090(01)01632-7.
- [82] G. B. Raupp, D. A. Levedakis, and T. S. Cale, “Conformality of SiO₂ films from tetraethoxysilane-sourced remote microwave plasma-enhanced chemical vapor deposition,” *J. Vac. Sci. Technol. A Vacuum, Surfaces, Film.*, vol. 13, no. 3, pp. 676–680, 1995, doi: 10.1116/1.579806.
- [83] A. Hofrichter, P. Bulkin, and B. Drévuillon, “Plasma enhanced chemical vapour deposition of SiO_xNy in an integrated distributed electron cyclotron resonance reactor,” *Appl. Surf. Sci.*, vol. 142, no. 1, pp. 447–450, 1999, doi: 10.1016/S0169-4332(98)00645-X.
- [84] J. Stiegler, T. Lang, M. Nygård-Ferguson, Y. Von Kaenel, and E. Blank, “Low temperature limits of diamond film growth by microwave plasma-assisted CVD,” *Diam. Relat. Mater.*, vol. 5, no. 3–5, pp. 226–230, 1996, doi: 10.1016/0925-9635(95)00349-5.
- [85] B. A. Reshi, S. Kumar, A. Misra, and R. Varma, “Multivariable study on growth of diamond on diamond substrates by microwave plasma chemical vapour deposition,” *Mater. Res. Express*, vol. 6, no. 4, p. 46407, Jan. 2019, doi: 10.1088/2053-1591/aafae3.
- [86] C. S. Yan, Y. K. Vohra, H. K. Mao, and R. J. Hemley, “Very high growth rate chemical vapor deposition of single-crystal diamond,” *Proc. Natl. Acad. Sci. U. S. A.*, vol. 99, no. 20, pp. 12523–12525, 2002, doi: 10.1073/pnas.152464799.
- [87] H. Kakiuchi, H. Ohmi, T. Yamada, K. Yokoyama, K. Okamura, and K. Yasutake, “Silicon oxide coatings with very high rates (>10 nm/s) by hexamethyldisiloxane-oxygen fed atmospheric-pressure VHF plasma: Film-forming behavior using cylindrical rotary electrode,” *Plasma Chem. Plasma Process.*, vol. 32, no. 3, pp. 533–545, 2012, doi: 10.1007/s11090-012-9363-2.
- [88] H. Zhang, Z. Guo, Q. Chen, X. Wang, Z. Wang, and Z. Liu, “Deposition of silicon oxide coatings by atmospheric pressure plasma jet for oxygen diffusion barrier applications,” *Thin Solid Films*, vol. 615, pp. 63–68, 2016, doi: 10.1016/j.tsf.2016.06.042.
- [89] L. Zajíčková *et al.*, “Plasma modification of polycarbonates,” *Surf. Coatings Technol.*, vol. 142–144, pp. 449–454, 2001, doi: 10.1016/S0257-8972(01)01134-3.
- [90] Y. Sen Lin, Y. H. Liao, and M. S. Weng, “Enhanced scratch resistance of polycarbonate by low temperature plasma-polymerized organosilica,” *Thin Solid Films*, vol. 517, no. 17, pp. 5224–5230, 2009, doi: 10.1016/j.tsf.2009.03.181.
- [91] H. Nagel, A. Metz, and R. Hezel, “Porous SiO₂ films prepared by remote plasma-enhanced chemical vapour deposition - a novel antireflection coating technology for photovoltaic modules,” *Sol. Energy Mater. Sol. Cells*, vol. 65, no. 1, pp. 71–77, 2001, doi: 10.1016/S0927-0248(00)00079-9.

- [92] Y. Leterrier, "Durability of nanosized oxygen-barrier coatings on polymers," *Prog. Mater. Sci.*, vol. 48, no. 1, pp. 1–55, 2003, doi: 10.1016/S0079-6425(02)00002-6.
- [93] S. Steves *et al.*, "Silicon oxide barrier films deposited on PET foils in pulsed plasmas: Influence of substrate bias on deposition process and film properties," *J. Phys. D. Appl. Phys.*, vol. 46, no. 8, p. 84013, Feb. 2013, doi: 10.1088/0022-3727/46/8/084013.
- [94] A. S. da Silva Sobrinho, N. Schühler, J. E. Klemberg-Sapieha, M. R. Wertheimer, M. Andrews, and S. C. Gujrathi, "Plasma-deposited silicon oxide and silicon nitride films on poly(ethylene terephthalate): A multitechnique study of the interphase regions," *J. Vac. Sci. Technol. A Vacuum, Surfaces, Film.*, vol. 16, no. 4, pp. 2021–2030, 1998, doi: 10.1116/1.581305.
- [95] A. for T. S. and D. Registry, "Silica," 2011. <https://www.atsdr.cdc.gov/substances/toxsubstance.asp?toxid=290#>.
- [96] H. Quartz, N. Mineraloids, N. Polymorphs, S. Glass, and R. Compounds, "Overview of Silica Polymorphs," 2012. http://www.quartzpage.de/gen_mod.html#alpha.
- [97] Z. Peng and S. A. T. Redfern, "Mechanical properties of quartz at the α - β Phase transition: Implications for tectonic and seismic anomalies," *Geochemistry, Geophys. Geosystems*, vol. 14, no. 1, pp. 18–28, 2013, doi: 10.1029/2012GC004482.
- [98] W. Li *et al.*, "Microstructure study of phase transformation of quartz in potassium silicate glass at 900°C and 1000°C," *Crystals*, vol. 11, no. 12, 2021, doi: 10.3390/cryst11121481.
- [99] B. Mysen and P. Richet, "Silica," in *Silicate Glasses and Melts*, Second Edi., B. Mysen and P. Richet, Eds. Elsevier, 2019, pp. 143–183.
- [100] A. M. Svetlichnyj, V. V. Polyakov, and Y. N. Varzarev, "The formation of silicon dioxide films by TEOS photochemical decomposition," *Mikroelektronika*, vol. 30, no. 1, pp. 27–32, 2001.
- [101] S. Glogauer, "Plasma treatment: Reduction of VOC emissions and improvement of environmentally sensitive processes with plasma surface treatment prior to bonding, coating and printing applications," *SAE Tech. Pap.*, 2009, doi: 10.4271/2009-01-0572.
- [102] Z. Ziari *et al.*, "Chemical and electrical properties of HMDSO plasma coated polyimide," *Vacuum*, vol. 93, pp. 31–36, 2013, doi: 10.1016/j.vacuum.2012.12.009.
- [103] C. Vautrin-UI, F. Roux, C. Boisse-Laporte, J. L. Pastol, and A. Chausse, "Hexamethyldisiloxane (HMDSO)-plasma-polymerised coatings as primer for iron corrosion protection: Influence of RF bias," *J. Mater. Chem.*, vol. 12, no. 8, pp. 2318–2324, 2002, doi: 10.1039/b111509j.
- [104] D. S. Wavhal, J. Zhang, M. L. Steen, and E. R. Fisher, "Investigation of gas phase species and deposition of SiO₂ films from HMDSO/O₂ plasmas," *Plasma Process. Polym.*, vol. 3, no. 3, pp. 276–287, 2006, doi: 10.1002/ppap.200500140.
- [105] A. Sonnenfeld *et al.*, "Deposition process based on organosilicon

- precursors in Dielectric Barrier Discharges at atmospheric pressure - A comparison," *Plasmas Polym.*, vol. 6, no. 4, pp. 237–266, 2001, doi: 10.1023/A:1014414016164.
- [106] R. Barni, S. Zanini, and C. Riccardi, "Characterization of the chemical kinetics in an O₂/HMDSO RF plasma for material processing," *Adv. Phys. Chem.*, vol. 2012, pp. 1–6, 2012, doi: 10.1155/2012/205380.
- [107] D. Korzec, D. Theirich, F. Werner, K. Traub, and J. Engemann, "Remote and direct microwave plasma deposition of HMDSO films: comparative study," *Surf. Coatings Technol.*, vol. 74–75, no. PART 1, pp. 67–74, 1995, doi: 10.1016/0257-8972(95)08223-9.
- [108] W. Michaeli, K. Telgenbüscher, J. Striffler, J. Leiber, and M. Stollenwerk, "Broad range variation in surface tension by plasma-polymerized coatings on polymethyl methacrylate," *Surf. Coatings Technol.*, vol. 59, no. 1–3, pp. 338–341, 1993, doi: 10.1016/0257-8972(93)90108-Z.
- [109] G. Wang, L. Jing, H. Yang, and C. Qiang, "Preparation methods and application of silicon oxide films," *2014 Int. Conf. Mechatronics, Electron. Ind. Control Eng. MEIC 2014*, pp. 479–483, 2014, doi: 10.2991/meic-14.2014.108.
- [110] H. W. Liu, T. H. Chen, C. H. Chang, S. K. Lu, Y. C. Lin, and D. S. Liu, "Impact on the gas barrier property of silicon oxide films prepared by tetramethylsilane-based PECVD incorporating with ammonia," *Appl. Sci.*, vol. 7, no. 1, 2017, doi: 10.3390/app7010056.
- [111] A. Tahhana, Z. Dehouchea, T. Ansonb, and G. Fernc, "Nanostructured silicon oxide film for enhanced crystalline solar cell," *2014 IEEE 40th Photovolt. Spec. Conf. PVSC 2014*, pp. 1296–1298, 2014, doi: 10.1109/PVSC.2014.6925154.
- [112] S. Y. Lien, Y. S. Cho, C. H. Hsu, K. Y. Shen, S. Zhang, and W. Y. Wu, "Mechanism of dense silicon dioxide films deposited under 100 °C via inductively coupled plasma chemical vapor deposition," *Surf. Coatings Technol.*, vol. 359, pp. 247–251, 2019, doi: 10.1016/j.surfcoat.2018.12.068.
- [113] D. A. P. Bulla and N. I. Morimoto, "Deposition of thick TEOS PECVD silicon oxide layers for integrated optical waveguide applications," *Thin Solid Films*, vol. 334, no. 1–2, pp. 60–64, 1998, doi: 10.1016/S0040-6090(98)01117-1.
- [114] H. Juárez *et al.*, "Low temperature deposition: Properties of SiO₂ films from TEOS and ozone by APCVD system," *J. Phys. Conf. Ser.*, vol. 167, p. 12020, May 2009, doi: 10.1088/1742-6596/167/1/012020.
- [115] G. Kickelbick, "Nanoparticles and Composites," in *The Sol-Gel Handbook*, vol. 1–3, John Wiley & Sons, Ltd, 2015, pp. 225–244.
- [116] R. Miller, M. C. Öztürk, J. J. Wortman, F. S. Johnson, and D. T. Grider, "LPCVD of silicon dioxide by pyrolysis of teos in a rapid thermal processor," *Mater. Lett.*, vol. 8, no. 9, pp. 353–356, 1989, doi: 10.1016/0167-577X(89)90006-2.
- [117] S. Ponton, H. Vergnes, D. Samelor, D. Sadowski, C. Vahlas, and B. Caussat, "Development of a kinetic model for the moderate temperature

chemical vapor deposition of SiO₂ films from tetraethyl orthosilicate and oxygen," *AIChE J.*, vol. 64, no. 11, pp. 3958–3966, 2018, doi: 10.1002/aic.16222.

- [118] G. Tochitani, M. Shimosuma, and H. Tagashira, "Deposition of silicon oxide films from TEOS by low frequency plasma chemical vapor deposition," *J. Vac. Sci. Technol. A Vacuum, Surfaces, Film.*, vol. 11, no. 2, pp. 400–405, 1993, doi: 10.1116/1.578743.
- [119] C. E. Viana and O. F. Rocha, "TEOS Silicon Oxides Deposition to Low Temperature Applications," p. 2004, 2004.
- [120] M. C. Lin, C. H. Tseng, L. S. Chang, and D. S. Wu, "Characterization of the silicon oxide thin films deposited on polyethylene terephthalate substrates by radio frequency reactive magnetron sputtering," *Thin Solid Films*, vol. 515, no. 11, pp. 4596–4602, 2007, doi: 10.1016/j.tsf.2006.11.039.
- [121] C. C. Kuo, M. C. Li, S. F. Liao, C. L. Wei, H. Sen Wei, and C. C. Lee, "Improving the gas barrier property of SiO_x:C thin films deposited by RF magnetron sputtering," *Surf. Coatings Technol.*, vol. 279, pp. 161–165, 2015, doi: 10.1016/j.surfcoat.2015.08.018.
- [122] A. F. Jankowski, J. P. Hayes, T. E. Felter, C. Evans, and A. J. Nelson, "Sputter deposition of silicon-oxide coatings," *Thin Solid Films*, vol. 420–421, pp. 43–46, 2002, doi: 10.1016/S0040-6090(02)00741-1.
- [123] S. M. Edlou, A. Smajkiewicz, and G. A. Al-Jumaily, "Optical properties and environmental stability of oxide coatings deposited by reactive sputtering," *Appl. Opt.*, vol. 32, no. 28, p. 5601, 1993, doi: 10.1364/ao.32.005601.
- [124] Z. Liu, Z. H. Sun, X. X. Ma, and J. Lin, "RF magnetron sputtered SiO_x coatings on papers," in *Advanced Materials Research*, 2011, vol. 174, pp. 475–479, doi: 10.4028/www.scientific.net/AMR.174.475.
- [125] O. Zywitzki, H. Sahm, M. Krug, H. Morgner, and M. Neumann, "Comparison of structure and properties of SiO_x coatings deposited by reactive pulsed magnetron sputtering (PMS) and by hollow cathode activated EB evaporation (HAD)," *Surf. Coatings Technol.*, vol. 133, no. 134, pp. 555–560, 2000, doi: 10.1016/S0257-8972(00)00975-0.
- [126] D. Framil, M. Van Gompel, F. Bourgeois, I. Furno, and Y. Leterrier, "The Influence of Microstructure on Nanomechanical and Diffusion Barrier Properties of Thin PECVD SiO_x Films Deposited on Parylene C Substrates," *Front. Mater.*, vol. 6, 2019, doi: 10.3389/fmats.2019.00319.
- [127] R. P. Ribeiro, R. D. C. C. Rangel, F. O. Fernandes, N. C. Cruz, and E. C. Rangel, "Effect of plasma oxidation treatment on production of a SiO_x/SiO_xCyHz Bilayer to protect carbon steel against corrosion," *Mater. Res.*, vol. 24, 2021, doi: 10.1590/1980-5373-MR-2021-0039.
- [128] D. Pech, P. Steyer, A. S. Loir, J. C. Sánchez-López, and J. P. Millet, "Analysis of the corrosion protective ability of PACVD silica-based coatings deposited on steel," *Surf. Coatings Technol.*, vol. 201, no. 1–2, pp. 347–352, 2006, doi: 10.1016/j.surfcoat.2005.11.130.
- [129] R. M. Pilliar, "Sol-gel surface modification of biomaterials," in *Surface*

Coating and Modification of Metallic Biomaterials, C. Wen, Ed. Woodhead Publishing, 2015, pp. 185–217.

- [130] J. Gasiorek *et al.*, “Functionalizable sol-gel silica coatings for corrosion mitigation,” *Materials (Basel)*, vol. 11, no. 2, p. 197, Jan. 2018, doi: 10.3390/ma11020197.
- [131] M. Basiaga, W. Walke, Z. Paszenda, P. Karasiński, and J. Szewczenko, “The effects of a SiO₂ coating on the corrosion parameters cpTi and Ti-6Al-7Nb alloy,” *Biomatter*, vol. 4, p. e28535, 2014, doi: 10.4161/biom.28535.
- [132] V. Miguel-Pérez, A. Martínez-Amesti, M. L. Nó, J. Calvo-Angós, and M. I. Arriortua, “EB-PVD deposition of spinel coatings on metallic materials and silicon wafers,” *Int. J. Hydrogen Energy*, vol. 39, no. 28, pp. 15735–15745, 2014, doi: 10.1016/j.ijhydene.2014.07.115.
- [133] D. M. Mattox, “Vacuum Evaporation and Vacuum Deposition,” in *Handbook of Physical Vapor Deposition (PVD) Processing*, Second Edi., D. M. Mattox, Ed. Boston: William Andrew Publishing, 2010, pp. 195–235.
- [134] J. Yi, X. D. He, Y. Sun, and Y. Li, “Electron beam-physical vapor deposition of SiC/SiO₂ high emissivity thin film,” *Appl. Surf. Sci.*, vol. 253, no. 9, pp. 4361–4366, 2007, doi: 10.1016/j.apsusc.2006.09.063.
- [135] S. Yokoyama, K. Iseki, T. Ohya, S. Komeda, Y. Yamada, and H. Ishihara, “New ceramic-coated barrier film by Dual Element Electron Beam Evaporation,” *Proceedings, Annu. Tech. Conf. - Soc. Vac. Coaters*, pp. 420–424, 1999.
- [136] J. O. Carneiro *et al.*, “Compositional, optical and electrical characteristics of SiO_x thin films deposited by reactive pulsed DC magnetron sputtering,” *Coatings*, vol. 9, no. 8, 2019, doi: 10.3390/coatings9080468.
- [137] S. Iwamori, Y. Gotoh, and K. Moorthi, “Silicon oxide gas barrier films deposited by reactive sputtering,” *Surf. Coatings Technol.*, vol. 166, no. 1, pp. 24–30, 2003, doi: 10.1016/S0257-8972(02)00769-7.
- [138] V. Teixeira, J. Carneiro, P. Carvalho, E. Silva, S. Azevedo, and C. Batista, “High barrier plastics using nanoscale inorganic films,” in *Multifunctional and Nanoreinforced Polymers for Food Packaging*, J.-M. Lagarón, Ed. Woodhead Publishing, 2011, pp. 285–315.
- [139] T. H. Tran *et al.*, “How the chemical structure of the plasma-deposited SiO_x film modifies its stability and barrier properties: FTIR study,” *Prog. Org. Coatings*, vol. 137, 2019, doi: 10.1016/j.porgcoat.2019.105332.
- [140] V. G. Varanasi, M. F. Velten, T. Odatsu, A. Ilyas, S. M. Iqbal, and P. B. Aswath, “Surface Modifications and Surface Characterization of Biomaterials Used in Bone Healing,” in *Materials and Devices for Bone Disorders*, S. Bose and A. Bandyopadhyay, Eds. Academic Press, 2017, pp. 405–452.
- [141] L. A. Chow, “Equipment and Manufacturability Issues in CVD Processes,” in *Handbook of Thin Film Deposition: Techniques, Processes, and Technologies: Third Edition*, Third Edit., K. Seshan, Ed. Oxford: William Andrew Publishing, 2012, pp. 127–178.
- [142] K. Teshima, Y. Inoue, H. Sugimura, and O. Takai, “Gas barrier properties

of silicon oxide films prepared by plasma-enhanced CVD using tetramethoxysilane," *Vacuum*, vol. 66, no. 3–4, pp. 353–357, 2002, doi: 10.1016/S0042-207X(02)00143-4.

- [143] A. Grüniger, A. Bieder, A. Sonnenfeld, P. R. von Rohr, U. Müller, and R. Hauert, "Influence of film structure and composition on diffusion barrier performance of SiO_x thin films deposited by PECVD," *Surf. Coatings Technol.*, vol. 200, no. 14–15, pp. 4564–4571, 2006, doi: 10.1016/j.surfcoat.2005.03.044.
- [144] L. Körner *et al.*, "Oxygen permeation, mechanical and structural properties of multilayer diffusion barrier coatings on polypropylene," *J. Phys. D. Appl. Phys.*, vol. 43, no. 11, 2010, doi: 10.1088/0022-3727/43/11/115301.
- [145] R. Lamendola and R. D'Agostino, "Process control of organosilicon plasmas for barrier film preparations," *Pure Appl. Chem.*, vol. 70, no. 6, pp. 1203–1208, 1998, doi: 10.1351/pac199870061203.
- [146] A. M. Wrobel and I. Blaszczyk-Lezak, "Remote hydrogen microwave plasma CVD of silicon carbonitride films from a tetramethyldisilazane source. Part 1: Characterization of the process and structure of the films," *Chem. Vap. Depos.*, vol. 13, no. 11, pp. 595–600, 2007, doi: 10.1002/cvde.200706586.
- [147] T. K. Won *et al.*, "SiO_x Process Chemistry Development Using Microwave Plasma CVD," US8906813B2, 2014.
- [148] F. Fei, C. Qiang, L. Zhongwei, L. Fuping, and A. Solodovnyk, "The application of nano-sio_x coatings as migration resistance layer by plasma enhanced chemical vapor deposition," *Plasma Chem. Plasma Process.*, vol. 32, no. 4, pp. 755–766, 2012, doi: 10.1007/s11090-012-9370-3.
- [149] H. Wang, L. Yang, and Q. Chen, "Investigation of microwave surface-wave plasma deposited SiO_x coatings on polymeric substrates," *Plasma Sci. Technol.*, vol. 16, no. 1, pp. 37–40, 2014, doi: 10.1088/1009-0630/16/1/08.
- [150] A. G. Erlat *et al.*, "SiO_x Gas Barrier Coatings on Polymer Substrates: Morphology and Gas Transport Considerations," *J. Phys. Chem. B*, vol. 103, no. 29, pp. 6047–6055, 1999, doi: 10.1021/jp990737e.
- [151] P. Dave, N. Chandwani, S. K. Nema, and S. Mukherji, "Enhancement in gas diffusion barrier property of polyethylene by plasma deposited SiO_x films for food packaging applications," *Trends Appl. Adv. Polym. Mater.*, pp. 255–273, 2017, doi: 10.1002/9781119364795.ch14.
- [152] B. M. Henry *et al.*, "The effect of thermal cycling damage on the permeability and structure of transparent gas barrier films," *Chem. Eng. Technol.*, vol. 22, no. 12, pp. 1010–1011, 1999, doi: 10.1002/(SICI)1521-4125(199912)22:12<1010::AID-CEAT1010>3.0.CO;2-Q.
- [153] D. Hegemann, U. Vohrer, C. Oehr, and R. Riedel, "Deposition of SiO_x films from O₂/HMDSO plasmas," *Surf. Coatings Technol.*, vol. 116–119, pp. 1033–1036, Sep. 1999, doi: 10.1016/S0257-8972(99)00092-4.
- [154] M. R. Alexander, R. D. Short, F. R. Jones, M. Stollenwerk, J. Zabold, and W. Michaeli, "An X-ray photoelectron spectroscopic investigation into the

- chemical structure of deposits formed from hexamethyldisiloxane/oxygen plasmas,” *J. Mater. Sci.*, vol. 31, no. 7, pp. 1879–1885, 1996, doi: 10.1007/BF00372203.
- [155] G. Cataldo, E. J. Wollack, A. D. Brown, and K. H. Miller, “Infrared dielectric properties of low-stress silicon oxide,” *Opt. Lett.*, vol. 41, no. 7, p. 1364, 2016, doi: 10.1364/ol.41.001364.
- [156] S. K. Ray, C. K. Maiti, and N. B. Chakrabarti, “Electrical Properties of Silicon Dioxide Deposited at Low Temperature By Metal-Organic Microwave Plasma CVD Technique,” *Electron. Lett.*, vol. 26, no. 14, pp. 1082–1083, 1990, doi: 10.1049/el:19900701.
- [157] H. Bartzsch, D. Glöß, B. Böcher, P. Frach, and K. Goedicke, “Properties of SiO₂ and Al₂O₃ films for electrical insulation applications deposited by reactive pulse magnetron sputtering,” *Surf. Coatings Technol.*, vol. 174–175, pp. 774–778, 2003, doi: 10.1016/S0257-8972(03)00384-0.
- [158] H. Miyazaki, “Refractive index and dielectric constant of SiO_x films deposited by reactive sputtering,” *Phys. Chem. Glas. Eur. J. Glas. Sci. Technol. Part B*, vol. 51, no. 2, pp. 136–137, 2010.
- [159] V. Gold, Ed., *The IUPAC Compendium of Chemical Terminology*. Research Triangle Park, NC: International Union of Pure and Applied Chemistry (IUPAC), 2019.
- [160] K. Hughes, “Corrosion Control: Part 1 – Types of Corrosion,” 2017. <https://www.performance-painting.com/blog/corrosion-control-part-1-types-of-corrosion> (accessed May 06, 2021).
- [161] E. McCafferty, *Introduction to corrosion science*. New York, NY: Springer New York, 2010.
- [162] P. Maaß, “Corrosion and Corrosion Protection,” in *Handbook of Hot-Dip Galvanization*, Wiley, 2011, pp. 1–19.
- [163] C. Verma, E. E. Ebenso, and M. A. Quraishi, “Ionic liquids as green and sustainable corrosion inhibitors for metals and alloys: An overview,” *J. Mol. Liq.*, vol. 233, pp. 403–414, 2017, doi: 10.1016/j.molliq.2017.02.111.
- [164] J. De Damborenea, A. Conde, and M. A. Arenas, “Corrosion inhibition with rare earth metal compounds in aqueous solutions,” in *Rare Earth-Based Corrosion Inhibitors*, M. Forsyth and B. Hinton, Eds. Woodhead Publishing, 2014, pp. 84–116.
- [165] N. Muthukumar, “Petroleum Products Transporting Pipeline Corrosion-A Review,” in *The Role of Colloidal Systems in Environmental Protection*, M. Fanun, Ed. Amsterdam: Elsevier, 2014, pp. 527–571.
- [166] Z. Ahmad, “Chapter 5 - Cathodic Protection,” in *Principles of Corrosion Engineering and Corrosion Control*, Z. Ahmad, Ed. Oxford: Butterworth-Heinemann, 2006, pp. 271–351.
- [167] W. Walke, Z. Paszenda, M. Basiaga, P. Karasiński, and M. Kaczmarek, “EIS study of SiO₂ oxide film on 316L stainless steel for cardiac implants,” in *Advances in Intelligent Systems and Computing*, vol. 284, 2014, pp. 403–410.
- [168] P. Galliano, J. J. De Damborenea, M. J. Pascual, and A. Durán, “Sol-Gel

- Coatings on 316L Steel for Clinical Applications,” *J. Sol-Gel Sci. Technol.*, vol. 13, no. 1–3, pp. 723–727, 1998, doi: 10.1023/a:1008653208083.
- [169] W. Walke *et al.*, “Evaluation of physicochemical properties of SiO₂-coated stainless steel after sterilization,” *Mater. Sci. Eng. C*, vol. 63, pp. 155–163, 2016, doi: 10.1016/j.msec.2016.02.065.
- [170] A. Delimi, Y. Coffinier, B. Talhi, R. Boukherroub, and S. Szunerits, “Investigation of the corrosion protection of SiO_x-like oxide films deposited by plasma-enhanced chemical vapor deposition onto carbon steel,” *Electrochim. Acta*, vol. 55, no. 28, pp. 8921–8927, 2010, doi: 10.1016/j.electacta.2010.08.008.
- [171] B. Nikrooz, M. Zandrahimi, and H. Ebrahimifar, “High temperature oxidation resistance and corrosion properties of dip coated silica coating by sol gel method on stainless steel,” *J. Sol-Gel Sci. Technol.*, vol. 63, no. 3, pp. 286–293, 2012, doi: 10.1007/s10971-012-2786-7.
- [172] O. De Sanctis, L. Gómez, N. Pellegrini, C. Parodi, A. Marajofsky, and A. Durán, “Protective glass coatings on metallic substrates,” *J. Non. Cryst. Solids*, vol. 121, no. 1–3, pp. 338–343, 1990, doi: 10.1016/0022-3093(90)90155-F.
- [173] D. C. L. Vasconcelos, J. A. N. Carvalho, M. Mantel, and W. L. Vasconcelos, “Corrosion resistance of stainless steel coated with sol-gel silica,” *J. Non. Cryst. Solids*, vol. 273, no. 1–3, pp. 135–139, 2000, doi: 10.1016/S0022-3093(00)00155-1.
- [174] D. Pech, P. Steyer, and J. P. Millet, “Electrochemical behaviour enhancement of stainless steels by a SiO₂ PACVD coating,” *Corros. Sci.*, vol. 50, no. 5, pp. 1492–1497, 2008, doi: 10.1016/j.corosci.2008.01.015.
- [175] Y. L. Kuo and K. H. Chang, “Atmospheric pressure plasma enhanced chemical vapor deposition of SiO_x films for improved corrosion resistant properties of AZ31 magnesium alloys,” *Surf. Coatings Technol.*, vol. 283, pp. 194–200, 2015, doi: 10.1016/j.surfcoat.2015.11.004.
- [176] A. Pepe, P. Galliano, M. Aparicio, A. Durán, and S. Ceré, “Sol-gel coatings on carbon steel: Electrochemical evaluation,” *Surf. Coatings Technol.*, vol. 200, no. 11, pp. 3486–3491, 2006, doi: 10.1016/j.surfcoat.2005.07.102.
- [177] A. Gangan, M. ElSabbagh, M. Bedair, M. El-Sabbah, and A. Fahmy, “Plasma Power Impact on Electrochemical Performance of Low Carbon Steel Coated By Plasma Thin Teos Films,” *Al-Azhar Bull. Sci.*, vol. 31, no. 1, pp. 51–58, 2020, doi: 10.21608/absb.2020.111474.
- [178] A. Gangan *et al.*, “Influence of pH values on the electrochemical performance of low carbon steel coated by plasma thin SiO_xCy films,” *Arab. J. Chem.*, vol. 14, no. 10, 2021, doi: 10.1016/j.arabjc.2021.103391.
- [179] A. González-Cortés, “Electrochemical Impedance Spectroscopy,” *Agric. Food Electroanal.*, vol. 1, no. 1, pp. 381–419, Dec. 2015, doi: 10.1002/9781118684030.ch14.
- [180] J. Telegdi, A. Shaban, and G. Vastag, “Biocorrosion-steel,” in *Encyclopedia of Interfacial Chemistry: Surface Science and Electrochemistry*, K. Wandelt, Ed. Oxford: Elsevier, 2018, pp. 28–42.

- [181] A. R. C. Bredar, A. L. Chown, A. R. Burton, and B. H. Farnum, "Electrochemical Impedance Spectroscopy of Metal Oxide Electrodes for Energy Applications," *ACS Appl. Energy Mater.*, vol. 3, no. 1, pp. 66–98, 2020, doi: 10.1021/acsaem.9b01965.
- [182] M. C. S. S. Macedo, I. C. P. Margarit-Mattos, F. L. Fragata, J. B. Jorcín, N. Pébère, and O. R. Mattos, "Contribution to a better understanding of different behaviour patterns observed with organic coatings evaluated by electrochemical impedance spectroscopy," *Corros. Sci.*, vol. 51, no. 6, pp. 1322–1327, 2009, doi: 10.1016/j.corsci.2009.03.016.
- [183] E. Angelini *et al.*, "PECVD Organosilicon thin films for corrosion protection of metals," pp. 979–999, 2004.
- [184] W. Grzesik, "Cutting Tool Materials," in *Advanced Machining Processes of Metallic Materials*, Second Edi., W. Grzesik, Ed. Elsevier, 2017, pp. 35–63.
- [185] Otai Special Steel, "High Speed Steel M2 | 1.3343 | HS-6-5-2C | SKH51," 2021. <https://www.astmsteel.com/product/m2-tool-steel/> (accessed May 12, 2021).
- [186] S. W. Park, J. S. Jung, K. S. Kim, K. H. Kim, and N. M. Hwang, "Effect of bias applied to the substrate on the low temperature growth of silicon epitaxial films during RF-PECVD," *Cryst. Growth Des.*, vol. 18, no. 10, pp. 5816–5823, 2018, doi: 10.1021/acs.cgd.8b00384.
- [187] M. Wang, X. G. Diao, A. P. Huang, P. K. Chu, and Z. Wu, "Influence of substrate bias on the composition of SiC thin films fabricated by PECVD and underlying mechanism," *Surf. Coatings Technol.*, vol. 201, no. 15, pp. 6777–6780, 2007, doi: 10.1016/j.surfcoat.2006.09.065.
- [188] C. Ingelbrecht, N. Jennett, R. Jacobs, and J. Meneve, "Report EUR 20986. The certification of critical coating failure loads: a reference material for scratch testing according to ENV 1071-3: 1994," 2004.
- [189] S. S. Sadhal, *Transport Phenomena with Drops and Bubbles*. New York, NY: Springer New York, 2011.
- [190] L. Kong, M. Ostadhassan, S. Zamiran, B. Liu, C. Li, and G. G. Marino, "Geomechanical upscaling methods: Comparison and verification via 3D printing," *Energies*, vol. 12, no. 3, p. 382, 2019, doi: 10.3390/en12030382.
- [191] S. Bec, A. Tonck, J. M. Georges, E. Georges, and J. L. Loubet, "Improvements in the indentation method with a surface force apparatus," *Philos. Mag. A Phys. Condens. Matter, Struct. Defects Mech. Prop.*, vol. 74, no. 5, pp. 1061–1072, 1996, doi: 10.1080/01418619608239707.
- [192] W. C. Oliver and G. M. Pharr, "An improved technique for determining hardness and elastic modulus using load and displacement sensing indentation experiments," *J. Mater. Res.*, vol. 7, no. 6, pp. 1564–1583, 1992, doi: 10.1557/jmr.1992.1564.
- [193] NanoPhysics, "SEM-EDX," 2018. <https://www.nanophysics.nl/services-view/edx-analysis/>.
- [194] M. El-Dairi and R. J. House, "Nanocomposite coatings based on quaternary metal-nitrogen and nanocarbon systems," 2012.

- [195] F. Ay and A. Aydinli, "Comparative investigation of hydrogen bonding in silicon based PECVD grown dielectrics for optical waveguides," *Opt. Mater. (Amst.)*, vol. 26, no. 1, pp. 33–46, 2004, doi: 10.1016/j.optmat.2003.12.004.
- [196] P. G. Pai, S. S. Chao, Y. Takagi, and G. Lucovsky, "Infrared spectroscopic study of SiO_x films produced by plasma enhanced chemical vapor deposition," *J. Vac. Sci. Technol. A Vacuum, Surfaces, Film.*, vol. 4, no. 3, pp. 689–694, 1986, doi: 10.1116/1.573833.
- [197] M. I. Alayo, I. Pereyra, W. L. Scopel, and M. C. A. Fantini, "On the nitrogen and oxygen incorporation in plasma-enhanced chemical vapor deposition (PECVD) SiO_xN_y films," *Thin Solid Films*, vol. 402, no. 1–2, pp. 154–161, 2002, doi: 10.1016/S0040-6090(01)01685-6.
- [198] H. Takai and T. Itoh, "Porous silicon layers and its oxide for the silicon-on-insulator structure," *J. Appl. Phys.*, vol. 60, no. 1, pp. 222–225, 1986, doi: 10.1063/1.337686.
- [199] M. Nakamura, Y. Mochizuki, K. Usami, Y. Itoh, and T. Nozaki, "Infrared absorption spectra and compositions of evaporated silicon oxides (SiO_x)," *Solid State Commun.*, vol. 50, no. 12, pp. 1079–1081, 1984, doi: 10.1016/0038-1098(84)90292-8.
- [200] H. Buijs, "Infrared Spectroscopy," in *Springer Handbooks*, vol. 2018, no. 14th September, New York, NY: Springer New York, 2006, pp. 607–613.
- [201] D. of I. T. for the P. of M. Science, "Experimental matters: Production and measurement of X-Rays," 2018. <https://www.doitpoms.ac.uk/tlplib/xray-diffraction/production.php>.
- [202] G. K. Williamson and R. E. Smallman, "III. Dislocation densities in some annealed and cold-worked metals from measurements on the X-ray Debye-Scherrer spectrum," *Philos. Mag.*, vol. 1, no. 1, pp. 34–46, 1956, doi: 10.1080/14786435608238074.
- [203] S. K. Mastoor and D. H. Authority, "Monitoring iron corrosion by direct current techniques," vol. 27, no. 6, pp. 4963–4969, 2015.
- [204] M. Sun *et al.*, "Characterisation and Electrochemical Evaluation of Plasma Electrolytic Oxidation Coatings on Magnesium with Plasma Enhanced Chemical Vapour Deposition Post-Treatments," *Plasma Process. Polym.*, vol. 13, no. 2, pp. 266–278, Feb. 2016, doi: 10.1002/ppap.201500059.
- [205] V. Matveev, "Complex Variables," in *Electrochemical Impedance Spectroscopy*, vol. 2, Hoboken, NJ, USA: John Wiley & Sons, Inc., 2008, pp. 1–21.
- [206] N. Spinner, "EIS Data Plotting Plotting Conventions - Nyquist Plots," *PINE research*, 2019. <https://pineresearch.com/shop/kb/theory/eis-theory/eis-data-plotting/> (accessed Apr. 08, 2022).
- [207] I. C. P. Margarit-Mattos, "EIS and organic coatings performance: Revisiting some key points," *Electrochim. Acta*, vol. 354, p. 136725, 2020, doi: 10.1016/j.electacta.2020.136725.
- [208] R. C. C. Rangel, N. C. Cruz, A. Milella, F. Fracassi, and E. C. Rangel, "Barrier and mechanical properties of carbon steel coated with SiO_x/SiO_xCyHz gradual films prepared by PECVD," *Surf. Coatings*

Technol., vol. 378, p. 124996, Nov. 2019, doi:
10.1016/j.surfcoat.2019.124996.

- [209] C. S. Yang, Y. H. Yu, K. M. Lee, H. J. Lee, and C. K. Choi, "The influence of carbon content in carbon-doped silicon oxide film by thermal treatment," *Thin Solid Films*, vol. 435, no. 1–2, pp. 165–169, 2003, doi: 10.1016/S0040-6090(03)00356-0.
- [210] S. Sahli, Y. Segui, S. Ramdani, and Z. Takkouk, "R.f. plasma deposition from hexamethyldisiloxane-oxygen mixtures," *Thin Solid Films*, vol. 250, no. 1–2, pp. 206–212, 1994, doi: 10.1016/0040-6090(94)90187-2.
- [211] S. V. Bhoraskar, T. Bhawe, and T. A. Railkar, "Crystallite-size-dependent characteristics of porous silicon," *Bull. Mater. Sci.*, vol. 17, no. 5, pp. 523–531, 1994, doi: 10.1007/BF02757898.
- [212] D. B. Mawhinney, J. A. Glass, and J. T. Yates, "FTIR study of the oxidation of porous silicon," *J. Phys. Chem. B*, vol. 101, no. 7, pp. 1202–1206, 1997, doi: 10.1021/jp963322r.
- [213] J. A. Luna-López, "FTIR and photoluminescence of annealed silicon rich oxide films," *Superf. y Vacío*, vol. 22, no. 1, pp. 11–14, 2009.
- [214] A. Luna-López, M. Aceves-Mijares, and A. Malik, "Spectroscopy infrared characterization of annealed silicon rich oxide films," in *2nd International Conference on Electrical and Electronics Engineering, ICEEE and XI Conference on Electrical Engineering, CIE 2005*, 2005, vol. 2005, pp. 435–439, doi: 10.1109/ICEEE.2005.1529663.
- [215] C. Huang and Q. Yu, "Deposition of silicon oxide hard coatings by low-temperature radio-frequency plasmas," *J. Appl. Polym. Sci.*, vol. 116, no. 1, pp. 245–251, 2010, doi: 10.1002/app.31440.
- [216] C. Gamonpilas and E. P. Busso, "On the effect of substrate properties on the indentation behaviour of coated systems," *Mater. Sci. Eng. A*, vol. 380, no. 1, pp. 52–61, 2004, doi: 10.1016/j.msea.2004.04.038.
- [217] G. Subhash, P. Hittepole, and S. Maiti, "Mechanical properties of PECVD thin ceramic films," *J. Eur. Ceram. Soc.*, vol. 30, no. 3, pp. 689–697, 2010, doi: 10.1016/j.jeurceramsoc.2009.09.020.
- [218] F. Benítez, E. Martínez, and J. Esteve, "Improvement of hardness in plasma polymerized hexamethyldisiloxane coatings by silica-like surface modification," *Thin Solid Films*, vol. 377–378, pp. 109–114, 2000, doi: 10.1016/S0040-6090(00)01393-6.
- [219] Z. Cao and X. Zhang, "Nanoindentation stress-strain curves of plasma-enhanced chemical vapor deposited silicon oxide thin films," *Thin Solid Films*, vol. 516, no. 8, pp. 1941–1951, 2008, doi: 10.1016/j.tsf.2007.09.033.
- [220] I. N. Reddy *et al.*, "High emittance surface engineered metallic surfaces," *Ceram. Int.*, vol. 40, no. 9 PART A, pp. 14549–14554, 2014, doi: 10.1016/j.ceramint.2014.05.143.
- [221] N. E. Blanchard, V. V. Naik, T. Geue, O. Kahle, D. Hegemann, and M. Heuberger, "Response of Plasma-Polymerized Hexamethyldisiloxane Films to Aqueous Environments," *Langmuir*, vol. 31, no. 47, pp. 12944–12953, 2015, doi: 10.1021/acs.langmuir.5b03010.

- [222] B. Torda, L. Rachdi, A. Mohamed Okasha Mohamed Okasha, P. Saint-Cast, and M. Hofmann, "The effects of carbon incorporation on the refractive index of PECVD silicon oxide layers," *AIP Adv.*, vol. 10, no. 4, p. 045331, Apr. 2020, doi: 10.1063/1.5142017.
- [223] R. Hofman, J. G. F. Westheim, I. Pouwel, T. Fransen, and P. J. Gellings, "FTIR and XPS studies on corrosion-resistant SiO₂ coatings as a function of the humidity during deposition," *Surf. Interface Anal.*, vol. 24, no. 1, pp. 1–6, 1996, doi: 10.1002/(SICI)1096-9918(199601)24:1<1::AID-SIA73>3.0.CO;2-I.
- [224] M. Zarchi and S. Ahangarani, "Effect of Oxygen Concentration on the Structure and Optical Properties of SiO_x Coatings," *Surf. Eng. Appl. Electrochem.*, vol. 54, no. 1, pp. 47–54, 2018, doi: 10.3103/S1068375518010167.
- [225] A. Barranco, J. Cotrino, F. Yubero, T. Girardeau, S. Camelio, and A. R. González-Elipe, "A structural study of organo-silicon polymeric thin films deposited by remote microwave plasma enhanced chemical vapour deposition," *Surf. Coatings Technol.*, vol. 180–181, pp. 244–249, 2004, doi: 10.1016/j.surfcoat.2003.10.031.
- [226] H.-P. Ma *et al.*, "Systematic Study of the SiO_x Film with Different Stoichiometry by Plasma-Enhanced Atomic Layer Deposition and Its Application in SiO_x/SiO₂ Super-Lattice," *Nanomaterials*, vol. 9, no. 1, p. 55, Jan. 2019, doi: 10.3390/nano9010055.
- [227] R. Alfonsetti, G. De Simone, L. Lozzi, M. Passacantando, P. Picozzi, and S. Santucci, "SiO_x surface stoichiometry by XPS: A comparison of various methods," *Surf. Interface Anal.*, vol. 22, no. 1–12, pp. 89–92, 1994, doi: 10.1002/sia.740220122.
- [228] L. A. O'Hare, B. Parbhoo, and S. R. Leadley, "Development of a methodology for XPS curve-fitting of the Si 2p core level of siloxane materials," *Surf. Interface Anal.*, vol. 36, no. 10, pp. 1427–1434, 2004, doi: 10.1002/sia.1917.
- [229] J. Sun, Z. Xu, W. Li, and X. Shen, "Effect of nano-SiO₂ on the early hydration of alite-sulphoaluminate cement," *Nanomaterials*, vol. 7, no. 5, 2017, doi: 10.3390/nano7050102.
- [230] H. W. Yang, J. H. Lee, S. C. Jung, S. T. Myung, W. S. Kang, and S. J. Kim, "Fabrication of Si/SiO_x Anode Materials by a Solution Reaction-Based Method for Lithium Ion Batteries," *J. Korean Inst. Met. Mater.*, vol. 54, no. 10, pp. 780–786, Oct. 2016, doi: 10.3365/KJMM.2016.54.10.780.
- [231] J. Kim, S. Y. Kim, C.-M. Yang, and G. W. Lee, "Possibility of Recycling SiO_x Particles Collected at Silicon Ingot Production Process as an Anode Material for Lithium Ion Batteries," *Sci. Rep.*, vol. 9, no. 1, pp. 1–7, Dec. 2019, doi: 10.1038/s41598-019-50011-8.
- [232] J. Park, S. S. Park, and Y. S. Won, "In situ XRD study of the structural changes of graphite anodes mixed with SiO_x during lithium insertion and extraction in lithium ion batteries," *Electrochim. Acta*, vol. 107, pp. 467–472, 2013, doi: 10.1016/j.electacta.2013.06.059.
- [233] G. Liu *et al.*, "Green and scalable fabrication of sandwich-like ng/sio_x/ng homogenous hybrids for superior lithium-ion batteries," *Nanomaterials*,

vol. 11, no. 9, p. 2366, Sep. 2021, doi: 10.3390/nano11092366.

- [234] H. J. Jeong *et al.*, "Electrochemical properties of chemically processed SiO_x as coating material in lithium-ion batteries with Si anode," *Sci. World J.*, vol. 2014, 2014, doi: 10.1155/2014/528496.
- [235] R. F. H. Hernandha *et al.*, "Supercritical CO₂-Assisted SiO_x/Carbon Multi-Layer Coating on Si Anode for Lithium-Ion Batteries," *Adv. Funct. Mater.*, vol. 31, no. 40, p. 2104135, Oct. 2021, doi: 10.1002/adfm.202104135.
- [236] Y. Cao, R. A. Dunlap, and M. N. Obrovac, "Electrochemistry and Thermal Behavior of SiO_x Made by Reactive Gas Milling," *J. Electrochem. Soc.*, vol. 167, no. 11, p. 110501, 2020, doi: 10.1149/1945-7111/ab9e83.
- [237] Y. T. Prabhu, K. V. Rao, V. S. S. Kumar, and B. S. Kumari, "X-Ray Analysis by Williamson-Hall and Size-Strain Plot Methods of ZnO Nanoparticles with Fuel Variation," *World J. Nano Sci. Eng.*, vol. 04, no. 01, pp. 21–28, 2014, doi: 10.4236/wjnse.2014.41004.
- [238] S. Takebayashi, T. Kunieda, N. Yoshinaga, K. Ushioda, and S. Ogata, "Comparison of the dislocation density in martensitic steels evaluated by some X-ray diffraction methods," *ISIJ Int.*, vol. 50, no. 6, pp. 875–882, 2010, doi: 10.2355/isijinternational.50.875.
- [239] R. Kužel, "Kinematical diffraction by distorted crystals - Dislocation X-ray line broadening," *Zeitschrift für Krist.*, vol. 222, no. 3–4, pp. 136–149, Mar. 2007, doi: 10.1524/zkri.2007.222.3-4.136.
- [240] V. Mote, Y. Purushotham, and B. Dole, "Williamson-Hall analysis in estimation of lattice strain in nanometer-sized ZnO particles," *J. Theor. Appl. Phys.*, vol. 6, no. 1, p. 6, Dec. 2012, doi: 10.1186/2251-7235-6-6.
- [241] K. R. Sriraman, S. Ganesh Sundara Raman, and S. K. Seshadri, "Influence of crystallite size on the hardness and fatigue life of steel samples coated with electrodeposited nanocrystalline Ni-W alloys," *Mater. Lett.*, vol. 61, no. 3, pp. 715–718, 2007, doi: 10.1016/j.matlet.2006.05.049.
- [242] X. Liu, F. Yuan, and Y. Wei, "Grain size effect on the hardness of nanocrystal measured by the nanosize indenter," *Appl. Surf. Sci.*, vol. 279, pp. 159–166, 2013, doi: 10.1016/j.apsusc.2013.04.062.
- [243] W. Zhang *et al.*, "Experimental study on the thickness-dependent hardness of SiO₂ thin films using nanoindentation," *Coatings*, vol. 11, no. 1, pp. 1–12, 2021, doi: 10.3390/coatings11010023.
- [244] A. Atrens, G. L. Song, Z. Shi, A. Soltan, S. Johnston, and M. S. Dargusch, "Understanding the corrosion of Mg and Mg alloys," in *Encyclopedia of Interfacial Chemistry: Surface Science and Electrochemistry*, K. Wandelt, Ed. Oxford: Elsevier, 2018, pp. 515–534.
- [245] K. Kakaei, M. D. Esrafil, and A. Ehsani, "Graphene and Anticorrosive Properties," in *Interface Science and Technology*, vol. 27, K. Kakaei, M. D. Esrafil, and A. Ehsani, Eds. Elsevier, 2019, pp. 303–337.
- [246] S. Kirtay, "Improvement of oxidation resistance of mild steel by SiO₂-Al₂O₃ sol gel coating," *Acta Phys. Pol. A*, vol. 128, no. 2, pp. 90–92, 2015, doi: 10.12693/APhysPolA.128.B-90.

- [247] G. Viramontes-Gamboa, B. F. Rivera-Vasquez, and D. G. Dixon, "The Active-Passive Behavior of Chalcopyrite," *J. Electrochem. Soc.*, vol. 154, no. 6, p. C299, 2007, doi: 10.1149/1.2721782.
- [248] T. P. Hoar, "The production and breakdown of the passivity of metals," *Corros. Sci.*, vol. 7, no. 6, pp. 341–355, Jan. 1967, doi: 10.1016/S0010-938X(67)80023-4.
- [249] S. Choudhary, K. Ogle, O. Gharbi, S. Thomas, and N. Birbilis, "Recent insights in corrosion science from atomic spectroelectrochemistry," *Electrochem. Sci. Adv.*, pp. 1–24, Dec. 2021, doi: 10.1002/elsa.202100196.
- [250] M. Serdechnova, P. Volovitch, F. Brisset, and K. Ogle, "On the cathodic dissolution of Al and Al alloys," *Electrochim. Acta*, vol. 124, pp. 9–16, 2014, doi: 10.1016/j.electacta.2013.09.145.
- [251] S. Kirtay, "Preparation of hybrid silica sol-gel coatings on mild steel surfaces and evaluation of their corrosion resistance," *Prog. Org. Coatings*, vol. 77, no. 11, pp. 1861–1866, 2014, doi: 10.1016/j.porgcoat.2014.06.016.
- [252] C. Liu, Q. Bi, A. Leyland, and A. Matthews, "An electrochemical impedance spectroscopy study of the corrosion behavior of PVD coated steels in 0.5 N NaCl aqueous solution: Part II. EIS interpretation of corrosion behaviour," *Corros. Sci.*, vol. 45, no. 6, pp. 1257–1273, 2003, doi: 10.1016/S0010-938X(02)00214-7.
- [253] J. C. Rowlands and D. J. Chuter, "No Title," in *Metallic Corrosion: Proceedings, 8th International Congress on Metallic Corrosion*, 1981, p. 1068.
- [254] J. W. Nicholson, "Evaluation of the Anti-Corrosion Performance of Water-Borne Ionomer Coatings Using Ac Impedance," *JOCCA-Surface Coatings Int.*, vol. 77, no. 11, p. 472 ff., 1994, [Online]. Available: <https://www.tib.eu/de/suchen/id/olc%3A1711757721>.
- [255] M. S. Islam, K. Otani, and M. Sakairi, "Effects of metal cations on mild steel corrosion in 10 mM Cl⁻ aqueous solution," *Corros. Sci.*, vol. 131, pp. 17–27, 2018, doi: 10.1016/j.corsci.2017.11.015.
- [256] D. D. Macdonald, "The Point Defect Model for the Passive State," *J. Electrochem. Soc.*, vol. 139, no. 12, pp. 3434–3449, Dec. 1992, doi: 10.1149/1.2069096.
- [257] H. J. Engell, "Stability and breakdown phenomena of passivating films," *Electrochim. Acta*, vol. 22, no. 9, pp. 987–993, 1977, doi: 10.1016/0013-4686(77)85010-X.
- [258] E. McCafferty, "Sequence of steps in the pitting of aluminum by chloride ions," *Corros. Sci.*, vol. 45, no. 7, pp. 1421–1438, 2003, doi: 10.1016/S0010-938X(02)00231-7.
- [259] K. Otani and M. Sakairi, "Effects of metal cations on corrosion of mild steel in model fresh water," *Corros. Sci.*, vol. 111, pp. 302–312, 2016, doi: 10.1016/j.corsci.2016.05.020.
- [260] S. Qi, X. Li, Z. Zhang, and H. Dong, "Fabrication and characterisation of electro-brush plated nickel-graphene oxide nano-composite coatings,"

Thin Solid Films, vol. 644, pp. 106–114, 2017, doi: 10.1016/j.tsf.2017.06.064.

- [261] X. Yuan, Z. F. Yue, X. Chen, S. F. Wen, L. Li, and T. Feng, “EIS study of effective capacitance and water uptake behaviors of silicone-epoxy hybrid coatings on mild steel,” *Prog. Org. Coatings*, vol. 86, pp. 41–48, 2015, doi: 10.1016/j.porgcoat.2015.04.004.
- [262] Y. Shinata and Y. Nishi, “NaCl-induced accelerated oxidation of chromium,” *Oxid. Met.*, vol. 26, no. 3–4, pp. 201–212, 1986, doi: 10.1007/BF00659184.
- [263] G. Mori *et al.*, “The influence of NaCl and CaCl₂ induced high temperature corrosion on the aqueous corrosion resistance of stainless steels,” *Mater. Corros.*, vol. 70, no. 6, pp. 1071–1086, Jun. 2019, doi: 10.1002/maco.201810451.
- [264] F. K. Crundwell, “On the Mechanism of the Dissolution of Quartz and Silica in Aqueous Solutions,” *ACS Omega*, vol. 2, no. 3, pp. 1116–1127, 2017, doi: 10.1021/acsomega.7b00019.
- [265] J. P. Icenhower and P. M. Dove, “The dissolution kinetics of amorphous silica into sodium chloride solutions: Effects of temperature and ionic strength,” *Geochim. Cosmochim. Acta*, vol. 64, no. 24, pp. 4193–4203, 2000, doi: 10.1016/S0016-7037(00)00487-7.
- [266] B. Grambow, “General Rate Equation for Nuclear Waste Glass Corrosion,” *Mater. Res. Soc. Symp. Proc.*, vol. 44, pp. 15–27, Feb. 1985, doi: 10.1557/proc-44-15.

Appendix A: SEM imaging

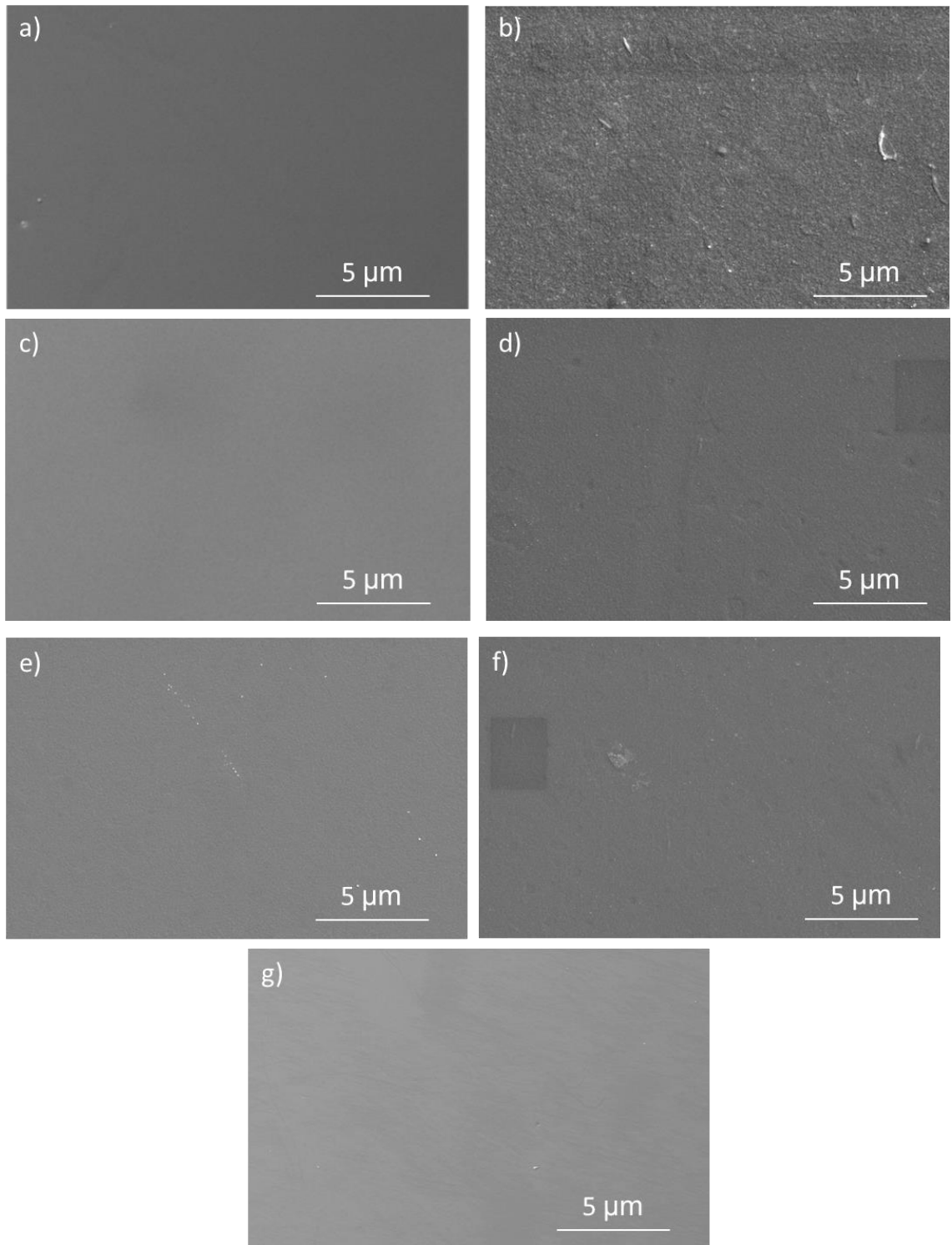


Figure A.9.1 SEM micrographs for the SiO_x samples coated at varying HMDSO: O_2 ratios a) 1:10, b) 1:12, c) 1:14, d) 1:16, e) 1:20, f) 1:24 and g) 1:36, all with a 2 μm DOE thickness.

Appendix B: Nyquist and Bode plots

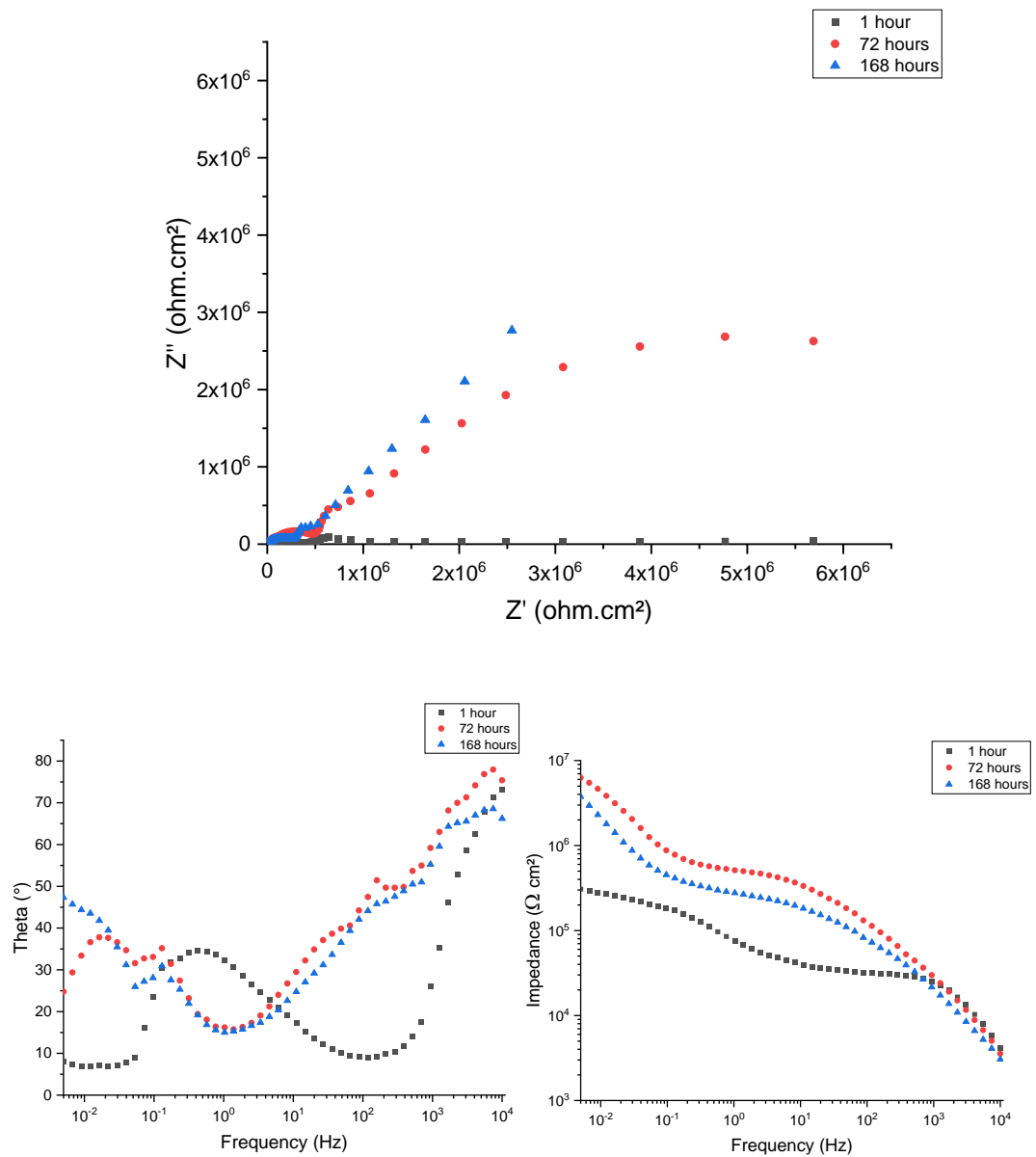


Figure B.1 – Nyquist and Bode plots for SiO_x coating with HMDSO:O₂ ratio 1:10 and DOE thickness 2 μm.

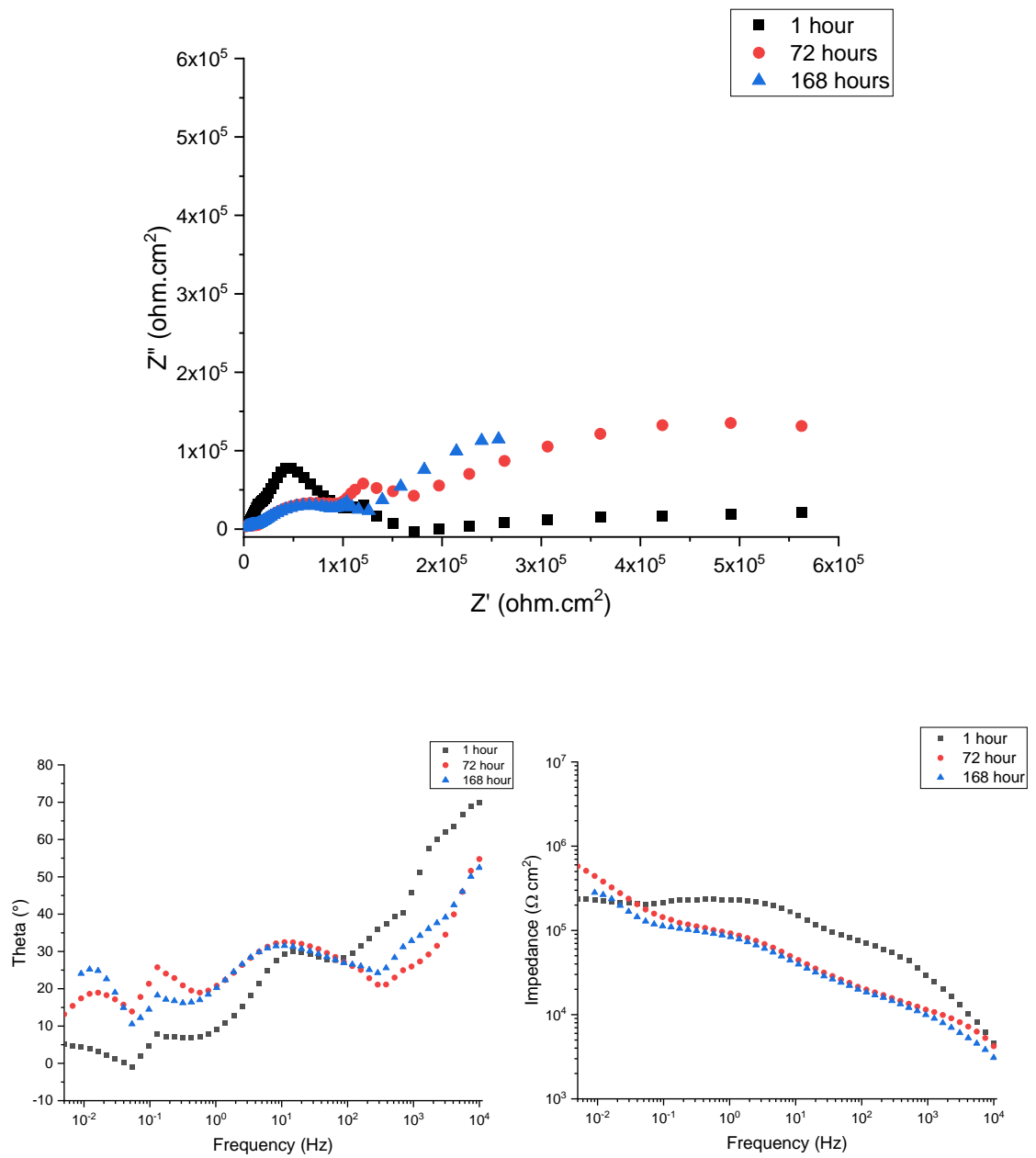


Figure B.2 – Nyquist and Bode plots for SiO_x coating with HMDSO:O₂ ratio 1:12 and DOE thickness 2 μm.

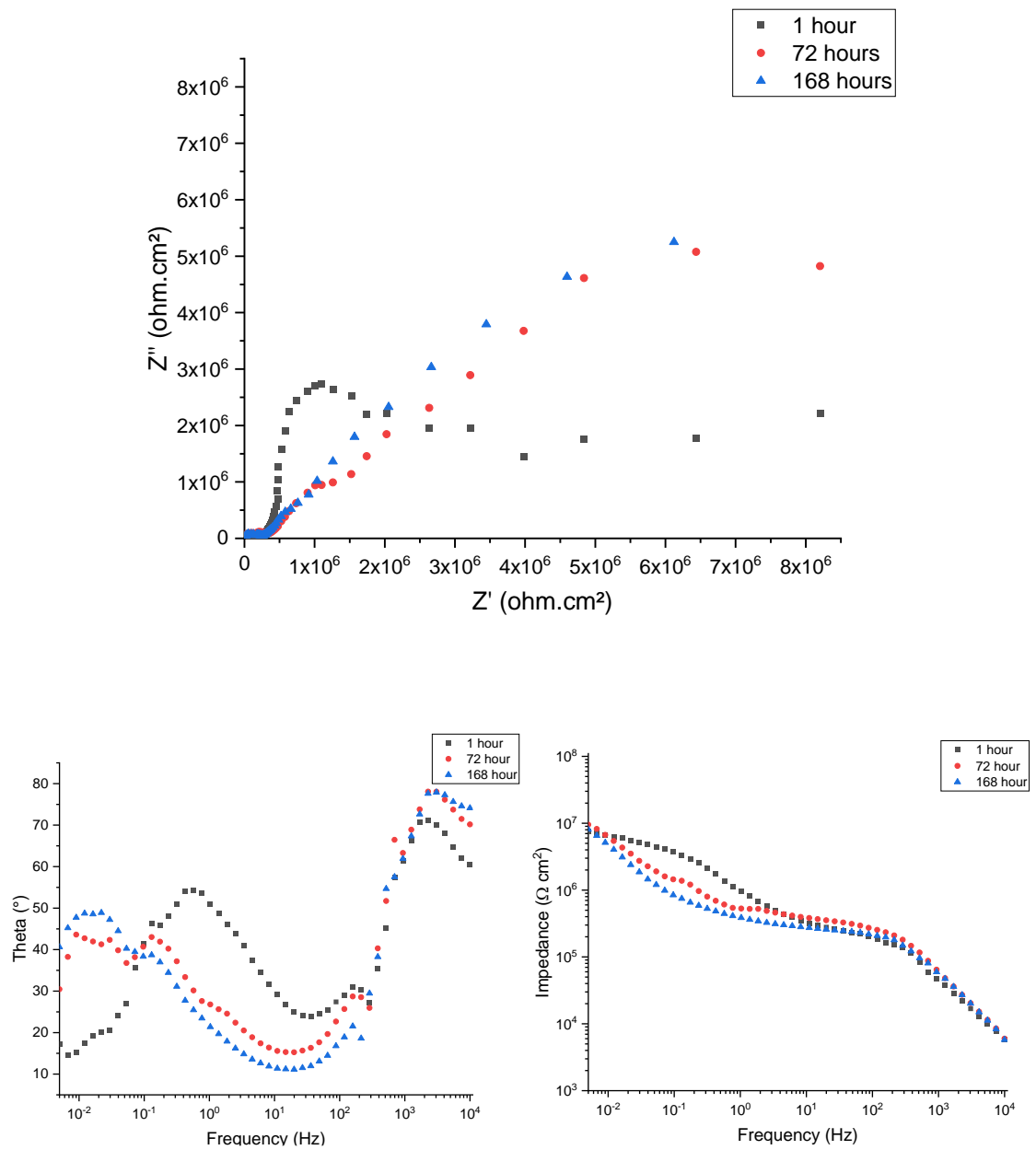


Figure B.3 – Nyquist and Bode plots for SiO_x coating with HMDSO:O₂ ratio 1:14 and DOE thickness 2 μm .

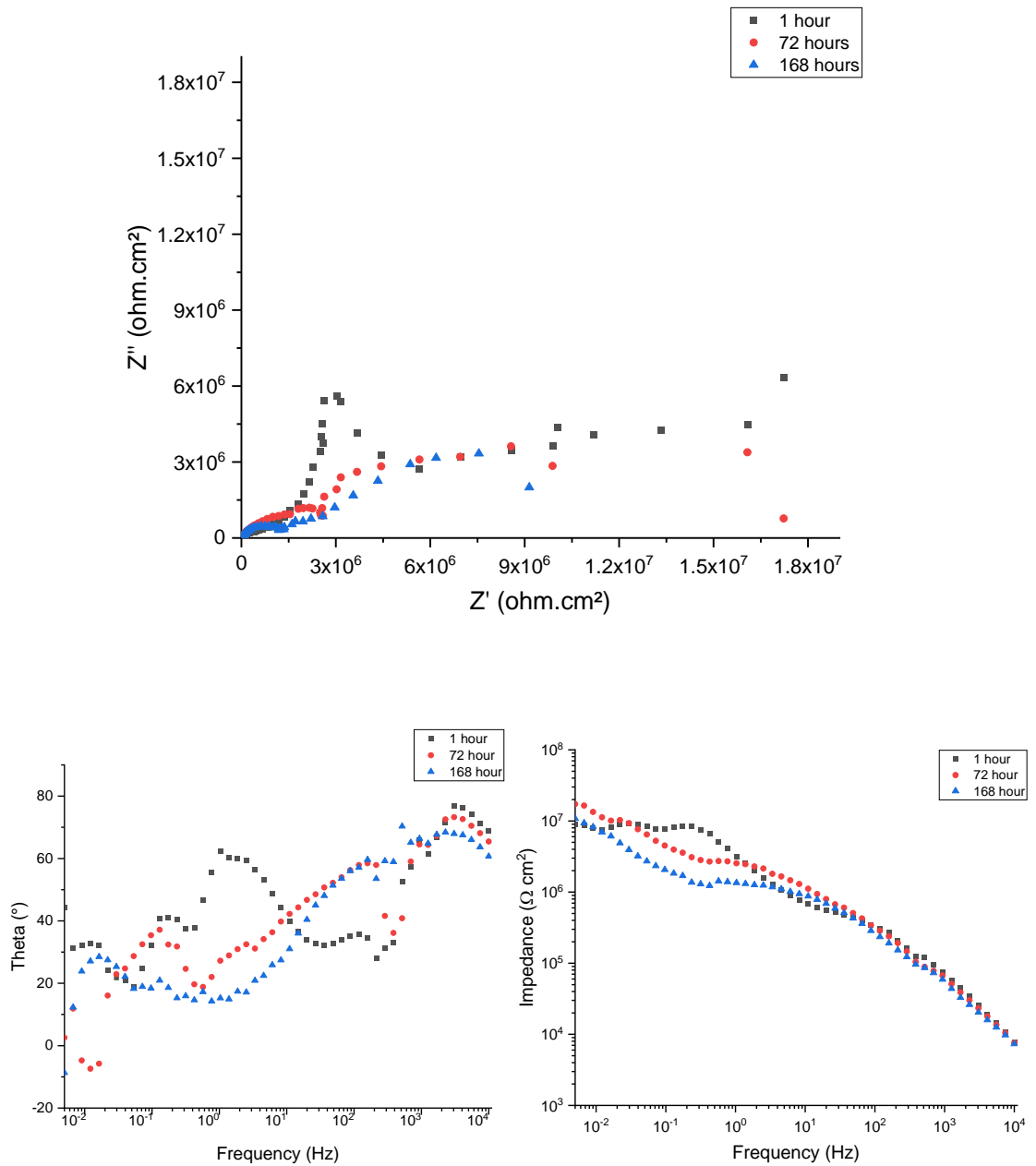


Figure B.4 – Nyquist and Bode plots for SiO_x coating with HMDSO:O₂ ratio 1:16 and DOE thickness 2 μm .

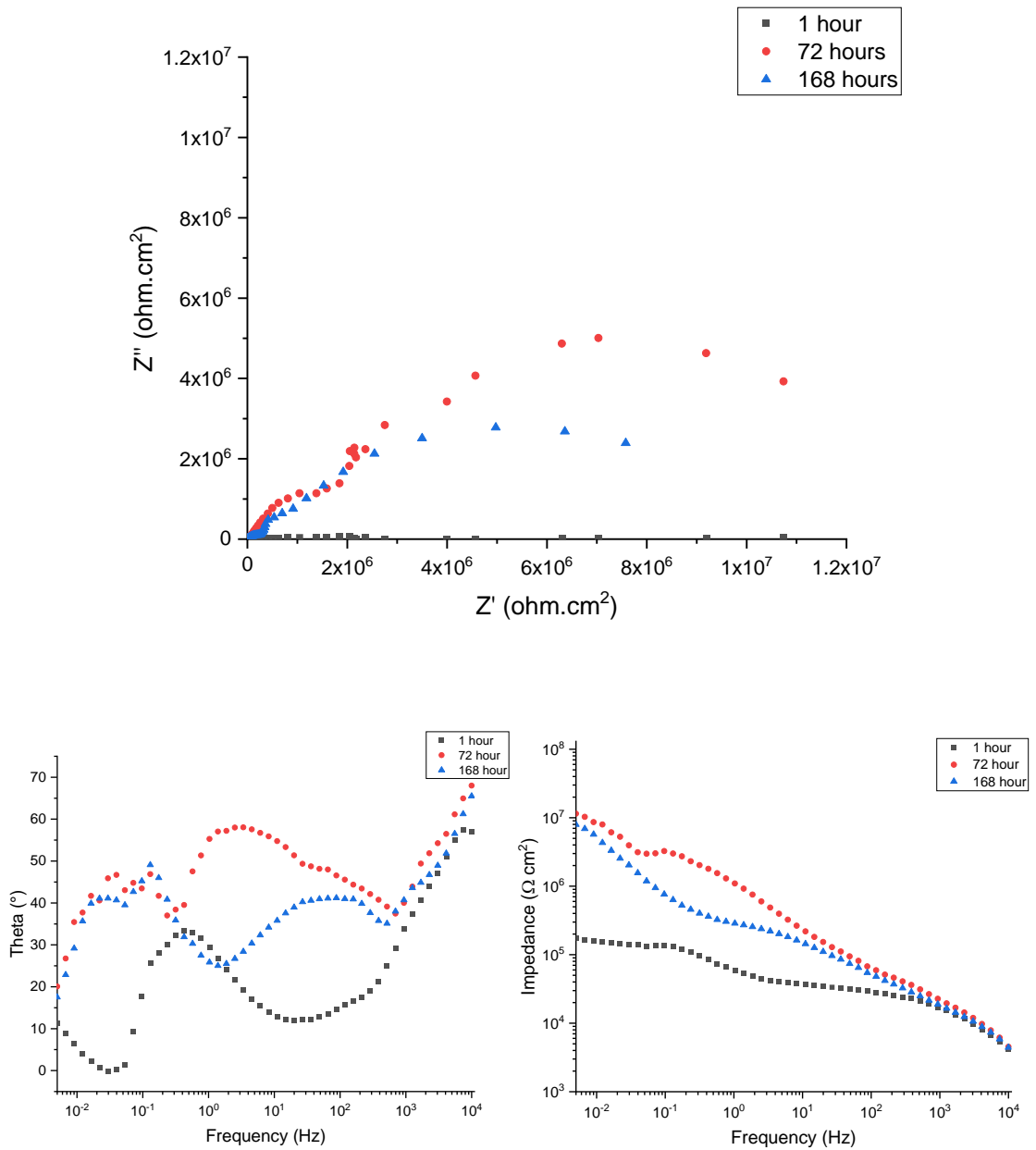


Figure B.5 – Nyquist and Bode plots for SiO_x coating with HMDSO: O_2 ratio 1:24 and DOE thickness $2 \mu\text{m}$.

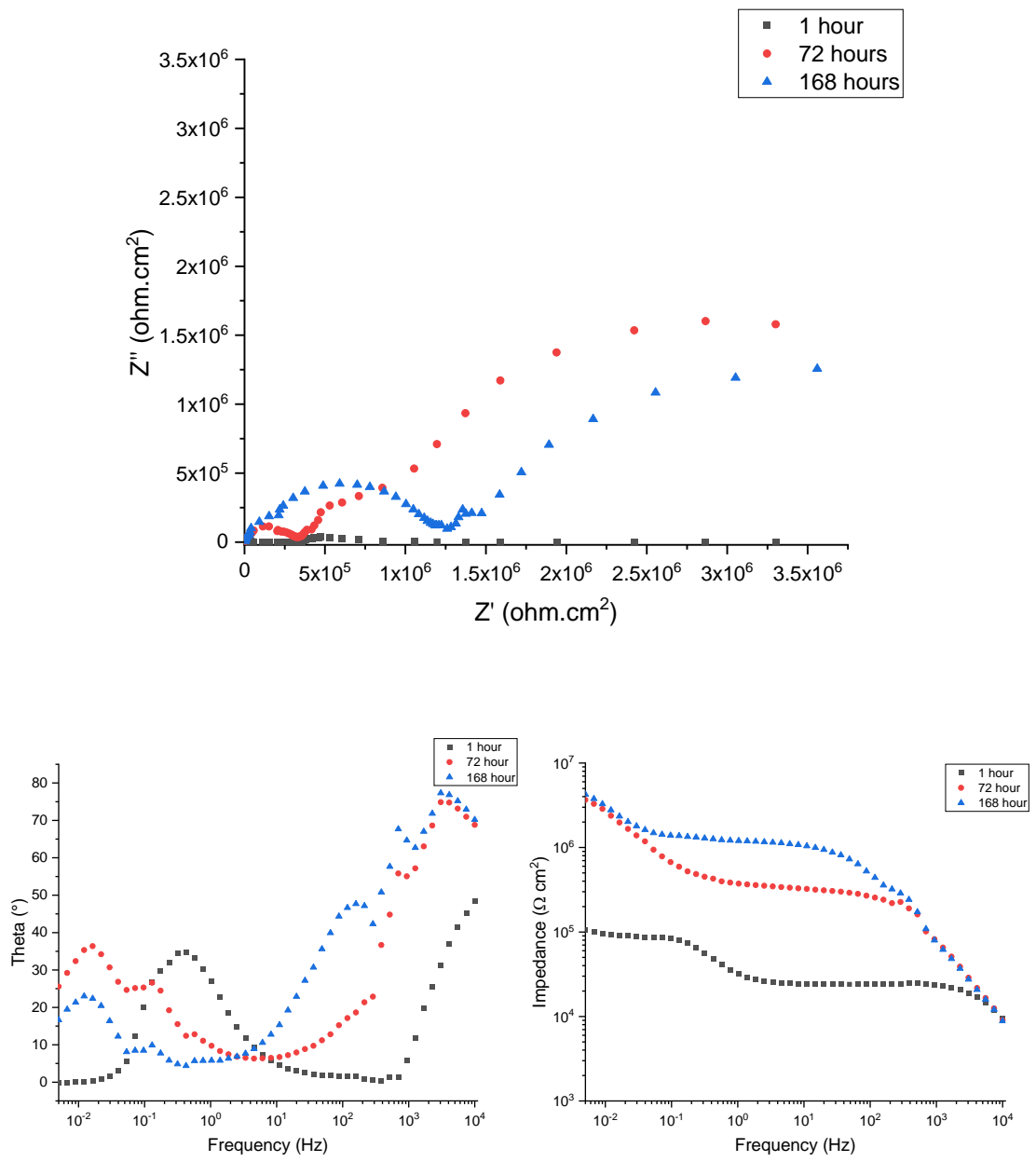


Figure B.6 – Nyquist and Bode plots for SiO_x coating with HMDSO:O₂ ratio 1:36 and DOE thickness 2 μm.